# A COMPUTATIONAL AND EXPERIMENTAL MODELLING OF THERMO-HYDRO-MECHANICAL PROCESSES IN A LOW PERMEABILITY GRANITE

by

Meysam Najari

August, 2013

Department of Civil Engineering and Applied Mechanics

McGill University, Montreal

A thesis submitted to

McGill University

in partial fulfillment of the requirements of the degree of

Doctor of Philosophy

© 2013 Meysam Najari



#### **ABSTRACT**

This thesis deals with the computational and experimental study of non-isothermal fluid transport in Stanstead Granite, a low-permeability rock. The study has several topics of interest to modern environmental geomechanics. These include the deep geologic disposal of heat-emitting nuclear fuel wastes, the extraction of geothermal energy, oil and gas recovery, and the geologic sequestration of carbon dioxide in supercritical form.

The equations governing the fully-coupled isothermal and non-isothermal behaviour of linear elastic porous geomaterials are presented and a finite element scheme is used to solve these equations. The basic physical and mechanical properties of Stanstead Granite are determined through a series of standard experiments. The permeability characteristics of the selected rock type were investigated using both steady state and hydraulic pulse testing techniques. The range of applicability of the conventional piezo-conduction equation for the interpretation of hydraulic pulse test results was investigated by comparing the fluid decay curves obtained form the solution of both the linear poroelastic equations and piezo-conduction equation for two typical rock types: Indiana Limestone and Westerly Granite. A series of hydraulic pulse tests were performed on Stanstead Granite samples at the bench-scale with different geometries and boundary conditions. It was observed that regardless of how precisely the cavity was filled with de-aired water, air bubbles can still exist in the cavity and this air fraction can influence the results of hydraulic pulse tests. A novel technique is suggested for taking into account the influence of the volume of trapped air and eliminating its effect on the estimation of permeability. The alteration of permeability of Stanstead Granite under isotropic loading and unloading using steady state permeability measurement technique was also examined. The applicability of conventional THM models for the characterization of the Stanstead Granite subjected to heating was investigated. The experiments used in the research included THM tests on a cylindrical sample of saturated Stanstead Granite containing a fluid-filled cylindrical cavity. An apparatus capable of changing the temperature in a controlled fashion was designed and fabricated. The outer boundaries of the specimen were subjected to cycles of heating and cooling and the temperature and fluid pressure in the sealed cavity were recorded. The results obtained in the simulations compared favourably with measured temperature and pore pressure values.

### **RÉSUMÉ**

Cette dissertation étudie le transport fluide non-isotherme dans le granite de Stanstead, une roche de faible perméabilité, au moyen de simulations numériques et de tests expérimentaux. Elle est relative à plusieurs questions d'intérêt en géomécanique environnementale, dont notamment le stockage en couches géologiques profondes de déchets nucléaires actifs, l'extraction d'énergie d'origine géothermique, l'extraction de gaz et de pétrole, et le stockage géologique de dioxyde de carbone supercritique.

Les équations décrivant le comportement couplé isotherme et non-isotherme des (géo) matériaux poreux linéaires élastiques sont présentées, et la méthode des éléments finis est utilisée pour les résoudre. Les principales caractéristiques physiques et mécaniques du granite de Stanstead sont déterminées via une série de tests expérimentaux standards. Les propriétés de perméabilité du type de roche choisie sont investiguées à la fois au moyen de tests stationnaires et de techniques utilisant des impulsions hydrauliques. Le domaine de validité de l'équation conventionnelle de piézo-conduction pour l'interprétation de ces tests d'impulsion hydraulique est investigué en comparant les courbes de décroissance de pression fluide obtenues par les solutions de la poroélasticité linéaire et l'équation de piézo-conduction pour deux roches types: le calcaire d'Indiana et le granite de Westerley.

Une série de tests d'impulsion hydraulique est réalisée sur des échantillons de granite de Stanstead à l'échelle du laboratoire pour différentes géométries d'échantillon et différentes conditions aux limites. Indépendamment de la précision avec laquelle la cavité est remplie d'eau supposée ne pas contenir d'air, des bulles d'air sont observées dans la cavité, et leur présence influence les résultats obtenus par les techniques d'impulsion hydraulique. Une nouvelle technique est alors suggérée pour prendre en compte l'influence du volume d'air inclus, et éliminer son effet sur l'estimation de la perméabilité. La modification de

la perméabilité du granite de Stanstead sous chargement et déchargement isotrope est également analysée au moyen de tests de perméabilité stationnaires. L'applicabilité des modèles thermo-hydro-mécaniques pour la caractérisation du granite de Stanstead soumis à échauffement a également est aussi investiguée. Les tests expérimentaux utilisés dans cette partie de la recherche comprennent notamment des tests thermo-hydro-mécaniques appliqués à un cylindre de granite de Stanstead saturé contenant une cavité cylindrique remplie de fluide. Un équipement en vue de modifier la température de façon contrôlée a été conçu et réalisé, permettant de soumettre les frontières extérieures du spécimen à des cycles d'échauffement et de refroidissement, tout en enregistrant la température et la pression de fluide dans la cavité isolée. Les résultats obtenus par simulation présentent un bon accord avec les mesures de température et de pression.

#### **ACKNOWLEDGEMENS**

The author would like to express his immense appreciation to his supervisor, Professor A.P.S. Selvadurai for suggesting the topic of the research, continuous and extensive guidance and mentoring, and the sustained encouragement and support throughout the entire thesis program. The author feels deeply indebted for all he learned from his supervisor.

The author is grateful to his colleagues in the Geomechanics Group at the Department of Civil Engineering and Applied Mechanics, McGill University for their support and assistance; namely, Mr. L. Jenner, Mr. B. Hekimi, Mr. A. Glowacki, Mr. P. Selvadurai, Dr. A. Suvorov, Mr. A. Katebi, Mr. D. Cuneo, Mr. M. Boyd, and Mr. A. Gallagher. The author would also like to acknowledge the extensive technical assistance he received from Mr. J. Bartczak, Dr. W. Cook, Mr. S. Kecani, Mr. G. Bechard, and Mr. M. Przykorski in design, fabrication and assembly of the experimental facilities he used over the course of the research. The author is also thankful of Ms. G. Keating from the Department of Earth and Planetary Sciences, McGill University for conducting an XRF test and Mr. L. Martinez from the Department of Building, Civil and Environmental Engineering, Concordia University for conducting an MIP test. Special thanks are due to Mrs. Sally Selvadurai for her extensive editorial corrections of the current thesis and all the papers that resulted from the research. Sincere thanks go to Professor Thierry Massart, Université Libre de Bruxelles, for his assistance in translating the abstract of this thesis to French.

The research conducted in this thesis was supported by NSERC Strategic and Discovery Grants awarded to Professor A.P.S. Selvadurai, as well as the support of the NWMO. The author also wishes to acknowledge the financial support he received from Global, Environmental and Climate Change Center, Montreal, through FQRNT.

Finally, the author would like to express his deepest thanks to his parents and his sister who provided him with nothing but support and love throughout the course of this research. This thesis is dedicated to them.

## TABLE OF CONTENTS

AB	STRACT	iii
RÉ	SUMÉ	V
AC	KNOWLEDGMENTS	vii
LIS	T OF TABLES	xiii
LIS	T OF FIGURES	XV
LIS	T OF PUBLICATIONS	xxiv
1	INTRODUCTION AND LITERATURE REVIEW	
1.1	General	1
1.2	Isothermal poroelasticity	4
1.3	Permeability	7
1.4	Non-isothermal poroelasticity	12
1.5	Objectives and scope of the research	15
2	MECHANICAL AND PHYSICAL CHARACTERIZATION	OF
	STANSTEAD GRANITE	
2.1	General description	17
2.2	Chemical composition	18
2.3	Porosity	19
	2.3.1 Conventional saturation test	20
	2.3.2 Mercury intrusion porosimetry	21
2.4	Elasticity parameters and compressive strength	26
2.5	Tensile strength	29
2.6	Summary remarks	30
3	MECHANICS OF ISO-THERMAL POROELASTIC MEDIA	
3.1	Introduction	33

3.2	2 Terzaghi's theory of consolidation		
3.3	Theor	y of linear poroelasticity	37
	3.3.1	Governing equations	38
	3.3.2	Skempton's coefficient	40
	3.3.3	Constrained specific storage	40
	3.3.4	Fluid phase equation	41
	3.3.5	Solid phase equation	43
	3.3.6	Uncoupling stress from pore pressure	44
3.4	Summ	ary remarks	45
4	PERM	MEABILITY MEASUREMENT: THEORY AND	
	EXPI	ERIMENT	
4.1	Introd	uction	47
4.2	Hydra	ulic pulse testing: theory	48
	4.2.1	Governing equations	49
	4.2.2	Theoretical modelling	51
	4.2.3	Computational study of the effect of poroelastic coupling	54
	4.2.4	The effect of aspect ratio on the coupling behaviour	65
4.3	Hydra	Hydraulic pulse testing: experiment	
	4.3.1	Radially symmetric hydraulic pulse tests	69
	4.3.2	Patch pulse tests	74
4.4	Summ	ary remarks	78
5	THE	EFFECT OF AIR BUBBLES ON THE INTERPRETA	ATION
	OF H	YDRAULIC PULSE TESTS	
5.1	Introd	uction	80
5.2	Gover	ning equations	81
5.3	Comp	utational modelling of the effect of air inclusion on hydraulic tests	84
5.4	•	ability measurement of the small size sample	86

	5.4.1	Steady state tests	87
	5.4.2	Hydraulic pulse tests	88
	5.4.3	Back-calculation of compressibility change from the experiment	90
	5.4.4	Estimation of permeability range	92
	5.4.5	Injecting air in the cavity	94
5.5	Perme	ability measurement of the large sample	97
	5.5.1	Steady state tests	98
	5.5.2	Hydraulic pulse tests	99
5.6	Summ	ary remarks	102
6.	PERM	MEABILITY HYSTERESIS UNDER ISOTROPIC	
	COM	PRESSION	
6.1	Introd	uction	104
6.2	Sampl	e preparation	105
6.3	Testin	g facility and sample assembly	107
6.4	Steady	state permeability measurement	109
	6.4.1	Steady state test results	110
	6.4.2	Discussion on the steady state test results	113
6.5	Summ	ary remarks	114
7	THE	RMO-HYDRO-MECHANICS OF POROUS	
	GEON	MATERIALS	
7.1	Introd	uction	116
7.2	Gover	ning equations	117
	7.2.1	The constitutive equation for the porous solid	117
	7.2.2	Liquid phase equation	117
	7.2.3	Energy equation	119
	7.2.4	Computational modelling of fluid inclusion	120
7.3	Therm	al damage experiment	122
	7.3.1	Testing procedure	123

7.4	Immer	rsion thermal experiment	125
	7.4.1	Permeability measurement	126
	7.4.2	Thermo-hydro-mechanical experiment	128
	7.4.3	Experimental results and numerical simulations	129
7.5	Therm	o-hydro-mechanical experiment under controlled	133
	tempe	erature changes	
	7.5.1	The testing apparatus	133
	7.5.2	Permeability measurement	135
	7.5.3	Thermo-hydro-mechanical experiment	138
	7.5.4	Experimental results and computational modelling	140
7.6	Summ	ary	148
8	CON	CLUSIONS AND SCOPE FOR FUTURE RESEARCH	
8.1	Summ	ary and concluding remarks	151
8.2	Scope	for future research	155
	REFE	ERENCES	158
	APPE	ENDIX A: Petrological description of Stanstead Granite	176
	(unpu	blished report)	

## LIST OF TABLES

Table 2.1	The weight percentage of the chemical compounds of	19
	Stanstead Granite, compared with similar igneous rocks.	
Table 2.2	Details of the measurements and calculations done to Measure the porosity of Stanstead Granite.	20
Table 2.3	Experimental results of MIP tests performed on three samples of Stanstead Granite.	26
Table 2.4	The result of the splitting tensile strength tests performed on four samples of Stanstead Granite.	30
Table 2.5	The measured physical parameters compared to similar values available in the literature.	31
Table 2.6	Comparison of the UCS test results with similar results available in the literature.	32
Table 4.1	The mechanical, physical and hydraulic parameters applicable to Westerly Granite and Indiana Limestone.	61
Table 4.2	Storativity terms for Westerly Granite and Indiana Limestone.	62
Table 4.3	Permeability values for Stanstead Granite	74
Table 5.1	The results of steady state tests performed on Stanstead Granite sample S-SG.	88
Table 5.2	The results of steady state tests performed on the large sample of Stanstead Granite, L-SG.	98
Table 6.1	Steady state permeability tests on Stanstead Granite sample GDS1 at various confining pressures.	111
Table 6.2	Steady state permeability of Stanstead Granite Sample GDS2 at different confining pressures.	112

Table 6.3	Steady state permeability of Stanstead Granite sample GDS3	112
	at different confining pressures.	
Table 6.4	Change in the degree of anisotropy ( $K_{\rm GDS2}/K_{\rm GDS3}$ ) with the	114
	change of isotropic compression.	
Table 7.1	Range of values of permeability before and after thermal	125
	loading.	
Table 7.2	The results of sealing tests performed on a stainless steel	138
	cylinder.	
Table 7.3	Values of the parameters in the computational modelling of	144
	the THM experiment.	

### LIST OF FIGURES

Figure 1.1	Conceptual layout of the deep geological repository site below the Bruce site, Ontario, Canada (OPG, 2008).	3
Figure 1.2	The apparatus used by Darcy for the study of fluid flow through soils (Courtesy of Prof. Olivier Coussy, LCPC, Paris)	5
Figure 1.3	Changes in the pore pressure with time in the center of a sphere subjected to compressive surface traction (reproduced after Gibson et al., 1963)	7
Figure 2.1	The MIP testing apparatus at the Building Materials Laboratories at Concordia University.	22
Figure 2.2	The penetrometer with the bulb filled with mercury at the end of the low pressure range test.	23
Figure 2.3	Equilibrium of forces acting inside a capillary; forcing $(F_1)$ and opposing $(F_2)$ mercury intrusion into the capillary (after Aligizaki, 2006)	23
Figure 2.4	Cumulative porosity change versus pore diameter for samples $A$ , $B$ , and $C$ .	25
Figure 2.5	The Stanstead Granite cylinder, instrumented with two rosette strain gauges prepared for the uniaxial compressive test.	27
Figure 2.6	Axial stress-axial strain curve for an unconfined compression test performed on a Stanstead Granite sample.	27

Figure 2.7	The axial stress-strain curve for the last unloading curve before failure of the Stanstead Granite sample	28
Figure 2.8	The change of circumferential strain with axial strain for the last unloading cycle before failure in a Stanstead Granite sample.	28
Figure 2.9	The testing assembly used for performing Brazilian tensile strength tests (the assembly is shown from two different angles).	30
Figure 4.1	Geometry and boundary conditions assumed for the axisymmetric one-dimensional stress hydraulic pulse test.	55
Figure 4.2	Geometry and boundary conditions assumed for the one- dimensional strain hydraulic pulse test.	55
Figure 4.3	Schematic view for the radially symmetric hydraulic pulse testing of an infinitely extended rock mass	58
Figure 4.4	The geometry and boundary conditions of the problem examined by Hart and Wang (1998).	58
Figure 4.5	Comparison of the results obtained by Hart and Wang (1998) with the results of the current study. The figure also shows the detail of the initial 120 seconds and the geometry and boundary conditions of the problem.	60
Figure 4.6	Mesh configuration for modelling: (a) one-dimensional hydraulic pulse test (25028 elements), (b) radially symmetric hydraulic pulse test (30017 elements).	62

Figure 4.7 Comparison of the pressure decay curves obtained from 63 Biot's theory of poroelasticity with those obtained using the piezo-conduction equation for the one-dimensional hydraulic pulse test. Figure 4.8 Comparison of the pressure decay curves obtained from 64 Biot's theory of poroelasticity with those obtained using the piezo-conduction equation for a radially symmetric hydraulic pulse test. Figure 4.9 Comparison of the computational results obtained from 67 the Biot poroelasticity equations with the piezoconduction equation for one-dimensional constant stress and constant strain hydraulic pulse testing for different aspect ratios. Figure 4.10 Comparison of the computational results obtained from 68 the Biot poroelasticity equations with the piezoconduction equation for radially symmetric hydraulic pulse testing for different aspect ratios. 70 Figure 4.11 Experimental faculty for measuring the permeability of low permeability geomaterials (Frame designed by Mr. A. Chevrier, Carleton University). Figure 4.12 Components of the permeameter used to perform 71 hydraulic pulse tests on fully-drilled samples. 72 Figure 4.13 Decay of cavity pressure in 3 hydraulic pulse tests performed on a dummy aluminum cylinder, using an Oring for the sealing.

Figure 4.14	Results of hydraulic pulse tests performed on a fully drilled Stanstead Granite cylinder (sample $S_D$ ). The analysis of the data was done using the piezo-conduction equation and neglecting the compressibility of the solid grains.	73
Figure 4.15	Decay of cavity pressure in hydraulic pulse tests performed on a Plexiglas, using gasket for the sealing.	75
Figure 4.16	Components of the permeameter used to perform hydraulic pulse tests on undrilled samples.	75
Figure 4.17	Results of hydraulic pulse tests performed on an undrilled Stanstead Granite cylinder (sample $S_{\text{U}}$ ). The analysis of data was done using the piezo-conduction equation and neglecting the compressibility of the solid grains.	76
Figure 4.18	Sample $S_U$ : (a) Geometry and boundary conditions used for the piezo-conduction equation; (b) Geometry and boundary conditions used for Biot's poroelasticity equations.	77
Figure 5.1	Compressibility of air-water mixtures with different air fractions.	83
Figure 5.2	The geometry and boundary conditions of the one-dimensional hydraulic pulse test.	85
Figure 5.3	Effect of air bubbles on cavity pressure decay.	85
Figure 5.4	The assembly of sample S-SG.	86

Figure 5.5 Schematic view of the hydraulic pulse test experiment 87 performed on sample S-SG. 88 Figure 5.6 Changes in cavity pressure for steady state tests performed on Stanstead Granite sample S-SG, at different flow rates. Figure 5.7 Hydraulic pulse tests performed on sample Stanstead 89 Granite S-SG. Figure 5.8 91 Change of  $C_{eq}$  with cavity pressure increase in Stanstead Granite sample S-SG. Figure 5.9 Experimental results for the build-up of cavity pressure 92 due to pumping water at the rate of Q=2ml/min, for Stanstead Granite sample S-SG. 93 Figure 5.10 Hydraulic pulse test results performed on Stanstead Granite sample S-SG with a maximum cavity pressure of 120 kPa. Figure 5.11 Hydraulic pulse test results performed on Stanstead 94 Granite sample S-SG with a maximum cavity pressure of 265 kPa. Figure 5.12: Hydraulic pulse test results performed on Stanstead 94 Granite sample S-SG with a maximum cavity pressure of 660 kPa. Figure 5.13 Experimental results for the build-up of cavity pressure 96 due to pumping water at the rate of Q = 2ml/min, for the three sets of hydraulic pulse tests performed on Stanstead Granite sample S-SG.

Figure 5.14 Hydraulic pulse test results performed on Stanstead 96 Granite sample S-SG with three different air fractions. 98 Figure 5.15 A schematic view of the setup used for measuring the permeability of Stanstead Granite sample L-SG. Changes in cavity pressure with respect to time for the 99 Figure 5.16 steady state tests performed on Stanstead Granite sample L-SG. Figure 5.17 The measured fluid cavity pressure decay curves for 100 Stanstead Granite sample L-SG. 100 Figure 5.18 Experimental results for the build-up of cavity pressure due to pumping water at the rate of Q=2ml/min, for Stanstead Granite sample L-SG. Figure 5.19 Hydraulic pulse test results performed on Stanstead 101 Granite sample L-SG for the average initial cavity pressure of 130 kPa. Figure 5.20 Hydraulic pulse test results performed on Stanstead 101 Granite sample L-SG for the average initial cavity pressure of 330 kPa. Figure 5.21 Hydraulic pulse test results performed on Stanstead 102 Granite sample L-SG for the average initial cavity pressure of 640 kPa. Figure 6.1 (a) The Stanstead Granite slab that the specimens were 106 cored from; (b) the three Stanstead Granite cylinders used in the study of permeability hysteresis under isotropic loading.

Figure 6.2	Schematic layout of the saturation chamber (after Selvadurai et al., 2011).	106
Figure 6.3	Granite sample mounted on the pedestal and covered by a rubber gasket.	107
Figure 6.4	Schematic view of the GDS cell used for performing the permeability hysteresis tests on Stanstead Granite (reproduced after Glowacki, 2008).	108
Figure 6.5	The schematic arrangement of the setup used for steady state permeability measurement of cylindrical Stanstead Granite samples subjected to confining pressure (reproduced after Selvadurai et al., 2011).	110
Figure 6.6	The change of permeability with an isotropic compression change for Stanstead Granite samples GDS 1, GDS 2 and GDS 3.	113
Figure 7.1	Cross section of the permeameter connected to the sample surface and the components of the assembly.	123
Figure 7.2	Attainment of steady state flow in the granite sample before and after thermal loading.	124
Figure 7.3	Geometry of the Stanstead Granite sample (dimensions are in cm). The thermally insulated parts are shown as dashed lines.	126
Figure 7.4	Steady state tests with a flow rate of 0.01 ml/min (for 1800 seconds), followed by hydraulic pulse tests.	127
Figure 7.5	Steady state tests with a flow rate of 0.02 ml/min (for 1200 seconds), followed by hydraulic pulse tests	127

Figure 7.6	Schematic view of the thermo-hydro-mechanical experimental setup	128
Figure 7.7	Change of cavity pressure with time due to the immersion of the Stanstead Granite sample in hot and cold water containers.	129
Figure 7.8	Change of cavity temperature (average temperature of the cavity) with time due to the immersion of the Stanstead Granite sample in hot and cold water containers.	130
Figure 7.9	Geometry and boundary conditions of the THM problem.	131
Figure 7.10	Change of cavity pressure with respect to cavity temperature change, plotted on the phase diagram of water (The pressure in this diagram is absolute pressure).	132
Figure 7.11	Schematic view of the THM setup.	134
Figure 7.12	Steady state tests with a flow rate of 0.02 ml/min (for 7200 seconds), followed by transient decay tests.	137
Figure 7.13	The apparatus prepared for performing the THM experiment.	139
Figure 7.14	The measured temperature on the circumference of the sample during three experiments.	140
Figure 7.15	The measured change of temperature on the top surface of the sample during three experiments.	140
Figure 7.16	The change in the cavity temperature during the three cycles of heating and cooling.	141

Figure 7.17	Comparison of the results of THM experiments with computational results using pressure dependent compressibility values for the cavity fluid.	141
Figure 7.18	Geometry and boundary conditions of the THM problem.	143
Figure 7.19	Comparison of compressibility changes with pressure for cavity fluids containing different amounts of dissolved air contributing to the compression.	145
Figure 7.20	Comparison of the results of THM experiments with computational results using constant compressibility values for the cavity fluid.	146
Figure 7.21	Volumetric expansion of the cavity due to a temperature increase on the sample surface at the start of the heating stage ( $\varphi$ =0.005).	147
Figure 7.22	Volumetric contraction of the cavity due to a temperature decrease on the sample surface at the start of the cooling stage ( $\varphi$ =0.005).	148
Figure 7.23	Change of cavity pressure (Absolute pressure) with respect to the cavity temperature change, plotted on phase diagram of water.	148

#### LIST OF PUBLICATIONS

- Selvadurai, A.P.S. & Najari, M. (2013), On the interpretation of hydraulic pulse test on rock specimens. *Advances in Water Resources*, Vol. **53**, 139-149.
- Najari, M. & Selvadurai, A.P.S. (2013), Thermo-hydro-mechanical response of granite to temperature changes. *Environmental Earth Sciences*, DOI 10.1007/s12665-013-2945-3.
- Najari, M. & Selvadurai, A.P.S. (2013), Hydraulic pulse testing at the bench-scale, role of air voids, *Journal of Geophysical Research-Solid Earth* (submitted).
- Najari, M. & Selvadurai, A.P.S. (2012), Thermo-hydro-mechanical behaviour of a low permeability geomaterial. In *Proceedings of the 46<sup>th</sup> US Rock Mechanics/Geomechanics Symposium*, Chicago, *USA* (ed. A., Bobet, R., Ewy, M., Gadde, J., Labouz, L., Pyrak-Nolte, A. Tutuncu, & E. Westman,), pp. 163-167. New York: Curran Associates Inc.
- Selvadurai, A.P.S. & Najari, M. (2011), Modelling of hydraulic pulse tests. In *Proceedings of the 13<sup>th</sup> International Conference of International Association for Computer Methods and Advances in Computational Mechanics (IACMAG)*, Melbourne, Australia (ed. N., Khalili & M., Oeser), pp. 431-435. Sidney: Center of Infrastructure Engineering and Safety.
- Najari, M. & Selvadurai, A.P.S. (2011), Hydraulic pulse testing of granite. In *Proceedings of the 2011 CSCE Annual Conference-Engineers-Advocates for Future Policy*, pp. 8-15. New York: Curran Associates Inc.

#### CHAPTER 1

#### INTRODUCTION AND LITERATURE REVIEW

#### 1.1 . General

The study of non-isothermal fluid transport in porous geomaterials has several applications of interest to modern environmental geomechanics. These include the deep geologic disposal of heat-emitting nuclear fuel wastes (Selvadurai and Nguyen, 1997; Tsang et al., 2000; Rutqvist et al., 2001), the extraction of geothermal energy (Brownell et al., 1977; Bodvarsson and Stefansson, 1989; Nakao and Ishido, 1998; Ilyasov et al., 2010), the geologic sequestration of carbon dioxide in supercritical form (Bachu, 2008; Lemieux, 2011; Shukla et al., 2012; Selvadurai, 2013) and oil and gas recovery (Vaziri, 1988; Bai and Roegiers, 1994; Gutierrez and Makurat, 1997; Pao et al., 2001). Despite the major use of nuclear energy in world-wide production of electric power, its wider acceptance as a safe option for energy production is prevented because of a lack of a suitable strategy for the disposal of heat-emitting radioactive waste. It is generally accepted that the deep geologic disposal of heat emitting waste in stable rock formations is more preferable to the continual storage of the spent fuel in water pools at the reactor sites themselves. The development of an acceptable strategy for deep geologic disposal will become more urgent and the reactor sites themselves age and will have to be decommissioned.

The deep geologic disposal of high level nuclear wastes relies on several engineered and natural barriers to retard the migration of radionuclides from the waste repository to the geosphere. The expected lifetime of the contaminant can range from 10,000 years to 100,000 years which is the time scale required to allow the radiation levels of the waste to approach the natural background radiation levels in rock masses. The containment strategy for the development and construction of a high level waste repository relies on several engineered and natural geological barriers. These include (i) waste containers made of copper or titanium that will seal the heat emitting fuel bundles (ii) engineered geological barriers composed of bentonitic clay which has buffering capabilities in the event of an accidental damage to the waste containers and (iii) a stable rock mass with sparsely located stable fractures. As an example of a nuclear waste repository site, Figure 1.1 shows the conceptual layout of the deep geological repository (DGR) site, that is planned to be constructed below the Bruce nuclear site in Ontario, Canada. The DGR site will be excavated at a depth of 680 m within the low permeability Cobourg Limestone formation (OPG, 2008).

The rock mass is considered as an integral part of the containment strategy for minimizing the release of radionuclides to the geosphere and subsequently to the biosphere, through contamination of potable water resources. This research is a contribution to the study of the thermo-hydro-mechanical (THM) that can occur in the intact saturated rock mass that can be subjected to the heat emitted from the stored waste. The topic of THM investigation of both crystalline and sedimentary rock masses that have been proposed as target rock formations for high emitting nuclear waste repositories have been studied by a number of countries including Belgium, Canada, France, Japan, Spain, Sweden, Switzerland, Russia, and USA. The DECOVALEX initiative (Jing et al., 1995; Dewiere et al., 1996; Tsang et al., 2005; Rutqvist et al., 2005; Chijimatsuet al., 2005) is an exercise that has brought together research being conducted in these countries for the modelling and assessment of THM behaviour in both rocks and engineered clay barriers.

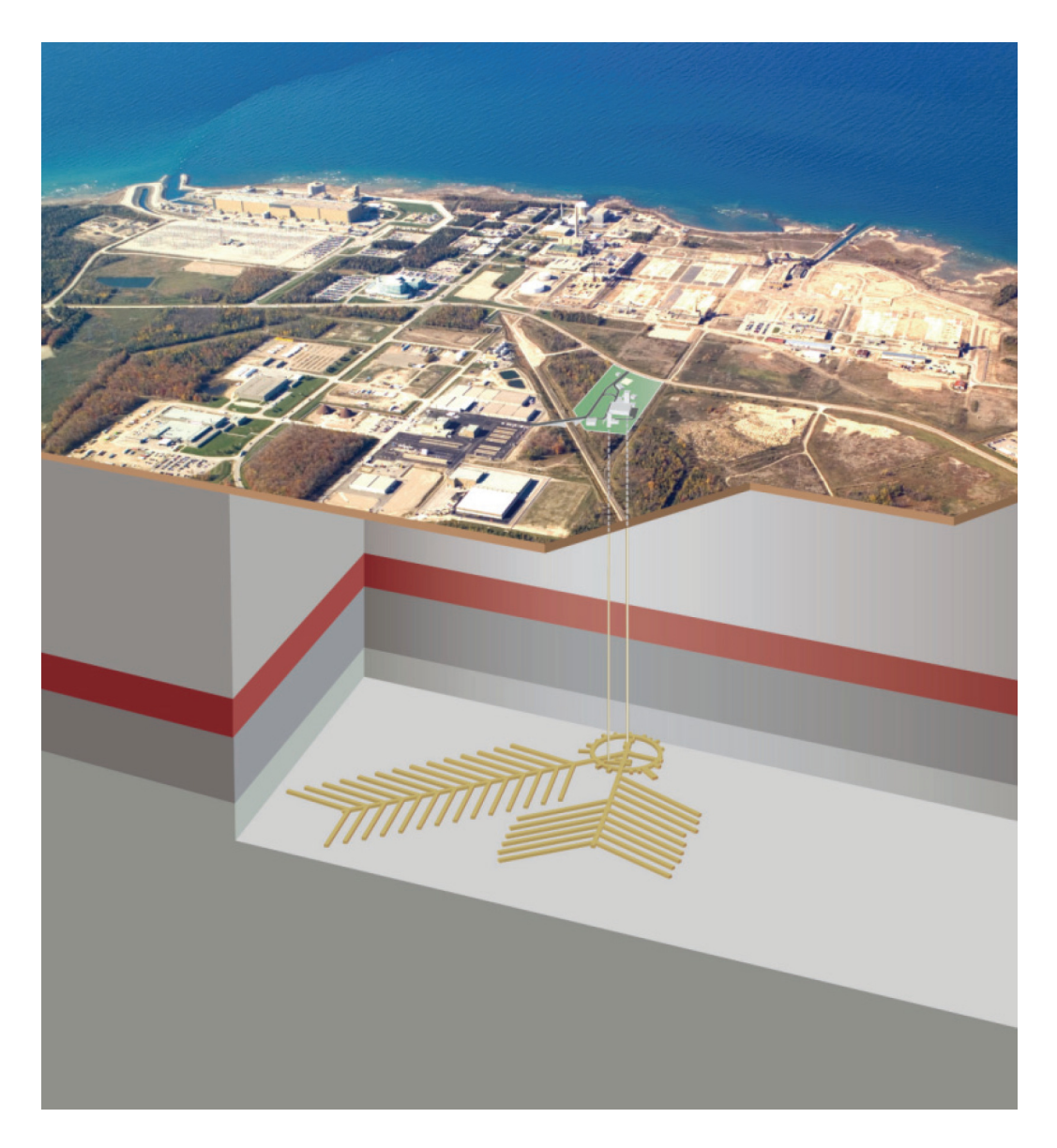


Figure 1.1: Conceptual layout of the deep geological repository site below the Bruce site, Ontario, Canada (OPG, 2008).

There are three processes that contribute to the transport of heat and moisture in saturated porous geomaterials: Thermal (T), Hydraulic (H), and Mechanical (M) processes. In this research, the thermo-hydro-mechanical (THM) behaviour of Stanstead Granite, which is a low permeability rock, was examined using experiments and computational modelling. Stanstead Granite, similar to granites found in the Canadian Shield, have been considered as suitable locations for deep geological disposal of nuclear wastes. Conceptual, computational and

experimental investigations were carried out to examine the validity of theories that have been proposed to describe the Thermo-Hydro-Mechanical behaviour of the granitic rock.

In this research, the isothermal hydro-mechanical (H-M) behaviour of Stanstead Granite was studied and then extended to include the interaction of thermal, hydraulic, and mechanical processes in the same rock type.

#### 1.2. Isothermal poroelasticity

The first contribution to the study of transport of fluid through non-deformable porous media was made by Henry Darcy (Darcy, 1856). He performed basic experiments on soils and found that the rate of fluid discharge through a column of soil is proportional to the cross sectional area of the column, the fluid potential (consisting of the Datum Head and Pressure Head), and inversely proportional to the length of the column. Figure 1.2 shows the apparatus used by Darcy for the study of fluid flow through a soil column.

The incorporation of the influence of deformability of the flow of fluids through porous media is generally attributed to Terzaghi (1923), although contributions of other investigators including Fillunger (1936) should also be noted. (De Boer 2005). Terzaghi proposed a one-dimensional theory that took into consideration the coupled interaction between the fluid flow and the deformations of a porous soil skeleton. This resulted in the one-dimensional theory of soil consolidation that is widely used in the calculation of consolidation settlement (Naylor and Doran, 1948; Row and Barden, 1966; Schmertmann, 1953; Scot, 1961). The theory was extended by Rendulic (1936) to include three-dimensional effects but the resulting theory is incomplete. Several investigators including Barron (1948), Murayama and Aka (1954) and Richart (1957) have applied what is basically Terzaghi's one-dimensional theory extended to axisymmetric and radially-symmetric states to investigate the consolidation of sand drains and other consolidation rate-enhancing engineering solutions (Barron, 1948; Rowe, 1968; Hansbo, 1979; Hansbo, 1981).

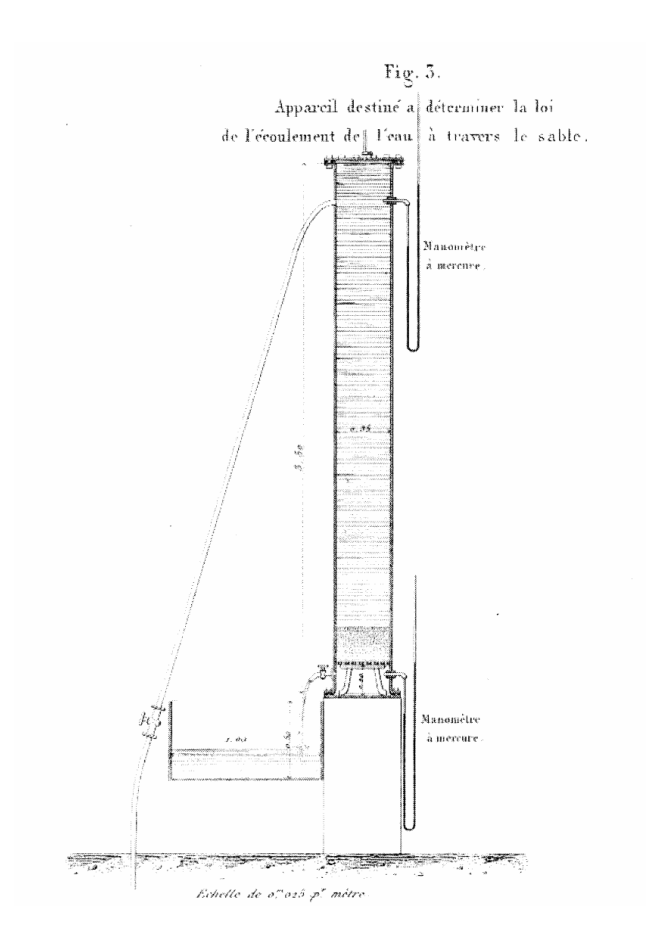


Figure 1.2: The apparatus used by Darcy for the study of fluid flow through soils (Courtesy of Prof. Olivier Coussy, LCPC, Paris).

The first complete theory of three-dimensional consolidation did not appear until the definitive study by Biot (1941a, b). Biot's fundamental contribution to poromechanics is based on the following assumptions (i) the application of external stress to a fluid-saturated porous medium can result in a change in the pore fluid pressures (ii) the change in the pore water pressure has a corresponding volume change in the porous structure and (iii) the stress-strain relations are linear (iv) the stress-strain relations under final equilibrium conditions are reversible (v) strains are small (vi) the water flow through the porous medium follows Darcy's law.

The early applications of Biot's three-dimensional theory of poroelasticity were obtained by Biot (1941b), Biot and Clingan (1941, 1942) Biot (1956), Paria (1957), McNamee and Gibson (1960a, b) and further references are given by Yue

(1992), Nguyen (1995), Selvadurai (1996a, 2000, 2007) and Selvadurai and Suvorov (2012).

The first attempt to compare the consolidation theories of Terzaghi and Biot was made by Cryer (1963) who used both theories to develop a result for the pore pressure induced at the center of a surface-drained porous sphere by the application of an isotropic compressive radial traction. Biot's theory showed that the pore pressure increases to a value higher than the surface traction, depending on the Poisson's ratio, and then decays until the pore pressure is completely dissipated. The reason for the excessive increase in the pore pressure is that drainage from the outermost layer of the sphere causes a decrease in the volume of that layer, which consequently exerts a compressive stress state to inner layers. Figure 1.3 shows the changes in the pore pressure at the center of the sphere for three different values of Poisson's ratio. The vertical axis shows the normalized pore pressure at the center of the sphere and the horizontal axis is a dimensionless time factor,  $\sqrt{T}$ , defined as

$$\sqrt{T} = \sqrt{\frac{C_v t}{a^2}} \tag{1.1}$$

where  $C_{v}$  is the coefficient of consolidation, t is the elapsed time, and a is the radius of the sphere.

Cryer (1963) showed that since Terzaghi's theory does not couple the pore pressure and skeletal deformations it fails to predict the pore pressure rise at the early stages of the consolidation. The effect was observed earlier by Mandel (1953) in an experiment involving the compression induced consolidation of a rectangular region under a plane strain deformation due to a uniaxial load. The observation related to the pore pressure rise is referred to as the Mandel-Cryer effect. Thereafter, the effect was investigated by a number of researchers, including Verruijt (1965), de de Josselin de Jong and Verruijt (1965), Schiffman

et al. (1969), Sills (1975), Gibson et al. (1963, 1989), Mason et al. (1991), Selvadurai and Shirazi (2004) and Selvadurai and Suvorov (2012).

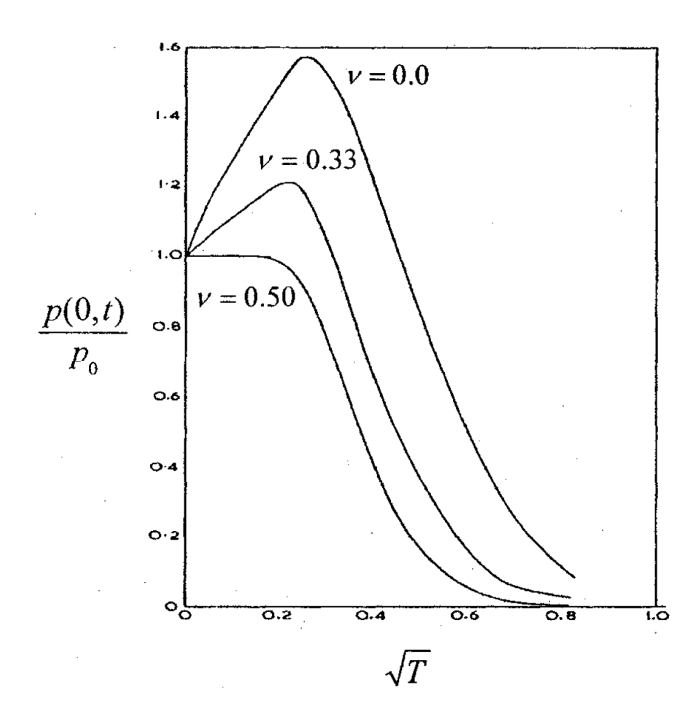


Figure 1.3: Changes in the pore pressure with time in the center of a sphere subjected to compressive surface traction (reproduced after Gibson et al., 1963).

The Biot's theory of poroelasticity, also known as *theory of linear poroelasticity*, is well documented in the literature and alternative expositions and representations are presented in a number of key articles including Rice and Cleary (1976), Detournay and Cheng (1993), Coussy (1995), Lewis and Schrefler (1998). Reviews of the subject of isothermal poroelasticity can be found in Scheidegger (1960), Paria (1963), Selvadurai (1996a, 2007), de Boer (1999), Wang (2000) and Schanz (2009).

#### 1.3. Permeability

Permeability is the key parameter in the study of poroelastic behavior of geomaterials under isothermal and non-isothermal conditions. Permeability of a porous medium is the parameter which governs the rate at which a fluid flows

through the pore structure (Harr, 1966; Bear, 1972; Selvadurai et al. 2005). The permeability of geomaterials can be determined using either steady state or transient tests depending on the relative values of the anticipated permeability.

Steady state tests are more reliable, since the only measurements needed to estimate the permeability are the hydraulic potential difference applied to initiate the fluid flow, the constant flow rate attained and the geometry of the flow domain. The steady state technique has been used extensively to measure the permeability of porous media with various geometries and boundary conditions, including in situ and laboratory tests. Very recently, Selvadurai and Selvadurai (2010) discussed the steady state patch permeability measurement of an Indiana Limestone block measuring 508 mm. Their experimental technique for measuring the near surface permeability of rock used a sealed annular patch. They measured the near surface permeability of the block and then used inverse analysis procedures to estimate the permeability characteristics of the interior of the rock.

Selvadurai and Glowacki (2008) examined the hysteresis of permeability in Indiana Limestone during isotropic loading and unloading. A steady state technique was used to measure the changes in permeability under confining pressures that varied between 5 to 60 MPa. They observed a two order of magnitude decrease in the permeability of the rock at 60 MPa confining pressure, compared to the permeability measured at a confining pressure of 5 MPa. There was no recovery of the permeability during the unloading. Heystee and Roegiers (1980) studied the effect of tensile and compressive stresses on the evolution of permeability. They developed a radial permeameter to measure the permeability of rocks under compressive and tensile stresses using the steady state technique. They tested three different types of rock: Indiana Limestone, red limestone, and granite. The samples measured 6.4 cm in diameter and 10 cm in length, with a central co-axial partially drilled cylindrical cavity, measuring 0.64 cm in diameter and drilled 8.7 cm deep. An increase in permeability was observed under increasing tensile stresses and a decrease in permeability was noted when the compressive stress increased. Heiland (2003) performed an exhaustive literature review on the experimental studies performed to determine the evolution of permeability under different loading and unloading trends associated with hydrostatic compression, triaxial compression, and uniaxial compression.

For low permeability geomaterials, with permeabilities in the range  $K \in (10^{-18}, 10^{-22}) m^2$ , the accurately verifiable steady flow rates that can be initiated in unstressed samples without causing damage (e.g. micro-mechanical hydraulic fracture) to the porous fabric can be small. For this reason, fluid transport characteristics of low permeability geomaterials are usually determined from transient flow tests. The use of transient flow tests was pioneered by Brace et al. (1968). They analyzed the decay of water pressure in a reservoir connected to one end of a cylindrical Westerly Granite sample. The samples tested measured 1.61 cm in length and 2.5 cm in diameter and were used to study the change of permeability with depth. In their formulation, they included the compressibility of the porous skeleton, pore fluid, and solid grains. These compressibilities contribute to the specific storage of a porous medium. However, for simplicity they neglected these compressibility values in the analysis of their experimental results. Lin (1977) discussed the analysis of the transient permeability tests including the specific storage term, using numerical methods. Bredehoeft and Papadopulos (1980) discussed the application of a technique for the in situ measurement of permeability of tight rocks, achieved by pressurizing a finite length of a shut-in well. They assumed fully radial fluid flow and presented a mathematical solution for the problem. Hsieh et al. (1981) and Neuzil et al. (1981) obtained an analytical solution for the piezo-conduction equation. Their method was able to obtain both the permeability and specific storage term from experimental data. Trimmer (1982) presented a confining cell similar to that used by Brace et al (1968) but of a larger size. The experiments focused on the measurement of the permeability of different low permeability rock types using samples of dimensions of 15 cm in diameter and 28 cm in height, using steady state tests for permeabilities higher than  $10^{-17}$  m<sup>2</sup> and the transient technique for lower permeabilities. Morin and Olsen (1987) suggested using the initial transient pressure buildup of the reservoir connected to the sample surface in a steady state experiment. They showed that the permeability can be estimated to an acceptable accuracy even before the water pressure in the downstream reaches a stabilized steady state value. Kranz et al. (1990) employed the technique of oscillating boundary conditions commonly used for the measurement of thermal diffusivity to measure the permeability of tight rocks. They proposed a mathematical formula to estimate the permeability and diffusivity of the tested rock by applying an oscillating pressure boundary condition at the upstream of the sample and measuring the oscillation of the pressure in the reservoir connected to the sample surface at the downstream. Their technique, however, was limited to the range of measurable diffusivities, since the optimum frequency of the oscillation on the ratio of upstream to downstream pore pressure depends upon sample size and permeability value. Selvadurai and Carnaffan (1997) measured the permeability of a cement grout sample measuring 75 mm in diameter and 150 mm in height. The sample contained a fully-drilled central cavity measuring 25 mm in diameter, giving a radially symmetric fluid flow. They applied a transient technique for measuring the permeability parameter. Selvadurai et al. (2005) discussed the development of an experimental facility to test the permeability of Barre Granite samples measuring 457 mm in diameter and 510 mm in height, containing a central cavity of diameter 51 mm, fully-drilled along the axis of symmetry of the cylinder. They used a transient technique to measure the permeability of intact samples. They also investigated the effect of temperature changes on the alteration of the permeability parameter. They observed that a temperature increase from ambient laboratory temperature to 140 °C did not affect the permeability of the rock. Song and Renner (2006) proposed an experimental technique to measure both the permeability and specific storage of a rock by performing a single transient test. They connected water reservoirs to the two ends of a cylindrical rock sample and pressurized the upstream reservoir linearly while monitoring the change of water pressure in the downstream. They also obtained the solution for the proposed boundary conditions. Selvadurai et al (2011a) used a one-dimensional hydraulic pulse testing technique to measure the permeability hysteresis of the Cobourg Limestone under isotropic compressive loading and unloading ranging from 5 to 20 MPa. Two samples measuring 100 mm in diameter and 200 mm in height were tested. Unlike similar tests performed on homogenous rock types, the Cobourg Limestone tested showed a permeability increase both in loading and unloading. The micromechanical damage or cracking at the inter-nodular boundaries due to the inhomogeneity of the material was associated with this observation. Selvadurai and Jenner (2013) examined the permeability of the same rock type under unconfined conditions. Four samples were tested using steady state and transient techniques. The samples measured 107 mm in diameter and 117 to 174 mm in height; they all contained a central cavity 13 mm in diameter. Radial flow was established along the bedding plane of the rock. The measured permeability ranged within three orders of magnitude. Selvadurai (2009) theoretically studied the influence of residual pore pressure gradients on decay curves for one-dimensional transient tests. The residual pore pressure can be due to a saturation process either under negative pressure or under a steady state flow that was induced prior to the transient test.

All experimental and computational studies mentioned above used transient fluid flow formulations that weakly take into account the effect of skeletal deformations through the incorporation of storativity terms. However, neglecting the poroelastic coupling between the pore water and porous skeleton can introduce errors in the estimation of permeability from transient tests. Walder and Nur (1986) examined the effect of poroelastic phenomena on the interpretation of pressure pulse decay curves in transient tests. They assumed that short samples had a state of constant strain while long samples were in a state of constant stress and showed that the hydraulic diffusivity for these two cases are size dependent and, therefore, one should expect a size dependency in the interpretation of the permeability from hydraulic pulse test results. They also performed some experiments to further investigate their claim; transient tests were conducted on several samples measuring 5.1 cm in diameter, with lengths varying from 21.7 mm to 47.6 mm. However, the effect was not clearly observed in the experiments. The variability in material properties from core to core was explained as the

probable reason that masked the influence of sample size dependency. Adachi and Detournay (1997) modified the formulation proposed by Kranz et al. (1990) for the oscillating pore pressure method used in the transient measurement of permeability. They analytically solved the coupled poroelastic problem of a very slender specimen tested for permeability using a pore pressure oscillation technique. The possible influences of the two approaches for examining the results of hydraulic pulse tests on the interpretation of permeability values have lead to comparative investigations and two examples are provided by Walder and Nur (1986) and Hart and Wang (1998) (see also Wang, 2000). Both investigations deal with hydraulic pulse tests conducted under one-dimensional conditions with the first investigating the poroelastic phenomena including non-linear pore pressure diffusion associated with large pore pressure gradients while the latter considers the three-dimensional poroelastic influences that arise when modelling the one-dimensional hydraulic pulse tests. It should also be noted that the problem examined by Hart and Wang (1998) relates to the computational modelling of the propagation of a hydraulic pulse on a one-dimensional element that is hydraulically sealed at all surfaces other than at the region subjected to pressure.

#### 1.4. Non-isothermal Poroelasticity

The classical theory of poroelasticity, proposed by Biot (1941a), is restricted to isothermal processes in geomechanics of fluid-saturated media. In a variety of problems associated with deep geological disposal of nuclear wastes, oil and natural gas recovery and geothermal energy extraction, the processes encountered are non-isothermal. Biot's isothermal theory of linear poroelasticity can be extended for including effects of temperature on the hydro-mechanical behavior of porous media.

The first attempts to formulate the coupled thermo-hydro-mechanical behavior of mixtures of porous and fluid media were presented by Brownell et al. (1977) and Morland (1978). In these studies the deformations of the porous solid are represented by approximate mixture formulations that do not reduce to the Navier equations applicable to a porous solid. Noorishad et al. (1984) used a finite

element approach to examine the coupled thermo-hydro-mechanical phenomena in saturated fractured rocks, investigating the fracture inflow near a heater. Booker and Savvidou (1984, 1985) performed analytical studies of the thermoelastic consolidation of a saturated soil containing a buried point heat source and a spherical heat source. They obtained the changes of pore pressure and stresses around the heat source with time. Savvidou and Booker (1988) later obtained the analytical solution for a spherical heat source with a decaying power output, located in a saturated infinite porous medium. Aboustit et al. (1985) developed a variational approach based on the results of Gurtin (1966) to examine the thermoelastic consolidation of porous media. The solid matrix was assumed to be linear elastic and the fluid was assumed to be incompressible. McTigue (1986) proposed a coupled thermo-hydro-mechanical formulation which was an extention of the Biot's isothermal theory of linear poroelasticity. The formulation accounted for the compressibility of the fluid, the deformability of the porous skeleton, and the solid constituents. Coussy (1989) developed a formulation for thermo-poro-elastoplasticity. He derived the equations from the thermodynamics of open systems and irreversible processes. Selvadurai and Nguyen (1995) presented a comprehensive development of the equations governing a fluid-saturated porous medium with compressible grains and compressible fluid. The heat conduction in the porous medium is represented by the uncoupled formulation which implies that neither the deformations nor the fluid flow will generate heating. Nguyen and Selvadurai (1995) also applied this development to examine pore pressure generation due to heating of a cementitious material. Rehbinder (1995) obtained an analytical solution for the stationary coupled thermo-hydro-mechanical problem of a spherical or a cylindrical heat source in an infinite medium, imposing simplifications to the physical process. These results provided a benchmark solution to be used for the validation of finite element codes. Zhou et al. (1998), also presented coupled thermo-hydro-mechanical formulation, based on Biot's isothermal poroelastic equations. They obtained the Laplace transform domain solutions for spherical and cylindrical cavities embedded in homogeneous and non-homogeneous infinite media, subjected to a temperature increase on the

cavity surface for simplified cases and used numerical techniques for Laplace transform inversion. It was observed that for low permeability geomaterials, the thermodynamically coupled heat and water flow has a negligible effect on heat flow. Also, the effects of mechanical deformation and pore pressure change on temperature change can be neglected, and thus the temperature distribution can be fully uncoupled from pore pressure and skeletal deformations which were implicit in the development of Selvadurai and Nguyen (1995). Gens et al. (1998) analyzed the thermo-hydro-mechanical measurements of a full scale in situ test, carried out in the granitic rock in the underground laboratory at Grimsel, Switzerland. The test, referred to as the FEBEX experiment, used heaters emplaced in steel canisters to model the heat emitted by the decaying nuclear wastes and employed a finite element code to implement their THM formulation. Pao et al. (2001) obtained a fully coupled THM model for a three phase porous medium containing water, gas, and heavy crude oil. Suvorov and Selvadurai (2010) obtained macroscopic constitutive equations of thermo-poro-visco-elasticity using eigenstrains, and examined the one-dimensional response under temperature change and undrained conditions. Comparisons were provided between thee computational model (ABAQUS<sup>TM</sup>) and the analytical results. Chen et al. (2009) presented the equations to model the THM behaviour of unsaturated porous media. They took into account the six different processes of stress-strain, water flow, gas flow, vapour flow, heat transport, and porosity evolution in their model. They also accounted for the phase transition and gas solubility in liquid. The implementation of the model required knowledge of 16 physical and mechanical parameters. The equations were solved using the finite element technique and validated the results against two existing laboratory and in situ measurements. Belotserkovets and Prevost (2011) performed an analytical study of the thermoporo-elastic response of a fluid-saturated porous sphere to a surface compressive traction, similar to that which was assumed for the Mandel-Cryer problem. They observed that the maximum temperature increase due to a surface mechanical stress of 1 GPa for an arbitrary sphere of rock with a radius of 4 m was less than 3% of the ambient temperature. Selvadurai and Suvorov (2012) examined the problem of the boundary heating of poroelastic and poroelasto-plastic spheres. The governing equations were similar to those developed by Selvadurai and Nguyen (1995) for THM behavior of a poroelastic material. The analytical results for the poroelastic case displays the THM Mandel-Cryer effect and the computational results elaborate how elasto-plasticity can moderate the generation of pore pressure at the center of the sphere.

In addition to above studies, exhaustive research is underway to study the different geo-environmental aspects of geological disposal of spent nuclear fuel, under the auspices of the DECOVALEX project (DEvelopment of COupled Models and their VALidation against EXperiments in Nuclear Waste Isolation). The project group consists of five international research teams. Examples of the results of their collaboration are summarized in the articles by: Rutqvist et al. (2001), Chijimatsu et al. (2005), Millard et al. (2005), Rutqvist et al. (2005), Nguyen et al. (2009), Wang et al. (2011). Their investigations included a comparison of different formulations to model the coupled unsaturated thermohydro-mechanical behaviour of the host rock under the thermal loading of nuclear wastes, for intact and fractured rocks, and also the analysis of large scale in situ tests performed at various underground research laboratories (URL), in different countries including Canada, Switzerland, and Japan.

#### 1.5. Objectives and scope of the research

The research presented in this thesis deals with the experimental and computational study of the Thermo-Hydro-Mechanical behavior of low permeability geomaterials. The experiments were performed on Stanstead Granite samples. The granitic rock is found in Eastern Canada, but is similar to the rocks of Canadian Shield being considered as a host rock for a deep geological repository for nuclear fuel wastes.

The physical and mechanical characteristics of the rock are examined through a series of standard experiments and the results are compared with similar values in the literature.

The application of Biot's theory of isothermal linear poroelasticity is discussed along with the limiting case where the stress field decouples from the fluid flow equation leading to the conventional piezo-conduction equation for the pressure decay. The effect of the compressibility of the porous skeleton, the solid grains and the permeating fluid on the hydro-mechanical behavior of geomaterials is also studied.

The permeability of the granitic rock was measured using steady state and hydraulic pulse testing techniques and over various one-dimensional and radially symmetric geometries and boundary conditions. The range of applicability of the piezo-conduction equation, which is used as a procedure for determining the hydraulic properties of rocks, is examined using alternative theoretical formulations. The influence of both free-air and dissolved air in the pressurized cavity that is used in the hydraulic pulse tests is also studied and a computational technique is proposed to minimize their effect on the estimation of permeability from experimental results.

Since the pressure of overburden in situ can affect the permeability characteristics of the rock, the change of permeability in Stanstead Granite was studied under isotropic loading and unloading using the technique developed by Selvadurai and Glowacki (2008).

The non-isothermal application of Biot's theory of poroelasticity is discussed. A testing facility was designed and fabricated in order to examine the thermo-hydromechanical behavior of low permeability geomaterials. Two samples of Stanstead Granite were tested to study the coupling effects of skeletal deformations, pore pressure and temperature changes on Stanstead Granite.

The finite element code of COMSOL Multiphysics<sup>TM</sup> was used throughout this research to develop computational results for isothermal and non-isothermal poroelastic theories.

#### **CHAPTER 2**

# MECHANICAL AND PHYSICAL CHARACTERIZATION OF THE STANSTEAD GRANITE

## 2.1. General description

Stanstead Granite is a medium gray, medium to coarse-grained rock, recovered from the Beebe region of the Eastern Townships in Quebec, Canada. The minerals are clear, sharply defined quartz (2.5 to 5 mm); feldspar laths (2 to 3 mm), which are semi transparent to milky white; muscovite flakes (0.5 mm), in small amounts; sharply contrasting biotite in flakes and clusters (3 mm) and some chlorite flakes (to 1mm). The grains are subhedral and give an interlocking granular fabric (Appendix A). The samples of Stanstead Granite used in this research showed no visual evidence of stratifications that could lead to anisotropic or transversely-isotopic estimates of properties.

A series of tests were performed to characterize the chemical composition, and physical and mechanical properties of the rock. These tests included X-ray fluorescence spectrometry (XRF), conventional saturation porosity measurement, mercury intrusion porosimetry (ASTM, D4404-84) and a uniaxial compression test (ASTM D7012-04) to measure Young's modulus, Poisson's ratio, and the uniaxial compressive strength of Stanstead Granite. In addition, Brazilian Tests

(ASTM D3967-08) were used to estimate the tensile strength of Stanstead Granite.

## 2.2. Chemical composition

The X-ray Fluorescence Spectrometry (XRF) method was used to characterize the chemical composition of Stanstead Granite. The technique relies on the response of atoms to X-ray excitations. X-rays are electro-magnetic short wavelength radiation with high energy and high frequency. Excitation of minerals with X-ray radiation ionizes them. The X-ray radiation, if powerful enough, can dislodge an electron from an inner shell of an atom that will be replaced by an outer shell electron. This process emits energy since an inner shell electron has a stronger bound than an outer bound electron; the emitted energy is in the form of fluorescent radiation. Since the energy difference between the electron shells are fixed and known, an analysis of the emitted fluorescence radiation can be used to characterize the elements contained in a sample (Shackley, 2011).

An XRF test of Stanstead Granite was performed in the Earth and Planetary Sciences Department of McGill University. The weight percentage of the major elements is shown in Table 2.1 and compared to similar results from the literature. Analyzes were performed on fused beads prepared from ignited samples. It can be seen that silicon (Si) and aluminum (Al) are the two major elements in Stanstead Granite and igneous rocks, in general. These elements form the minerals of the rock.

Table 2.1: The weight percentage of the chemical compounds of Stanstead Granite, compared with similar igneous rocks.

	Stanstead Granite (Gray)	Average for granite rocks		
	Current XRF test results	Carmichael (1982)	Blatt et al. (2005)	
SiO <sub>2</sub>	69.50	72.08	72.04	
TiO <sub>2</sub>	0.3641	0.37	0.3	
$Al_2O_3$	15.48	13.86	14.42	
$Fe_2O_3$	2.8290	2.53	2.9	
MnO	0.0386	0.06	0.05	
MgO	1.35	0.52	0.71	
CaO	2.74	1.33	1.82	
Na <sub>2</sub> O	4.3392	3.08	3.69	
K <sub>2</sub> O	2.69	5.46	4.12	
$P_2O_5$	0.139	0.18	0.12	
BaO	884	-	-	
Ce	15	-	-	
$Cr_2O_3$	88	1	1	
Cu	2	1	1	
Ni	17	1	1	
V	45	-	-	
Zn	45	-	-	
LOI	0.75	-	-	
OTHER				
MINERALS	=	=	=	
Total	100.33	99.47	100.17	

<sup>\*.</sup> The results are expressed as weight percent from  $SiO_2$  to  $P_2O_5$ , and as ppm for the trace elements (BaO to Zn).

## 2.3. Porosity

Porosity is defined as the ratio of the volume of the pores to the bulk volume of the material. There are several methods available for measuring the porosity of porous media. Two of the most common techniques are conventional saturation test and mercury intrusion porosimetry (ASTM D4404-10). In this research, the conventional saturation test and mercury intrusion porosimetry (MIP) were used to estimate the porosity of Stanstead Granite.

#### 2.3.1. Conventional saturation test

Three disk-shape specimens were prepared from a cylindrical Stanstead Granite sample. The specimens measured,  $S_1$ : D=48.04±0.00 mm, H=16.39±0.35 mm;  $S_2$ : D=47.96±0.00 mm, H=19.23±0.06 mm;  $S_3$ : D=47.97±0.00 mm, H=20.31±0.43 mm, where D is the diameter and H is the height of the disks. The values are the average of three diameter and height measurements done on each sample. The samples were dried in the oven, at a temperature of 160 °C, for 48 hours. They were then removed from the oven and weighed, using a digital scale with a precision of ± 0.0001 g. The samples were saturated in a vacuum chamber for 24 hours and kept in the chamber for another 48 hours in order to allow the negative pressure to dissipate. The samples were then removed from the water, surface-dried using a cloth and weighed. The same testing procedure was repeated for each of the three samples but this time they were surface-dried using air flow from a blower at room temperature. The results of both measurements are given in Table 2.2.

Table 2.2: Details of the measurements and calculations done to measure the porosity of Stanstead Granite.

Sample	D	Н	$V_{\it bulk}$	$W_{Dry}$	$W^{1}_{sat}$	$W^2_{sat}$	$ ho_{ extit{dry}}$	$n^1$	$n^2$
	mm	mm	$mm^3$	g	g	g	g/cm <sup>3</sup>	%	%
<b>S</b> 1	48.04	16.39	29708.17	78.7618	78.9754	78.9100	2.651	0.72	0.50
S2	47.96	19.23	34739.90	92.4040	92.6483	92.5850	2.660	0.70	0.52
<b>S</b> 3	47.97	20.31	36706.27	97.6540	97.9211	97.8200	2.660	0.73	0.45

<sup>\*.</sup> The superscript 1 represents the results for the samples surface-dried using a cloth and superscript 2 represents the results for the samples surface-dried using blowing air.

The average porosity of the rock was measured as 0.7% for the samples surface-dried using a cloth and 0.5%, for the samples surface-dried using blowing air. The blowing air dries the sample to a greater depth, compared to using a cloth to dry the surface; therefore, a lower porosity value is obtained. Also, using the above results, the bulk density of the dry sample was calculated to be 2.65 g/cm<sup>3</sup>.

#### **2.3.2.** Mercury intrusion porosimetry

Mercury intrusion porosimetry (MIP) has proved to be a useful technique in measuring the porosity of porous materials, specially those with low porosity. The technique was first proposed by Washburn (1921). Ritter and Drake (1945) built the first MIP testing apparatus, which was able to inject mercury into pores with a diameter of less than 2 nm.

The parameters that can be measured using the MIP technique are the total pore volume, pore size distribution, density of solids and powders, and the specific surface area of pores (Aligizaki, 2006). Mercury is chosen as the intruding fluid since it has low vapour pressure, it is inert in terms of chemical reactivity with many materials, and has non-wetting properties for most surfaces. Because of the non-wetting property of mercury, if a porous specimen is immersed in mercury at atmospheric temperature, the mercury does not intrude into the pores. A liquid can wet a solid surface if the attraction between the solid and the liquid molecules is greater than the attraction of liquid molecules to each other. For comparison, the contact angle between water and many surfaces is between 20° to 30° while for mercury it is usually greater than 90° (Aligizaki, 2006).

Three granite samples (*A*, *B*, *C*) were tested at the Building Materials Laboratories of the Department of Civil Engineering at Concordia University. The tests were performed in accordance with ASTM: D4404-84. Sample *A* was cored by the technical staff at Concordia University from a Stanstead Granite rock cylinder of 50 mm in diameter and 100 mm in length. Samples *B* and *C* were cored from a same size Stanstead Granite cylinder in Geomechanics Laboratory of McGill University.

The first step was to dry the sample using a vacuum drying technique. The sample was placed in the penetrometer and the total assembly was weighed before it was placed inside the MIP testing apparatus, Figure 2.1. The penetrometer number was 11-878. The next step was to de-air the penetrometer, which also helps remove any dust from the surface of the sample. The de-airing continued till the *absolute pressure* reached 13.33 Pa. After de-airing the penetrometer, the pressure was increased to atmospheric pressure and the inlet valve was opened to allow mercury to fill the bulb. The volume of mercury required to fill the bulb was measured and used to estimate the bulk volume of the sample.



Figure 2.1: The MIP testing apparatus at the Building Materials

Laboratories at Concordia University.

As mentioned previously, the pressure inside the bulb was increased gradually to atmospheric pressure. The minimum controllable pressure that can fill the pores of the material is very important because it determines the upper bound of the pore sizes that can be measured in the apparatus. The penetrometer was then taken out, weighed, and placed back in the MIP testing machine for performing high pressure test. Figure 2.2 shows the penetrometer containing the sample and filled with mercury.

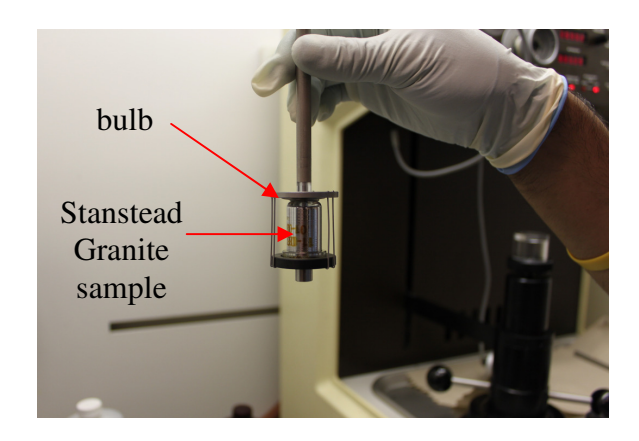


Figure 2.2: The penetrometer with a bulb that is filled with mercury at the end of the low pressure range test.

Pressure was increased incrementally in this step to 4000 atm, which corresponds to a pore diameter of 2 nm. After each pressure step increase, the system was allowed to equilibrate.

The relationship between the applied pressure and the radius of the intruded pore space can be estimated by assuming that the pore geometry is cylindrical with a circular opening. Figure 2.3 shows the free body diagram of the intrusion of mercury into a cylindrical pore with a diameter of  $r_p$  under a pore pressure of p.

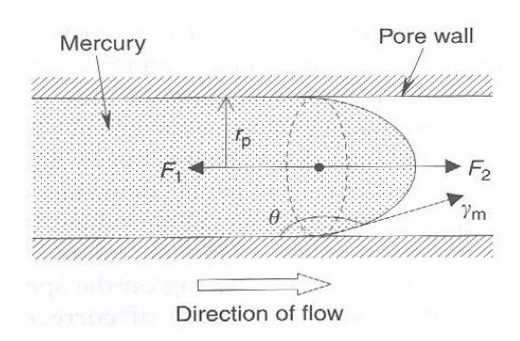


Figure 2.3: Equilibrium of forces acting inside a capillary; forcing  $(F_1)$  and opposing  $(F_2)$  mercury intrusion into the capillary (after Aligizaki, 2006).

Washburn (1921) wrote the equilibrium equation for the above free body diagram. From Figure 2.3, the resisting force can be written as

$$F_1 = -(2\pi r_p \omega_m \cos \theta) \tag{2.1}$$

where  $\omega_m$  is the surface tension between the inner wall of the cylinder and mercury and  $\theta$  is the contact angle between mercury and the solid surface.

Also, the driving force can be written as

$$F_2 = (\pi r_n^2) p \tag{2.2}$$

Given that the above driving and resisting forces should be equal under quasistatic conditions, the radius of the intruded force under the pore pressure p can be calculated

$$r_p = \frac{-2\omega_m \cos \theta}{p} \tag{2.3}$$

where,  $r_p$  is the pore radius.

Rootare and Prenzlow (1967) derived an equation to estimate the surface porosity of a porous material, using the measured pressure change versus intruded volume of mercury. The equation can be written for a simplified cylindrical pore geometry (Aligizaki, 2006). The work required to increase the surface area of a cylindrical pore wetted by mercury is

$$dW_1 = -dS\omega_m \cos\theta \tag{2.4}$$

where dS is the surface area of the pore wetted by mercury. The work required for driving mercury into the pore is

$$dW_2 = pdV (2.5)$$

where dV is the increment of the volume of mercury intruded into the pore by applying a pore pressure, i.e. p. Assuming that the intrusion of mercury in pores is reversible and thus no heat is produced in the process, the above two equations can be equated and the surface area of the wetted pore can be calculated

$$dS = \frac{pdV}{\omega_m \cos \theta} \tag{2.6}$$

Integrating from both sides of the above equation gives the total surface area of the material wetted by mercury

$$S = \frac{1}{\omega_m \cos \theta} \int_0^V p dV \tag{2.7}$$

Figure 2.4 shows the change of cumulative porosity with respect to pore diameter for the three samples tested. The average pore diameter varied between 200 and 0.01 microns.

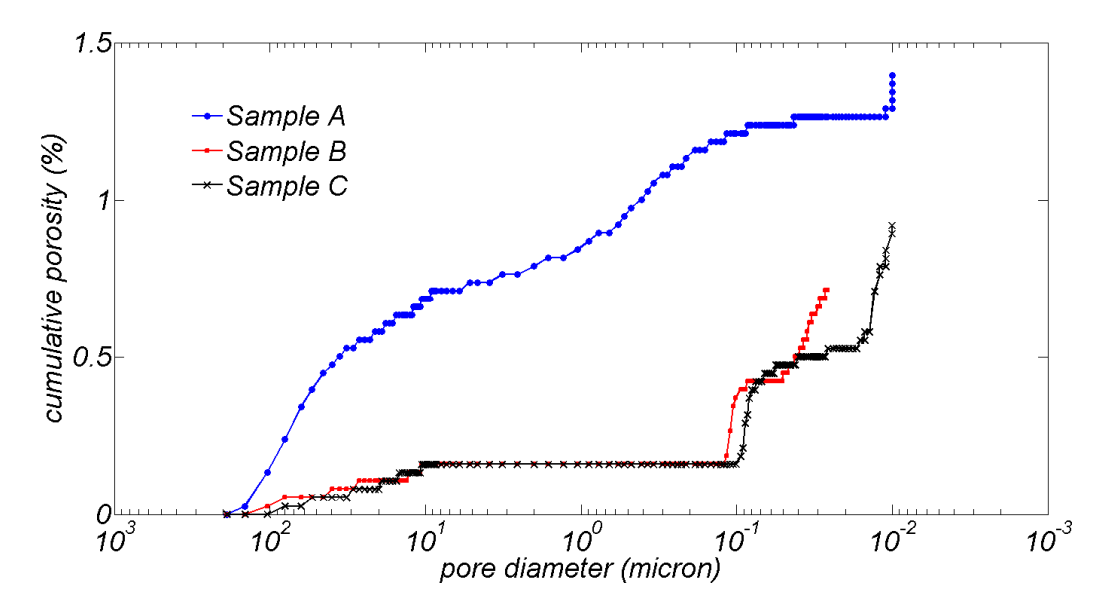


Figure 2.4: Cumulative porosity change versus pore diameter for samples A, B, and C.

The contact angle between the granite surface and the mercury was  $130^{\circ}$  (measured in the Construction Materials laboratories of Concordia University for the provided Stanstead Granite specimens) and the mercury surface tension was 485 dyn/cm (Aligizaki, 2006). Table 2.3 shows the results of the experiment. The porosity was measured as 1.40% for sample A, 0.71% for sample B and 0.92% for sample C. When compared to sample A, the samples B and C were prepared with

more attention at Geomechanics Laboratory of McGill University, resulting in less damage during the preparation phase. This would explain the slight discrepancy between the measured results of porosity for sample *A* when compared to samples *B* and *C*. It should be noted that the mercury intrusion porosimetry technique measures the total porosity, where it is composed of both connected and non-connected pores. Therefore, compared to the conventional saturation technique, the MIP result gives an upper bound for the porosity of a porous geomaterial.

Table 2.3: Experimental results of MIP tests performed on three samples of Stanstead Granite.

Sample	Dry Weight	Bulk Volume	Bulk density	Grain density	Porosity
	(g)	(ml)	(g/ml)	(g/ml)	%
A	7.141	2.7107	2.634	2.671	1.396
B	4.423	1.6743	2.645	2.660	0.713
C	4.150	1.5803	2.634	2.650	0.919

## 2.4. Elasticity parameters and compressive strength

The Young's modulus, Poisson's ratio, and uniaxial compressive strength of Stanstead Granite were measured and compared with the data available in the literature. Four uniaxial compression tests were performed on dry cylindrical samples measured 5 cm in diameter and 10 cm in height. The ASTM standard test method (ASTM, D7012-04) was used to determine the compressive strength and elastic moduli of the specimen. The samples were machined to obtain parallel surfaces. Two rosette strain gauges were attached to each sample at mid-height on opposite sides of the diameter and connected to a data acquisition system. Figure 2.5 shows a sample with the attached rosette strain gauge. Each sample was loaded in the MTS machine at a controlled load rate of 0.25 kN/s. The samples were initially loaded up to 35 MPa uniaxial compression; they were then unloaded at the same rate to 10 MPa; this cycle was repeated four times, and then the pressure increased to 65 MPa. Another four cycles of loading-unloading were applied to the samples at between 25 and 65 MPa; finally the pressure was

increased to failure. Figure 2.6 shows the axial stress-strain curve from the results of the uniaxial compression test performed on a cylindrical sample. The samples failed at an average compressive stress of 132 MPa. Reasonably well-formed cones were observed on both ends of the samples. The result of the last unloading cycle on each sample was used to estimate the Young's modulus and Poisson's ratio of the material.

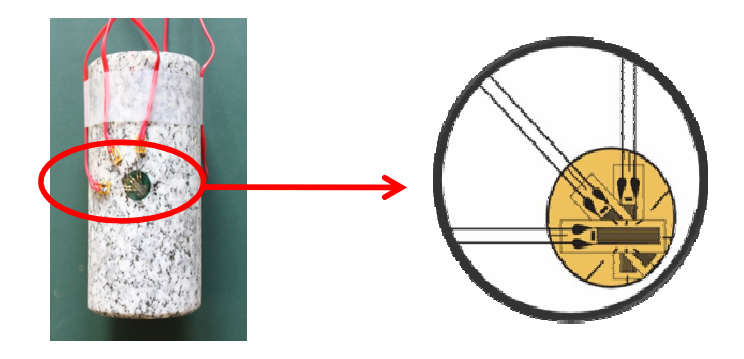


Figure 2.5: A Stanstead Granite cylinder, instrumented with two rosette strain gauges prepared for the uniaxial compressive test.

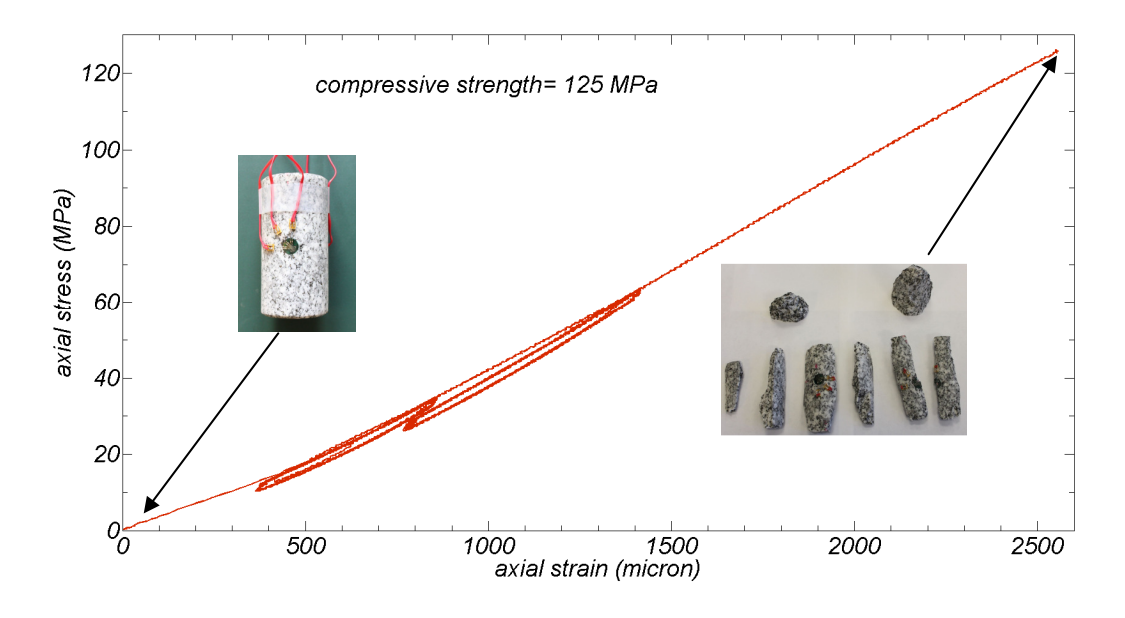


Figure 2.6: Axial stress-axial strain curve for an unconfined compression test performed on a Stanstead Granite sample.

Figure 2.7 shows the variation of axial strain with respect to axial stress for the so-called unloading cycle. The average slope of the curves obtained from the four

tested specimens, which gives the Young's modulus of the rock, was 61 GPa. Also, in order to estimate the Poisson's ratio, the fractional value of the circumferential strain with respect to the axial strain was calculated. Figure 2.8 shows the variation of the circumferential strain with axial strain. The average Poisson's ratio (i.e. the slope of the curve for the last unloading stage) was measured to be 0.17.

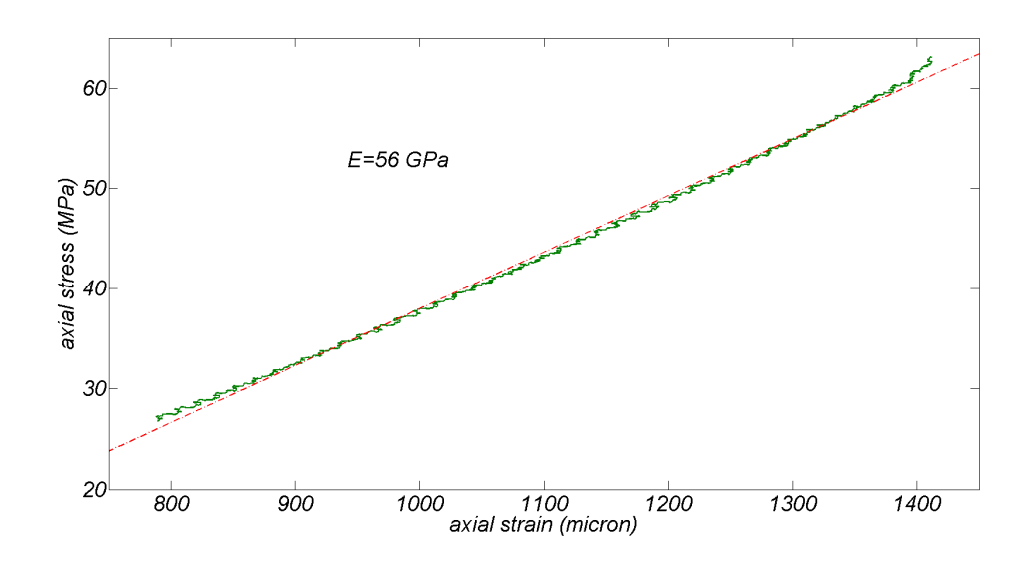


Figure 2.7: The axial stress-strain curve for the last unloading curve before failure of the Stanstead Granite sample.

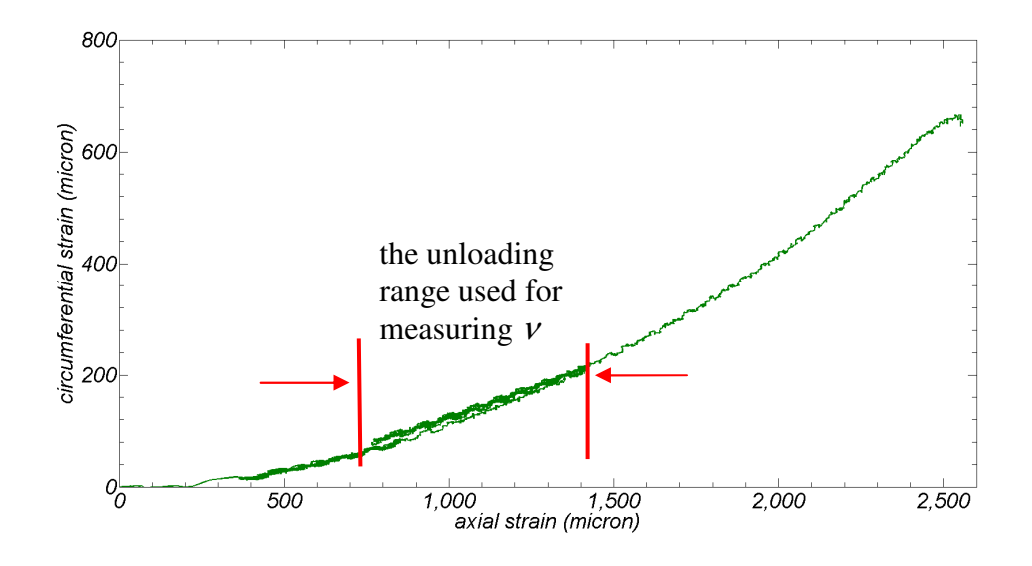


Figure 2.8: The change of circumferential strain with axial strain for the last unloading cycle before failure in a Stanstead Granite sample.

#### 2.5. Tensile strength

The splitting tensile strength of Stanstead Granite was measured by performing a series of experiments in accordance with ASTM D3967-08. It should be noted that the tensile strength is obtained by performing direct uniaxial tensile test (ASTM D2936-08), which is difficult and expensive. Splitting tensile test (Brazilian test) on the other hand is easy to perform and inexpensive and for this reason is the common test to examine the tensile strength of rock and concrete specimens.

Four cylindrical Stanstead Granite samples were tested. The ratio of thickness (t) to diameter (D) of the samples was between 0.72 to 0.74, which is within the specified range in the standard (0.2 to 0.75). The samples were cored from a Stanstead Granite slab and the thicknesses were reduced to comply with the above mentioned t/D specification using a diamond saw. The dimensions of the samples are shown in Table 2.4. Each dimension is the average of four measurements.

Figure 2.9 shows the testing apparatus. The samples were tested in an MTS 315.03 Load Frame with the capacity of 4500 kN. In order to avoid high stress concentration and local damage, plywood strips with the thickness of 4 mm were placed between the loading platens and the sample at the top and bottom contact areas. The samples were loaded at a constant displacement rate of 0.5 mm/min to failure. A 450 kN Strainsert<sup>TM</sup> load cell was used to measure the applied load.

The splitting tensile strength was calculated using the following equation (ASTM D3967-08)

$$\sigma_{t} = \frac{2P}{\pi t D} \tag{2.8}$$

where  $\sigma_t$  is the splitting tensile strength, P is the failure load, t is the thickness of the specimen, and D is the diameter of the specimen. The splitting tensile strength of the tested Stanstead Granite specimens ranged between (7.9 to 8.8) MPa with the average value of 8.4 MPa.

Table 2.4: The result of the splitting tensile strength tests performed on four samples of Stanstead Granite.

Sample	Height (mm)	Diameter (mm)	t/D	Loading Rate (mm/min)	Failure Load (kN)	Splitting tensile strength (MPa)
BT-1	79.58	107.11	0.74	0.5	115	8.6
BT-2	77.83	106.78	0.73	0.5	102	7.8
BT-3	77.22	106.24	0.73	0.5	110	8.5
BT-4	76.03	105.58	0.72	0.5	111	8.8





Figure 2.9: The testing assembly used for performing Brazilian tensile strength tests (the assembly is shown from two different angles).

## 2.6. Summary

Stanstead Granite is a medium gray, medium to coarse grained rock with crystal sizes ranging from 0.5 mm to 5 mm. The main minerals in Stanstead Granite are quartz, plagioclase, potassium feldspar, biotite and epidote. The porosity of the rock was measured using a classic saturation technique and mercury intrusion porosimetry (MIP). Using a standard saturation technique, the porosity was found to be in the range of 0.5% to 0.7%, while the MIP technique measured the

porosity in the range of 0.7% to 1.4%. Along with porosity measurements, the dry density of the material was also measured. Table 2.5 shows the results of the measurements compared to results of similar experiments performed on granitic rocks. The bulk dry density of the rock was (2630 to 2660) kg/m³ and the grain density was in the range of (2650 to 2670) kg/m³.

Table 2.5: The measured physical parameters compared to similar values available in the literature.

Rock type	Poro		Bulk Density (kg/m³)	Grain Density (kg/m³)
	Saturation	MIP	_	
Stanstead Granite (Current Study)	(0.45-0.73) <sub>3</sub>	(0.71-1.40) <sub>3</sub>	(2630-2660)*	(2650-2670)*
Stanstead Granite (Iqbal and Mohanty, 2007)	0.62 <sub>3</sub>	-	2650 <sub>3</sub>	-
Barre Granite (Selvadurai et al., 2005)	1.01	-	2630	2660
Barre Granite (Iqbal and Mohanty, 2007)	0.59 <sub>3</sub>	-	2660 <sub>3</sub>	-
Laurentian Granite (Iqbal and Mohanty, 2007)	0.64 <sub>3</sub>	-	2630 <sub>3</sub>	-

<sup>•</sup> The subscripts denote the number of samples tested for each parameter.

The mechanical properties of Stanstead Granite were also measured by performing 4 unconfined compression tests and four splitting tensile strength tests. The uniaxial compressive strength of the samples was measured as 132 MPa. The Young's modulus and the Poisson's ratio were measured as 61 GPa and 0.17, respectively. The splitting tensile strength of Stanstead Granite was also

<sup>•</sup> The values with an asterisk are the results of three samples tested using the saturation technique and three samples tested with MIP technique.

measured by conducting four Brazilian tests. The splitting tensile strength of the rock was within the range of (7.9 to 8.8) MPa. Table 2.6 shows the results of the uniaxial compression test and the Brazilian tests performed on the Stanstead Granite samples, compared to the similar results available in the literature.

Table 2.6: Comparison of the UCS test results with similar results available in the literature.

Rock type	Young's  Modulus	Poisson's	Compressive Strength	Brazilian tensile
1001 0/40	(GPa)	2400	(MPa)	(MPa)
Stanstead Granite (Current Study)	61 <sub>4</sub>	0.17 <sub>4</sub>	1324	8.44
Stanstead Granite (Iqbal and Mohanty, 2007)	66 <sub>3</sub>	0.16 <sub>3</sub>	173 <sub>3</sub>	7.96
Barre Granite (Selvadurai et al., 2005)	60	0.13	126	9.0
Barre Granite (Iqbal and Mohanty, 2007)	82 <sub>3</sub>	0.16 <sub>3</sub>	212 <sub>3</sub>	12.7 <sub>6</sub>
Laurentian Granite (Iqbal and Mohanty, 2007)	92 <sub>3</sub>	0.21 <sub>3</sub>	259 <sub>3</sub>	12.8 <sub>6</sub>

<sup>•</sup> The subscripts denote the number of samples tested for each parameter.

#### **CHAPTER 3**

## ISOTHERMAL BEHAVIOUR OF POROELASTIC MEDIA

#### 3.1. Introduction

This chapter deals with the iso-thermal hydro-mechanical behaviour of linear elastic porous geomaterials. The mechanical deformation and pore pressure have coupling effects and the study of these effects are important to several geomechanical applications, including consolidation of soils (Biot, 1941b; Biot and Clingan, 1941, 1942), heave and subsidence of the geologic media due to groundwater discharge or oil withdrawal (Geertsma, 1973; Hsieh, 1996; Burbey, 2008), and hydraulic fracturing (Detournay and Cheng, 1990; Boone and Detournay, 1990). Although the contributions made by Terzaghi (1923) in the development of the one-dimensional theory of consolidation are important, we focus attention on the three-dimensional theory of poroelasticity proposed by Biot (1941a, 1955, 1956, and 1957). The theory proposed by Biot (1941a) and its applications to fluid saturated media are documented by Paria (1957), Scheidegger (1960), Detourney and Cheng (1993), Coussy (1995), Selvadurai (1996a, 2007). An important study that outlines an alternative exposition of Biot's (1941a) theory in terms of parameters used in geomechanics practice is given by Rice and Cleary (1976). This chapter presents the equations governing two wellknown formulations of Terzaghi's theory of one-dimensional consolidation theory

and Biot's theory of linear poroelasticity. The presentation also gives a derivation of the piezo-conduction equation, which is used in the estimation of hydraulic conductivity parameters of porous fluid-saturated media.

## 3.2. Terzaghi's theory of consolidation

The first attempt to derive an expression for the transient flow of fluids in porous media was made by Terzaghi (1923) and became known as the theory of one dimensional consolidation. This theory is well-known in practice and is the most common technique for the estimation of time dependent settlement of soils induced by the loading of the soil surface. Terzaghi derived his formulation based on simplifying assumptions: (i) the soil is homogenous and isotropic, (ii) the soil is fully saturated, (iii) the compressibility of the water and solid grains is negligible, compared to that of the porous skeleton, (iv) the strains are infinitesimal, (v) the fluid flow and deformation are both one-dimensional, (vi) the fluid flow follows Darcy's Law throughout the process of consolidation that involves changes in the void ratio.

The mass conservation equation for a rigid porous medium, saturated with a compressible fluid is (Selvadurai, 2000a):

$$\nabla \cdot (\rho \mathbf{v}) + \frac{\partial}{\partial t} (\rho) = 0 \tag{3.1}$$

where  $\mathbf{v}$  is the velocity vector,  $\rho$  is the density of the fluid and  $\nabla$ . is the divergence operator.

However, for a deformable porous medium saturated with an incompressible fluid, as assumed by Terzaghi, Eq. (3.1) can be re-written as

$$\nabla . (\mathbf{v}) = \frac{\partial n}{\partial t} \tag{3.2}$$

where n is the porosity of the medium. Since the constituting solid grains are also incompressible, the whole deformation of the porous medium can be attributed to

the porosity change. Therefore, for one-dimensional fluid flow and deformation and assuming that the isotropic stress is positive in tension and the pore pressure is positive in compression, Eq. (3.2) can be written as

$$\frac{dv_z}{dz} = -\frac{d\varepsilon_z}{dt} \qquad \text{or} \qquad \frac{dv_z}{dz} = -\frac{1}{E_{oed}} \frac{d\sigma_z'}{dt}$$
 (3.3)

where  $v_z$  is the fluid velocity in the z direction,  $\varepsilon_z$  is the strain in the z direction and  $E_{oed}$  is the oedometric modulus defined as

$$E_{oed} = \frac{E(1-\nu)}{(1+\nu)(1-2\nu)}$$
 (3.4)

where E is the Young's modulus and  $\nu$  is the Poisson's ratio. Also,  $\sigma'_z$  in Eq. (3.3) is the effective stress in the z direction as defined by Terzaghi

$$\sigma_z' = \sigma_z + p \tag{3.5}$$

where  $\sigma_z$  is the total stress and p is the pore pressure. Also, from Darcy's Law, the velocity in the z direction can be written as a function of the pore pressure

$$v_z = -\frac{\tilde{k}}{\gamma_w} \frac{\partial p}{\partial z} \tag{3.6}$$

where  $\tilde{k}$  is the hydraulic conductivity. Using Eqs. (3.6) and (3.5) in Eq. (3.3) and assuming that the total stress on the soil mass does not change during consolidation

$$-\frac{\tilde{k}}{\gamma_w} \frac{\partial}{\partial z} \frac{\partial p}{\partial z} = -\frac{1}{E_{oed}} \frac{\partial p}{\partial t}$$
 (3.7)

Equation (3.7) is a diffusion type differential equation and can be re-written in the more common form as

$$C_{\nu} \frac{\partial^2 p}{\partial z^2} = \frac{\partial p}{\partial t} \tag{3.8}$$

where  $C_{\nu}$  is the consolidation coefficient given by

$$C_{\nu} = \frac{\tilde{k}}{\gamma_{\nu}} \frac{E(1-\nu)}{(1+\nu)(1-2\nu)}$$
 (3.9)

Equation (3.8) is the most commonly used, practical relationship for the study of consolidation in saturated soils.

Rendulic (1936) extended Terzaghi's one-dimensional theory of consolidation to obtain the diffusion equation in three dimensions. The mass conservation equation in a three-dimensional Cartesian coordinate system for a deformable porous medium saturated with an incompressible fluid, takes the form

$$\nabla . \mathbf{v} = -\frac{\partial \mathcal{E}_{v}}{\partial t} \tag{3.10}$$

Also, the generalized Darcy's Law for homogenous, isotropic saturated porous media takes the form

$$\mathbf{v} = -\frac{\tilde{k}}{\gamma_w} \nabla p \tag{3.11}$$

where  $\nabla$  is the gradient operator. Combining Eq. (3.11) and (3.12) gives

$$-\frac{\tilde{k}}{\gamma_w} \nabla^2 p = -\frac{\partial \varepsilon_v}{\partial t}$$
 (3.12)

The volumetric strain,  $\varepsilon_v$ , of an elastic porous medium can be written as a function of the effective stress and bulk modulus, i.e. K

$$\varepsilon_{\nu} = \frac{\sigma_{\nu}'}{K} \tag{3.13}$$

where  $\sigma'_{v}$  is the mean effective stress, defined as

$$\sigma_{\nu}' = \frac{1}{3} (\sigma_1 + \sigma_2 + \sigma_3) + p \tag{3.14}$$

where  $\sigma_1$ ,  $\sigma_2$  and  $\sigma_3$  are the principal total stresses. Rendulic (1936) assumed that the first invariant of total stress, i.e.  $J_1 = \sigma_1 + \sigma_2 + \sigma_3$ , does not change during the consolidation process. Based on the assumption of a constant invariant, Eq. (3.12) takes the form

$$-\frac{\tilde{k}}{\gamma_{w}}\nabla^{2}p = -\frac{1}{K}\frac{\partial p}{\partial t}$$
(3.15)

Therefore, for the three-dimensional consolidation we have

$$C_{\nu}\nabla^{2}p = \frac{\partial p}{\partial t} \tag{3.16}$$

The consolidation coefficient in three-dimensions,  $C_{\nu}$  , is

$$C_{\nu} = \frac{\tilde{k}K}{\gamma_{\nu}}$$
 or  $C_{\nu} = \frac{\tilde{k}E}{3\gamma_{\nu}(1-2\nu)}$  (3.17)

The classical theory of soil consolidation proposed by Terzaghi and its threedimensional extension (Rendulic, 1936), do not take into account the fully coupled interaction between the skeletal deformation and pore pressure.

# 3.3. Theory of linear poroelasticity

The partial differential equations governing coupled fluid flow and linear elastic deformation of a fluid-saturated isotropic porous medium were developed by Biot (1941a, 1955, 1956) and Biot and Willis (1957). There are two coupling effects: (i) the increase in pore pressure dilates the porous skeleton, (ii) the changes to the stress state in the porous skeleton induces pore pressure (Detournay and Cheng, 1993). These effects were taken into account in Biot's theory. The classical theory

of poroelasticity takes into account Hookean isotropic elastic behaviour of the porous skeleton, the elastic deformations of the solid material composing the porous skeleton, the compressibility of the pore fluid and fluid flow behaviour, that is characterized by Darcy's Law.

#### 3.3.1. Governing Equations

The constitutive equations relating the change in the pore pressure and the mean stress to the change in the volumetric strain and increment of fluid content for isotropic loading are defined as (Wang, 2000)

$$\begin{cases} \varepsilon_{v} = a_{11}\sigma_{v} + a_{12}p \\ \zeta = a_{21}\sigma_{v} + a_{22}p \end{cases}$$
(3.18)

where  $\sigma_{v}$  is the mean total stress, p is the pore pressure,  $\varepsilon_{v}$  is the volumetric strain and  $\zeta$  is the increment of fluid content, which is the increment of water volume per unit volume of soil.

The volumetric strain and increment of fluid content are defined as follows

$$\varepsilon_{v} = \frac{\delta V}{V} = \varepsilon_{1} + \varepsilon_{2} + \varepsilon_{3} \tag{3.19}$$

$$\zeta = \frac{\delta V_p - \delta V_f}{V} \tag{3.20}$$

where  $V_p$  is the pore volume,  $V_f$  is the fluid volume and V is the reference volume. Also, the indices,  $a_{ij}$ , are the coefficients of field variables defined by applying certain constraints on an elementary control volume (Wang, 2000). Maintaining the pore pressure constant (i.e. drained condition) and differentiating from the volumetric strain with respect to the mean total stress gives the coefficient  $a_{11}$ 

$$a_{11} = \frac{\partial \varepsilon_{v}}{\partial \sigma_{v}} \bigg|_{p=0} = \frac{1}{K}$$
 (3.21)

where *K* is the drained bulk modulus.

Maintaining the mean total stress constant and differentiating the volumetric strain with respect to pore pressure gives

$$a_{12} = \frac{\partial \mathcal{E}_{v}}{\partial p} \bigg|_{\sigma_{v}=0} = \frac{1}{H}$$
 (3.22)

where H is the poroelastic expansion coefficient.

A similar approach can be pursued for deriving the coefficients  $a_{21}$  and  $a_{22}$  in the fluid increment equation

$$a_{21} = \frac{\partial \zeta}{\partial \sigma_{\nu}} \bigg|_{p=0} = \frac{1}{H_1} \tag{3.23}$$

Energy conservation leads to the result that the  $H=H_1$  (Wang, 2000). Therefore, the linear transformation matrix is symmetric. Now we define

$$a_{22} = \frac{\partial \zeta}{\partial p} \bigg|_{\sigma_{c}=0} = \frac{1}{R} \tag{3.24}$$

where R is the unconstrained specific storage coefficient, or specific storage at constant stress, i.e.  $S_{\sigma}$ .

Substituting Eqs. (3.21) to (3.24) into Eq. (3.18) gives the constitutive equations for linear elastic porous media under isotropic loading as a function of the mean total stress and pore pressure

$$\begin{cases} \varepsilon_{v} = \frac{1}{K}\sigma_{v} + \frac{1}{H}p \\ \zeta = \frac{1}{H}\sigma_{v} + \frac{1}{R}p \end{cases}$$
(3.25)

## 3.3.2. Skempton's coefficient

Skempton's coefficient is defined as the ratio of the induced pore pressure to the change in applied stress for undrained conditions ( $\zeta = 0$ )

$$\delta \zeta = \frac{1}{H} \delta \sigma_{v} + \frac{1}{R} \delta p = 0 \quad \rightarrow \quad \delta p = -\frac{R}{H} \delta \sigma_{v} \quad ; \quad B = \frac{R}{H}$$
 (3.26)

where  $\frac{R}{H} = B$  is called Skempton's Coefficient (Rice and Cleary, 1976).

## 3.3.3. Constrained specific storage

The constrained specific storage or specific storage at constant strain is defined by

$$S_{\varepsilon} = \frac{\partial \zeta}{\partial p} \bigg|_{\varepsilon = 0} = \frac{1}{M} \tag{3.27}$$

Eliminating  $\sigma_{\nu}$  from the increment of fluid content in Eq. (3.25) gives

$$\zeta = \frac{K}{H} \varepsilon_{v} + \left(\frac{1}{R} - \frac{K}{H^{2}}\right) p \tag{3.28}$$

Therefore, the coefficient of p in Eq. (3.28) is the constrained specific storage term. Comparing Eq. (3.28) with the relationship for the unconstrained specific storage term (i.e. Eq. (3.24)), it can be concluded that

$$S_{\varepsilon} = S_{\sigma} - \frac{K}{H^2} \tag{3.29}$$

Also, K/H is called Biot-Willis coefficient (Wang, 2000)

$$\frac{K}{H} = \alpha \tag{3.30}$$

Thus, Eq. 28 can be re-written as

$$\zeta = \alpha \varepsilon_{v} + \frac{1}{M} p \tag{3.31}$$

Based on Eqs. (3.26) and (3.30), the constrained storage term can be written as

$$S_{\sigma} = \frac{\alpha}{KB} \tag{3.32}$$

## 3.3.4. Fluid phase equation

The fluid phase equation is comprised of Darcy's Law and the mass conservation equation. From Darcy's Law

$$\mathbf{v} = -\frac{\tilde{k}}{\gamma_w} \nabla p \tag{3.33}$$

where  $\tilde{k}$  is the hydraulic conductivity of the homogeneous isotropic porous material and  $\gamma_w$  is the specific unit weight of water.

The mass conservation law for a deformable porous medium saturated with a compressible fluid can be written as

$$\frac{\partial \zeta}{\partial t} + \nabla \cdot \mathbf{v} = 0 \tag{3.34}$$

Substituting the fluid velocity from Eq. (3.33) into Eq. (3.34) gives

$$\frac{\partial \zeta}{\partial t} - \frac{\tilde{K}}{\mu} \nabla^2 p = 0 \tag{3.35}$$

where  $\tilde{K}$  is the permeability of the homogeneous isotropic medium. Substituting the fluid increment, as a function of the mean total stress and pore pressure from Eq. (3.25), while replacing the moduli R and H from Eqs. (3.26) and (3.30), gives

$$\frac{\alpha}{KB} \left[ \frac{B}{3} \frac{\partial \sigma_{v}}{\partial t} + \frac{\partial p}{\partial t} \right] - \frac{\tilde{K}}{\mu} \nabla^{2} p = 0$$
 (3.36)

Recalling Eq. (3.32), the above equation can be re-written as

$$S_{\sigma} \left[ \frac{B}{3} \frac{\partial \sigma_{\nu}}{\partial t} + \frac{\partial p}{\partial t} \right] - \frac{\tilde{K}}{\mu} \nabla^{2} p = 0$$
 (3.37)

This equation can also be re-written if the volumetric strain  $(\mathcal{E}_{\nu})$  and pore pressure (p) are taken as the two independent variables. Substituting Eq. (3.30) into Eq. (3.25) gives

$$\sigma_{v} = K\varepsilon_{v} - \alpha p \tag{3.38}$$

Substituting the mean total stress from Eq. (3.38) into Eq. (3.37) gives

$$\alpha \frac{\partial \mathcal{E}_{v}}{\partial t} + S_{\sigma} (1 - \alpha B) \frac{\partial p}{\partial t} - \frac{\tilde{K}}{\mu} \nabla^{2} p = 0$$
 (3.39)

From Eqs. (3.29) and (3.32) it can be shown that

$$S_{\sigma}(1 - \alpha B) = S_{c} \tag{3.40}$$

Also, the volumetric strain can be written as the divergence of the displacement vector,  $\mathbf{u}$ . Therefore, the fluid flow equation in Biot's poroelasticity formulation takes the form

$$\alpha \frac{\partial (\nabla \mathbf{u})}{\partial t} + S_{\varepsilon} \frac{\partial p}{\partial t} - \frac{\tilde{K}}{u} \nabla^{2} p = 0$$
(3.41)

From micromechanical analysis, the specific storage terms can be associated with the compressibilities of the fluid, the porous skeleton and the solid grains (Detournay and Cheng, 1993; Wang, 1993, 2000). Also, the experimental measurements of the poroelastic parameters are reported in a number of articles including those by Berge et al. (1993), Hart and Wang (1995), and Lecampion et al. (2006).

The unconfined storage term, shown in Eq. (3.42), is defined as the increment of fluid content with the increase in pore pressure, while keeping the mean applied stress constant

$$S_{\sigma} = nC_{w} + C_{eff} - (n+1)C_{s}$$
(3.42)

where  $C_w$  is the compressibility of water,  $C_{eff}$  (defined as the inverse of the bulk modulus of the porous skeleton) is the compressibility of the porous skeleton,  $C_s$  is the compressibility of the solid grains, and n is the porosity of the medium.

The confined storage term is defined as the increment of the water content with the pore pressure increase while keeping the control volume constant. The confined storage term can be expressed as a weighted sum of the phase compressibility term (Wang, 2000)

$$S_{\varepsilon} = nC_w + (\alpha - n)C_s$$
 ;  $\alpha = \left(1 - \frac{C_s}{C_{eff}}\right)$  (3.43)

## 3.3.5. Solid phase equation

The solid phase equation of Biot's theory of linear poroelasticity is based on the assumptions of linear elastic behaviour for the porous skeleton (Hooke's Law), and small deformations. In the absence of body forces and inertia effects the equilibrium equation is

$$\nabla . \mathbf{\sigma} = \mathbf{0} \tag{3.44}$$

where  $\sigma$  is the total stress tensor. The relationship between the displacement and strain for small strains is

$$\mathbf{\varepsilon} = \frac{1}{2} \left[ \nabla \mathbf{u} + \left( \nabla \mathbf{u} \right)^T \right] \tag{3.45}$$

where  $\mathbf{\varepsilon}$  is the strain tensor and  $\mathbf{u}$  is the displacement vector. Assuming that the isotropic stress is positive in tension and the pore pressure is positive in compression, the stress strain relationship for a linear elastic material takes the form

$$\mathbf{\sigma} = 2G\mathbf{\varepsilon} + \lambda \varepsilon_{\mathbf{n}} \mathbf{I} - \alpha p \mathbf{I} \tag{3.46}$$

where G is the shear modulus,  $\lambda$  is the Lamé coefficient, and  $\mathbf{I}$  is the unit tensor. The effective stress,  $\mathbf{\sigma}'$ , in poroelasticity is defined by

$$\mathbf{\sigma}' = \mathbf{\sigma} + \alpha p \mathbf{I} \tag{3.47}$$

Combining Eqs. (3.44) and (3.46) and writing the volumetric strain as a function of displacement gives the solid phase equation of Biot's theory of linear poroelasticity

$$G\nabla^{2}\mathbf{u} + \frac{G}{1 - 2\nu}\nabla(\nabla \cdot \mathbf{u}) - \alpha\nabla p = \mathbf{0}$$
(3.48)

The generalization of the Biot's formulation to transverse isotropy and fully anisotropic cases can be found in Biot (1955) and Biot and Willis (1957).

# 3.3.6. Uncoupling stress from pore pressure

In the limiting case when there is negligible or no change in the mean total stress Eq. (3.37) reduces to

$$S_{\sigma} \frac{\partial p}{\partial t} - \frac{\tilde{K}}{\mu} \nabla^2 p = 0 \tag{3.50}$$

Therefore, the pore pressure uncouples from the stress field. This equation is called the piezo-conduction equation. This equation was proposed by Brace et al. (1968), and applied by Lin (1977), Hsieh et al. (1981) and Neuzil et al. (1981) in order to model hydraulic pulse tests.

When  $C_s$  reduces to zero,  $S_{\sigma}$  in Eq. (3.50) reduces to the conventional storativity term and gives rise to the piezo-conduction equation that is used quite extensively in the interpretation of permeability in hydrogeological problems (Bear, 1972; Barenblatt et al., 1989; Selvadurai, 2000a, 2009, 2013); i.e.

$$\left(nC_{w} + C_{eff}\right)\frac{\partial p}{\partial t} - \frac{\tilde{K}}{\mu}\nabla^{2}p = 0$$
(3.51)

Finally, it should be mentioned that the fully coupled theory of poroelasticity requires the formulation of the initial boundary value problem with precise conditions relevant to an experimental configuration, where consistent initial and boundary conditions are applied to all the dependent variables. The solution of the conventional piezo-conduction equation requires the formulation of an initial boundary value problem where consistent initial and boundary conditions are prescribed only on the pore fluid pressure.

# 3.4. Summary

In this chapter the hydro-mechanical behaviour of porous materials was theoretically studied under isothermal conditions. Two theories were discussed: Terzaghi's consolidation theory and Biot's theory of linear poroelasticity. Terzaghi's theory uses a formulation that uncouples the equations governing the mechanical deformation and the pore pressure changes. It assumes that the fluid and the solid grains are incompressible, compared to the porous skeleton. The theory was originally derived for one-dimensional consolidation induced by the application of a surface traction at the upper boundary of a soil column. The works of Rendulic (1936) extended Terzaghi's approach to three-dimensions. The fully coupled formulation for the study of the hydro-mechanical behaviour of porous media was proposed by Biot (1941a). In Biot's approach the skeletal stress-strain behaviour is assumed to be elastic and the solid grains forming the porous medium are assumed to be compressible. Fluid flow through the porous medium is developed by Darcy's law. The constitutive hydro-mechanical equations for isotropic porous media were presented in this chapter. It was shown that four independent poroelastic parameters are needed to model the behaviour of linear poroelastic media. These parameters can be chosen as  $(E, \nu, R, H)$  or  $(E, \nu, R, H)$  $\nu$ ,  $S_{\varepsilon}$ ,  $\alpha$ ) or any other four independent poroelastic constants. It was also shown that, for isotropic loading where the shear strains are zero, the number of independent parameters needed to describe the behaviour of isotropic porous media reduces to three. These parameters can be chosen as (K, R, H). The chapter also examined the limiting cases where the fluid flow equation in Biot's theory

can be uncoupled from the solid phase equation, resulting in the piezo-conduction equation.

#### **CHAPTER 4**

# PERMEABILITY MEASUREMENT: THEORY AND EXPERIMENT

#### 4.1. Introduction

Permeability is the ability of a fluid to flow through the accessible pore space of a porous medium. This is an important parameter in several areas of geoenvironmental engineering, including groundwater flow, disposal of hazardous wastes and CO<sub>2</sub> sequestration. Methods for measuring permeability can be categorized into steady state and transient methods. Steady state tests are more reliable, since the only measurements needed to estimate the permeability are the hydraulic potential difference applied to initiate the flow, the constant flow rate attained and the geometry of the flow domain. Steady state testing is applicable to rocks with permeabilities in the range  $10^{-14}$  m<sup>2</sup> to  $10^{-18}$  m<sup>2</sup> as relevant to rocks such as sandstones, limestones and rocks with defect continuity (Heystee and Roegieres, 1981; Gobran et al., 1987; Zhu and Wong, 1997; Selvadurai and Selvadurai, 2007; Selvadurai and Glowacki, 2008; Selvadurai and Selvadurai, 2010). Low permeability materials, however, (e.g. granite, limestone, etc.) require a long time to attain steady state condition. Also, the flow rates required to achieve a steady state in low permeability materials can be small and require the use of precision pumps. The main limitation is that the volume of fluid migrating through the sample will be small and the accurate measurement of the exit flow rate is not feasible. For these materials the preferred method to measure permeability is the transient pulse test. This method was first introduced by Brace et al. (1968) to measure the permeability of Westerly Granite, and has been further discussed and applied by Papadopoulos et al. (1973), Hsieh et al. (1981), Neuzil et al. (1981), Bernabe (1986), and Selvadurai and Carnaffan (1997) for testing a variety of geomaterials. This chapter discusses the application of the hydraulic pulse method to measure the permeability of low permeability geomaterials.

## 4.2. Hydraulic pulse testing: theory

For low permeability geomaterials, with permeabilities in the range  $\tilde{K} \in (10^{-18}, 10^{-22})\,\mathrm{m}^2$ , the accurately verifiable steady flow rates that can be initiated in unstressed samples without causing damage (e.g. micro-mechanical hydraulic fracture) to the porous fabric can be small. For this reason, the permeability characteristics of such geomaterials are usually determined from transient flow tests.

Two sets of partial differential equations can be used to model and interpret the hydraulic pulse test: (i) the piezo-conduction equation and (ii) an analysis based on Biot's equations of poroelasticity. Brace et al. (1968) developed an elastic-drive equation, assuming a zero specific storage term for the rock. The more generalized equations were then proposed by other researchers such as, Hsieh et al. (1981) and the accuracy of the application of the test to a finite domain was examined by Selvadurai and Carnafan (1997) and Selvadurai et al. (2005) among others.

The development of the theory for the piezo-conduction equation is carried out by imposing certain restrictions on the mechanical response of the porous skeleton of the geomaterial. For example, the theory can only account for the compressibility of the porous skeleton and that of grains composing the porous skeleton. A more accurate development of fluid pressure decay in pulse tests should take into

consideration the influence of complete coupling between a deformable porous skeleton and a compressible permeating fluid. An example is the classical theory of poroelasticity proposed by Biot (1941a) that takes into consideration the elastic deformations of the porous skeleton, the compressibility of the material composing the porous skeleton and Darcy flow in the connected pore space.

The interpretation of permeability from results of hydraulic pulse tests can vary depending on which of these two approaches is used. This has resulted in comparative investigations and two examples are provided by Walder and Nur (1986) and Hart and Wang (1998) (see also Wang (2000)). Both investigations deal with hydraulic pulse tests conducted under one-dimensional conditions; the first investigates the poroelastic phenomena including a non-linear pore pressure diffusion associated with large pore pressure gradients while the latter considers the three-dimensional poroelastic influences that arise when modelling one-dimensional hydraulic pulse tests. It should also be noted that the problem examined by Hart and Wang (1998) relates to the computational modelling of the propagation of a hydraulic pulse in a one-dimensional element that is hydraulically sealed at all surfaces other than at the region subjected to pressure, but allows radial deformations at these surfaces.

#### 4.2.1. Governing equations

The partial differential equations governing coupled fluid flow and linear elastic deformation of a fluid-saturated isotropic porous medium were developed by Biot (1941a). The theory was thoroughly explained in Chapter 3. The dependent variables in the formulation consist of the skeletal deformation  $\mathbf{u}(\mathbf{x},t)$  and the pore fluid pressure  $p(\mathbf{x},t)$  (p>0 for compressive pore fluid pressure), where  $\mathbf{x}$  is the position vector and t is time. Considering only quasi-static processes, the governing fully coupled partial differential equations take the form

$$\frac{\tilde{K}}{\mu} \nabla^2 p - S_{\varepsilon} \frac{\partial p}{\partial t} - \alpha \frac{\partial}{\partial t} (\nabla \cdot \mathbf{u}) = 0$$
(3.41)

$$G\nabla^{2}\mathbf{u} + \frac{G}{1 - 2\nu}\nabla(\nabla \cdot \mathbf{u}) - \alpha\nabla p = \mathbf{0}$$
(3.48)

where G and  $\nu$  are, respectively, the shear modulus and the Poisson's ratio of the porous skeleton,  $\tilde{K}$  is the permeability,  $\mu$  is the dynamic viscosity of the fluid and  $S_{\varepsilon}$  and  $\alpha$  are, respectively, the constrained storativity term and the Biot coefficient defined by

$$S_{\varepsilon} = nC_w + (\alpha - n)C_s$$
 ;  $\alpha = \left(1 - \frac{C_s}{C_{eff}}\right)$  (3.43)

The partial differential equation governing flow of a compressible fluid through the accessible pore space of a porous medium with a skeletal compressibility  $C_{eff}$  (i.e. the inverse of K) and a grain compressibility  $C_s$  was derived by Brace et al. (1968) and takes the form

$$\frac{\tilde{K}}{\mu}\nabla^2 p - S_\sigma \frac{\partial p}{\partial t} = 0 \tag{3.50}$$

where

$$S_{\sigma} = \left\{ nC_w + C_{eff} - (n+1)C_s \right\}$$
 (3.42)

The above piezo-conduction equation is derived by neglecting the changes in the mean total stress during the hydraulic pulse test process, as explained in chapter 3. When  $C_s$  reduces to zero, Eq. (3.42) reduces to the conventional storativity term and gives rise to the piezo-conduction equation used quite extensively in the interpretation of permeability in hydrogeological problems (Bear, 1972; Barenblatt et al., 1989; Selvadurai, 2000a; Selvadurai, 2009); i.e.

$$S_C = [nC_w + C_{eff}] \tag{4.1}$$

At the outset, it should be mentioned that the fully coupled theory of poroelasticity requires the formulation of the initial boundary value problem with

precise conditions relevant to an experimental configuration, where consistent initial and boundary conditions are applied to all the dependent variables. The solution of the conventional piezo-conduction equation requires the formulation of an initial boundary value problem where consistent initial and boundary conditions are prescribed only on a single dependent variable, namely the pore fluid pressure.

## 4.2.2. Theoretical modelling

In this section, the solution of the piezo-conduction equation to the initial boundary value problem governing hydraulic pulse tests conducted under one-dimensional and radially symmetric conditions is presented.

The piezo-conduction equation of the type Eq. (3.50) can be examined for relatively simple geometries involving axial, radially symmetric and spherically symmetric flow conditions. In the case of purely axial diffusion of a pressure pulse applied to a fluid chamber of volume  $V_w$  in contact with the boundary of a semi-infinite fluid-saturated region, the initial boundary value problem has been investigated quite extensively (see Selvadurai (2009) for a presentation of the relevant literature); it is sufficient to record the relevant boundary and initial conditions applicable to a semi-infinite domain. These are

$$p(0,t) = \overline{p}(t) \qquad ; \qquad \overline{p}(0) = \overline{p}_0 \tag{4.2}$$

$$\Phi\left(\frac{\partial p}{\partial z}\right)_{z=0} = \left(\frac{\partial p}{\partial t}\right)_{z=0} \tag{4.3}$$

$$p(z,0) = 0 (4.4)$$

where  $\overline{p}(t)$  is the position independent fluid chamber pressure, which is a function of time only and  $\overline{p}_0$  is the chamber pressure at the start of the axial flow pulse test and

$$\Phi = \left(\frac{A\tilde{K}}{\mu V_w C_w}\right) \tag{4.5}$$

In Eq. (4.5) A is the cross-sectional area of the one-dimensional semi-infinite domain and  $V_w$  is the volume of the pressurized reservoir used in the test. One-dimensional pulse tests are invariably conducted on low permeability materials of finite extent and it is usually assumed that the far-field boundary has a limited influence on the observed pulse decay. If this condition is satisfied, the solution to the piezo-conduction equation should also satisfy the regularity condition,  $p(z,t) \to 0$  as  $z \to \infty$ . The extent to which the assumption of 'infinite extent' is valid for a finite sample tested in the lab was analytically examined by Selvadurai and Carnaffan (1997) (it is not a requirement that this far field condition be satisfied (Hsieh et al, 1981; Neuzil et al., 1981); its inclusion, however, leads to a simplified result applicable to a semi-infinite domain). Considering the above, the solution of the initial boundary value problem can be expressed in the non-dimensional form

$$\frac{\overline{p}(t)}{\overline{p}_0} = \exp(\Omega^2 t) \operatorname{Erfc}(\sqrt{\Omega^2 t})$$
(4.6)

where

$$\Omega = \Phi \omega \quad ; \quad \omega^2 = \frac{S_i \mu}{\tilde{K}} \tag{4.7}$$

and the storativities  $S_i$  can be given values  $S_{\sigma}$  and  $S_C$  that correspond to the expressions (4.5) and (4.6), respectively.

A similar analysis can be applied to examine purely radial flow hydraulic pulse tests conducted through the pressurization of a borehole located in a fluid-saturated porous medium of infinite extent over a borehole length  $\overline{H}$ , containing the fluid volume  $V_w$ . The details of the analysis are given in Cooper et al. (1967); Papadopulos et al., 1973; Bredehoeft and Papadoulos, 1980. Applications of the

radial flow technique to measure the permeability characteristics of a cement grout cylinder measuring 152 mm in diameter and granite cylinders measuring 450 mm in diameter are given, respectively, in the articles by Selvadurai and Carnaffan (1997) and Selvadurai et al. (2005). More recently, Selvadurai and Jenner (2013) used the radial flow pulse test to determine the permeability characteristics of the very low permeability argillaceous Lindsay-Cobourg Limestone ( $\tilde{K} \in (10^{-22} \text{ to} 10^{-19} \text{ m}^2)$ ). The boundary conditions and initial conditions applicable to the purely radial flow problem are

$$\tilde{p}(a,t) = \tilde{p}(t) \qquad ; \qquad \tilde{p}(0) = \tilde{p}_0 \tag{4.8}$$

$$\frac{2\pi a\tilde{K}\bar{H}}{\mu} \left(\frac{\partial p}{\partial r}\right)_{r=a} = V_w C_w \left(\frac{\partial p}{\partial t}\right)_{r=a} \tag{4.9}$$

$$p(r,0) = 0 (4.10)$$

where  $\tilde{p}(t)$  signifies the position independent cavity pressure and  $\tilde{p}_0$  is the pressure in the cavity at the start of the radial flow pulse test. In addition, if the modelling is applicable to an infinite domain, the pressure field should satisfy the regularity condition,  $p(r,t) \to 0$  as  $r \to \infty$ . The decay of the pressure within the cavity is given by

$$\frac{\tilde{p}(t)}{\tilde{p}_0} = \frac{8\tilde{\alpha}}{\pi^2} \int_0^\infty \frac{\exp(-\tilde{\beta}u^2/\tilde{\alpha})}{u f(u,\tilde{\alpha})} du$$
 (4.11)

where

$$f(u,\tilde{\alpha}) = \left[uJ_0(u) - 2\tilde{\alpha}J_1(u)\right]^2 - \left[uY_0(u) - 2\tilde{\alpha}Y_1(u)\right]^2 \tag{4.12}$$

 $J_0$  and  $J_1$  are, respectively, the zeroth-order and first-order Bessel functions of the first kind and  $Y_0$  and  $Y_1$  are, respectively, the zeroth-order and first-order

Bessel functions of the second kind. Also, in Eq. (4.11), the non-dimensional parameters  $\tilde{\alpha}$  and  $\tilde{\beta}$  are given by

$$\tilde{\alpha} = \frac{\pi a^2 \bar{H} S_i}{C_w V_w} \quad ; \quad \tilde{\beta} = \frac{\pi \tilde{K} \bar{H} t}{\mu V_w C_w} \tag{4.13}$$

Similarly,  $S_i$  can be assigned the expressions defined by Eqs. (4.5) and (4.6).

### 4.2.3. Computational study of the effect of poroelastic coupling

The analytical treatment of the initial boundary value problem in Biot's theory of poroelasticity associated with one-dimensional axial flow and radial flow pulse tests is non-routine and to the author's knowledge there are no analytical results that examine the pulse decay effects, which incorporate fully coupled influences of poromechanics. For this reason, a fully coupled analysis of the one-dimensional axial flow and purely radial flow pulse tests was conducted using a computational approach. Finite element modelling of problems in poroelasticity is well established and a consistent formulation of the initial boundary value problems is described by Lewis and Schrefler (1998); these procedures have also been implemented in several computational codes including ABAQUS<sup>TM</sup> and COMSOL<sup>TM</sup>.

Detailed calibration exercises involving the COMSOL<sup>TM</sup> code were presented by Selvadurai and Suvorov (2010, 2012) and Selvadurai et al. (2011b). In these studies, the accuracy of the computational algorithms for coupled transient problems has been validated through comparisons with either known or newly developed analytical solutions. The axial hydraulic pulse test was first examined using a one-dimensional axisymmetric domain as shown in Figure 4.1.

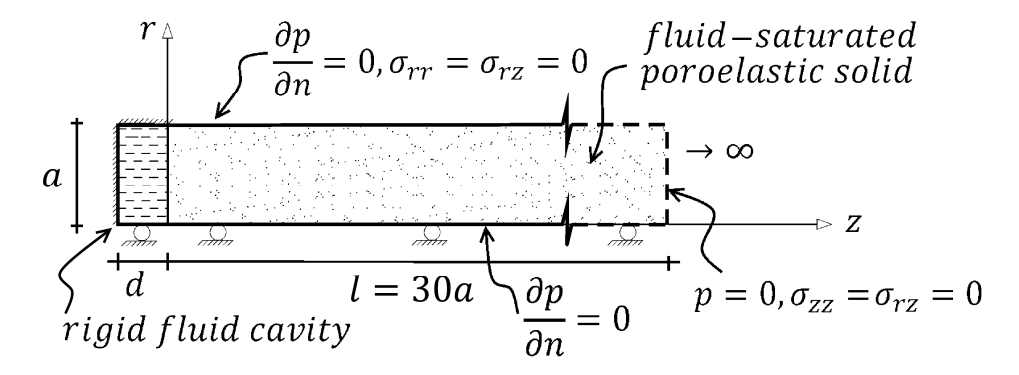


Figure 4.1: Geometry and boundary conditions assumed for the axisymmetric one-dimensional stress hydraulic pulse test.

Figure 4.1 shows a fluid-saturated cylindrical porous region of radius a and length l=30a. The domain of the porous region is  $r \in (0,a)$ ;  $z \in (0,l)$  and the plane boundary z=0;  $r \in (0,a)$  is in contact with a fluid reservoir of volume  $(0.01\pi)a^3$  for Westerly Granite and  $(0.4\pi)a^3$  for Indiana Limestone. The external boundary of the reservoir is non-deformable and encloses a fluid volume  $V_w$ . The computational modelling of the one-dimensional hydraulic pulse test can be developed considering two approaches: (i) the state of stress is assumed to be one-dimensional (Figure 4.1) or (ii) the state of strain is assumed to be one-dimensional (Figure 4.2).

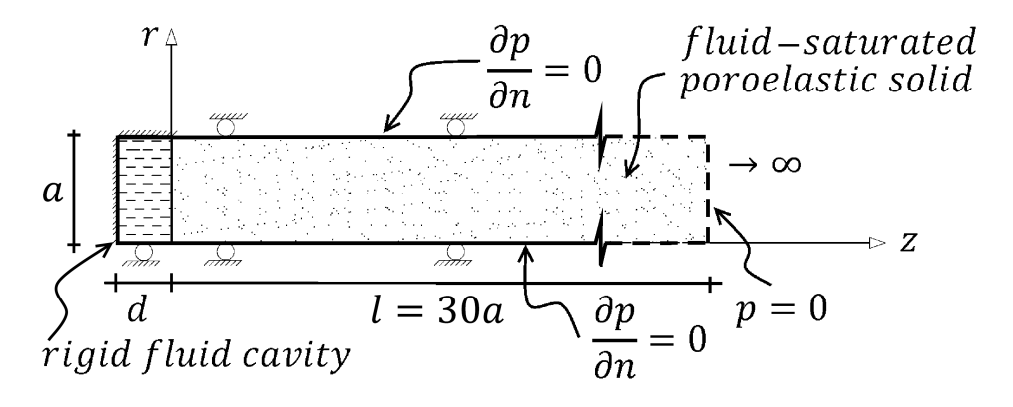


Figure 4.2: Geometry and boundary conditions assumed for the onedimensional strain hydraulic pulse test.

In addition, the pore fluid pressure boundary condition should satisfy the no-flow boundary condition on the cylindrical surfaces of the one-dimensional domain. For the case (i), the boundary conditions applicable to the stresses, displacements and pore fluid pressures are

$$u_{r}(0,z,t) = 0 \quad ; \quad 0 \prec z \prec 30a$$

$$u_{z}(r,0,t) = 0 \quad ; \quad 0 \prec r \prec a$$

$$\sigma_{zz}(r,0,t) = 0 \quad ; \quad 0 \prec r \prec a$$

$$\sigma_{zz}(r,l,t) = 0 \quad ; \quad 0 \prec r \prec a$$

$$\sigma_{rz}(r,0,t) = 0 \quad ; \quad 0 \prec r \prec a$$

$$\sigma_{rz}(r,0,t) = 0 \quad ; \quad 0 \prec r \prec a$$

$$\sigma_{rz}(a,z,t) = 0 \quad ; \quad 0 \prec z \prec 30a$$

$$\sigma_{rz}(r,l,t) = 0 \quad ; \quad 0 \prec r \prec a$$

$$\sigma_{rr}(a,z,t) = 0 \quad ; \quad 0 \prec z \prec 30a$$

$$\left(\frac{\partial p}{\partial r}\right)_{r=a} = 0 \quad ; \quad p(r,l,t) = 0$$

In addition, the initial conditions correspond to

$$\mathbf{u}(r,z,0) = 0$$
 ;  $p(r,z,0) = 0$  (4.15)

applicable to the one-dimensional domain with 0 < r < a; 0 < z < 30a. The hydraulic pulse test is initiated by the application of a pressure pulse to the reservoir with a rigid boundary in contact with the poroelastic medium. If the domain of the reservoir is denoted by  $\Omega_R$ , the pore fluid pressure boundary condition at the reservoir and reservoir-poroelastic medium interface are given by

$$p(r,0,0) = p_0 (4.16)$$

where  $p_0$  is the pressure in the reservoir at the start of the pulse test.

Similarly, for the pulse test conducted under the one-dimensional strain condition the boundary conditions corresponding to Eq. (4.14) are

$$\sigma_{rz}(r,0,t) = 0 ; u_{r}(0,z,t) = 0 
\sigma_{rz}(a,z,t) = 0 ; u_{r}(a,z,t) = 0 
\sigma_{rz}(r,l,t) = 0 ; u_{z}(r,0,t) = 0 
\sigma_{zz}(r,l,t) = 0 ; p(r,l,t) = 0$$

$$\left(\frac{\partial p}{\partial r}\right)_{r=a} = 0 ; p(r,l,t) = 0$$

In Eq. (4.17) the extent of the region is specified by 0 < r < a and 0 < z < 30a. The initial conditions for the hydraulic pulse test conducted under one-dimensional strain are identical to Eq. (4.15) and the pulse test is initiated by a condition similar to Eq. (4.16).

Purely radial pulse testing was also examined (Figure 4.3). The modeled element has a fluid cavity radius of a and a height of  $\overline{H} = 20a$  for Westerly Granite and  $\overline{H} = 0.5a$  for Indiana Limestone.

Unlike the one-dimensional model, here the size of the cavity can change as the cavity pressure changes. The corresponding boundary conditions are:

$$\sigma_{rr}(0,z,t) = 0 \qquad ; \qquad \sigma_{rz}(0,z,t) = 0$$

$$\sigma_{rr}(R,z,t) = 0 \qquad ; \qquad \sigma_{rz}(R,z,t) = 0$$

$$u_{z}(r,-\overline{H}/2,t) = 0 \qquad ; \qquad u_{z}(r,\overline{H}/2,t) = 0$$

$$u_{r}(0,z,t) = 0 \qquad ; \qquad \left(\frac{\partial p}{\partial z}\right)_{r=0} = 0$$

$$\left(\frac{\partial p}{\partial z}\right)_{z=-\overline{H}/2} = 0 \qquad ; \qquad \left(\frac{\partial p}{\partial z}\right)_{z=\overline{H}/2} = 0$$

$$(4.18)$$

In Eq. (4.18) the extent of the region is specified by 0 < r < R and  $-\overline{H}/2 < z < \overline{H}/2$ . The initial conditions for the purely radial flow pulse test are again identical to Eq. (4.15) and the initiating pressure is

$$p(r, z, 0) = p_0 (4.19)$$

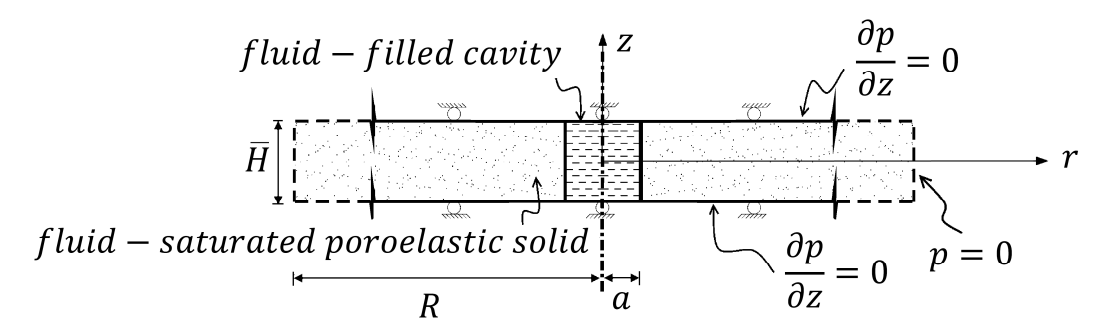


Figure 4.3: Schematic view for the radially symmetric hydraulic pulse testing of an infinitely extended rock mass.

To further establish the accuracy of the fully coupled poroelastic modelling of the hydraulic pulse test, the computational approach was applied to examine the one-dimensional problem that is given by Hart and Wang (1998). The problem involves a cylinder measuring 0.0254 m in radius and 0.0309 m in height. The sample was sealed at the base and at the circumference such that no water flow could take place through these surfaces. The upper surface  $(r \in (0,a); z = l)$  was subjected to a unit constant pore pressure pulse and the whole specimen was under constant total stress for the duration of the experiment. Figure 4.4 shows the geometry and boundary conditions of the problem.

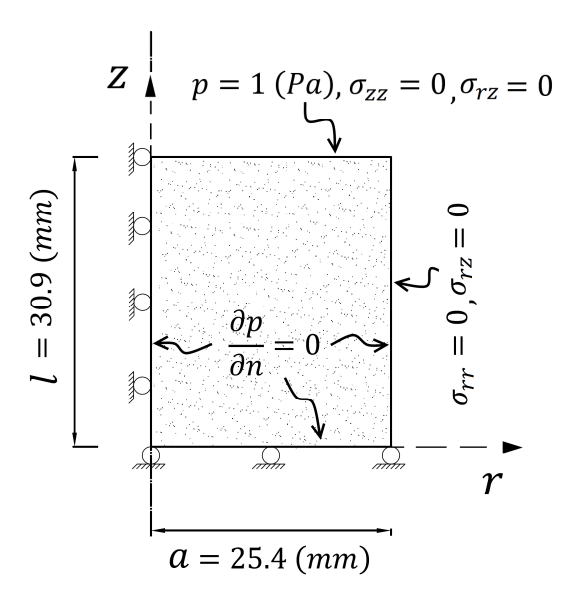


Figure 4.4: The geometry and boundary conditions of the problem examined by Hart and Wang (1998).

The rock used in the initial investigation was Berea Sandstone, which has hydromechanical parameters as follows (Hart and Wang, 1998; Wang, 2000): skeletal Young's modulus (E) = 13 (GPa); skeletal Poisson's ratio (V) = 0.17; Biot coefficient ( $\alpha$ )=0.764; permeability ( $\tilde{K}$ )=1.91×10<sup>-19</sup> (m²); porosity (n) =5%; dynamic viscosity of water at 20 °C ( $\mu$ ) = 0.001 (Pa s); density of water ( $\rho$ ) = 1000 (kg/m³); compressibility of water ( $C_w$ ) = 4.35×10<sup>-10</sup> (Pa<sup>-1</sup>). The test problem was modelled for a duration of 2500 s. The boundary and initial conditions used by Hart and Wang (1998), who employed the ABAQUS<sup>TM</sup> code, are as follows

$$\begin{split} & \sigma_{rr}(a,z,t) = 0 & ; & \sigma_{rz}(a,z,t) = 0 \\ & \sigma_{zz}(r,0,t) = 0 & ; & \sigma_{rz}(r,0,t) = 0 \\ & \sigma_{zz}(r,l,t) = 0 & ; & \sigma_{rz}(r,l,t) = 0 \\ & u_{r}(0,z,t) = 0 & ; & u_{z}(r,0,t) = 0 \\ & \left(\frac{\partial p}{\partial r}\right)_{r=a} = 0 & ; & z \in (0,l) \\ & \left(\frac{\partial p}{\partial r}\right)_{z=l} = 0 & ; & r \in (0,a) \end{split}$$

The extent of the region for Eq. (4.20) is  $z \in (0,l)$  and  $r \in (0,a)$ . The identical boundary conditions were specified in the current analysis, which was performed using the COMSOL<sup>TM</sup> code. Figure 4.5 also shows a comparison between the results obtained by Hart and Wang (1998) and the current investigation; there is good correlation between the two sets of computational results. A detail of the short term pressure response at the sample end (i.e. z = 0) is also shown.

Figure 4.5 also illustrates, for purposes of comparison, the results obtained from the piezo-conduction equation presented by Hart and Wang (1998) along with the results of the piezo-conduction modelling that (i) takes into consideration the influence of grain compressibility and (ii) that omits grain compressibility. For purposes of reference, we note that the piezo-conduction equation is also modelled using COMSOL<sup>TM</sup>, although an analytical solution can be developed

using standard procedures (see e.g. Carslaw and Jaeger, 1959; Neuzil et al. 1981; Selvadurai, 2000a).

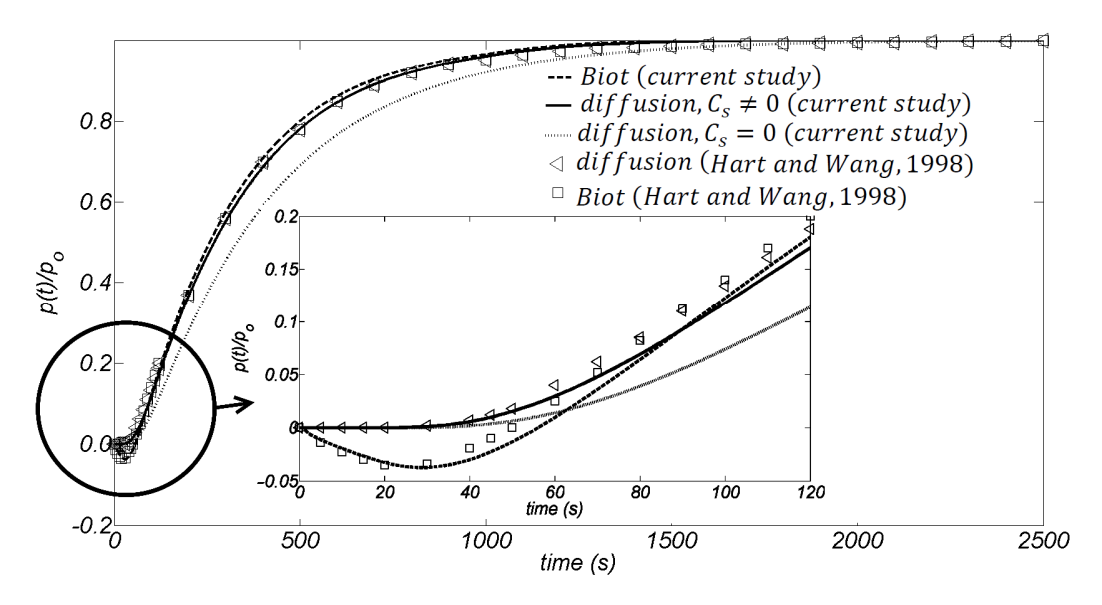


Figure 4.5: Comparison of the results obtained by Hart and Wang (1998) with the results of the current study. The figure also shows the detail of the initial 120 seconds and the geometry and boundary conditions of the problem.

The general observation arising from the computational modelling of the onedimensional pulse test is that the influence of poromechanical coupling manifests only in the very early stages of the pulse response; this is characteristically similar to the Mandel-Cryer effect that gives rise to an increase in the pore pressure response due to skeletal deformations that produce an additional strain (Mandel, 1953; Cryer, 1963; Gibson et al., 1963; Selvadurai and Shirazi, 2004; Selvadurai and Suvorov, 2012). Also, when poromechanical coupling is omitted, the Mandel-Cryer effect does not materialize. In terms of the relevance of the observation to the interpretation of hydraulic pulse tests, it should be emphasized that the results of pulse tests in the very early stages of the pulse decay should not be used to estimate permeability. Similarly, the piezo-conduction equation modelling using a storativity term that includes the effects of grain compressibility is expected to correlate closely with the results of the fully-coupled modelling involving Biot poroelasticity. The results of hydraulic pulse test conducted on low permeability geomaterials can be expected to produce differing responses depending on (i) the use of fully coupled analyses, (ii) the piezo-conduction equation that uses the conventional definition of storativity, which includes compressibilities of the pore fluid and the porous skeleton, (iii) the piezo-conduction equation that takes into consideration the definition of storativity including fluid compressibility, skeletal compressibility and grain compressibility, and (iv) the state of deformation and flow associated with the hydraulic pulse test (i.e. axial flow, one-dimensional tests, radial flow well tests, etc.).

In order to examine the relative influences of factors (i) to (iv) on the results of pulse tests, computational simulations were carried out for hypothetical hydraulic pulse tests conducted on typical rocks such as Westerly Granite and Indiana Limestone. The input data used in the computational simulations is given in Table 4.1.

Table 4.1: The mechanical, physical and hydraulic parameters applicable to Westerly Granite and Indiana Limestone

Rock Type	E	ν	α	$ ilde{K}$	n
Rock Type	(GPa)			$(m^2)$	%
Westerly Granite <sup>a</sup>	37.5	0.25	0.47	4.0×10 <sup>-19</sup>	1.0
Indiana Limestone <sup>b</sup>	24	0.14	0.85	73.75×10 <sup>-15</sup>	16.6

<sup>&</sup>lt;sup>a</sup>Wang (2000)

Table 4.2 gives the values for the compressibilities and storativity terms used in the model. The computational results for the one-dimensional and radial flow hydraulic pulse tests were conducted using the boundary conditions and initial conditions defined by Eq. (4.14) to Eq. (4.20).

Figure 4.6 shows the mesh configuration used in the axial and radial flow modelling. The interface between the fluid cavity and the rock was modelled

<sup>&</sup>lt;sup>b</sup>Selvadurai and Selvadurai (2010)

using a very fine mesh to account for the Heaviside step function-type discontinuous pressure gradients that will be present at the start of the test, when the pore fluid pressure in the saturated geomaterial is set to zero everywhere within the region.

Table 4.2: Storativity terms\* for Westerly Granite and Indiana Limestone

Rock type	$C_{eff}$ (Pa <sup>-1</sup> )	$C_s$ (Pa <sup>-1</sup> )	$S_{\varepsilon}$ (Pa <sup>-1</sup> )	$S_{\sigma}$ (Pa <sup>-1</sup> )	S <sub>C</sub> (Pa <sup>-1</sup> )
Westerly Granite	4.00×10 <sup>-11</sup>	2.12×10 <sup>-11</sup>	1.43×10 <sup>-11</sup>	2.31×10 <sup>-11</sup>	4.45×10 <sup>-11</sup>
Indiana Limestone	9.00×10 <sup>-11</sup>	1.35×10 <sup>-11</sup>	8.46×10 <sup>-11</sup>	1.50×10 <sup>-10</sup>	1.65×10 <sup>-10</sup>

\*In all estimates for *S*, the compressibility of water is taken as  $4.54 \times 10^{-10}$  (Pa<sup>-1</sup>) (White, 1986)

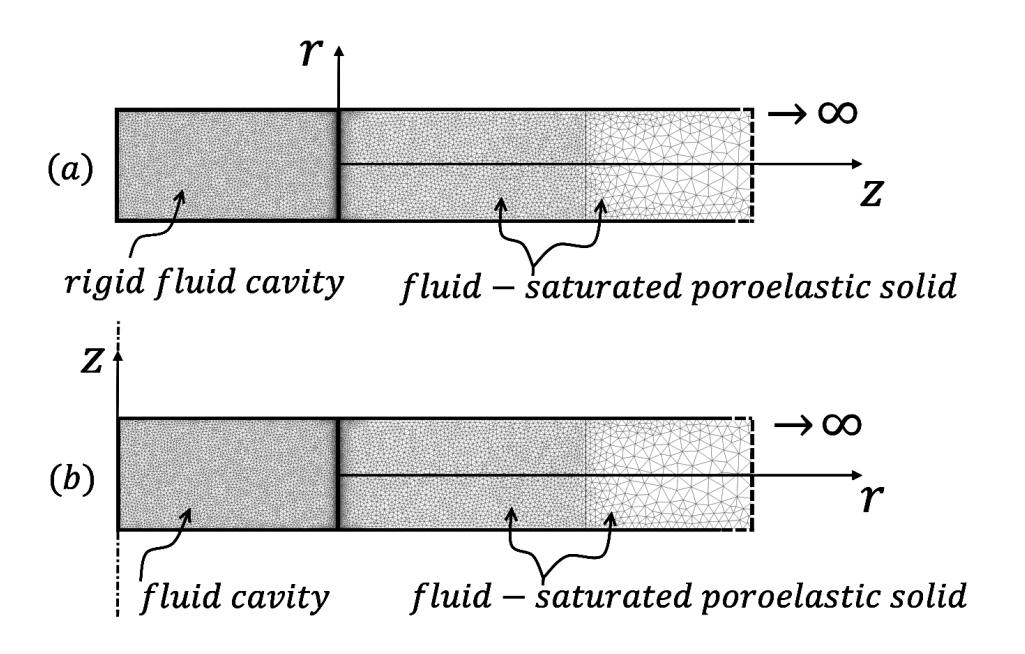


Figure 4.6: Mesh configuration for modelling: (a) one-dimensional hydraulic pulse test (25028 elements), (b) radially symmetric hydraulic pulse test (30017 elements).

A Lagrange-quadratic element with three degrees of freedom at each node was used in the finite element model. The displacements and pore fluid pressure are prescribed at all nodes.

Figures 4.7 and 4.8 illustrate, respectively, the computational results for onedimensional and radial flow hydraulic pulse tests conducted on Westerly Granite and Indiana Limestone.

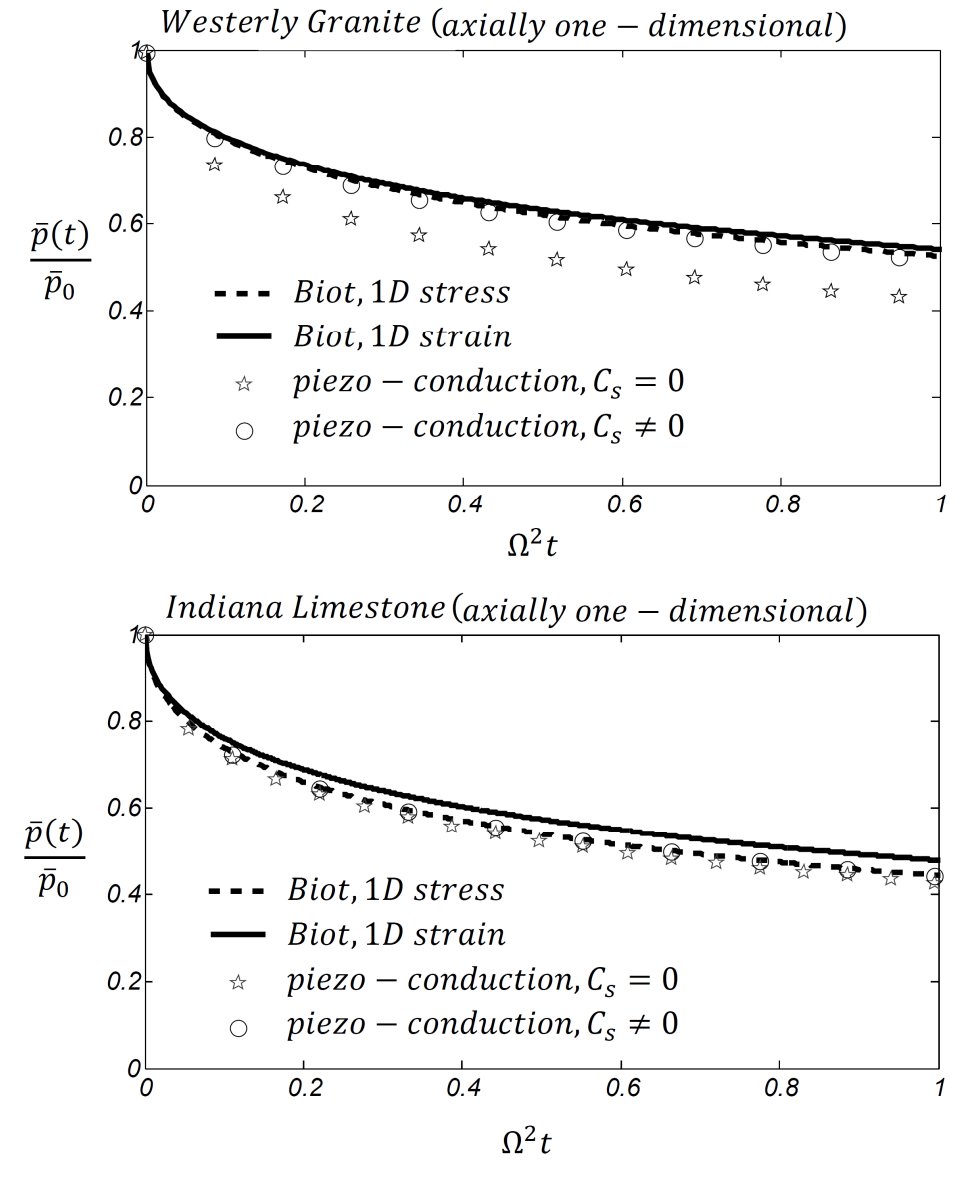
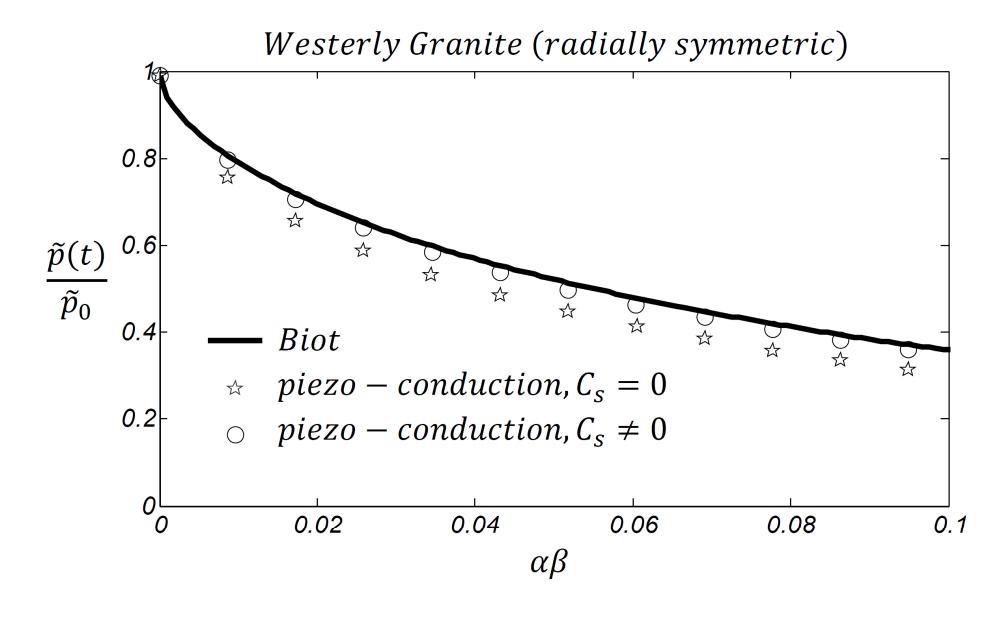


Figure 4.7: Comparison of the pressure decay curves obtained from Biot's theory of poroelasticity with those obtained using the piezo-conduction equation for the one-dimensional hydraulic pulse test.



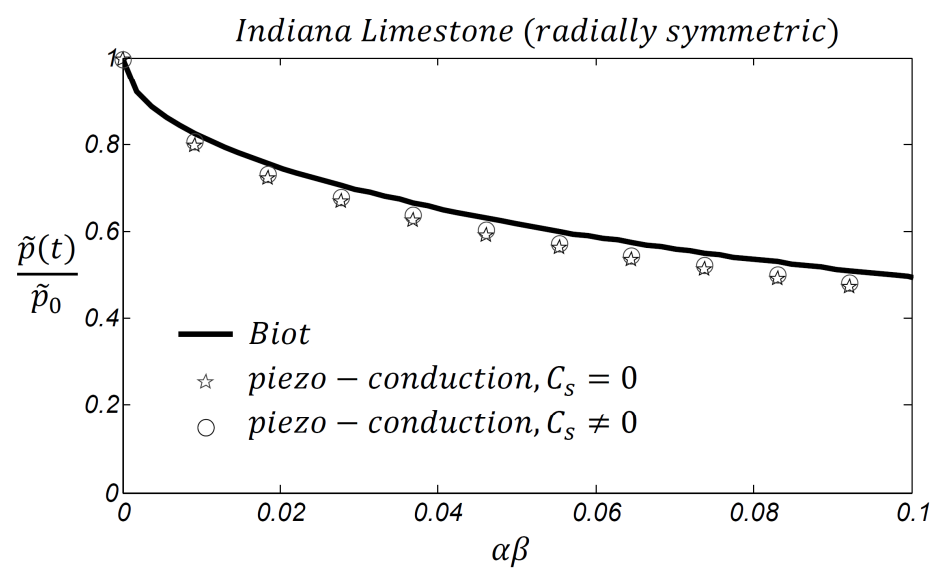


Figure 4.8: Comparison of the pressure decay curves obtained from Biot's theory of poroelasticity with those obtained using the piezo-conduction equation for a radially symmetric hydraulic pulse test.

The following observations can be made, although these are not to be interpreted as results of a general nature:

#### For the one-dimensional flow tests:

(i) The results for hydraulic pulse tests conducted under one-dimensional states of stress and strain and incorporating Biot's fully coupled theory of poromechanics give very close results for one-dimensional Westerly Granite and relatively close results for the Indiana Limestone (maximum discrepancy of 1.3 %).

(ii) The piezo-conduction equation analysis that also incorporates the influence of grain compressibility provides a closer correlation with the results obtained from a Biot poroelastic analysis with a one-dimensional stress condition. This is not an unexpected result since the fully coupled Biot model takes into account the influence of grain compressibility through the inclusion of the  $\alpha$  parameter.

#### For the radial flow tests:

- (i) In general, the radial flow hydraulic pulse tests are less influenced by fully poroelastic coupling when compared to the one-dimensional axial flow hydraulic pulse tests. The results for the fully coupled poroelastic hydraulic pulse decay compare favorably with the piezo-conduction equation results that incorporate grain compressibility.
- (ii) The result from the conventional piezo-conduction equation analysis tends to under-estimate the permeability of the medium.

There is no single non-dimensional parameter that would allow an identification of the discrepancy that might be expected between the fully coupled analysis and the conventional piezo-conduction equation analysis (with or without consideration of grain compressibility). It would appear that the discrepancies between the fully coupled analysis of the hydraulic pulse test and the result derived from the conventional piezo-conduction equation with storativity defined by Eq. (4.1) becomes more noticeable as the permeability of the material decreases.

#### 4.2.4. The effect of aspect ratio on the coupling behaviour

It is well known that under certain conditions the pressure diffusion equation (i.e.

Eq. (3.48)) decouples from the skeletal deformation (i.e.  $\alpha \frac{\partial}{\partial t} (\nabla . \mathbf{u}) \rightarrow 0$ ). Two of these conditions are the irrotational displacement in the finite or semi-finite

domains (e.g. radially symmetric hydraulic pulse testing in an infinite medium) and the limit of the relatively compressible pore fluid (Detournay and Cheng, 1993). It should, however, be noted that in such limiting cases the pore pressure decay obtained from the piezo-conduction equation is not equal to that obtained from Biot's poroelasticity formulation, since the estimates for storativity are different in the two formulations. The effect of the sample dimensions on the coupling parameters in Biot's poroelasticity has been studied by a number of researchers (Detournay and Cheng, 1993; Lecampion et al., 2006). Since slender samples were utilized in the previously cited computational treatments  $(L/a \approx 30)$ , the influence of the aspect ratio on the decay of the hydraulic pulse was briefly investigated. The size of the cavity was kept constant for both onedimensional and radial flow hydraulic pulse tests and either the length or the outer radius of the porous domain was changed. The hydraulic pulse tests were modeled for different sample sizes using the linear equations of poroelasticity and also for the piezo-conduction equation, with or without taking into account the compressibility of the solid grains. The problem was modeled for each geometry for the first 50% reduction in the cavity pressure obtained from the Biot poroelasticity formulation and then re-examined using the piezo-conduction equation over the same time duration. Finally, the cavity pressure at the end of each modelling exercise was compared with the poroelasticity solution to obtain the percentage error  $(\delta(\%) = 100 \times (p^{p-c} - p^{Biot})/p^{Biot})$  in the estimation of cavity pressure using the piezo-conduction equation. Figures 4.9 and 4.10 show the calculated percentage error for, respectively, the one-dimensional and radially symmetric hydraulic pulse tests. It is evident that for both the one-dimensional and radially symmetric problems the piezo-conduction equation provides results close to Biot's poroelasticity solution and, for smaller aspect ratios, the discrepancy between the results obtained from the two solutions becomes negligible.

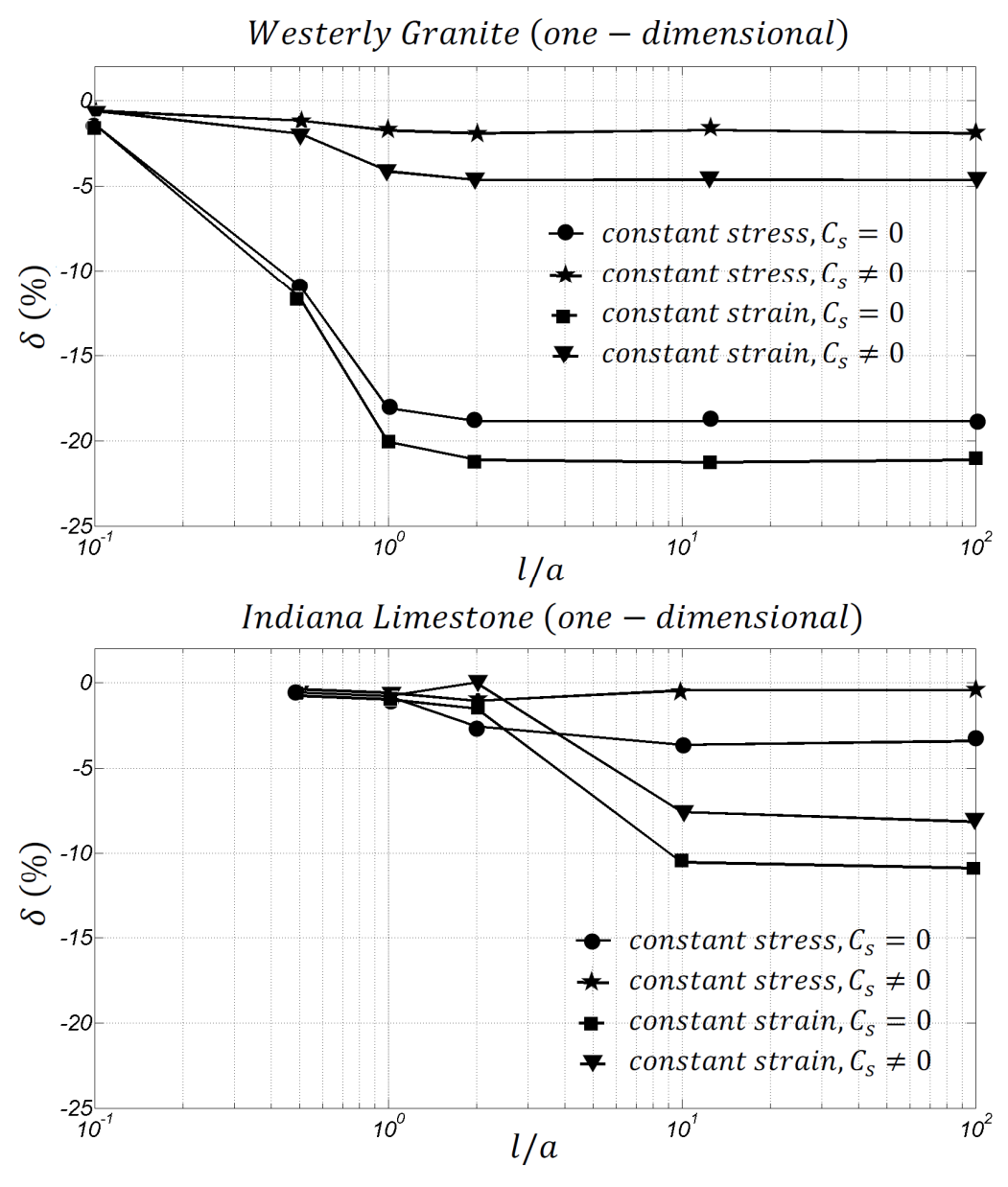
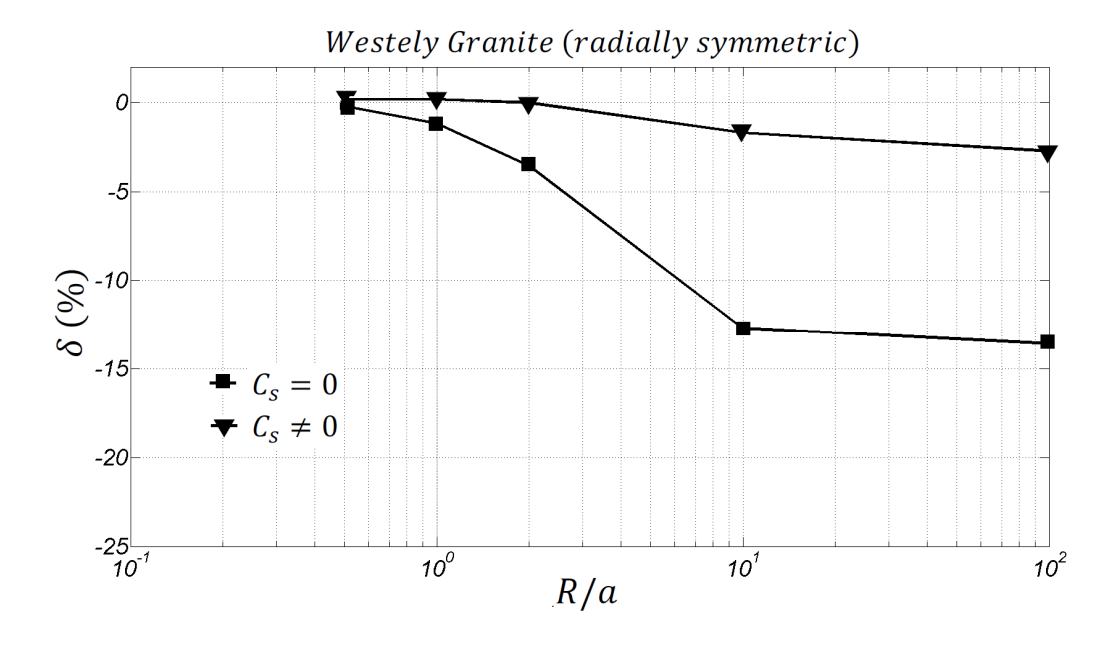


Figure 4.9: Comparison of the computational results obtained from the Biot poroelasticity equations with the piezo-conduction equation for one-dimensional constant stress and constant strain hydraulic pulse testing for different aspect ratios.



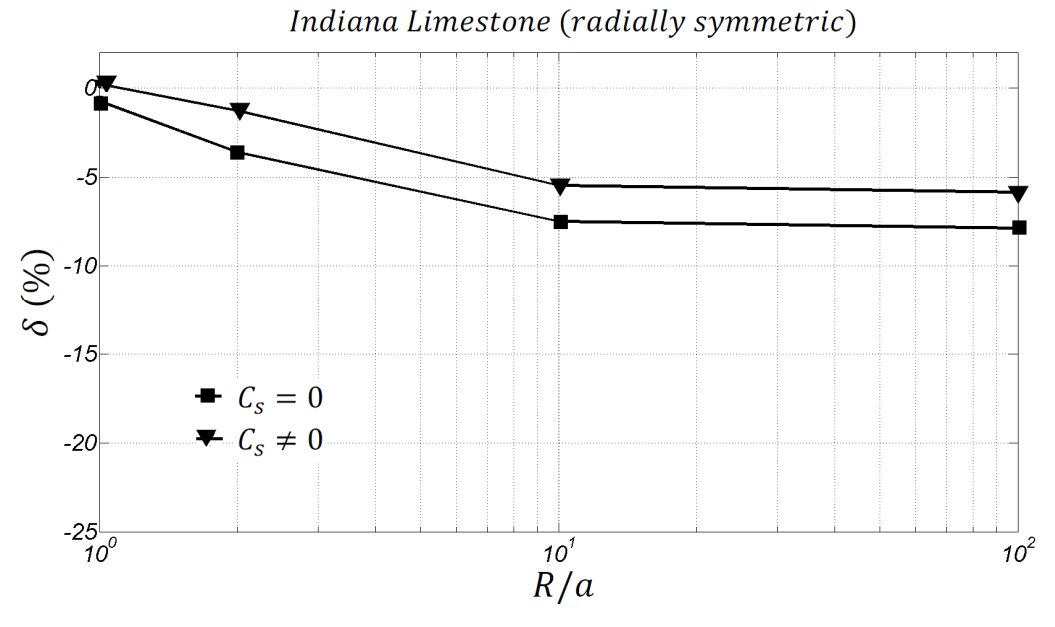


Figure 4.10: Comparison of the computational results obtained from the Biot poroelasticity equations with the piezo-conduction equation for radially symmetric hydraulic pulse testing for different aspect ratios.

# 4.3. Hydraulic pulse testing: experiment

In this section the developments presented in the previous sections is used to examine the results of isothermal hydraulic pulse tests conducted on Stanstead Granite. The parameters used in the modelling were as follows: drained Young's modulus (E) = 61 (GPa); drained Poisson's ratio (V) = 0.17 (measured in

accordance with ASTM D7012-04); Biot coefficient ( $\alpha$ )=0.44; porosity (n) =0.5% to 1.4% (measured in accordance with ASTM D4404-84); dynamic viscosity of water at 20 °C ( $\mu$ ) = 0.001 (Pa.s) (White, 1986); density of water ( $\rho$ ) = 1000 (kg/m³); compressibility of water ( $C_w$ ) = 4.54×10<sup>-10</sup> (Pa<sup>-1</sup>) (White, 1986). The value of the dynamic viscosity ( $\mu$ ) was adjusted to account for the actual water temperature recorded for each test (White, 1986). Two types of hydraulic pulse tests were conducted on the granite. The first involved pulse testing cylindrical samples of the granite under purely radial flow conditions and the second used an axisymmetric patch pulse test.

#### 4.3.1. Radially symmetric hydraulic pulse tests

The cylindrical sample used in the experimental investigations measured 15.24 cm in diameter and 14.76 cm in height. The cylindrical surfaces of the samples were cored from a larger sample and the plane ends were machined smooth to accommodate a sealing gasket. The central cavity was prepared using a 2.54 cm diameter diamond drill and the surface of the cavity was air-blown to remove any debris that might be embedded on the surface of the cavity that could impede fluid flow by clogging the pore space.

Radial flow hydraulic pulse testing involves the application of a pressure pulse to a central cavity drilled into the rock specimen. The sample was vacuum saturated for a period of 7 days to ensure that the pore space was saturated. There are no assurances that the entire pore space would be saturated but experience from previous experimental investigations involving cement grouts (Selvadurai and Carnaffan, 1997), Barre Granite (Selvadurai et al., 2005), Indiana Limestone (Selvadurai, 2009) and Cobourg Limestone (Selvadurai and Jenner, 2013) using such techniques have resulted in reliable results concerning saturation. The plane surfaces of the hollow cylinder were sealed with Bondo<sup>TM</sup> fibreglass resin to ensure that the flow pattern corresponds to radial flow (see e.g. Jenner, 2012). A schematic view of the experimental faculty is shown in Figure 4.11.

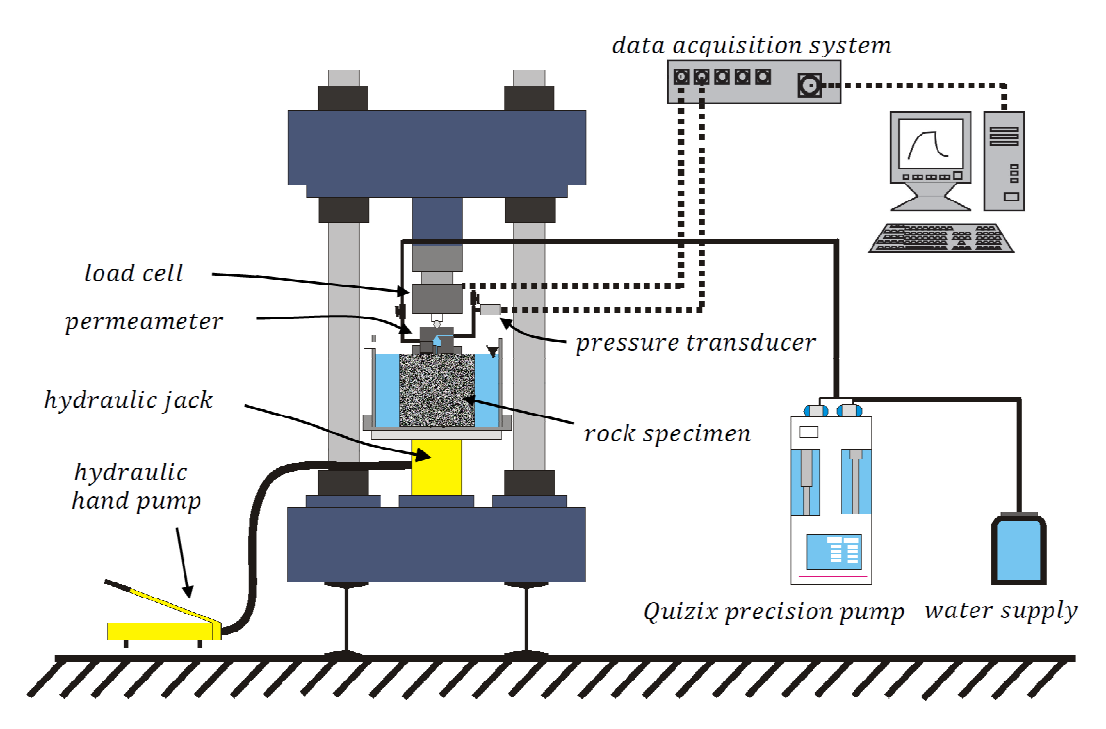
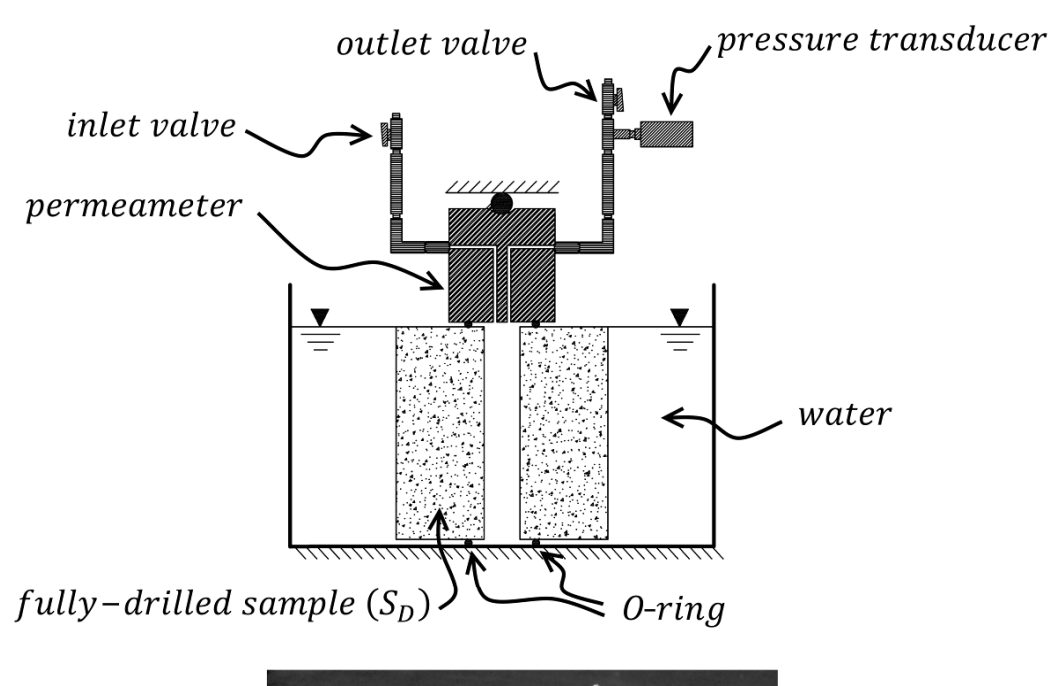


Figure 4.11: Experimental faculty for measuring the permeability of low permeability geomaterials (Frame designed by Mr. A. Chevrier, Carlton University).

The apparatus consists of a test frame to provide a seal between the centrally cored Stanstead Granite specimen and a stainless steel "permeameter" that has a water inflow, an outlet and a connection to a 1400 kPa Honeywell pressure transducer. This arrangement, in principle, is the same as experimental technique used by Carnaffan (1994) and Selvadurai and Carnaffan (1997) when performing hydraulic pulse tests on cementitious grout and by Selvadurai and Selvadurai (2010) when performing steady state patch permeability tests. The permeameter has provisions for extracting air from the central cavity that could influence the performance of the hydraulic pulse test. Figure 4.12 shows the details of the permeameter.

The procedure for performing the radial flow pulse test involves a preliminary test that is performed on a machined aluminum cylinder to test the efficiency of the seals used to maintain radial flow. In these trial tests, the upper flat surface of the aluminum cylinder was covered with epoxy in exactly the same way as the

surface of the granite sample. A sealing pressure of 1.5 MPa was applied to the Oring contact area and three hydraulic pulse tests were performed. The load applied to the sample for sealing purposes was measured using a 45 kN Futek load cell. Each test started with the instantaneous build up of pressure in the permeameter cavity.



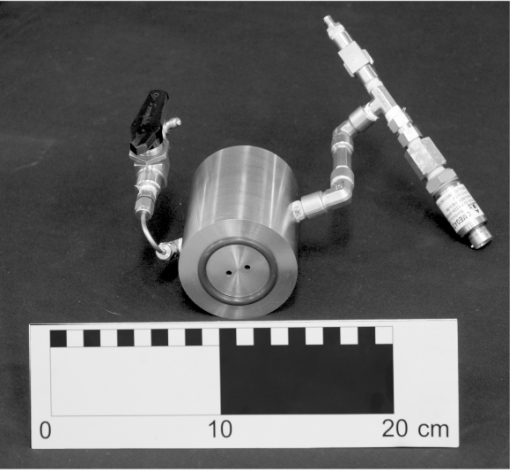


Figure 4.12: Components of the permeameter used to perform hydraulic pulse tests on fully-drilled samples.

Figure 4.13 shows the cavity pressure decay curves for these pulse tests. The maximum observed cavity pressure decay was less than 4% of the initial pressure pulse during the first 5000 seconds.

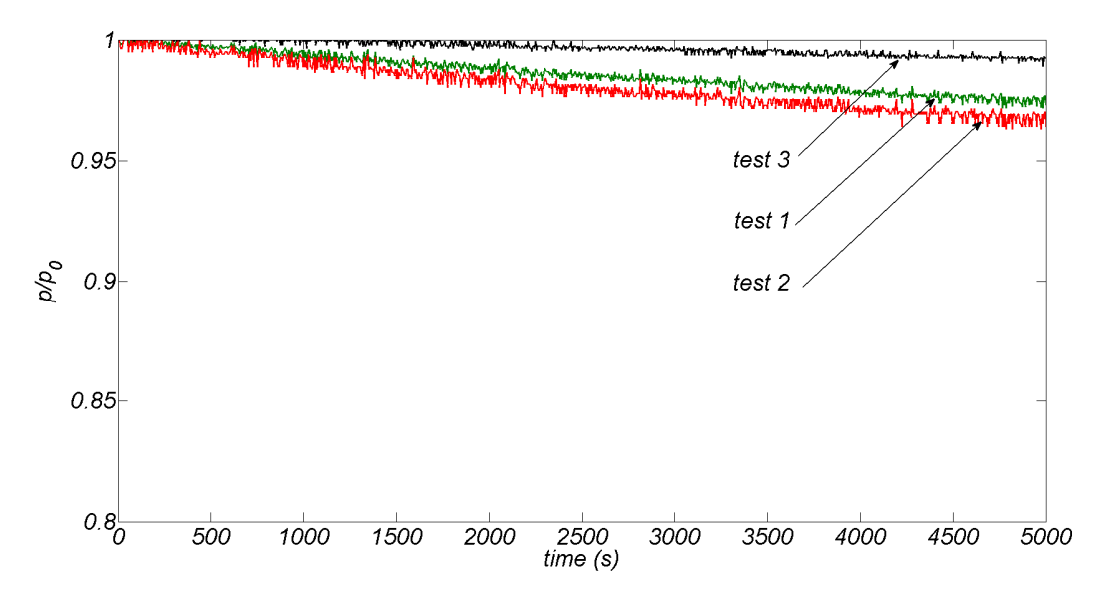


Figure 4.13: Decay of cavity pressure in 3 hydraulic pulse tests performed on a dummy aluminum cylinder, using an O-ring for the sealing.

Opening the inlet and outlet valves, the water was pumped into the permeameter using a Quizix Precision Pump (Model: QX-6000; minimum flow rate, 0.00034 ml/min; accuracy of the flow rate +/- 0.1% of set flow rate; maximum pressure: 41000 MPa) for about 5 minutes in order to make sure that no air was trapped within the permeameter. Subsequently, the outlet valve was closed and the cavity pressure was increased to 100-150 kPa in less than 60 seconds. This time interval can be regarded as representative of a hydraulic pressure pulse of a delta function-type. The inlet valve was then closed and the pressure decay was recorded each second for 5000 seconds. The temperature during the test was also recorded. Several tests were performed on each sample of Stanstead Granite in order to ensure repeatability of the results. After performing each test, all the valves of the permeameter were opened in order to allow any excess pore pressure generated within the sample to dissipate. Figure 4.14, shows the results for the time-

dependent pressure decay obtained during 10 pulse tests conducted on Stanstead Granite.

The interpretation of pulse tests to estimate the permeability can be performed in a variety of ways and the most convenient procedure is to develop a set of pulse decay curves that can be used to "bound" the value of permeability (Selvadurai and Carnaffan, 1997; Selvadurai et al., 2005). The bounding procedure for obtaining a range of values for  $\tilde{K}$  is considered to be more realistic than obtaining a specific value. The bounding data were determined from three different approaches: (i) the conventional piezo-conduction equation analyses ( $\tilde{K}_{pc}$ ), (ii) the conventional piezo-conduction equation, which also accounts for the compressibility of grains, analyses ( $\tilde{K}_{pcc}$ ), and (iii) a fully coupled analysis of the radial flow pulse decay problem ( $\tilde{K}_{fc}$ ).

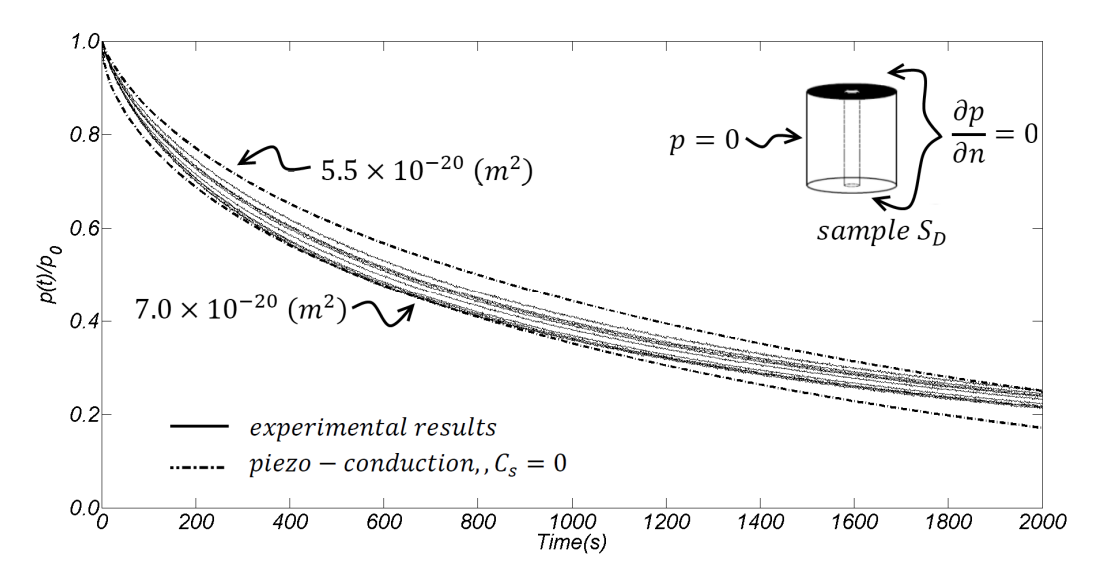


Figure 4.14: Results of hydraulic pulse tests performed on a fully drilled Stanstead Granite cylinder (sample  $S_D$ ). The analysis of the data was done using the piezo-conduction equation and neglecting the compressibility of the solid grains.

The bounding curves shown in Figure 4.14 are only estimates based on the approach (i) while Table 4.3 summarizes the permeability ranges estimated from

all three methods. There are only marginal differences between the three estimates.

Table 4.3: Permeability values for Stanstead Granite.

Sample	$\tilde{K}_{fc}$ (m <sup>2</sup> )	$\tilde{K}_{pcc}$ (m <sup>2</sup> )	$\tilde{K}_{pc}$ (m <sup>2</sup> )
$S_{\mathrm{U}}$	$(1.2 \text{ to } 1.7) \times 10^{-20}$	$(1.2 \text{ to } 1.7) \times 10^{-20}$	$(1.1 \text{ to } 1.6) \times 10^{-20}$
$S_D$	$(6.0 \text{ to } 7.7) \times 10^{-20}$	$(6.0 \text{ to } 7.7) \times 10^{-20}$	$(5.5 \text{ to } 7.0) \times 10^{-20}$

#### 4.3.2. Patch pulse tests

We next consider the problem of pulse loading applied at a patch located on the plane surface of a cylinder of Stanstead Granite. The patch pulse tests have been successfully used to estimate the permeability characteristics of rocks such as Berea Sandstone (Tidwell and Wilson, 1997) and Indiana Limestone (Selvadurai and Selvadurai, 2010). Here we present an application that investigates the transient behaviour of a hydraulic pulse applied at a circular opening located at the axis of the sealed plane surface of a cylindrical sample of Stanstead Granite. The sealing between the permeameter and the granite cylinder is achieved by applying an axial stress of 1.5 MPa. Similar to the O-ring sealing test, a series of hydraulic pulse tests were performed on a Plexiglas plate to establish any leakage from the sealing technique. The permeameter was placed on top of a Plexiglas surface and a sealing stress of 1.5 MPa was applied to the gasket.

Figure 4.15 shows the results of 5 hydraulic pulse tests. A maximum cavity pressure drop of 8% was observed during the first 5000 seconds. The pressure pulses applied within the opening are kept to a maximum of 150 kPa to eliminate any leakage at the sample-rubber gasket interface. The procedure adopted to constrain the gasket during its compression is similar to that used by Selvadurai (2010) and Selvadurai and Selvadurai (2010) and provides a successful sealing technique. A schematic view of the test arrangement is shown in Figure 4.16.

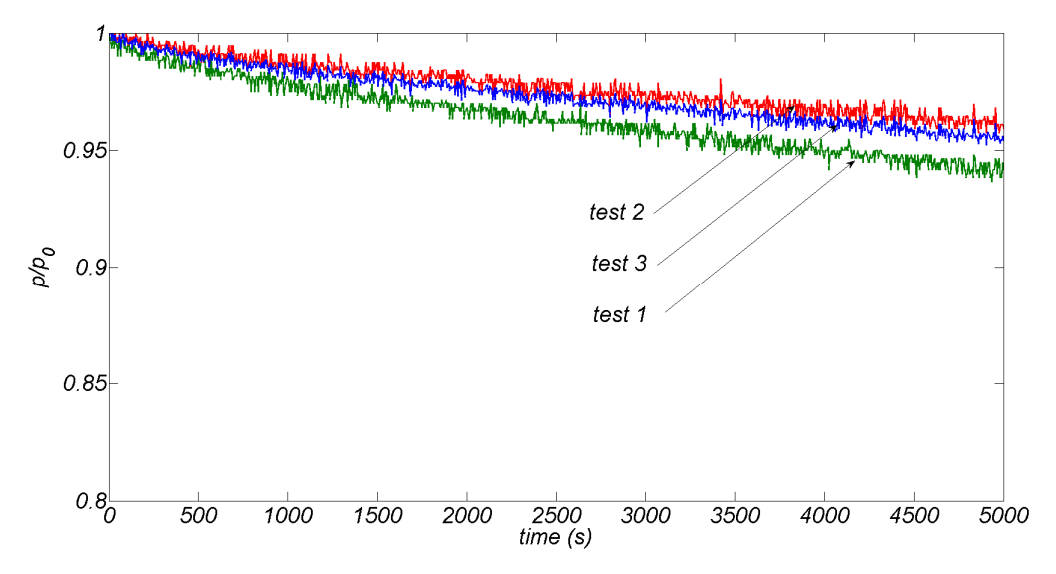
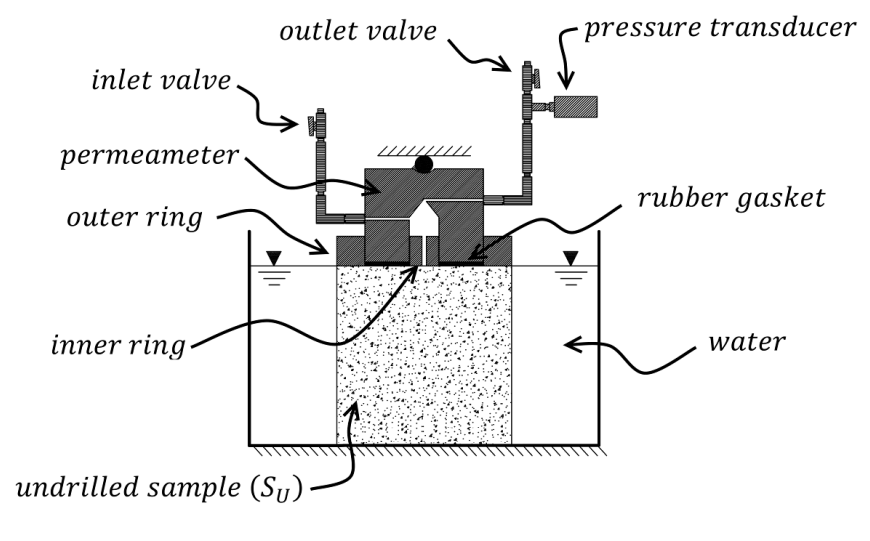


Figure 4.15: Decay of cavity pressure in hydraulic pulse tests performed on a Plexiglas, using gasket for the sealing.



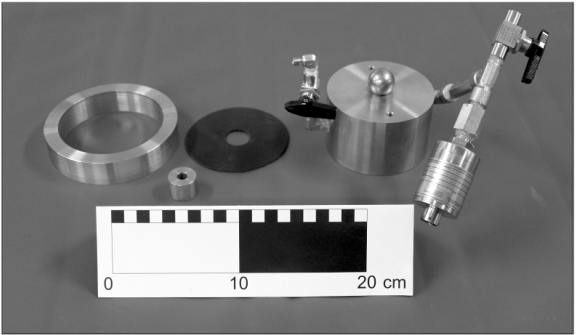


Figure 4.16: Components of the permeameter used to perform hydraulic pulse tests on undrilled samples.

The gasket has an inner diameter of 2.54 cm and an outer diameter of 10.16 cm. The annular region of the plane surface of the cylinder is maintained in a sealed and submerged condition.

The residual pore pressure fields created during saturation of the sample under vacuum were allowed to dissipate over a 7 day period. The fluid cavity was subjected to a pressure pulse to initiate the pulse tests. Figure 4.17 shows the results of surface pulse tests derived from 10 experiments conducted on the cylindrical sample of Stanstead Granite.

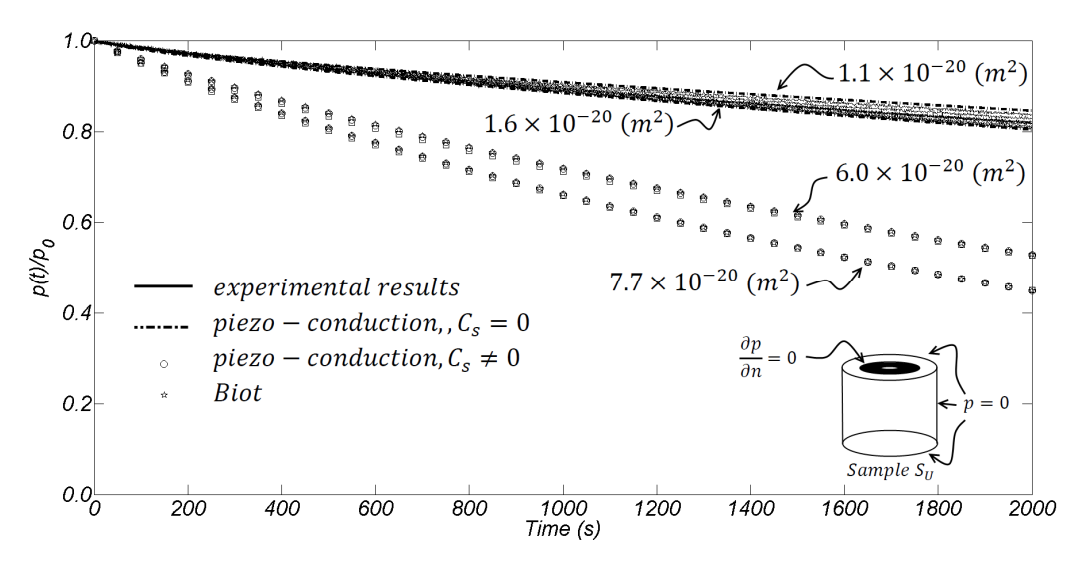


Figure 4.17: Results of hydraulic pulse tests performed on an undrilled Stanstead Granite cylinder (sample  $S_U$ ). The analysis of data was done using the piezo-conduction equation and neglecting the compressibility of the solid grains.

These results have been interpreted on the basis of the three sets of permeability estimates explained for radial flow hydraulic pulse tests in previous section. These estimated permeability values are also shown in Table 4.3. The pore pressure boundary condition applicable to the patch pulse testing that uses the piezo-conduction equation analysis (with and without the influence of grain compressibility) are shown in Figure 4.18 (a) and the pore pressure, displacement and traction boundary condition needed to perform a fully coupled analysis are

shown in Figure 4.18 (b). The results derived from the three sets of theoretical estimates for the permeability predicted the correct trends for the pulse decay, although the numerical predictions show deviations from the experimental data.

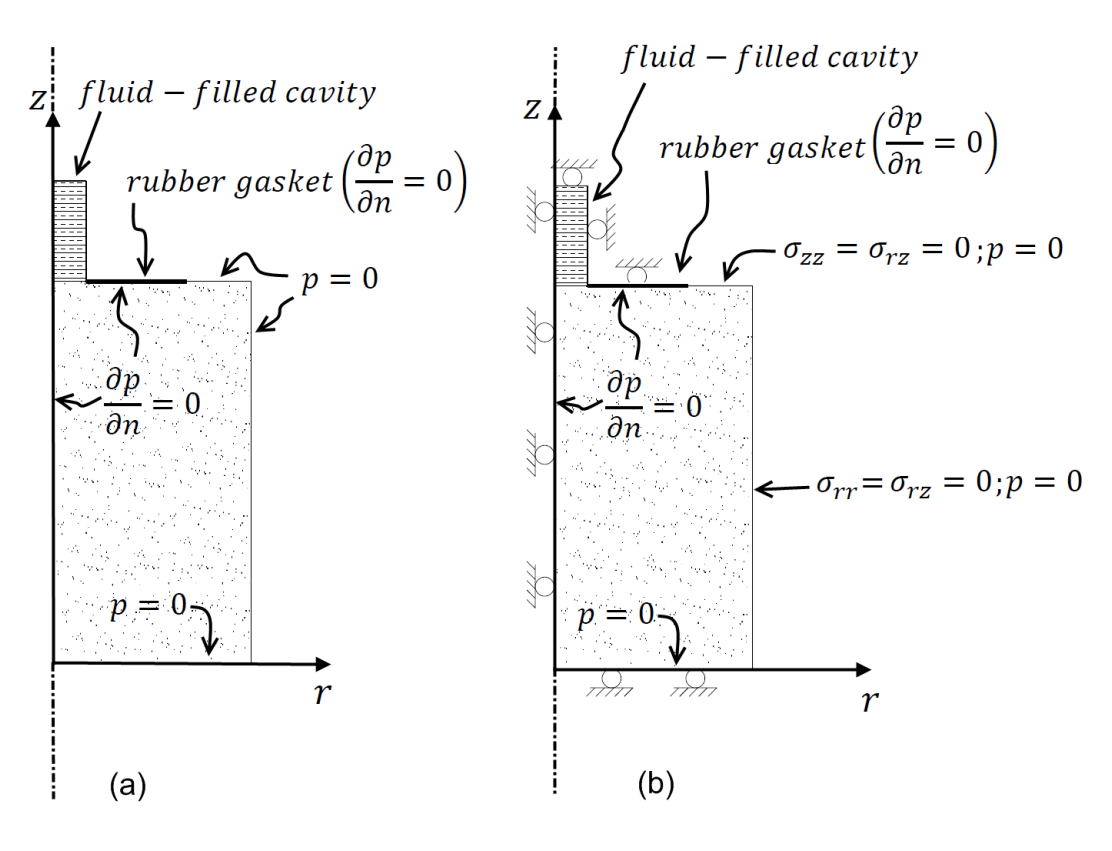


Figure 4.18: Sample S<sub>U</sub>: (a) Geometry and boundary conditions used for the piezo-conduction equation; (b) Geometry and boundary conditions used for Biot's poroelasticity equations.

The likely causes for the discrepancies seen between the experimental observations and theoretical predictions for the patch pulse tests could be due to several factors including leakage, damage during sample fabrication, transverse isotropy influences of permeability and air entrapment. The first two factors can be eliminated since this would have resulted in faster decay rates than those presented in Figure 4.17. There is little information on the estimation of permeability anisotropy of the Stanstead Granite. Literature on fracture toughness testing suggests the presence of some anisotropy in the fracture toughness properties (Nasseri et al., 2010). As a parametric exercise, hydraulic pulse test

behaviour was modelled with hydraulic transverse isotropy maintaining the range of values of the radial hydraulic conductivity estimated from the purely radial flow tests. It is estimated that the permeability in the axial direction should be 20 times smaller than the permeability in the radial direction in order to achieve a correlation between the computational predictions provided by the fully coupled analysis and the experimental data. Air entrapment in the system can be another reason for the discrepancy, the effect of which will be further discussed in Chapter 5.

#### 4.4. Summary

In this chapter, the use of the hydraulic pulse technique for measuring the permeability of low permeability geomaterials was discussed. The range of applicability of the piezo-conduction equation used to estimate the hydraulic properties of low permeability rocks was examined using Biot's poroelasticity theory. The results indicate that the prediction for the pressure decay can be influenced by both the model used to interpret the test and the test configuration; this in turn can influence the interpretation of the permeability of the porous medium. Conventional modelling of the test that uses the piezo-conduction equation does not account for the compressibility of the solid grains and this factor can have an influence on the estimation of the permeability of geomaterials with small Biot coefficient. A further consideration is the influence of generalized deformations of the porous skeleton; this can be accommodated for by modelling the piezo-conduction equation by appeal to Biot's classical theory of poroelasticity. The incorporation of the generalized deformations can also influence the interpretation of test results. The performance of the two modelling techniques is demonstrated by examining the pulse decay observed in two typical geologic media that have been investigated in the literature. Finally, the results of hydraulic pulse tests performed on two Stanstead Granite samples were analyzed by employing the separate approaches. Comparisons show that, although the permeability obtained from the different approaches change, the order of magnitude is consistent for the performed tests. Also, the computational studies performed show that the choice of a modelling technique has a greater influence

on the one-dimensional hydraulic pulse test than the radially symmetric test configurations. In general, the most complete approach to analyze the hydraulic pulse test results is to use Biot's poroelasticity theory, which accounts for deformability of the solid grains and models the coupled interaction of the porous skeleton deformation and the pressure change. This technique, however, is complicated and time consuming to employ. For simplicity, the permeability parameter can be estimated using the piezo-conduction equation that accounts for grain compressibility.

#### **CHAPTER 5**

# THE EFFECT OF AIR ON THE INTERPRETATION OF HYDRAULIC PULSE TESTS

#### 5.1. Introduction

The hydraulic pulse testing technique incorporates the compressibility of the constituents of the fluid-saturated porous medium, which includes the skeleton, the solid grains and the pore fluid. Each hydraulic pulse test starts with rapid pressurization of the fluid cavity in contact with a surface of the sample. The inlet valve to the cavity is then closed and the fluid cavity pressure dissipation is monitored. Since the compressibility of the pressurized fluid is low, a minimal migration of fluid to the porous medium causes the pressure in the cavity to drop. The compressibility of pure water at 20 °C is 4.54×10<sup>-10</sup> Pa<sup>-1</sup> (White, 1986), which is defined as the relative volume decrease induced by the pressure increase. As an example, a 100 kPa pressure drop in an arbitrary 20 ml fluid-filled cavity corresponds to 9.0×10<sup>-4</sup> ml of fluid loss. Therefore, the technique provides the resolution required to measure very small amounts of fluid flow, which makes the transient measurement of permeability of tight rocks feasible. However, the entrapment of air bubbles in the fluid cavity can significantly affect the compressibility of water. It was noted by Fredlund (1976) that air inclusion of only 1% increases the compressibility of water by three orders of magnitude.

Since, in practice, it is almost impossible to avoid air entrapment in the sealed fluid cavity used in hydraulic pulse testing, the effect of this phenomenon should be taken into account. The effects of compressibility of the air-water mixture was also studied by Schuurman (1966), Fredlund (1976), Teunissen (1982), Pietruszczak and Pande (1996), and Selvadurai and Ichikawa (2013).

#### **5.2.** Governing equations

Air can exist in water in two different forms: dissolved air and air in a gaseous form. Assuming that the air inclusions in the water is in the form of bubbles and neglecting the effects of the solubility of air in the water, the surface tension of the water and the vapour pressure, the compressibility of the air-water mixture can be calculated. The total volume of the mixture  $(V_t)$  is composed of pure water  $(V_w)$  and air bubbles  $(V_a)$ . The air fraction is defined as

$$\varphi = \frac{V_a}{V_w + V_a} \tag{5.1}$$

The isothermal compressibility of the mixture, pure water, and the air inclusion are, respectively, defined as

$$C_{eq} = -\frac{\frac{dV_t}{V_t}}{\frac{V_t}{dp}} \qquad ; \qquad C_w = -\frac{\frac{dV_w}{V_w}}{\frac{V_w}{dp}} \qquad ; \qquad C_a = -\frac{\frac{dV_a}{V_a}}{\frac{V_a}{dp}}$$
 (5.2)

Substituting  $V_t = V_w + V_a$  in the compressibility equation of the mixture (i.e. Eq. (5.2)) gives

$$C_{eq} = -\frac{\frac{dV_{t}}{V_{t}}}{dp} = -\frac{\frac{dV_{w}}{(V_{w} + V_{a})}}{dp} - \frac{\frac{dV_{a}}{(V_{w} + V_{a})}}{dp}$$
(5.3)

The two terms in the right hand side of Eq. (5.3) can be re-written in the form of  $C_a$  and  $C_w$ 

$$\frac{1}{V_a + V_w} \frac{dV_a}{dp} = \varphi \frac{1}{V_a} \frac{dV_a}{dp} = \varphi C_a \quad ; \quad \frac{1}{V_a + V_w} \frac{dV_w}{dp} = (1 - \varphi) \frac{dV_w}{dp} = (1 - \varphi) C_w \quad (5.4)$$

Substituting Eq. (5.4) into Eq. (5.3) gives

$$C_{eq} = \varphi C_a + (1 - \varphi) C_w \tag{5.5}$$

Eq. (5.5) gives the compressibility of a fluid-gas mixture with free air bubbles. The compressibility of air can be derived by considering the incremental variations to Boyle's Law in an isothermal condition; i.e.

$$PV_a = const.$$
;  $PdV_a + V_a dP = 0$   $\Rightarrow$   $C_a = \frac{-\frac{dV_a}{V_a}}{dP} = \frac{1}{P}$  (5.6)

where P is the absolute air pressure.

Boyle's law also determines the changes of air fraction with pressure. Assuming that the total volume of cavity (i.e.  $V_w + V_a$ ) is constant during hydraulic pressure decay, the air fraction equation can be re-written as

$$P^{0}V_{a}^{0} = PV_{a} \; ; \; \varphi = \frac{V_{a}}{V_{w} + V_{a}} \implies \varphi = \frac{\frac{P^{0}}{P}V_{a}^{0}}{V_{w} + V_{a}} = \frac{P^{0}}{P}\varphi^{0}$$
 (5.7)

where  $P^0$  is the initial absolute water pressure,  $V_a^0$  is the initial volume of air, and  $\varphi^0$  is the initial air fraction in the cavity.

Figure 5.1 shows the effect of the air fraction in the form of air bubbles on the compressibility of the air-water mixture (the effect of solubility of air is neglected, i.e. h=0).

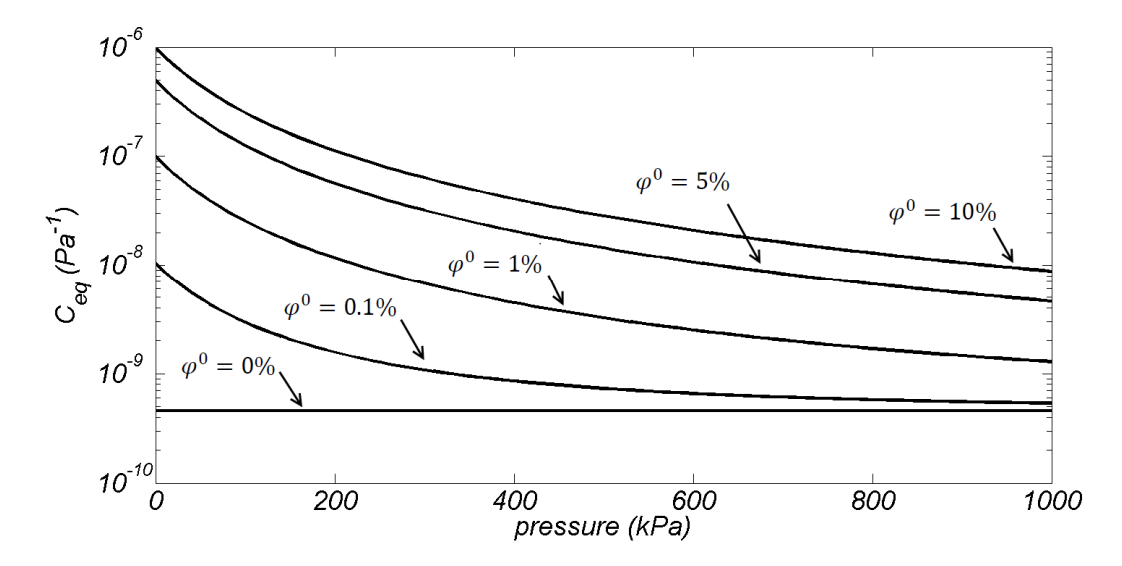


Figure 5.1: Compressibility of air-water mixtures with different air fractions.

From Figure 5.1 it can be seen that the amount of air inclusion has a significant effect on the compressibility of the mixture. For instance, for an air fraction of 1%, the compressibility is in the range of  $1\times10^{-9}$  (Pa<sup>-1</sup>) to  $1\times10^{-7}$  (Pa<sup>-1</sup>). Therefore, compared to the compressibility of de-aired water, only a 1% air fraction can increase the compressibility of the mixture by three orders of magnitude, (as also noted by Fredlund (1976).

Air can dissolve in water without any chemical interaction and occupy a certain volume of the water. This volume is only temperature-dependent; Henry's Law states that the weight of gas dissolved in a certain quantity of liquid at a constant temperature is directly proportional to the pressure of the gas above the solution. Also, Fick's Law can be used to describe the rate at which air goes into solution. Based on Henry's Law, the maximum volume fraction of air in solution is  $h(1-\varphi)$ , where h is Henry's constant and  $\varphi$  is the air fraction. Thus, in order to take into account the effect of gas solubility on the compressibility of the gas-fluid mixture, Eq. (5.6) is modified as follows

$$C_{eq} = \frac{\varphi + h(1 - \varphi)}{P} + (1 - \varphi)C_{w}$$
 (5.8)

The dissolved air fraction in Eq. (5.8) can contribute to the change in the compressibility of the air-water mixture only if the absolute pressure change in the system is slower than the rate of dissolution of air in the water. Otherwise, the effect can be neglected. Henry's constant (h) for air at a temperature of  $25\,^{\circ}$ C and atmospheric pressure is 0.01708. It should also be noted that as the volume fraction  $\varphi$  increases ( $\succ 0.05$ ) the compressibility of the mixture that incorporates solubility approaches the estimate for compressibility of a system that excludes solubility (Schuurman, 1966).

# 5.3. Computational modelling of the effect of air inclusions on hydraulic pulse tests

In order to study how the existence of air bubbles affects cavity pressure decay, a hydraulic pulse test was modeled using COMSOL<sup>TM</sup>. The simulated sample was a cylinder with dimensions of 100 mm in diameter and 200 mm in height. The piezo-conduction equation was used to model the phenomenon, taking into account the compressibility of the solid grains. Figure 5.2 shows the geometry and boundary conditions of the problem. The other parameters are as follows:

$$\begin{split} A \approx 7.85 \times 10^{-3} \text{ m}^2 & ; \ V_w \approx 10^{-5} \text{ m}^3 & ; \ n = 0.01 \ ; \ C_{eff} \approx 4.0 \times 10^{-11} \text{ Pa}^{-1} \ ; \ h = 0 \ ; \\ \alpha = 0.44 & ; \ C_w \approx 4.5 \times 10^{-10} \text{ Pa}^{-1} & ; \ \mu \approx 10^{-3} \text{ Pa/s} \ ; \ \tilde{K} \approx 1.0 \times 10^{-18} \text{ m}^2 \ ; \\ p_0 = 100 \text{ kPa} \end{split}$$

In order to draw normalized curves, we use the time factor T, as

$$T = \frac{A^2 Kt}{\mu V_w^2 C_w} \tag{5.9}$$

Substituting the values in *T* gives:

$$T = \frac{(7.853 \times 10^{-3})^2 \times 1.0 \times 10^{-18}}{10^{-3} \times (10^{-5})^2 \times 4.54 \times 10^{-10}} t = 1.36t$$

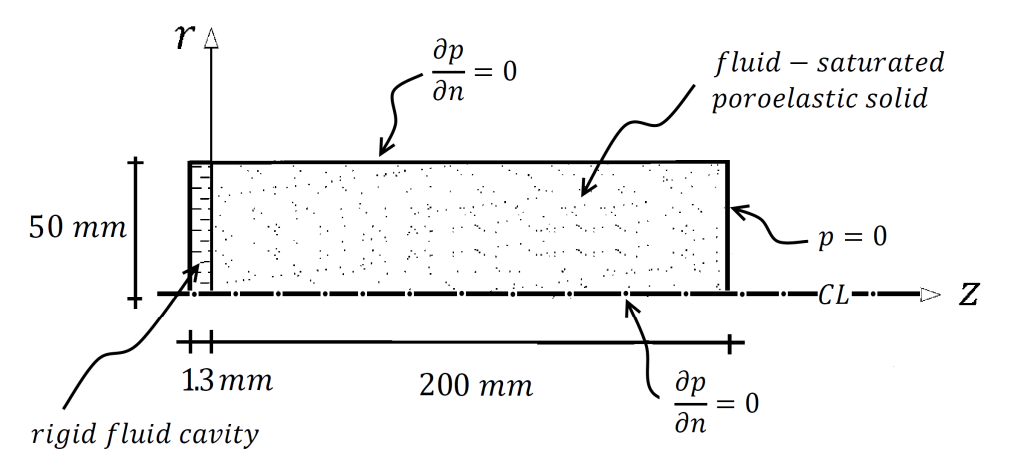


Figure 5.2: The geometry and boundary conditions of the one-dimensional hydraulic pulse test.

Figure 5.3 shows how air inclusion in the cavity can significantly affect the interpretation of permeability in hydraulic pulse tests. The problem was modelled for different air fractions varying from 0 to 10%.

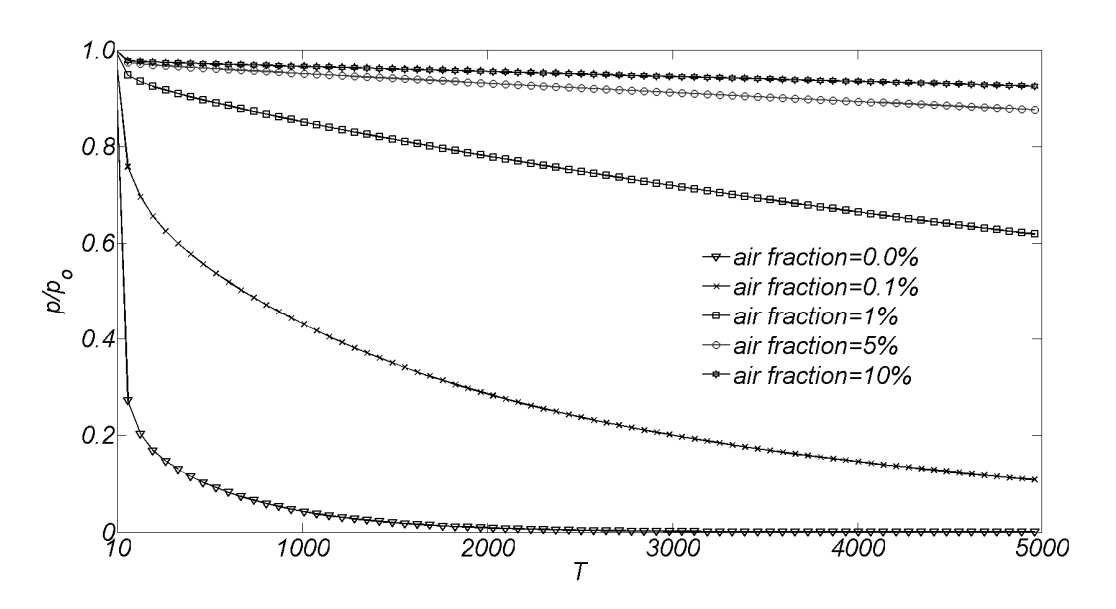


Figure 5.3: Effect of air bubbles on cavity pressure decay.

It can be seen that there is a significant difference between the hydraulic pressure decay curves for the different air fractions; if the effect of trapped air bubbles is not taken into account the interpretation of the permeability parameter from hydraulic pulse tests will be erroneous.

In order to further examine the effect of trapped air bubbles on the interpretation of hydraulic pulse test results, experiments were performed on two different samples of Stanstead Granite. Hydraulic pulse tests were performed on each sample and the estimated permeability values were compared with the steady state test results. The first set of experiments was performed on a small Stanstead Granite cylinder measuring approximately 50 mm in diameter and 100 mm in height. The second sample was a Stanstead Granite cylinder measuring approximately 150 mm in diameter and 300 mm in height. Each sample contained a partially drilled cavity.

#### 5.4. Permeability measurement of the small sample

The small Stanstead Granite cylinder, S-SG, measured 49 mm in diameter and 100 mm in height and was centrally cored with a core diameter of 7 mm, drilled to a depth of 61 mm. A stainless steel fitting was connected to the cavity using a marine epoxy. In order to make the sample surface impermeable, the top surface was coated with the same epoxy. The sample is shown in Figure 5.4.

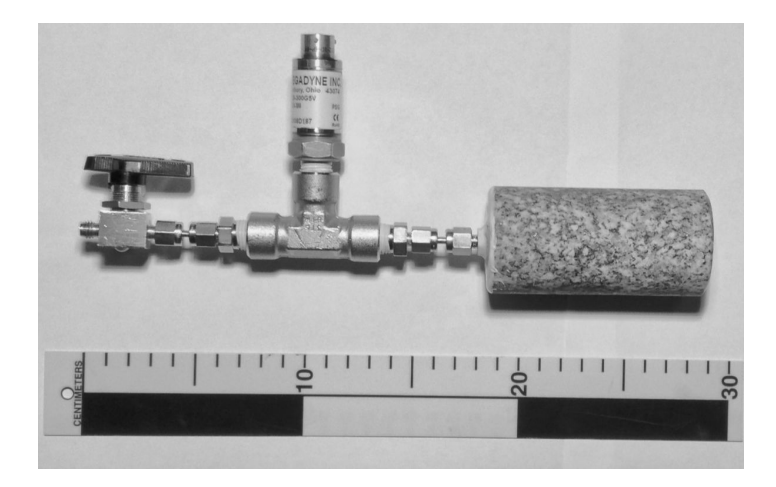


Figure 5.4: The assembly of sample S-SG.

The cavity pressure was measured using a 1400 kPa Omega pressure transducer connected to the fittings. Prior to performing the experiments, the sample was saturated in a vacuum chamber for 3 days. The central cavity of the sample and the connected fittings were filled with water using a syringe with a long needle. The total volume of the cavity including the volume of the drilled cavity, the

fittings and the pressure transducer, was measured as 10 ml. Figure 5.5 shows the schematic view of the experimental setup.

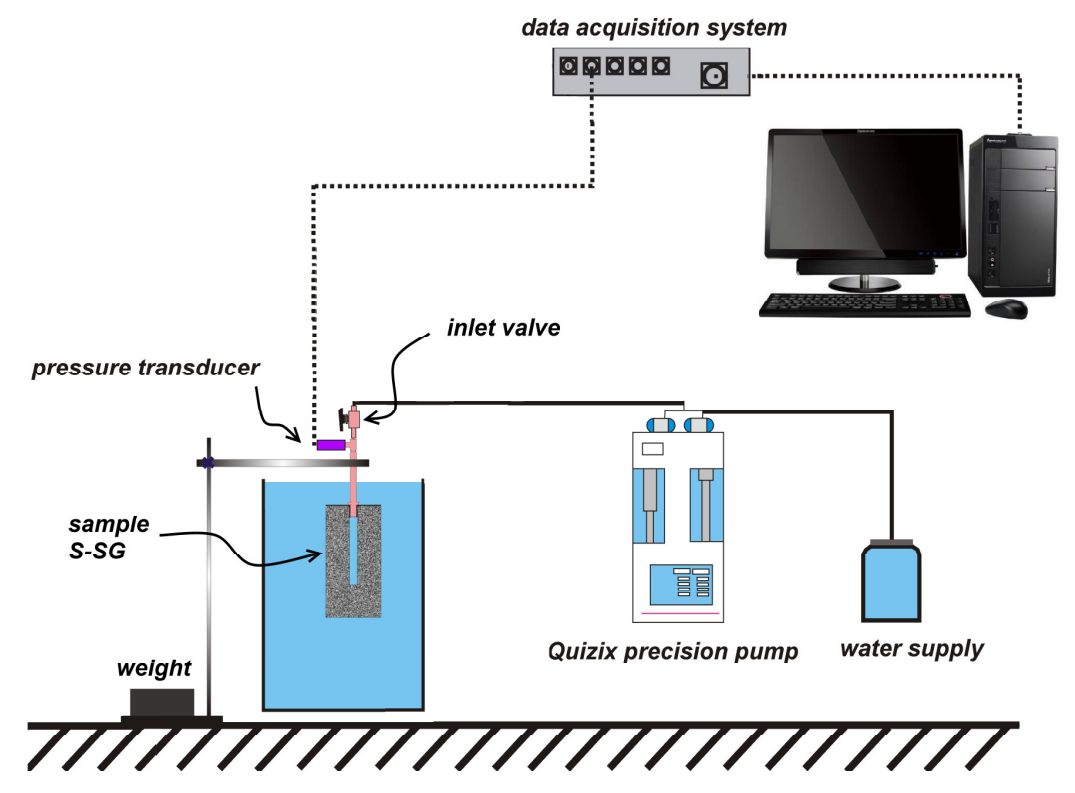


Figure 5.5: Schematic view of the hydraulic pulse test experiment performed on sample S-SG.

#### **5.4.1.** Steady state tests

Initially, the permeability of the sample was measured using a steady state technique under different flow rates of 0.0025, 0.005, 0.01, 0.02 ml/min. Figure 5.6 shows the cavity pressure recorded for the different flow rates. The problem was modelled using COMSOL Multiphysics<sup>TM</sup>. Table 5.1 shows the measured steady state pressure corresponding to each flow rate and the estimated permeability value.

The measured permeability was  $(3.45 \text{ to } 3.55) \times 10^{-18} (\text{m}^2)$ . The cavity pressure ranged from 55 kPa to 430 kPa and no pressure dependency was observed in the permeability measurement using the steady state technique.

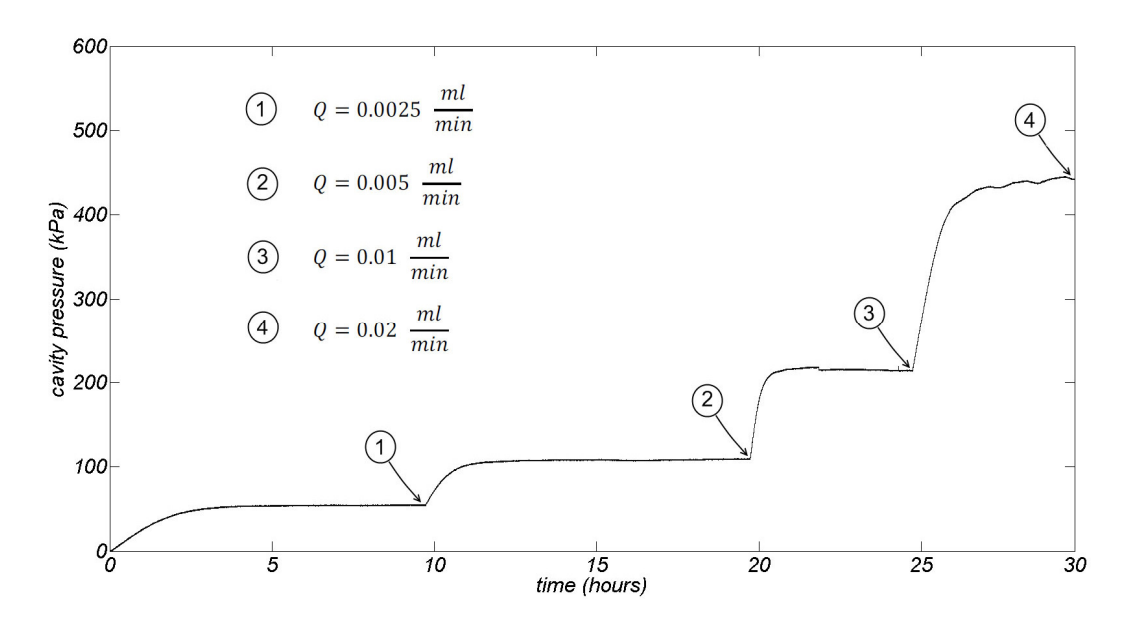


Figure 5.6: Changes in cavity pressure for steady state tests performed on Stanstead Granite sample S-SG, at different flow rates.

Table 5.1: The results of steady state tests performed on Stanstead Granite sample S-SG.

point	1	2	3	4
Q (ml/min)	0.0025	0.005	0.01	0.02
p (kPa)	55.1	110	215	433
$\tilde{K}$ (m <sup>2</sup> )	$3.45 \times 10^{-18}$	$3.45 \times 10^{-18}$	$3.55 \times 10^{-18}$	$3.52 \times 10^{-18}$

#### **5.4.2.** Hydraulic pulse tests

After performing the steady state tests, a set of hydraulic pulse tests was performed on the same sample, S-SG. Each test was initiated by pumping water into the sample at a constant flow rate of 2 ml/min. After reaching the desired cavity pressure, the inlet valve was closed and the dissipation of the cavity pressure was monitored. Before the start of each new test, sufficient time was allowed for dissipation of the excess pore pressure generated from the previous test. This procedure was adopted (Selvadurai, 2009) in order to eliminate any influence of residual pressures on the interpretation of the hydraulic pulse test results.

A total of 9 hydraulic pulse tests were performed on the sample. The target maximum cavity pressure values were 100, 250, and 600 kPa. Three hydraulic pulse tests were performed at each target pressure. The measured cavity pressure changes were then analyzed using the COMSOL Multiphysics<sup>TM</sup> software. The piezo-conduction equation was used to model the phenomenon, taking into account the compressibility of the solid grains. The parameters used in the analysis were as follows: Young's modulus (E) = 61 GPa, Poisson's ratio (v) =0.17; porosity (n) = 0.5% to 1.4%; Biot coefficient ( $\alpha$ ) = 0.44; compressibility of the fluid  $(C_w) = 4.54 \times 10^{-10} \,\mathrm{Pa}^{-1}$ . The measured cavity pressure curves along with the computed bounding decay curves are shown in Figure 5.7. Compared to the steady state tests, the hydraulic pulse test results showed very low permeability values. The estimated permeability range is one to three orders of magnitude different from the permeability value measured using the steady state technique. Also, a clear pressure dependency was observed in the measured cavity pressure dissipation curves. Since no pressure dependency was observed in the steady state technique, referring to the Eq. (5.8) it can be concluded that it was associated with the existence of air bubbles in the cavity.

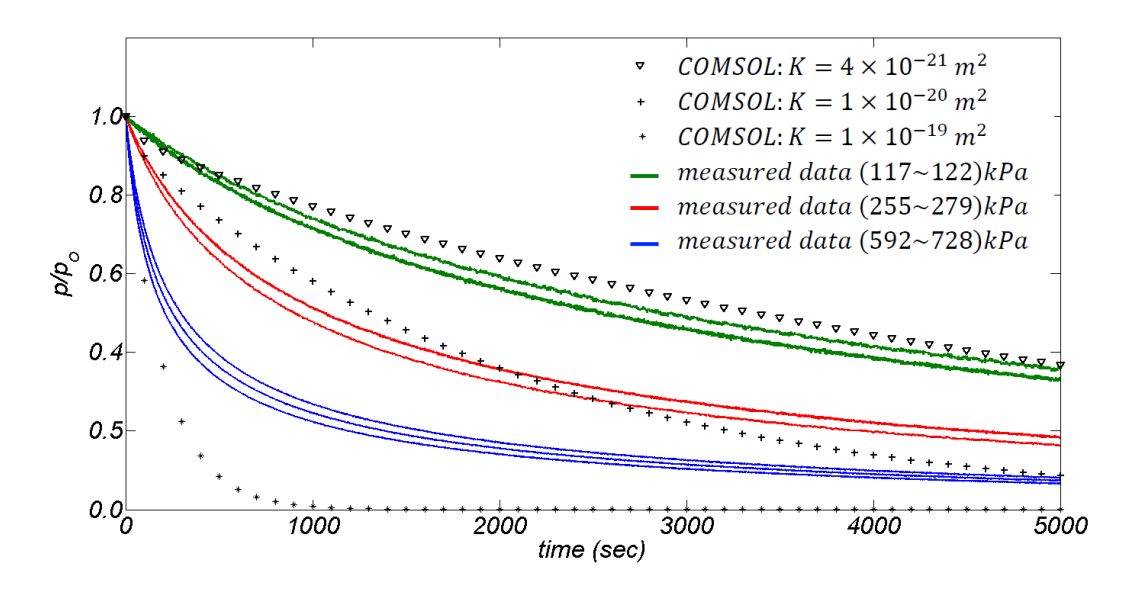


Figure 5.7: Hydraulic pulse tests performed on sample Stanstead Granite S-SG.

In order to take into account the effect that the compressibility of the air-water mixture has on the analysis of the hydraulic pulse tests and estimate the amount of trapped air in the fluid cavity, it was decided to study the pressure build-up curves.

# 5.4.3. Back-calculation of compressibility change using the experimental results

Assuming that the compressibility of the air-water mixture is  $C_{eq}$  and that water is pumped into the cavity at a constant flow rate, then

$$C_{eq} = -\frac{dV_{t}}{dp} \implies C_{eq} = -\frac{1}{V_{t}} \frac{dV_{t}}{dp}$$

$$(5.10)$$

where  $V_t$  is the volume of cavity while it is being pressurized. The volume includes the rock cavity, the cavity of the connection fittings and the volume of the pump cylinder. From the definition

$$Q = -\frac{dV_t}{dt}; \quad V_t(t) = V_t^0 - Qt$$
 (5.11)

where  $V_t^0$  is the initial total volume of the cavity, we obtain

$$C_{eq} \frac{dp}{dt} = \frac{Q}{V_t^0 - Qt} \tag{5.12}$$

The above equation can be approximated by

$$C_{eq} \approx \frac{Q/(V_t^0 - Qt)}{\Delta p/\Delta t} \tag{5.13}$$

In order to estimate the variation in the compressibility of the cavity fluid,  $C_{eq}$  for the hydraulic pulse tests performed on the Stanstead Granite sample S-SG, the pressure build-up curves recorded for the tests were used along with Eq. (5.13).

Figure 5.8 shows the change of  $C_{eq}$  with pressure for the cavity pressure build-up stage of the test. The range of compressibility of the cavity fluid was  $(7.0\times10^{-9})$  to  $3.4\times10^{-7}$  Pa<sup>-1</sup> for the applied pressure range, which is much higher than usually assumed for the parameter. Therefore, the assumption of constant compressibility of de-aired water,  $C_{w}=4.54\times10^{-10}$  (Pa<sup>-1</sup>), is not valid, since it introduces a significant error in the interpretation of hydraulic pulse test results.

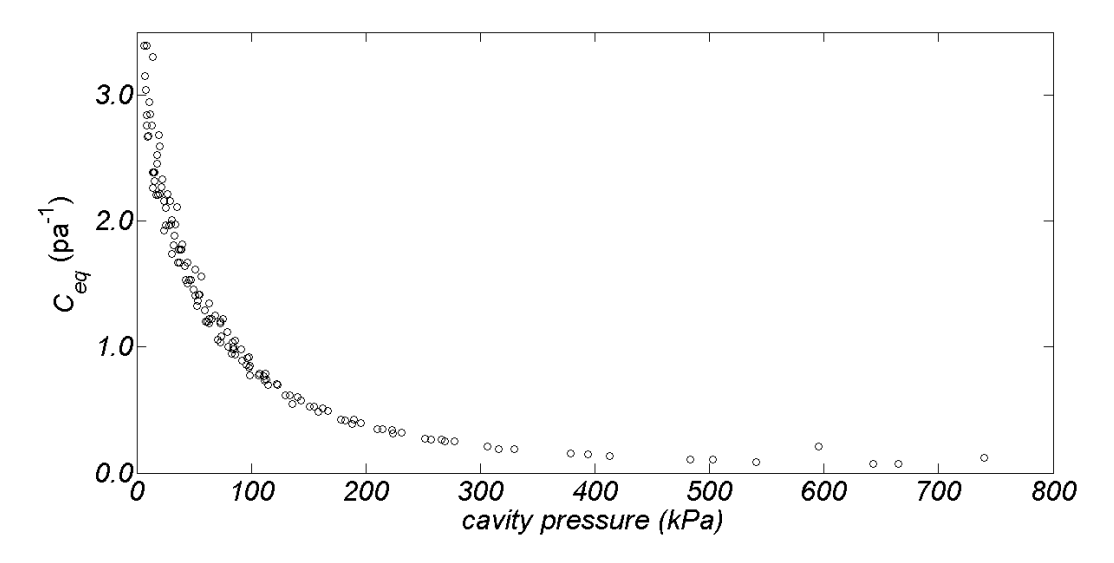


Figure 5.8: Change of  $C_{eq}$  with cavity pressure increase in Stanstead Granite sample S-SG.

Figure 5.9 shows the measured pressure build-up curve. In order to estimate the air fraction trapped in the cavity, the build-up of pressure in the sample was modelled using COMSOL Multiphysics<sup>TM</sup>. The parameters used in the model are:  $V_0 = 30.1$  ml (this includes the volumes of the rock cavity, the fittings, the connection tube, and the volume of water in the pump cylinder), Q = 2 ml/min,  $\tilde{K} = (3.2 \times 10^{-18} \text{ to } 1.0 \times 10^{-20})$  m<sup>2</sup> and n = 0.5% to 1.4%. The pressure build-up curves were fitted with the initial air fraction of  $\varphi^0 = 0.0298$ . Since the duration of pressure build-up is short, variations in permeability of the rock within the range of  $(3.2 \times 10^{-18} \text{ to } 1.0 \times 10^{-20})$  m<sup>2</sup> did not affect the pressure build-up curve.

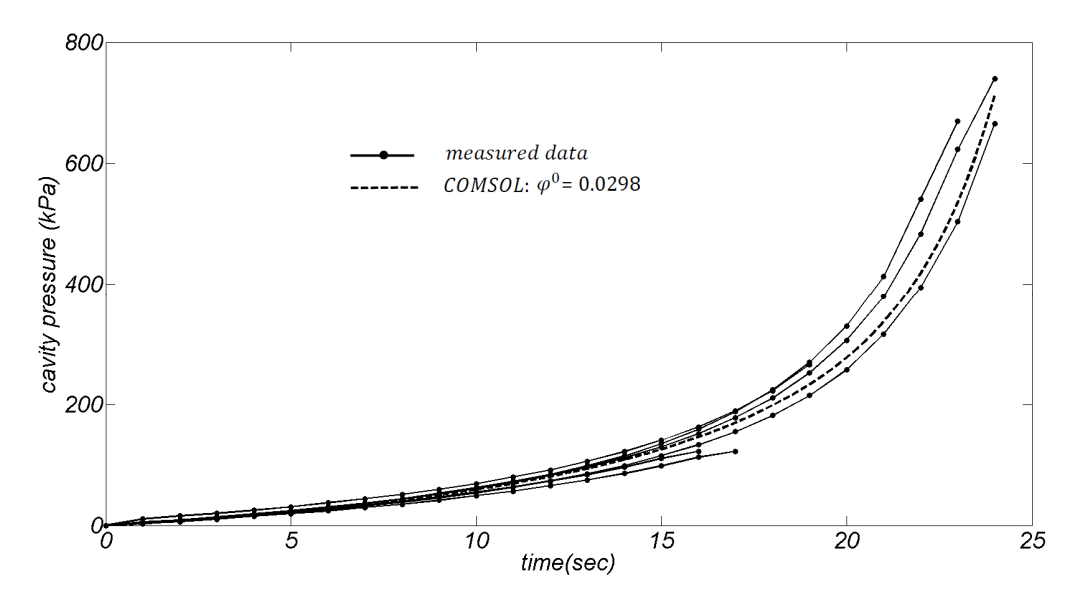


Figure 5.9: Experimental results for the build-up of cavity pressure due to pumping water at the rate of Q = 2ml/min, for Stanstead Granite sample S-SG.

#### 5.4.4. Estimation of the permeability range

As shown in Figure 5.7, the hydraulic decay curves for the pulse tests are dependent to the initial pressure, which cannot be explained by a constant  $C_{eq}$ . In order to estimate the permeability value, the results of hydraulic pulse tests were analysed using the compressibility of the air-water mixture for the cavity fluid. It was assumed that the sample was saturated and hence the compressibility of deaired water was used for modelling the specific storage of the porous medium. The results were studied for the first 50% drop in the cavity pressure.

The air fraction estimated from the pressure build-up curves was obtained with the assumption that the inlet valve was open, whereas during pressure decay the inlet valve is closed. Hence, in order for the estimated air fraction to be used in the analysis of hydraulic decay curves, it should be modified to account for the reduced volume of cavity. In the current experiment, the initial air fraction was estimated for a total fluid volume of 30.1 ml, whereas after closing the inlet valve the volume of cavity that is connected to the porous medium occupies 10 ml. Therefore, with the assumption that the air bubbles are trapped in the fittings

before the valve location the estimated air fraction should be multiplied by (30.1/10).

The problem was modelled in COMSOL<sup>TM</sup> for three different maximum cavity pressures of 120, 265, and 660 kPa. The values are the average of the cavity pressures measured in the experiments and the results are shown in Figures 5.10, 5.11 and 5.12.

In practice, with the increase in the cavity pressure, the trapped air gets partially dissolved in the water and the dissolution of the air decreases the cavity pressure. A complete model should also take into account the effect of the time and pressure-dependency of air in water. However, the simplified method proposed here provides an acceptable accuracy for the estimation of permeability using the hydraulic pulse testing technique. The estimated permeability for the Stanstead Granite sample S-SG is  $(3.2 \text{ to } 3.5) \times 10^{-18} \text{ m}^2$ .

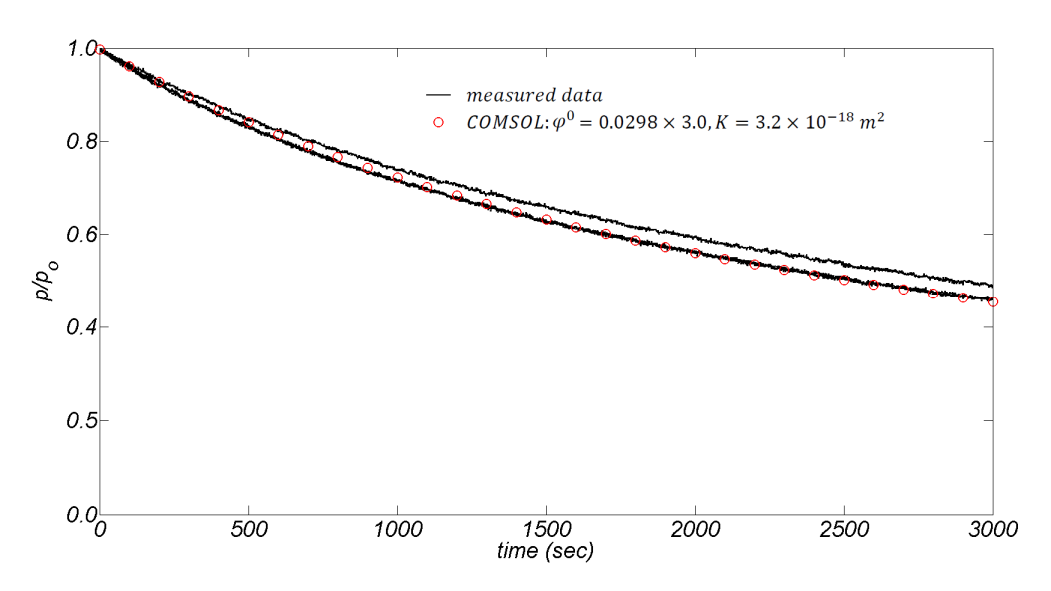


Figure 5.10: Hydraulic pulse test results performed on Stanstead Granite sample S-SG with a maximum cavity pressure of 120 kPa.

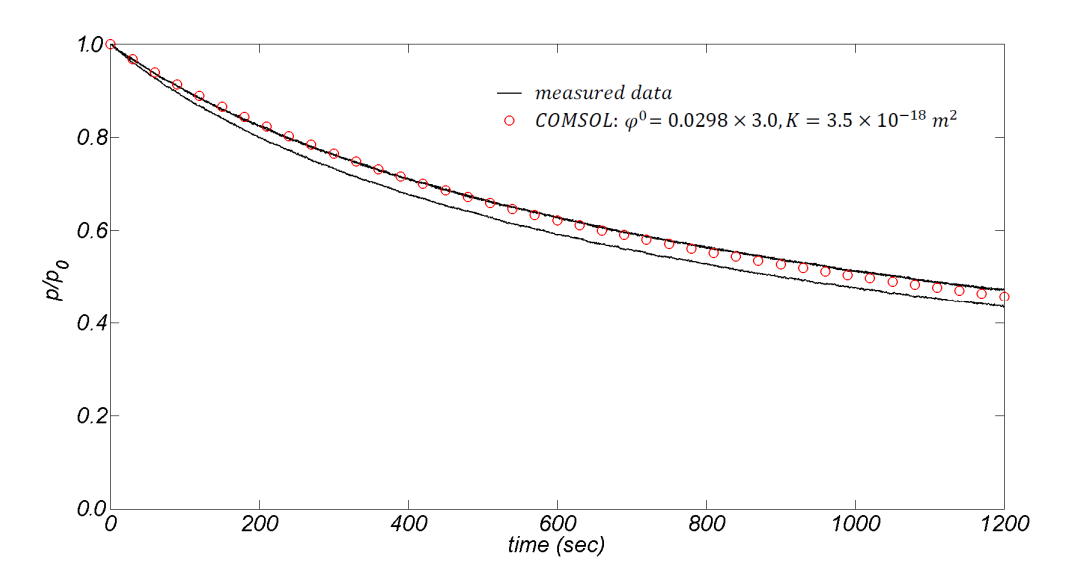


Figure 5.11: Hydraulic pulse test results performed on Stanstead Granite sample S-SG with a maximum cavity pressure of 265 kPa.

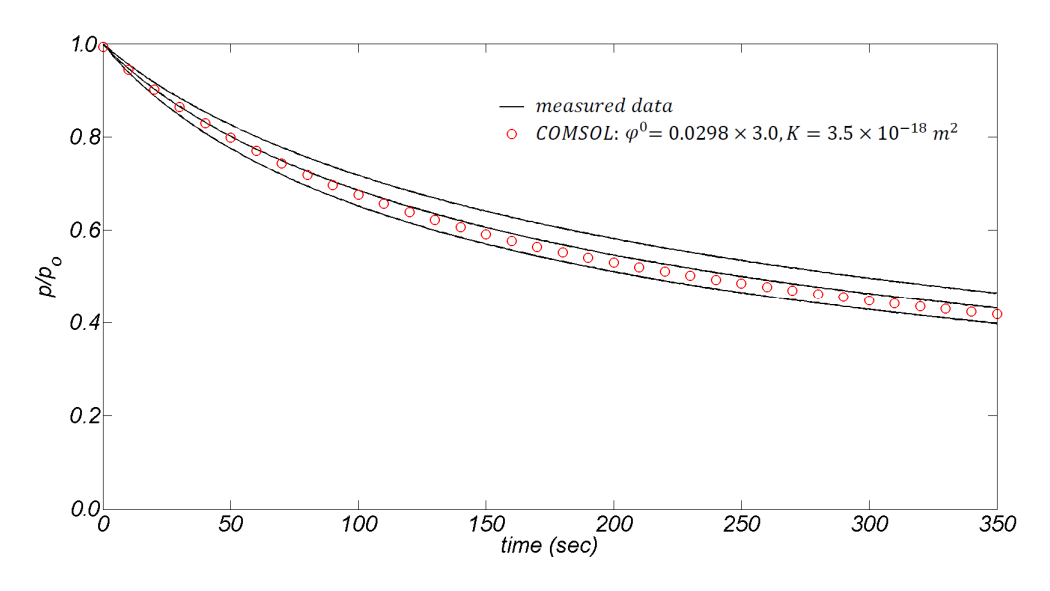


Figure 5.12: Hydraulic pulse test results performed on Stanstead Granite sample S-SG with a maximum cavity pressure of 660 kPa.

### 5.4.5. Injecting air in the cavity

In order to further investigate the effect of air inclusion on the hydraulic pressure decay, measured volumes of air were introduced to the fluid-filled cavity of sample S-SG in two steps. The sample was initially immersed in water and the fitting was connected to a Venturi pump that applied suction to the fluid-filled cavity. A transparent plastic pipe was used to connect the vacuum pump to the

cavity fitting in order to observe the extracted air bubbles. The applied suction helped to remove the trapped air bubbles from the cavity. The extraction of air bubbles appeared to have stopped after almost a day of suction; however, the suction was continued for another 24 hours in order to verify that the air bubble extraction was complete. The vacuum pump was then turned off and the negative pore pressure in the rock was allowed to dissipate for a day before starting the hydraulic pulse tests. The experiments were conducted in three steps: (i) three hydraulic pulse tests were performed on sample S-SG after suction removal of the trapped air bubbles, (ii) three hydraulic pulse tests were performed after deliberately introducing 0.035 ml of air into the fluid-filled cavity, and (iii) three hydraulic pulse tests were conducted after introducing another 0.106 ml of air into the fluid-filled cavity.

All of the hydraulic pulse tests commenced by pumping water into the cavity at a constant flow rate of 2 ml/min. When the fluid pressure in the cavity reached 300 kPa, the inlet valve was closed. A syringe with a long needle was used to remove water from the cavity for steps (ii) and (iii). The syringe was weighed before and after removing water from the cavity using a 104-s Mettler Toledo<sup>TM</sup> measuring scale with the accuracy of 0.1 mg; the difference between the measured weights of the syringe equals the amount of the extracted water. Since the volume of water extracted from the cavity is replaced by air, the calculated weight difference can be associated with the volume of air added to the cavity. Figure 5.13 shows the measured pressure build-up curves for the three sets of hydraulic pulse tests. The curves were fitted using COMSOL<sup>TM</sup>, assuming an air fraction of  $\varphi^0 = 0.0076$  for step (i),  $\varphi^0 = 0.0097$  for step (ii), and  $\varphi^0 = 0.0139$  for step (iii). The above mentioned air fractions were then used to back-calculate the volume of trapped air in each step. Using the total cavity volume of 22.3 ml (including the rock cavity, the fittings, the volume of water in the connection pipe and the pump cylinder) the air volumes were estimated as 0.169 ml for the suction-saturated state, 0.047 ml for the first injection of air and 0.094 ml for the second injection of air. The estimated injected air volumes compare favourably with the measured volumes.

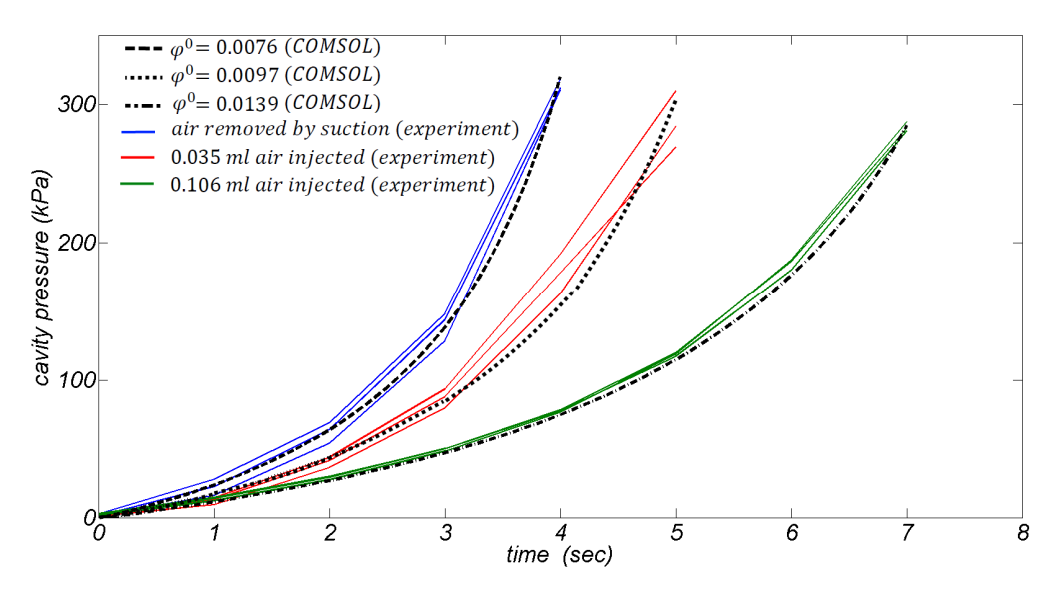


Figure 5.13: Experimental results for the build-up of cavity pressure due to pumping water at the rate of Q = 2ml/min, for the three sets of hydraulic pulse tests performed on Stanstead Granite sample S-SG.

Figure 5.14 shows the pressure decay curves for the three sets of hydraulic pulse tests performed on sample S-SG. As expected, as the air fraction increases, the cavity pressure decay decreases.

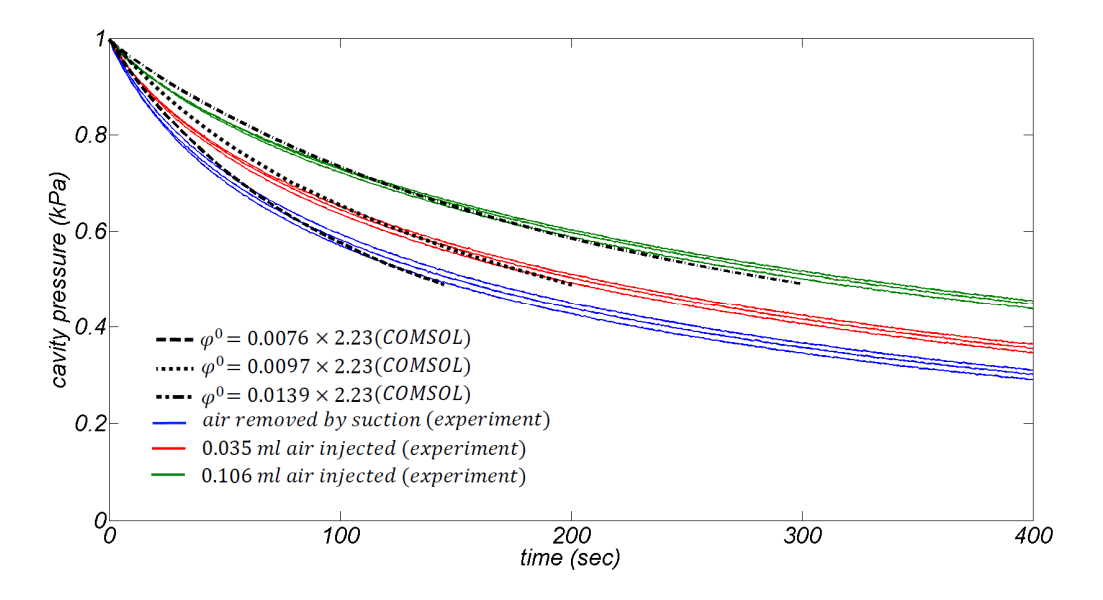


Figure 5.14: Hydraulic pulse test results performed on Stanstead Granite sample S-SG with three different air fractions.

The measured fluid pressure curves were then fitted using COMSOL<sup>TM</sup>. A permeability of  $3.6 \times 10^{-18}$  m<sup>2</sup> best fitted the results of the three sets of test for the first 50% pressure drop.

#### 5.5. Permeability measurement of the large sample

A large sample of Stanstead Granite, L-SG, was also tested to measure the permeability using both steady state and hydraulic pulse testing techniques. The diameter of the sample was 152.4 mm with a height of 304.8 mm. The sample contained a central cavity partially drilled along the central axis of the sample with a diameter of 25.4 mm and a height of 152.4 mm. The bottom surface of the sample, which was drilled through, was sealed using Bondo<sup>TM</sup> fibreglass resin. Hence, sample L-SG had flow boundary conditions similar to the smaller sample S-SG, which was tested previously. The L-SG sample was saturated in a vacuum chamber for a week.

In order to minimize the amount of air bubbles trapped in the central cavity of the sample, it was placed in the experimental container in a large water tank while both the container and the sample were submerged. Sealing between the epoxycoated sample surface and the bottom plate was provided using an O-ring. The sealing pressure on the O-ring was 3 MPa, which was sufficient to provide the sealing. Vacuum grease was also used on the O-ring surface to ensure better sealing conditions. Figure 5.15 is a schematic of the sample and the testing facility. The sealing pressure was measured using a 45 kN Futek<sup>TM</sup> load cell. The cavity pressure was measured using a 1400 kPa Honeywell pressure transducer. The total cavity volume (the drilled part of the sample and the connections and fittings) was 98.2 cm<sup>3</sup>.

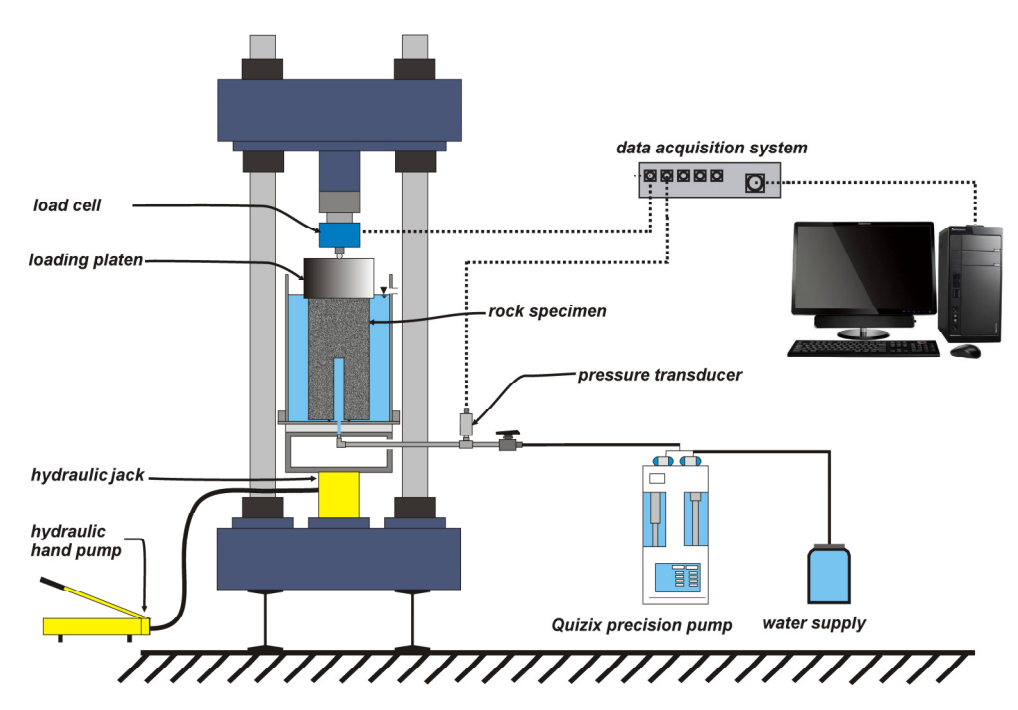


Figure 5.15: A schematic view of the setup used for measuring the permeability of Stanstead Granite sample L-SG.

#### **5.5.1.** Steady state tests

A set of steady state tests was performed on the sample, using a Quizix<sup>TM</sup> precision pump to apply flow rates of 0.025, 0.05, 0.1, and 0.15 ml/min. Table 5.2 gives the measured data and the corresponding permeability values estimated at each flow rate. The estimated permeability for the tested sample was (5.35 to 5.48) ×10<sup>-18</sup> m<sup>2</sup>. Figure 5.16 shows the change of cavity pressure with respect to time. The problem was also modelled in COMSOL<sup>TM</sup>.

Table 5.2. The results of steady state tests performed on the large sample of Stanstead Granite, L-SG.

Point	1	2	3	4
Q (ml/min)	0.025	0.05	0.1	0.15
p (kPa)	125.9	246.5	495.5	741.9
$\tilde{K}$ (m <sup>2</sup> )	$5.35 \times 10^{-18}$	$5.48 \times 10^{-18}$	$5.44 \times 10^{-18}$	$5.44 \times 10^{-18}$

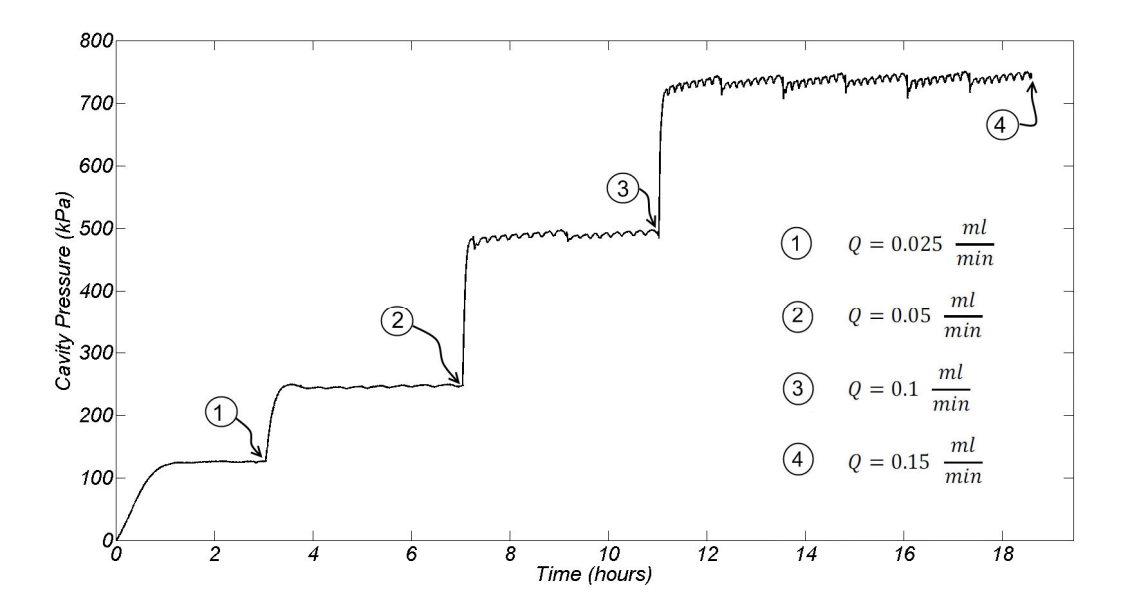


Figure 5.16: Changes in cavity pressure with respect to time for the steady state tests performed on Stanstead Granite sample L-SG.

#### **5.5.2.** Hydraulic pulse tests

Several hydraulic pulse tests were performed on the large Stanstead Granite sample L-SG, starting at initial cavity pressures ranging from 100 to 700 kPa. The water was pumped at a constant rate of 2 ml/min and the target initial pressures were 100, 300, and 600 kPa. As in the hydraulic pulse test results from sample S-SG, pressure dependency was observed in the measured cavity decay curves. Figure 5.17 shows the fluid cavity pressure decay curves. Assuming that the cavity fluid is de-aired, the permeability was estimated to be  $(0.5 \text{ to } 8) \times 10^{-20} \text{ m}^2$ , which is much lower than the permeability range estimated from the steady state tests.

The measured pressure build-up curves for the sample are shown in Figure 5.18. The curves were used to estimate the air fraction existing in the fluid cavity. Using COMSOL<sup>TM</sup>, the initial air fraction was estimated to be  $\varphi^0 = 0.007$  at zero pressure. Using the estimated air fraction, the results of hydraulic pulse tests were re-examined, taking into account the effect of air bubbles in the cavity.

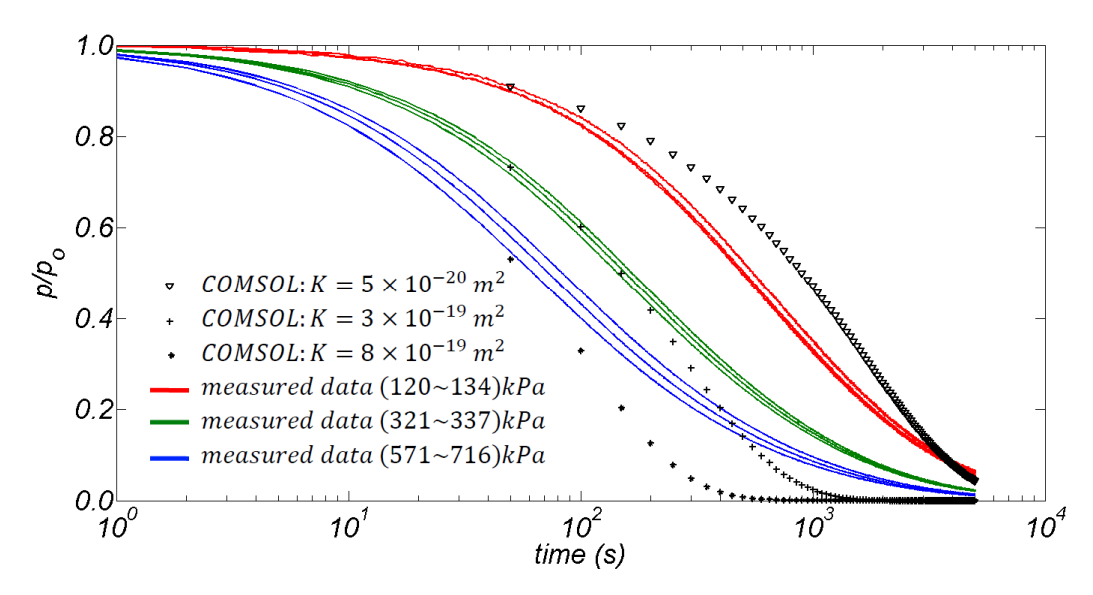


Figure 5.17: The measured fluid cavity pressure decay curves for Stanstead Granite sample L-SG.

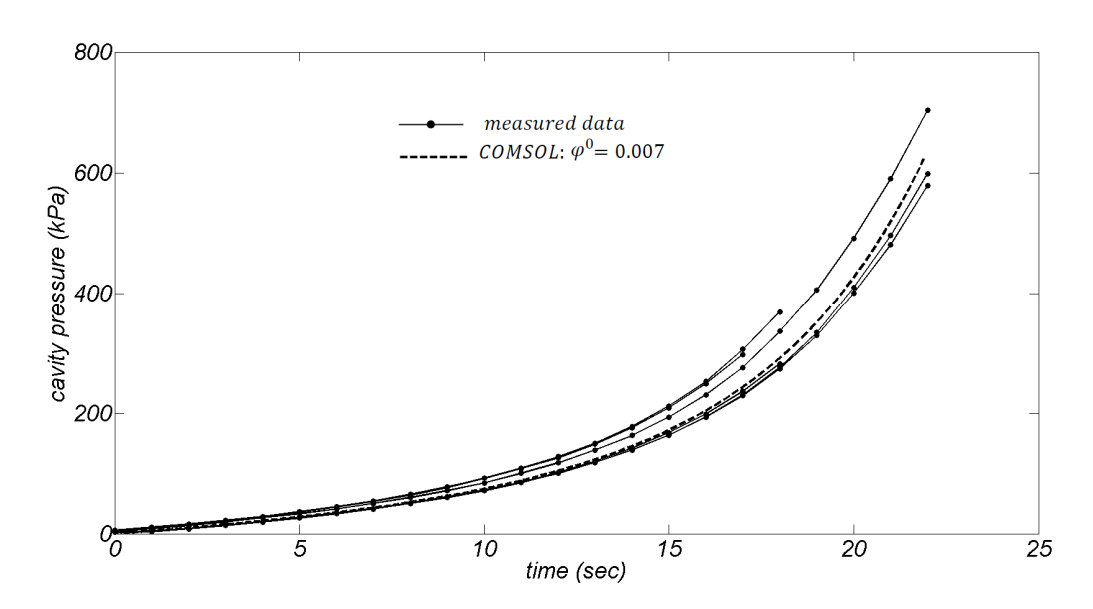


Figure 5.18: Experimental results for the build-up of cavity pressure due to pumping water at the rate of Q=2ml/min, for Stanstead Granite sample L-SG.

Figures 5.19 to 5.21 show the results of hydraulic pulse tests performed at the average initial cavity pressure values of 130, 330, and 640 kPa. The results were fitted with computational curves, using COMSOL<sup>TM</sup>. Only the first 50%

cavity pressure drop was used in the calculations. From the calculations, the permeability value was within the range of  $(5.4 \text{ to } 6.0) \times 10^{-18} \text{ m}^2$ .

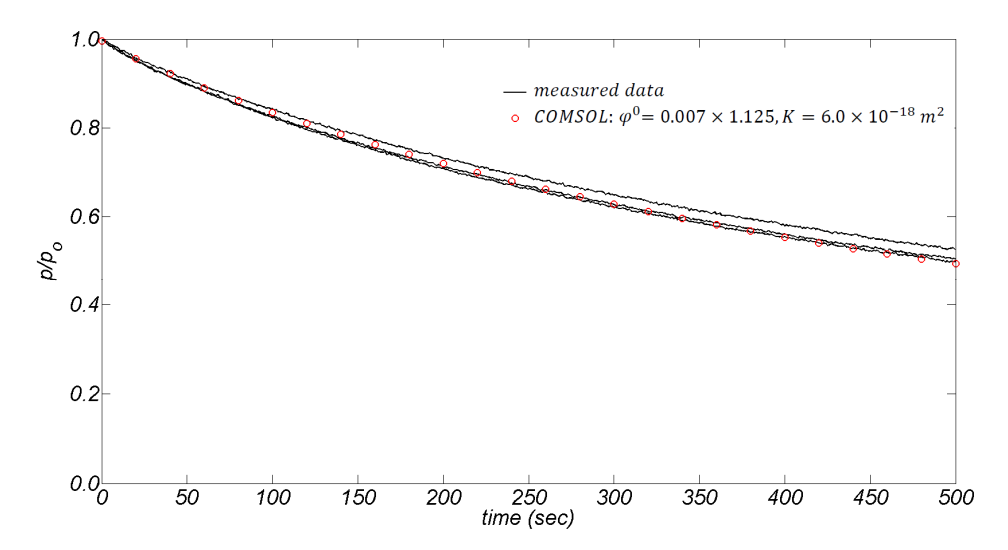


Figure 5.19: Hydraulic pulse test results performed on Stanstead Granite sample L-SG for the average initial cavity pressure of 130 kPa.

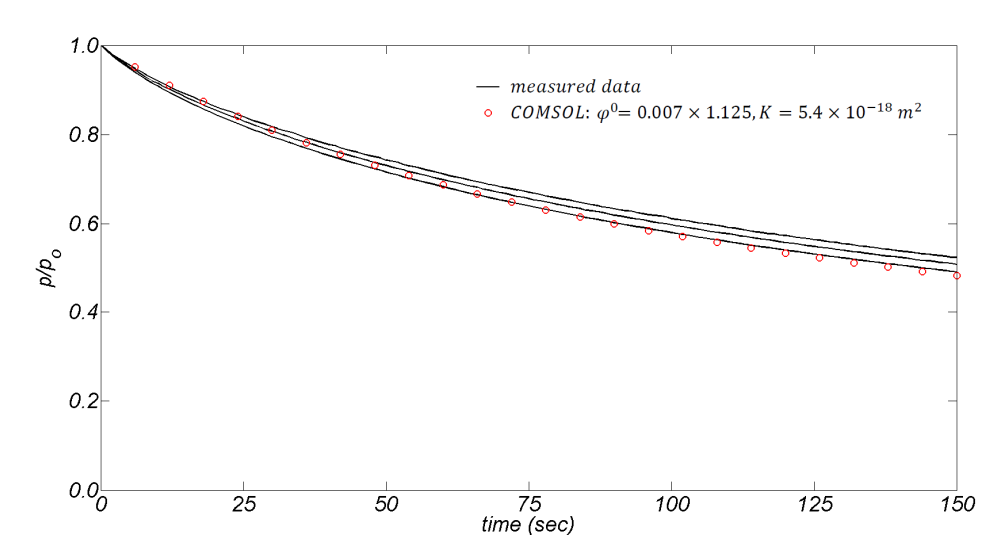


Figure 5.20: Hydraulic pulse test results performed on Stanstead Granite sample L-SG for the average initial cavity pressure of 330 kPa.

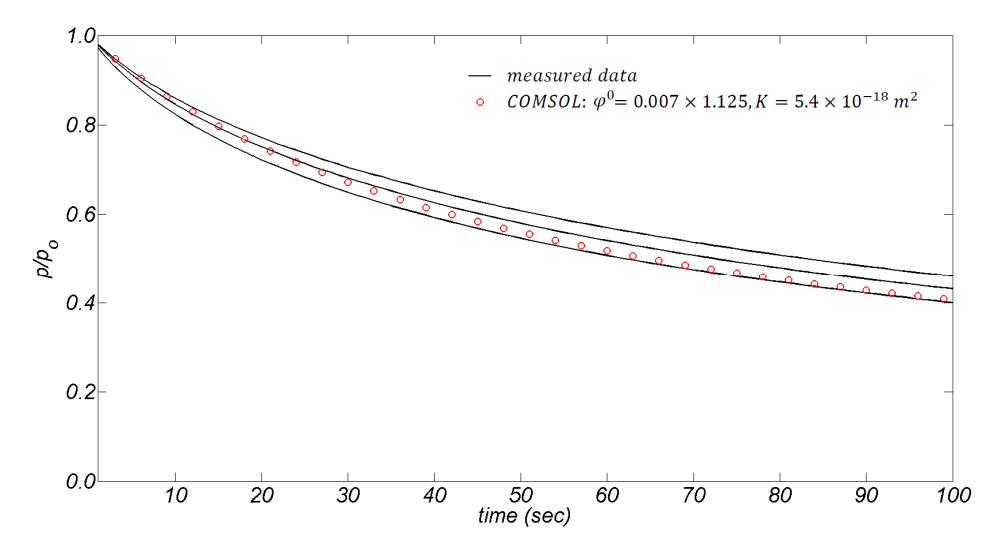


Figure 5.21: Hydraulic pulse test results performed on Stanstead Granite sample L-SG for the average initial cavity pressure of 640 kPa.

#### 5.6. Summary

In this chapter, a technique was proposed to correct for effects caused by the existence of air bubbles in the sealed cavity used in hydraulic pulse testing. Since, in practice, it is impossible to remove all the air bubbles from a sealed cavity, their effect should be taken into account. A relationship was presented to calculate the compressibility of the air-water mixture. It has been observed in the literature that the existence of 1% of air in the water increases the compressibility by three orders of magnitude. It was suggested that the amount of trapped air in the fluid cavity can be estimated from the pressure build-up curve. If the flow rate to the cavity is high enough, the pressure build-up becomes independent of the permeability of the rock. A series of steady state tests was performed on two different samples of Stanstead Granite by applying increasing flow rates. The permeability was measured to be within the range of  $(3.45 \text{ to } 5.48) \times 10^{-18} \text{ m}^2$  and no pressure dependency was observed in the permeability measurement. However, the hydraulic pulse decay curves were highly dependent on the initial cavity pressure, which can only be explained by the pressure dependency of water compressibility. The relationship between the compressibility of the cavity fluid and the cavity pressure was back-calculated from the pressure build-up stage of the hydraulic pulse test. It was seen that using the compressibility of pure water to interpret the hydraulic pulse test results is not accurate. Assuming constant compressibility of pure water for the sealed cavity,  $C_w$ =4.54×10<sup>-10</sup> Pa<sup>-1</sup>, the permeability was estimated to be within the range of  $(1\times10^{-19} \text{ to } 4\times10^{-21}) \text{ m}^2$  for sample S-SG and  $(8\times10^{-19} \text{ to } 5\times10^{-20}) \text{ m}^2$  for sample L-SG, which are not comparable with the results of steady state tests. However, after modifying the compressibility parameters for the tests, the permeability values for the pulse tests were estimated to be  $(3.2 \text{ to } 3.5)\times10^{-18} \text{ m}^2$  for the small Stanstead Granite sample and  $(5.4 \text{ to } 6.0)\times10^{-18} \text{ m}^2$  for the large sample, which are very close to the estimates obtained from steady state tests.

A set of hydraulic pulse tests was also performed on sample S-SG with deliberately injected measured volumes of air to the cavity. First, suction was applied to the cavity in order to remove the trapped air bubbles and then three hydraulic pulse tests were conducted on the sample. Measured volumes of air were then injected to the cavity in two steps and three hydraulic pulse tests were performed after each injection. The experimental cavity pressure curves were then analyzed using the suggested technique that takes into account the effect of air in the cavity. The estimated air fraction values were very close to the injected values and the technique was successful in estimating the permeability for different air fractions.

#### **CHAPTER 6**

## PERMEABILITY HYSTERESIS UNDER ISOTROPIC COMPRESSION

#### 6.1. Introduction

The evolution of permeability in Stanstead Granite under isotropic compressive loading and unloading was experimentally studied. In a practical application, the granite is under overburden stresses. For instance, the in situ isotropic stress state on a granite sample located at a depth of 1000 meters is estimated to be in the range of 24 MPa to 27 MPa, whereas a sample recovered from the same depth is generally regarded as unstressed. Therefore, it can be expected that the hydromechanical behaviour of the rock measured in the laboratory will be different from in situ behaviour. The increase of isotropic stresses in homogeneous rocks tends to close fissures, micro-cracks and the pore space. The expected result is a decrease in permeability, and an increase in Young's modulus and Poisson's ratio. Depending on the applied stress level, the changes in the hydro-mechanical parameters can be partially or completely recovered after unloading. The changes of permeability in granitic rocks under isotropic compression have been studied by a number of researchers, including Brace et al. (1968), Kranz et al. (1979), Heystee and Roegiers (1981), and Kiama et al. (1996).

In this chapter, the alteration of permeability in three Stanstead Granite cylinders, measuring approximately 100 mm in diameter and 100 mm in height, was studied. All of the samples were cored from the same rock slab; two of them were cored perpendicular to the slab surface and one parallel to the surface. The permeability of all three samples was tested under steady state conditions in a GDS Triaxial Cell (manufactured by GDS Instruments Inc.).

#### **6.2.** Sample preparation

Three cylindrical samples of Stanstead Granite were tested: GDS1 measured 9.98 cm in diameter and 10.63 cm in length, GDS2 measured 9.98 cm in diameter and 10.62 cm in length and GDS3 measured 9.90 cm in diameter and 10.05 cm in length. The samples were cored from the same granite slab. Samples GDS1 and GDS2 were cored at an orientation vertical to the slab surface while sample GDS3 was cored at a horizontal orientation. The two ends of the cored samples were cut using a diamond saw. The samples were then machined to obtain smooth surfaces and parallel ends. Figure 6.1 shows the three samples and the slab from which the samples were cored.

In order to examine the porosity of the samples, the dimensions were accurately measured and the samples were then left in an oven at a temperature of  $60 \,^{\circ}C$  for three days and the dry weight of the samples were measured. In order to saturate the samples, they were placed under water in the vacuum chamber (i.e. Figure 6.2) with a negative pressure of 90 kPa and weighed daily; after three days of saturation the weight remained unchanged. The samples, however, were kept in the vacuum chamber for a week, the saturated samples were weighed and the porosity of the samples was estimated. The average porosity value was  $0.67\% \pm 0.02\%$ .

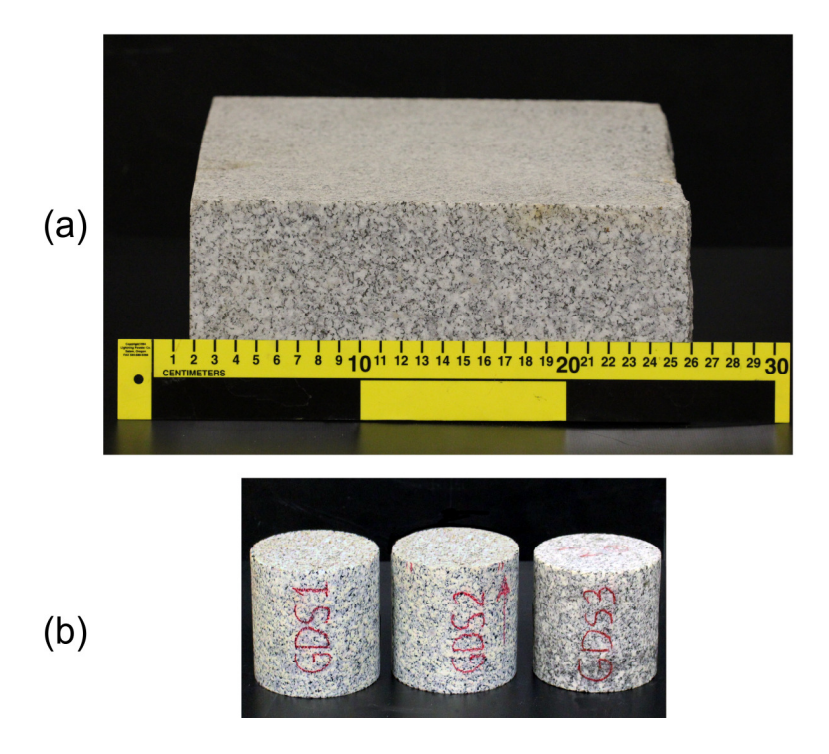


Figure 6.1: (a) The Stanstead Granite slab that the specimens were cored from; (b) the three Stanstead Granite cylinders used in the study of permeability hysteresis under isotropic loading.

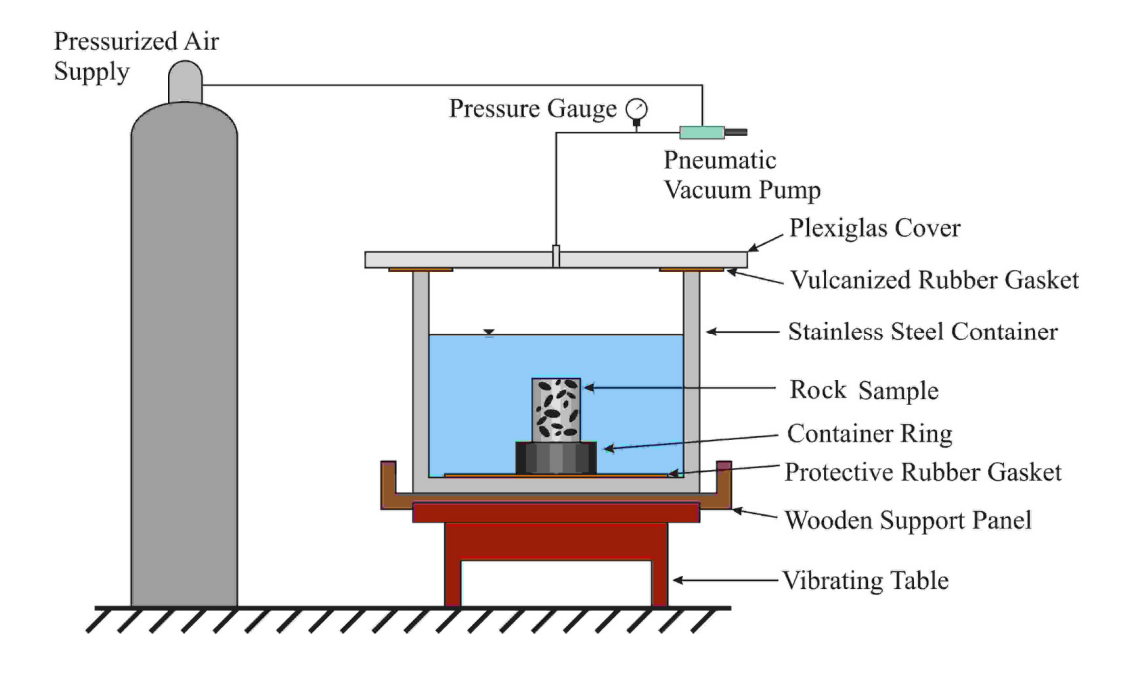


Figure 6.2: Schematic layout of the saturation chamber (after Selvadurai et al., 2011).

#### **6.3.** Testing facility and sample assembly

The GDS triaxial cell used in the study is capable of applying 65 MPa of confining pressure and a deviatoric load of 250 kN. The confining pressure was applied using a GDS controller pump with a maximum capacity of 65 MPa. The pump was capable of maintaining the confining pressure constant during the experiments and changeable to pressures that would vary linearly. Water was used in the cell to apply the confining pressure. The test procedures were similar to those adopted by Selvadurai et al. (2011) for testing Cobourg Limestone. The rock specimen was mounted on a pedestal and placed over a porous steel disc that acts as a diffuser. Subsequently, the sample was fitted with an impermeable nitrile rubber membrane in order to seal the cylindrical surface of the granite. Figure 6.3 shows the sample mounted on the pedestal and enclosed in a rubber gasket. The membrane creates an impervious boundary on the lateral surface of the sample, and thus imposes one-dimensional fluid transport through the rock.

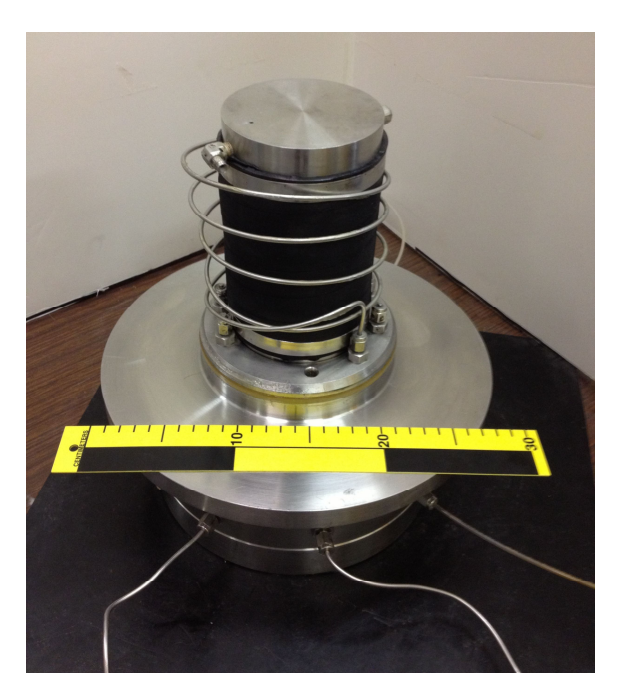


Figure 6.3: Granite sample mounted on the pedestal and covered by a rubber gasket.

An identical diffuser disc was placed at the top of the sample and a stainless steel top cap was placed on top of the diffuser disc. The pressures in the bottom pedestal and the top cap are separately controllable through the stainless steel lines rated for 65 MPa pressure and accessible from the outside the GDS cell. Figure 6.4 shows the GDS cell and the connections. In order to improve the sealing at the pedestal-membrane interface and the top cap-membrane interface hose clamps were used for each end of the sample, a technique that has proved to be effective (Selvadurai and Glowacki, 2008; Selvadurai et al., 2011a). Also, to further reduce leakage from the cell to the top and the bottom of the sample Sika<sup>TM</sup> sealant was applied at the interface of the nitrile gasket and the stainless steel top and bottom caps. The sealant provided a continuous sealing. The efficiency of the sealing technique and the apparent permeability of the system was examined by Selvadurai et al. (2011a) using an aluminum cylinder on the test specimen; from their results the leakage of the system was equivalent to permeability of  $3.0 \times 10^{-23}$  (m<sup>2</sup>).

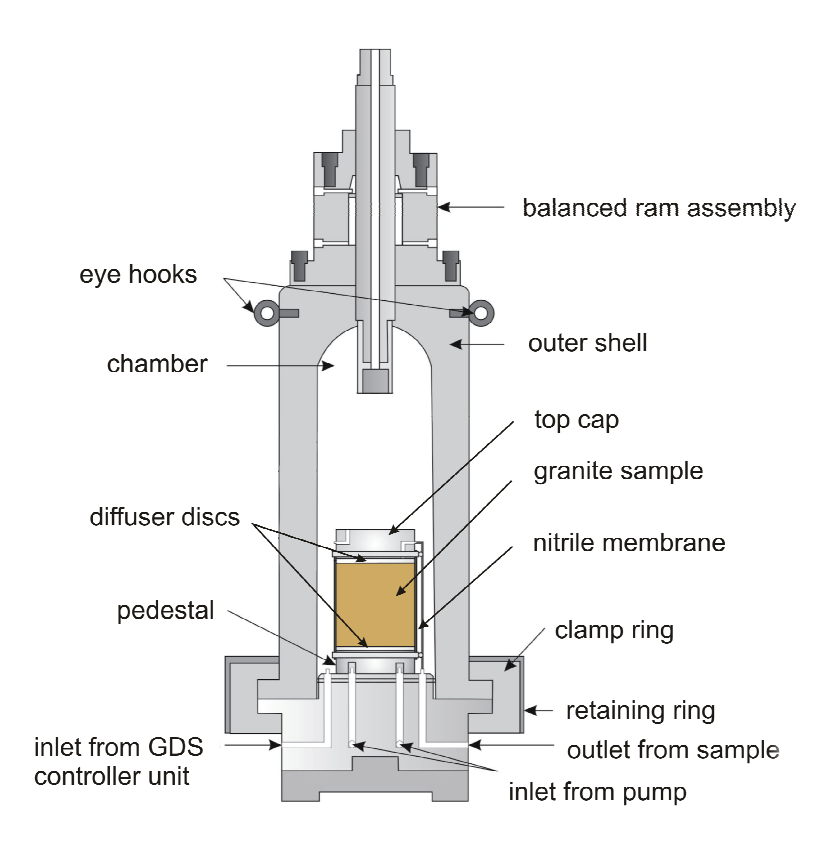


Figure 6.4: Schematic view of the GDS cell used for performing the permeability hysteresis tests on Stanstead Granite (from Glowacki, 2008).

A Quizix<sup>TM</sup> pump provided flow through the samples. Three pressure transducers were used to measure the water pressure; a 68 MPa Omega<sup>TM</sup> pressure transducer to measure the cell pressure and another 68 MPa Omega<sup>TM</sup> pressure transducer to measure the water pressure at the upstream.

#### 6.4. Steady-state permeability measurement

The sample was subjected to a cell pressure with complete drainage allowed to occur. Water was then pumped into the samples at a constant flow rate while subjecting them to different confining pressures during the loading and unloading stages. The water pressure at the upstream boundary that was required to keep the flow rate constant was recorded during the tests. The downstream was kept open to the atmosphere. Once the system reached a steady state, the pressure attained at the upstream boundary was recorded and the steady state permeability of the granite sample was calculated for the different values of confining pressure. Figure 6.5 shows the schematic layout of the testing setup.

Employing Darcy's Law for the one-dimensional steady state flow through a cylindrical porous rock, the relationship for the permeability can be written as

$$\tilde{K} = \frac{\mu QL}{\pi r^2 \Delta p} \tag{6.1}$$

where  $\tilde{K}$  is the permeability parameter, Q is the flow rate at a steady state condition,  $\mu$  is the dynamic viscosity of permeating fluid at test temperature, L is the length of the cylindrical sample, r is the radius of the cross section of the sample, and  $\Delta p$  is the pressure difference between the two ends of the sample under steady state conditions.

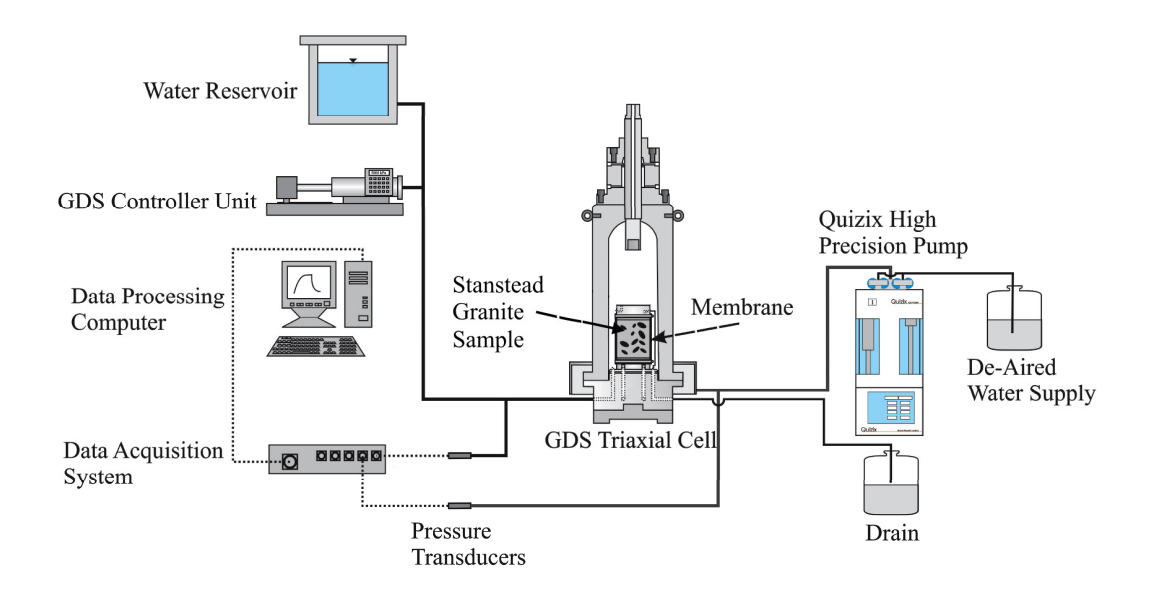


Figure 6.5: The schematic arrangement of the setup used for steady state permeability measurement of cylindrical Stanstead Granite samples subjected to confining pressure (from Selvadurai et al. (2011)).

#### **6.4.1.** Steady state test results

A constant flow rate of 0.0050 ml/min was applied to the first sample, GDS1, under varying confining pressures of 5, 10, 20 and 30 MPa. The time for attainment of a steady state was approximately 10 hours for the lowest permeability. The sample was subsequently unloaded to confining pressures of 20, 10 and 5 MPa. A single test was performed at each confining pressure. Table 6.1 shows the results of the experiments performed on sample GDS1.

For the second specimen, GDS2, a constant flow rate of 0.0010 ml/min was applied to the sample under confining pressures of 5, 10, 20, 30 and 40 MPa. The constant flow rate was then reduced to 0.0005 ml/min for the test at 50 MPa and further reduced to 0.0002 ml/min for the test at 60 MPa, in order to keep the upstream cavity pressure low. The sample was finally unloaded under similar confining stresses and flow rates. It should be noted that for the second specimen (i.e. GDS2), the tests were repeated three times for each confining pressure and the maximum steady state pressure difference was 5.8%. The results are shown in Table 6.2.

Table 6.1: Steady state permeability tests on Stanstead Granite sample GDS1 at various confining pressures.

Cell	Flow	Steady	Steady State
Pressure	Rate	State	Permeability
(MPa)	(ml/min)	Pressure	$(m^2)$
		(kPa)	
5	0.0050	681	15×10 <sup>-19</sup>
10	0.0050	1650	6.3×10 <sup>-19</sup>
20	0.0050	4130	2.5×10 <sup>-19</sup>
30	0.0050	8238	1.3×10 <sup>-19</sup>
20	0.0050	4936	2.1×10 <sup>-19</sup>
10	0.0050	2184	4.7×10 <sup>-19</sup>
5	0.0050	1039	9.9×10 <sup>-19</sup>

Sample GDS3 was tested at confining pressures of 5, 10, 20, 40, 60, 40, 20, 10, 5 kPa. A flow rate of 0.0002 ml/min was applied to the sample at all cell pressures, except for the 60 MPa cell pressure and 40 MPa cell pressure in the unloading stage, which were tested at a flow rate of 0.0001 ml/min. Since the measured permeability for sample GDS3 at the 60 MPa cell pressure was much lower than the corresponding value for sample GDS2, a constant pressure steady state test was also performed at this cell pressure on sample GDS3, in order to verify the estimated permeability. The base of the sample was subjected to the constant pressure of 1MPa and the pore pressure at the top end of the sample was kept open to atmospheric pressure. The decrease in the flow rate supplied by the pump that was necessary to keep the pressure boundary condition constant was monitored. The sample reached a steady state condition after 8 days, at a flow rate of 1.6×10<sup>-5</sup> ml/min. The so-called pressure and flow boundary conditions correspond to a permeability of 3.3×10<sup>-21</sup> m<sup>2</sup>, which confirmed the estimated permeability value at a constant flow rate. Table 6.3 shows the results of the steady state tests performed on sample GDS3.

Table 6.2: Steady state permeability of Stanstead Granite sample GDS2 at different confining pressures.

Cell Pressure	Flow Rate	Steady State Pressure (kPa)			Steady State Permeability (m <sup>2</sup> )				
(MPa)	(ml/min)	Test 1	Test 2	Test 3	Test 1	Test 2	Test 3	Average	
5	0.001	172	168	172	1.2×10 <sup>-18</sup>	1.2×10 <sup>-18</sup>	1.2×10 <sup>-18</sup>	1.2×10 <sup>-18</sup>	
10	0.001	330	350	339	6.3×10 <sup>-19</sup>	5.9×10 <sup>-19</sup>	6.1×10 <sup>-19</sup>	6.1×10 <sup>-19</sup>	
20	0.001	941	944	967	2.2×10 <sup>-19</sup>	2.2×10 <sup>-19</sup>	2.1×10 <sup>-19</sup>	2.2×10 <sup>-19</sup>	
30	0.001	2604	2666	2649	7.9×10 <sup>-20</sup>	7.7×10 <sup>-20</sup>	7.8×10 <sup>-20</sup>	7.8×10 <sup>-20</sup>	
40	0.001	4637	4741	4871	4.5×10 <sup>-20</sup>	4.4×10 <sup>-20</sup>	4.2×10 <sup>-20</sup>	4.3×10 <sup>-20</sup>	
50	0.0005	4272	4295	4518	2.4×10 <sup>-20</sup>	2.4×10 <sup>-20</sup>	2.3×10 <sup>-20</sup>	2.4×10 <sup>-20</sup>	
60	0.0002	3138	3235	3167	1.3×10 <sup>-20</sup>	1.3×10 <sup>-20</sup>	1.3×10 <sup>-20</sup>	1.3×10 <sup>-20</sup>	
50	0.0005	5845	5817	6058	1.8×10 <sup>-20</sup>	1.8×10 <sup>-20</sup>	1.7×10 <sup>-20</sup>	1.8×10 <sup>-20</sup>	
40	0.001	7854	7786	7761	2.6×10 <sup>-20</sup>	2.7×10 <sup>-20</sup>	2.7×10 <sup>-20</sup>	2.6×10 <sup>-20</sup>	
30	0.001	5338	5391	5357	3.9×10 <sup>-20</sup>	3.8×10 <sup>-20</sup>	3.9×10 <sup>-20</sup>	3.9×10 <sup>-20</sup>	
20	0.001	2782	2752	2759	7.4×10 <sup>-20</sup>	7.5×10 <sup>-20</sup>	7.5×10 <sup>-20</sup>	7.5×10 <sup>-20</sup>	
10	0.001	943	985	928	2.2×10 <sup>-19</sup>	2.1×10 <sup>-19</sup>	2.2×10 <sup>-19</sup>	2.2×10 <sup>-19</sup>	
5	0.001	410	399	417	5.1×10 <sup>-19</sup>	5.2×10 <sup>-19</sup>	5.0×10 <sup>-19</sup>	5.1×10 <sup>-19</sup>	

Table 6.3: Steady state permeability of Stanstead Granite sample GDS3 at different confining pressures.

Cell Pressure (MPa)	Flow Rate (ml/min)	Steady State Pressure (kPa)	Steady State Permeability (m <sup>2</sup> )
5	0.0002	43	9.6×10 <sup>-19</sup>
10	0.0002	79	5.3×10 <sup>-19</sup>
20	0.0002	348	1.2×10 <sup>-19</sup>
40	0.0002	1004	4.1×10 <sup>-20</sup>
60	0.0001	5750	3.6×10 <sup>-21</sup>
40	0.0001	3044	6.8×10 <sup>-21</sup>
20	0.0002	1887	2.2×10 <sup>-20</sup>
10	0.0002	550	7.5×10 <sup>-20</sup>
5	0.0002	205	2.0×10 <sup>-19</sup>

#### **6.4.2.** Discussion on the steady state test results

Figure 6.6 shows the change in permeability for the three samples tested with respect to the change in the confining pressure. The permeability of sample GDS1 reduced from  $1.5\times10^{-18}$  m<sup>2</sup> to  $1.3\times10^{-19}$  m<sup>2</sup> while the confining pressure increased from 5 MPa to 30 MPa. The permeability was then increased to  $9.9\times10^{-19}$  m<sup>2</sup> as the confining pressure was reduced to 5 MPa. For sample GDS2 which was loaded up to 60 MPa cell pressure, the permeability decreased from  $1.2\times10^{-18}$  m<sup>2</sup> to  $1.3\times10^{-20}$  m<sup>2</sup>. The permeability at the end of the unloading stage (e.g. 5 MPa cell pressure) was  $5.1\times10^{-19}$  m<sup>2</sup>. Finally, the measured permeability for sample GDS3 reduced from  $9.6\times10^{-19}$  m<sup>2</sup> to  $3.6\times10^{-21}$  m<sup>2</sup> for, respectively, 5 and 60 MPa in the loading stage and increased to  $2.0\times10^{-19}$  m<sup>2</sup> at 5 MPa in the unloading stage.

It can be seen that part of the permeability decrease in the loading stage is due to the elastic contraction of the pores, fissures and micro-cracks and part of it is due to permanent closure of micro-cracks and the collapse of pores.

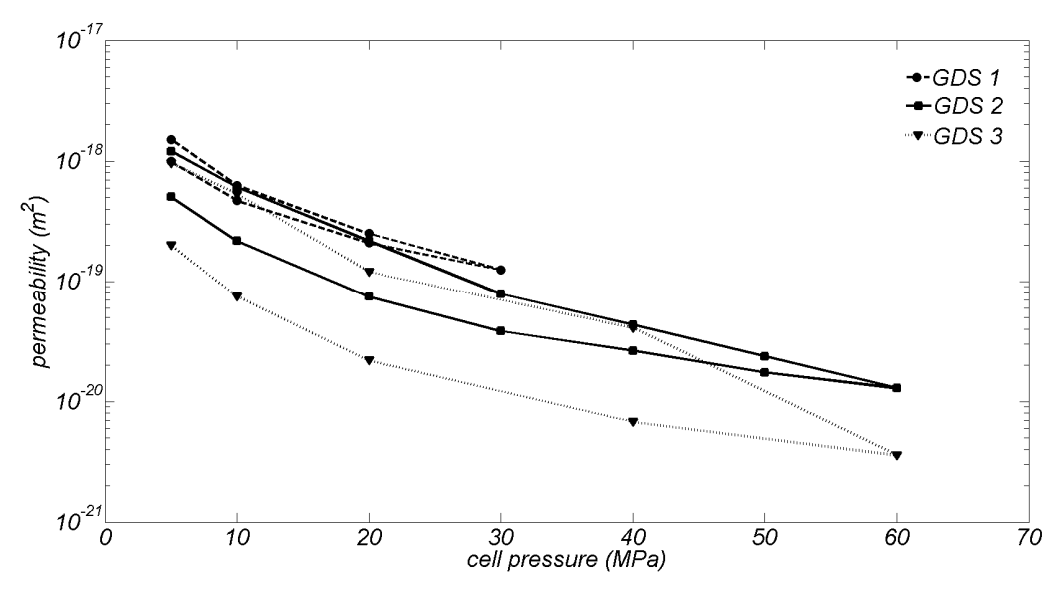


Figure 6.6: The change of permeability with an isotropic compression change for Stanstead Granite samples GDS 1, GDS 2 and GDS 3.

As expected, the maximum of 30 MPa isotropic compression in sample GDS1 had less permanent permeability decrease than the maximum 60 MPa isotropic compression on samples GDS2 and GDS3. Also, a comparison of the

permeability results from samples GDS2 and GDS3 shows anisotropy both in the permeability and in the evolution of damage under isotropic loading-unloading cycles. Therefore, not only the permeability evolves but also the degree of anisotropy changes. Table 6.4 shows the change in the permeability anisotropy for samples GDS2 and GDS3.

Table 6.4: Change in the degree of anisotropy  $(K_{GDS2}/K_{GDS3})$  with the change of isotropic compression.

	Loading					Unloading			
Cell Pressure (MPa)	5	10	20	40	60	40	20	10	5
Degree of anisotropy	1.25	1.15	1.83	1.04	3.61	3.82	3.41	2.93	2.55

Regarding any leakage from the system, since the minimum estimated permeability value was  $3.6 \times 10^{-21}$  m<sup>2</sup>, which is two orders of magnitude higher than the apparent permeability of the system, no correction was needed.

#### 6.5. Summary

In this chapter, the evolution of permeability in Stanstead Granite was studied under the effects of isotropic loading and unloading. Three cylindrical samples were tested in a triaxial cell, using the steady state technique. Two samples were cored with their cylindrical axis perpendicular to the granite slab (i.e. samples GDS1 and GDS2) and one sample was cored with the axis parallel to the surface of the slab (i.e. GDS3). The loading-unloading cycle ranged from confining stresses of 5 MPa to 30 MPa for sample GDS1 and 5 MPa to 60 MPa for samples GDS2 and GDS3. The isotropic loading decreased the permeability value by almost one order of magnitude for sample GDS1 and two to three orders of magnitude for samples GDS2 and GDS3. The permeability decrease is most likely to be attributed to the closure of the accessible pore space. The permeability was partially recovered when the sample was completely unloaded. The irrecoverable decrease in the permeability after one loading-unloading cycle, although negligible, can result from permanent pore closure during isotropic loading. Also,

a comparison of the permeability evolution in samples GDS2 and GDS3 showed isotropic hydraulic properties until the increase of cell pressure from 40MPa to 60 MPa; at these cell pressures the permeability parallel to the surface of the slab became almost 3 times less than the permeability perpendicular to the surface of the slab.

#### CHAPTER 7

#### THERMO-HYDRO-MECHANICS OF POROUS GEOMATERIALS

#### 7.1. Introduction

The thermo-hydro-mechanical behaviour of porous media is an extension to Biot's theory of poroelasticity (Biot, 1941a) that has been studied extensively both theoretically and experimentally (Mandel, 1953; Cryer, 1963; Gibson et al., 1963, Mason et al., 1991; Wang, 2000; Selvadurai, 2007). In a variety of problems such as deep geological disposal of nuclear wastes (Selvadurai and Nguyen, 1995; Selvadurai and Nguyen, 1997; Tsang et al. 2000; Zimmerman, 2000; Rutqvist et al., 2001; Stephansson et al., 2004; Alonso et al., 2005; Chijimatsu et al., 2005; Nguyen et al., 2005; Rutqvist et al., 2005; Selvadurai and Suvorov, 2012; Tsang et al., 2012), oil and natural gas recovery (Vaziri, 1988; Bai and Roegiers, 1994; Gutierrez and Makurat, 1997; Pao et al., 2001) and geothermal energy extraction (Brownell et al., 1977; Bodvarsson and Stefansson, 1989; Nakao and Ishido, 1998; Ilyasov et al., 2010), the role of temperature becomes important. Biot's isothermal theory of poroelasticity was extended by a number of researchers in order to include non-isothermal effects; examples of these developments are given by Noorishad et al. (1984), Booker and Savvidou (1984, 1985), Aboustit et al. (1985), McTigue (1986), Coussy (1989), Selvadurai and Nguyen (1995), Zhou et al. (1998), Gens et al. (1998), Pao et al. (2001),

Suvorov and Selvadurai (2010) and Selvadurai and Suvorov (2012). In this chapter the coupling effects of temperature, pore pressure and skeletal deformations are investigated. Experimental research involves the heating of Stanstead Granite cylinders each containing a fluid inclusion is performed to establish the applicability of currently available THM formulation.

#### 7.2. Governing Equations

In this section, the partial differential equations for the thermo-hydro-mechanical behavior of porous geomaterials are summarized for completeness.

#### 7.2.1. The constitutive equation for the porous solid

Temperature change induces volumetric deformation and, subsequently, isotropic stress in the porous skeleton. This effect can be implemented in Hooke's stress-strain relationship by adding the volumetric thermal expansion

$$\mathbf{\sigma} = 2G\mathbf{\varepsilon} + \lambda \varepsilon_{v} \mathbf{I} - \alpha p \mathbf{I} - \beta_{s} KT \mathbf{I}$$
 (7.1)

where G is the linear elastic shear modulus,  $\lambda$  is the Lamé coefficient,  $\varepsilon$  is the strain tensor,  $\varepsilon_v$  (= tr $\varepsilon$ ) is the volumetric strain,  $\beta_s$  is the volumetric thermal expansion coefficient of the solid material, K is the drained bulk modulus, T is the temperature measured from a reference state and I is the unit tensor. Substituting Eq. (7.1) into the equilibrium equation (i.e. Eq. (3.44)) and considering static equilibrium in the absence of body forces gives the solid phase equation for non-isothermal poroelastic materials:

$$G\nabla^{2}\mathbf{u} + \frac{G}{1 - 2\nu}\nabla(\nabla \cdot \mathbf{u}) - \alpha\nabla p - K\beta_{s}\nabla T = \mathbf{0}$$
(7.2)

#### 7.2.2. Liquid phase equation

Temperature change can affect the fluid flow in two ways: It changes the dynamic viscosity, the volumetric thermal expansion coefficient and the density of the fluid (Holzbecher, 1998); it also induces fluid flow due to the difference between thermal expansion of fluid and the solid skeleton. The volumetric strain  $\varepsilon_{\nu}$  can be

written as a function of the mean total stress (=  $\frac{1}{3}$  tr $\sigma$ ), pore pressure and temperature; i.e.

$$\varepsilon_{v} = \frac{\sigma_{v}}{K} + \frac{p}{H} + \beta_{s}T \tag{7.3}$$

where  $\sigma_{v}$  is the mean total stress and H is the poroelastic expansion coefficient. The increment of fluid content (i.e. (3.25)) can also be modified to include the effect of temperature change

$$\xi = \frac{\sigma_{\nu}}{H} + \frac{p}{R} + \xi_{T} \tag{7.4}$$

where  $\xi_T$  is the increment of fluid content induced by the temperature change. Using the definition in Eq. (3.20) and the fact that the change in pore volume under the temperature variation is the difference between the bulk volume change and the volume change of solid grains (Selvadurai and Nguyen, 1995),  $\xi_T$  can be written as

$$\xi_T = \frac{\left(\delta V^T - \delta V_s^T\right) - \delta V_f^T}{V} = \frac{\left\{V \beta_s T - (1 - n)V \beta_s T\right\} - nV \beta_f T}{V} \tag{7.5}$$

where n is the porosity,  $\beta_f$  is the volumetric thermal expansion coefficient of the permeating fluid and  $\delta V^T$ ,  $\delta V_s^T$ ,  $\delta V_f^T$  are the temperature induced volume change for, respectively, the bulk volume of the porous medium, the solid grains, and the fluid. Substituting Eq. (7.5) into Eq. (7.4) gives

$$\xi = \frac{\sigma_v}{H} + \frac{p}{R} + n(\beta_s - \beta_f)T \tag{7.6}$$

Substituting Eq. (7.6) into the mass conservation equation (i.e. Eq. (3.35)) gives the non-isothermal fluid phase equation

$$S_{\varepsilon} \frac{\partial p}{\partial t} + \nabla \cdot \left[ -\frac{\tilde{K}}{\mu(T)} \nabla p \right] + \alpha \frac{\partial (\nabla \cdot \mathbf{u})}{\partial t} - \left[ n\beta_{f}(T) + (\alpha - n)\beta_{s} \right] \frac{\partial T}{\partial t} = 0$$
 (7.7)

#### 7.2.3. Energy equation

Heat transfer in porous media can take place through conduction, convection and radiation. The radiation part of the heat transfer process is neglected. Convective heat transfer is due to the bulk movement of the permeating fluid. Since the current research is focused on the study of low permeability geomaterials where the fluid flows at very low velocities, the effect of convection in heat transfer can be neglected, compared to conduction. Employing Fourier's Law for conductive heat transfer gives

$$\mathbf{q}_{\mathrm{T}} = -k_{c}^{*} \nabla T \tag{7.8}$$

where  $\mathbf{q}_{\mathrm{T}}$  is the heat flux, and  $k_{c}^{*}$  is the overall thermal conductivity of the porous material. The overall thermal conductivity of the porous material can be found as the volume average of the phase thermal conductivities

$$k_{c}^{*} = nk_{cf} + (1 - n)k_{cs} \tag{7.9}$$

where  $k_{cf}$  and  $k_{cs}$  are the thermal conductivities of the liquid phase and solid phase, respectively.

If the mechanical and fluid flow contributions to the energy balance are neglected, the net rate of heat flux into any arbitrary element of material will be balanced by the increase in internal heat energy (Savvidou and Booker, 1988)

$$\nabla \mathbf{q}_{\mathrm{T}} + c^{*}_{p}(T) \frac{\partial T}{\partial t} = 0 \tag{7.10}$$

where  $c_p^*(T)$  is the specific heat capacity of the porous medium. The overall heat capacity is defined as the volume average of the phase heat capacities

$$c_{p}^{*}(T) = n\rho_{f}(T)c_{f} + (1-n)\rho_{s}c_{s}$$
(7.11)

where  $c_f$  and  $c_s$  are the specific heat capacity of the liquid phase and the solid phase, respectively. Substituting Eq. (7.8) into Eq. (7.10) provides the conductive heat transfer equation

$$c^*_{p}(T)\frac{\partial T}{\partial t} - k^*_{c}\nabla^2 T = 0$$
 (7.12)

#### 7.2.4. Computational modelling of a fluid inclusion

Since the measurement of fluid pressure and temperature in the sealed cavity is experimentally feasible, the concept of a fluid inclusion was implemented in the current research. The fluid inclusion was modelled as a porous medium with the porosity equal to unity and a relatively high permeability in order to create uniform pressure within the cavity (i.e. we set  $\tilde{K}/\tilde{K}_f=10^{-6}$ ). Also, to capture the effect of cavity volume change on the cavity pressure change, the elastic constants were assumed to be  $v_f=0.49$  and  $E=3(1-2v_f)/C_{eq}$ , where  $C_{eq}$  is the compressibility of the cavity fluid that contains trapped air. The equations used to model the fluid cavity are as follows:

$$(K + \frac{G_D}{3})\nabla(\nabla \cdot \mathbf{u}) + G\nabla^2 \mathbf{u} = 0$$
(7.13)

$$C_{eq}(p)\frac{\partial p}{\partial t} + \nabla \cdot \left[ -\frac{\tilde{K}}{\mu(T)} \nabla p \right] + \frac{\partial (\nabla \cdot \mathbf{u})}{\partial t} - \beta_f(T) \frac{\partial T}{\partial t} = 0$$
 (7.14)

$$\rho_f(T)c_f \frac{\partial T}{\partial t} - k_{cf} \nabla^2 T = 0 \tag{7.15}$$

In the above formulation, the compressibility of the fluid in the sealed cavity is higher than the compressibility of de-aired water due to unwanted entrapment of air bubbles in the fluid-filled cavity. Referred to Chapter 5, a simplified relationship for the compressibility of an air-water mixture can be written as

$$C_{qq} = \varphi C_{q} + (1 - \varphi) C_{w} \tag{7.16}$$

where  $\varphi$  is the air fraction in the fluid-air mixture (volume of air/volume of fluid-filled cavity), and  $C_w$  is the compressibility of the pure fluid, i.e.  $4.54\times10^{-10}$  Pa<sup>-1</sup> (White, 1986). Expressions analogous to Eq. (7.16) that take into account air solubility were also investigated in Chapter 5. For non-isothermal phenomena the behaviour of the air bubbles follows the ideal gas law

$$\frac{PV_a}{T} = nR. (7.17)$$

where  $V_a$  is the volume of the air, P is absolute pressure of the air bubble, n is the number of moles and R is the universal gas constant. Considering variations in Eq. (7.17) we have

$$PdV_a + V_a dP = nRdT \qquad \Rightarrow \qquad C_a = \frac{-\frac{dV_a}{V_a}}{dP} = \frac{1}{P} - \frac{1}{T} \frac{dT}{dp}$$
 (7.18)

The ideal gas law also determines the changes of air fraction with pressure and temperature. Assuming that the total volume of cavity (i.e.  $V_w + V_a$ ) is constant during the THM experiment, the air fraction equation can be re-written as

$$\frac{P_a^0 V_a^0}{T^0} = \frac{P_a V_a}{T} \quad ; \qquad \varphi = \frac{V_a}{V_w + V_a} \quad \Rightarrow \quad \varphi = \frac{\frac{P_a^0}{P_a}}{V_w + V_a} \frac{T}{V_a} = \frac{P_a^0}{P_a} \frac{T}{T^0} \varphi^0 \tag{12}$$

where  $P_a^0$  is the initial absolute air pressure,  $V_a^0$  is the initial volume of air,  $T^0$  is the reference temperature and  $\varphi^0$  is the initial air fraction in the cavity.

The other important factor in the compressibility of the air-water mixture is the dissolution of air into water. As stated in Henry's Law, the weight of air that goes into solution depends on the absolute pressure of the air. Based on Henry's Law, the volume of air present in water at 25 °C can be approximately 1.78% of the

volume of water (Fredlund, 1976). Also, the rate of dissolution depends on the diffusivity rate of the air into water, which is governed by Fick's Law. The diffusivity rate for air in water is  $2.0 \times 10^{-9}$  m<sup>2</sup>/s at 25 °C. Depending upon the rate of compression of an air-water mixture, the amount of air going into solution changes from 0 to  $h(1-\varphi)$  of the volume of water, where h is Henry's constant. Eq. (7.16) is a highly simplified relationship for estimating the compressibility of the air-water mixture and does not take into account the effect of water vapor pressure, surface tension and the time dependency for dissolution of air in the water.

In addition to Eq. (7.16), which was obtained based on physical phenomena, an empirical relationship that relates the compressibility of the air-fluid mixture to pore pressure was suggested

$$C_{eq}(p) = A\cot^{-1}(Bp) \tag{7.19}$$

where A and B are empirical parameters that can be obtained from isothermal hydraulic pulse tests. In this chapter both the air-water compressibility relationships Eq. (7.16) and Eq. (7.19) are implemented in the modelling of the THM experiments.

#### 7.3. Thermal damage experiment

Any sudden temperature change can induce damage in porous geomaterials. Two main reasons can be attributed to this damage: (i) the difference in the thermal expansion coefficient of the minerals in the compound, (ii) a sudden pore pressure increase in low permeability saturated geomaterials. The temperature range used in the experiments performed in current research was between 20 °C to 70 °C, where minimal thermal damage is expected. However, an experiment was performed to further investigate the issue. In this regard, the permeability of a Stanstead Granite cylinder was measured, using the steady state technique, both before and after a thermal shock.

## 7.3.1. Testing procedure

A cylindrical sample of Stanstead Granite measuring 15.24 cm in diameter and 30.48 cm in length was saturated in a vacuum chamber. The patch permeameter described in section 4.3.2 was used to perform steady state tests on the upper and lower plane surfaces of the sample. The details of the testing facility were explained in Section 4.3.2. A schematic cross section of the sample and the permeameter as well as a picture of the components of the assembly is presented in Figure 7.1. The sample was vacuum saturated for 7 days and then moved to the testing chamber for measuring its permeability prior to thermal shock.

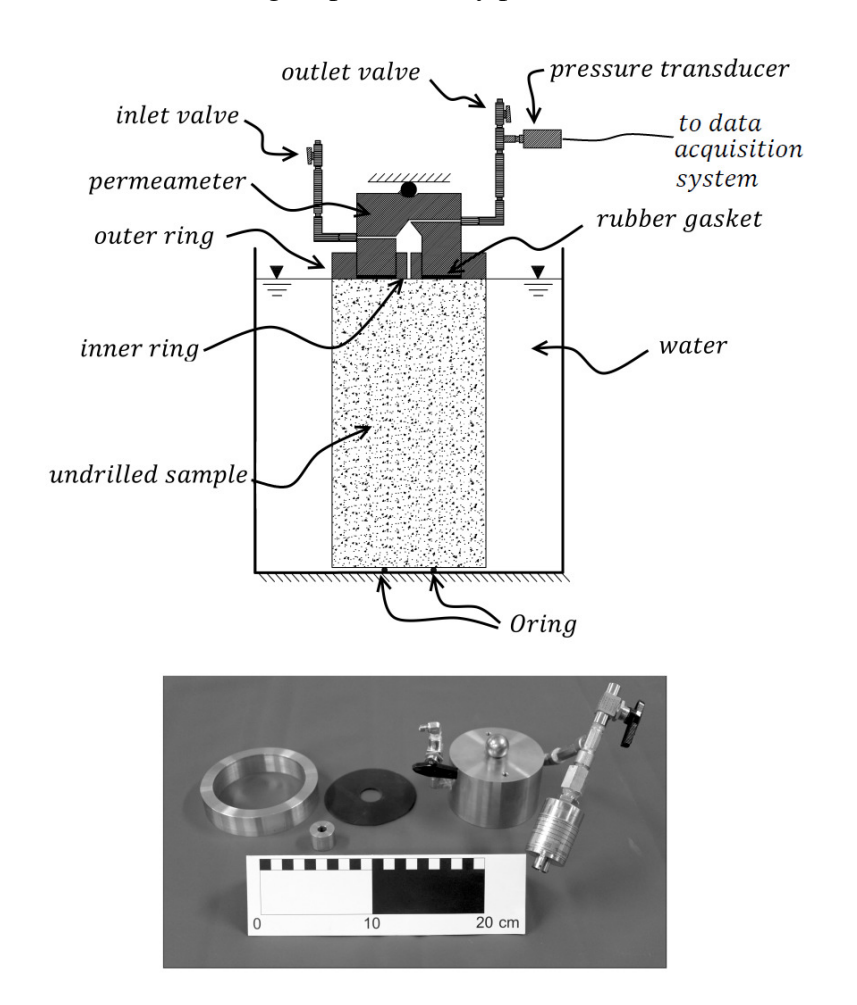


Figure 7.1: Cross section of the permeameter connected to the sample surface and the components of the assembly.

A sealing pressure of 1.5 MPa was applied to the gasket. A Quizix pump was connected to the inlet of the permeameter and it delivered a constant flow rate of

0.005ml/min to the exposed area of the top boundary of the sample. A 1400 kPa Honeywell pressure transducer was fixed to the permeameter in order to measure the water pressure in the cavity at the upstream. Once the system reached a steady state, the permeability was calculated and the test was repeated with the sample inverted to allow the fluid to enter through the opposite surface of the sample. The saturated sample was then placed in an oven at 100 °C for 24 hours in order to induce thermal damage to the specimen. The oven was then turned off and the sample was placed in a vacuum chamber containing water at a temperature of 20 °C. The sample was re-saturated in the chamber and was re-tested for permeability at the top and bottom surfaces of the sample. The results of the permeability tests are shown in Table 7.1. It was seen that a thermal shock of 80 °C (i.e. the difference between room temperature and the oven temperature) resulted in a 25% to 40% permeability increase. Figure 7.2 shows the attainment of steady state pressures at the exposed region of the boundary for the prescribed flow rate of 0.005 ml/min.

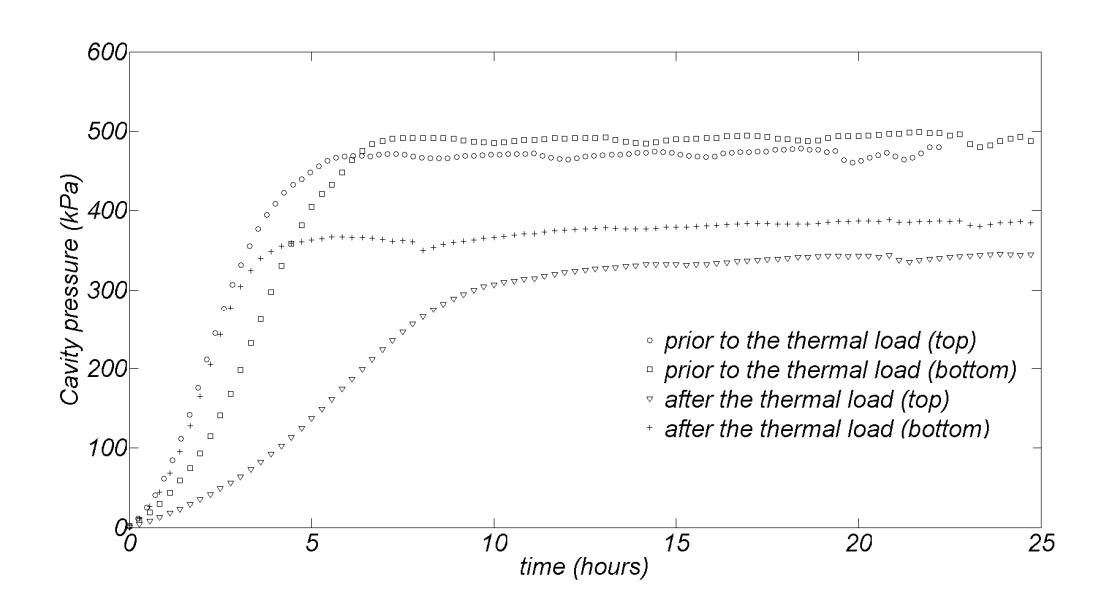


Figure 7.2: Attainment of steady state flow in the granite sample before and after thermal loading.

Table 7.1: Range of values of permeability before and after thermal loading.

Flow rate (ml/min)	Steady-state pressure (kPa)	Permeability (m <sup>2</sup> )	Face	Description
0.005	481.7	2.98×10 <sup>-18</sup>	Top	Prior to thermal shock
0.005	491.2	2.93×10 <sup>-18</sup>	Bottom	Prior to thermal shock
0.005	345.7	4.15×10 <sup>-18</sup>	Тор	After the thermal shock
0.005	364.9	3.64×10 <sup>-18</sup>	Bottom	After the thermal shock

## 7.4. Immersion thermal experiment

The first THM experiment focused on the boundary heating of a cylindrical sample of Stanstead Granite. The sample was 4.91 cm in diameter and 9.99 cm in height and it contained an axial cavity 1.38 cm in diameter and 6.29 cm in height (Figure 7.3). The open end of the cylindrical cavity was fitted with a stainless cylinder of average inner diameter 1.38 cm, height 15.7 cm and an average wall thickness of 0.2 cm. The height is calculated from the measured cavity volume and the measured average inner diameter. The total volume of the fluid in the cavity was 32.85 ml, as measured in the lab. The cylinder was attached to the granite using an epoxy seal. This sealing procedure was used quite successfully in other research activities involving isothermal tests (Selvadurai and Jenner, 2013). The stainless steel attachment (Figure 7.3) contains couplings to house a pressure transducer, two thermocouples and an outlet that can be used for water influx and de-airing.

In order to measure the temperature within the cavity, two thermocouples were installed in the top and bottom of the cavity. A 1400 kPa Honeywell pressure transducer was used to measure the pressure change within the cavity. The thermocouples and the pressure transducer were connected to a data acquisition system to monitor and record the temperatures and cavity pressure.

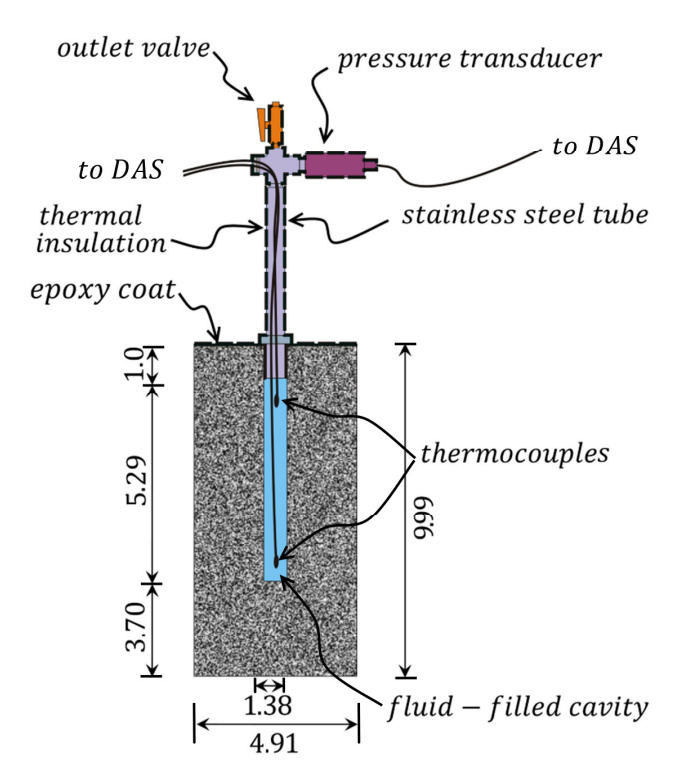


Figure 7.3: Geometry of the Stanstead Granite sample (dimensions are in cm). The thermally insulated parts are shown as dashed lines.

## 7.4.1. Permeability measurement

Two sets of isothermal tests were performed on the granite sample, in order to estimate the permeability and to calibrate the parameters used to estimate the compressibility of the cavity fluid (i.e. Eq. (7.19)). Each test began with pumping water at a constant rate into the cavity, giving sufficient time for the pressure to reach a steady state condition. The pressure attained at steady state condition was used to estimate the permeability value. The outlet valve of the cavity was then closed, allowing the excess pore pressure to decay. This testing procedure was primarily designed to calibrate Eq. (7.19) and is different from the conventional hydraulic pulse testing procedure since the sample tested usually has no residual pore pressure prior to cavity pressurization. Each set of experiments was repeated three times in order to ensure the repeatability of the results. The flow rates used were 0.01 ml/min and 0.02 ml/min. Figures 7.4 and 7.5 show the two sets of hydraulic pulse tests. COMSOL Multiphysics<sup>TM</sup> software was used to model the complete experimental procedure and calibrate Eq. (7.19). Details of modelling

the steady state and transient tests using COMSOL<sup>TM</sup> were explained in detail in the previous chapters. An analysis of the permeability experiments showed that the sample has a permeability of  $\tilde{K} = 3.0 \times 10^{-18}$  m<sup>2</sup>. Based on the calibration studies for Eq. (7.19),  $A = 2.2 \times 10^{-8}$  Pa<sup>-1</sup> and  $B = 2.0 \times 10^{-5}$  Pa<sup>-1</sup> provide the best numerical estimation of the experimental results. The current compressibility of the water-air mixture corresponds to the existence of approximately 0.1% air in the fluid cavity (i.e. 0.33 cm<sup>3</sup>).

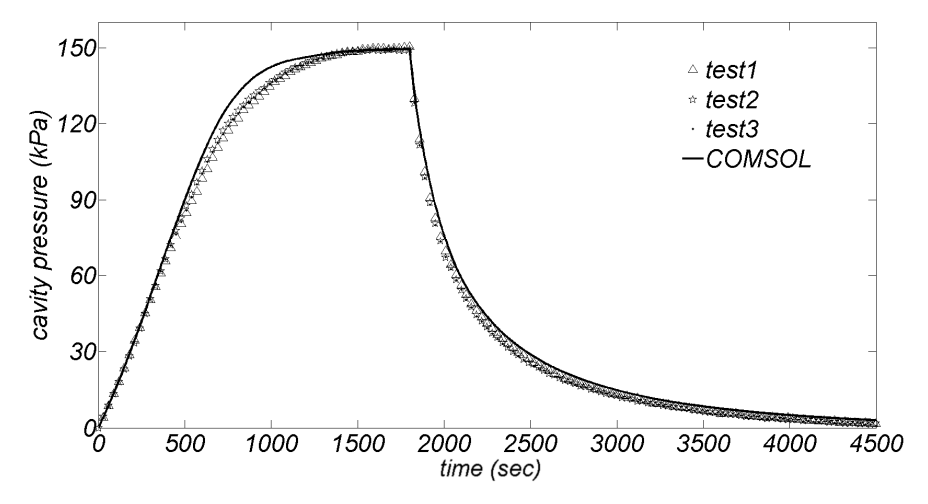


Figure 7.4: Steady state tests with a flow rate of 0.01 ml/min (for 1800 seconds), followed by hydraulic pulse tests.

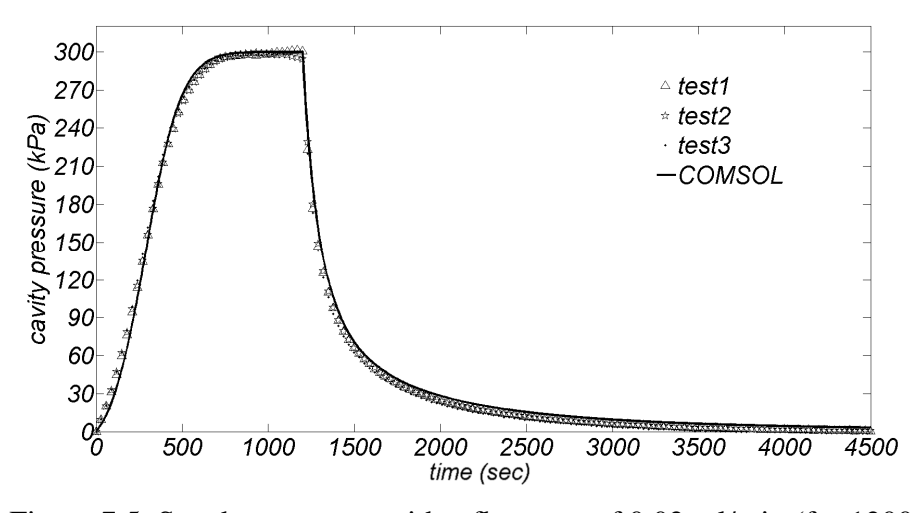


Figure 7.5: Steady state tests with a flow rate of 0.02 ml/min (for 1200 seconds), followed by hydraulic pulse tests.

## 7.4.2. Thermo-hydro-mechanical experiment

In order to study the transport of heat and fluid induced by temperature change, the experimental setup shown in Figure 7.6 was prepared. The sample was immersed in a water bath at a constant temperature of 50 °C, while the outlet valve of the fluid cavity was closed. The water temperature was kept constant using a temperature controller connected to an electrical heater and a thermocouple to measure the temperature of the water in the bath. The sample was kept in the hot water bath for 3600 seconds and then rapidly removed from the hot water bath and immersed into a cold water bath with a constant temperature of  $20^{\circ}C$  and kept there for 7200 seconds.

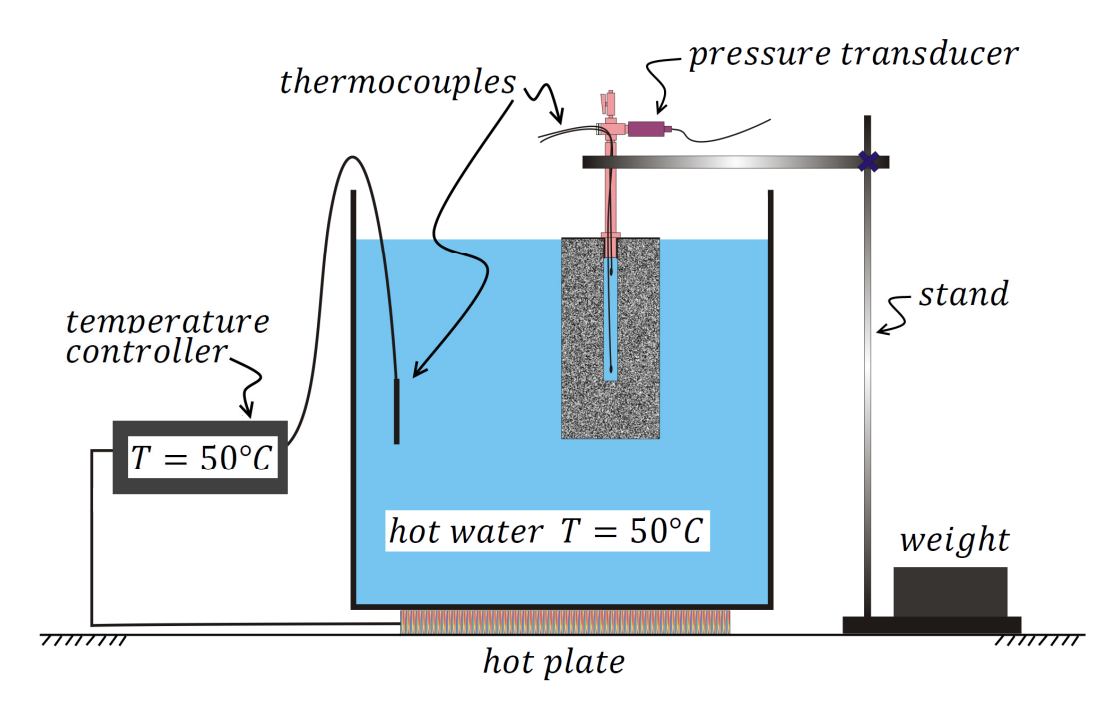


Figure 7.6: Schematic view of the thermo-hydro-mechanical experimental setup.

The experimental cycle, including both heating and cooling steps, was repeated six times in order to study the hysteretic behaviour of the material. It should be noted that each new testing cycle was started after sufficient time was allowed for the dissipation of residual pore pressure and temperature from the previous cycle. As mentioned in Section 7.4, the cavity fluid pressure and cavity fluid temperature were recorded using a pressure transducer and two thermocouples.

Also, the temperature in the cold and hot water baths was recorded using two thermocouples located at the top and bottom of each bath. It should be noted that the stainless steel fittings and tubes and the pressure transducer were thermally insulated using a foil-backed self adhesive foam to minimize heat loss to the ambient environment which was maintained at approximately 23 °C.

#### 7.4.3. Experimental results and numerical simulations

The changes in the cavity fluid pressure and cavity fluid temperature measured during the THM experiments are shown in Figures 7.7 and 7.8. The cavity temperature is the average value of the temperatures measured at the top and bottom of the cavity.

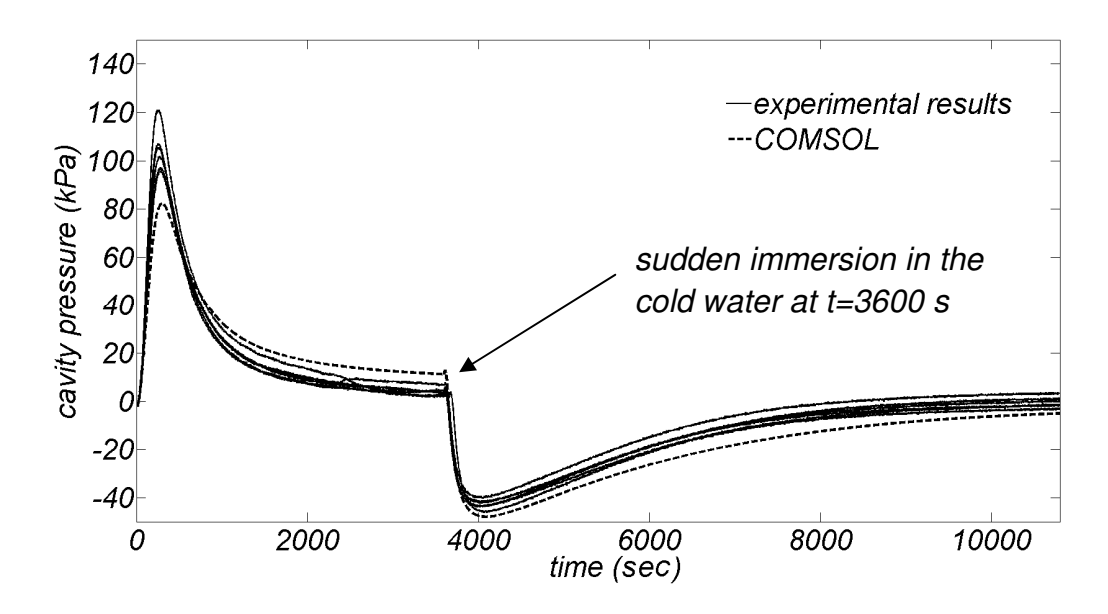


Figure 7.7: Change of cavity pressure with time due to the immersion of the Stanstead Granite sample in hot and cold water containers.

When the sample was immersed in the hot water reservoir, the cavity pressure initially rose, partly due to the thermal expansion of the fluid in the cavity that was induced by the temperature increase and partly due to the fluid flow towards the cavity that was induced by the thermal gradient. The cavity pressure then started to decay as a result of outflow from the cavity to the porous medium; once the sample was immersed in the cold water, the cavity pressure dropped to a

negative pressure as low as -48.0 kPa and then started to dissipate. The main reason for the negative pressure is that water has a higher thermal expansion coefficient than granite and thus the volume of water tends to decrease more than granite with a certain temperature decrease.

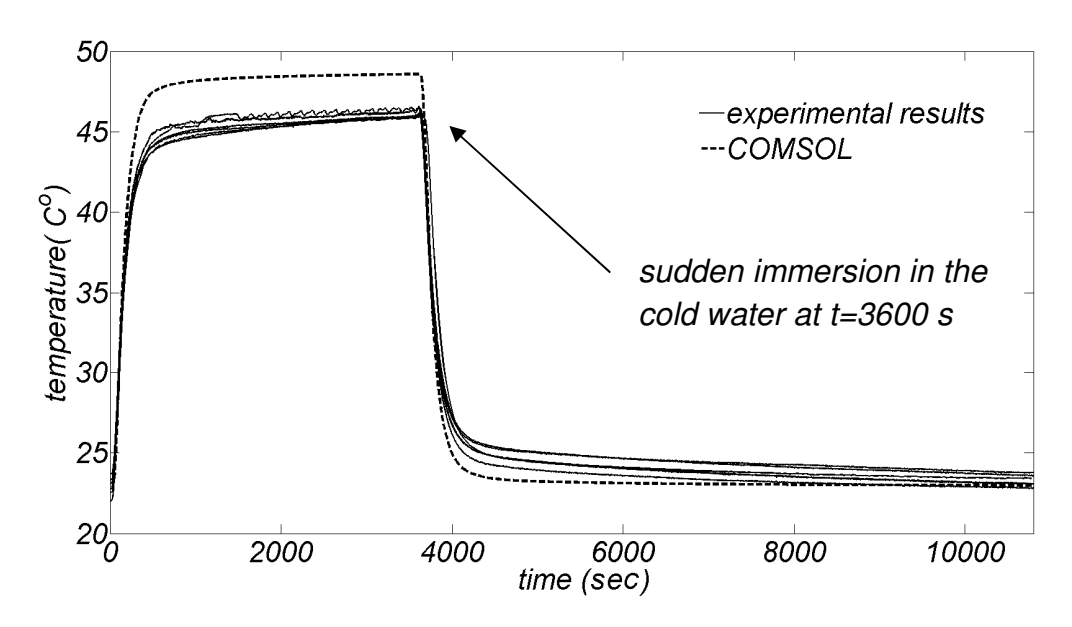


Figure 7.8: Change of cavity temperature (average temperature of the cavity) with time due to the immersion of the Stanstead Granite sample in hot and cold water containers.

order to model the thermo-hydro-mechanical problem, COMSOL Multiphysics<sup>TM</sup> software was used. The geometry and boundary conditions of the problem used in the modelling are shown in Figure 7.9. The average measured temperatures for the cold and hot water containers were 22.88 °C and 48.95 °C respectively. For simplicity, a null Neumann boundary condition was assumed for the heat flux from the stainless steel tube. The results of the computational modelling are shown in Figures 7.7 and 7.8, in dashed lines. The parameters used in the numerical simulations are as follows: Young's modulus (E) = 61 GPa, Poisson's ratio (v) =0.17; porosity (n) =0.6 %; Biot coefficient ( $\alpha$ )=0.44; permeability ( $\tilde{K}$ )=3.0×10<sup>-18</sup> m<sup>2</sup>; volumetric thermal expansion coefficient of the porous skeleton ( $\beta_s$ ) = 3.0×10<sup>-5</sup> °C<sup>-1</sup> (Nguyen et al., 2009); thermal conductivity of the porous skeleton ( $k_{cs}^*$ ) = 3.0 W.m<sup>-1</sup>.°C<sup>-1</sup> (Nguyen et al., 2009); thermal

conductivity of the fluid ( $k_{cf}^*$ ) = 0.58 W.m<sup>-1</sup>.°C<sup>-1</sup> (Holzbecher, 1998); specific heat capacity of the solid phase ( $c_s$ ) = 790 J.kg<sup>-1</sup>.°C<sup>-1</sup>; specific heat capacity of the liquid phase ( $c_f$ ) = 4187 J.kg<sup>-1</sup>.°C<sup>-1</sup> (Holzbecher, 1998). The dynamic viscosity ( $\mu$ ), volumetric thermal expansion coefficient ( $\beta_f$ ) and specific unit weight ( $\rho_f$ ) of water were assumed to be temperature dependent (Holzbecher, 1998). The parameters used for modelling the stainless steel tube are: Young's modulus ( $E_{ss}$ ) = 200 GPa; Poisson's ratio ( $v_{ss}$ ) = 0.3; volumetric thermal expansion coefficient ( $\beta_{ss}$ )=4.9×10<sup>-5</sup> °C<sup>-1</sup>; thermal conductivity ( $k_{ss}^*$ )= 16.5 W.m<sup>-1</sup>.°C<sup>-1</sup>; specific heat capacity ( $c_{ss}$ )= 480 J.kg<sup>-1</sup>.°C<sup>-1</sup> (McGuire, 2008).

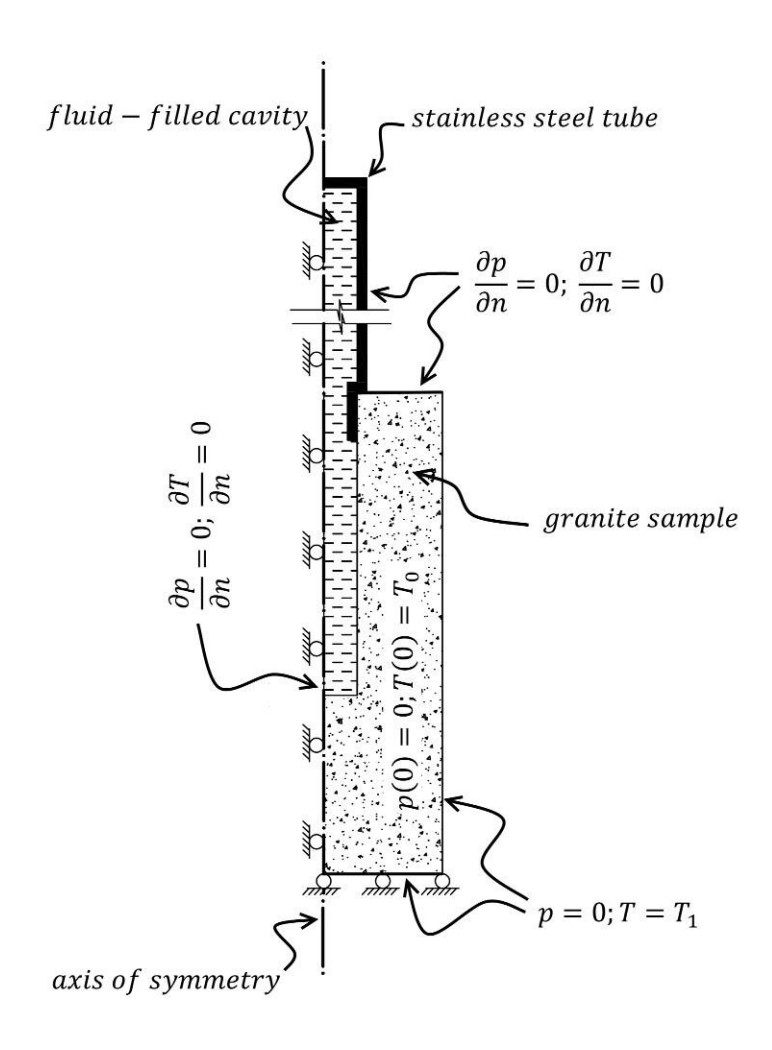


Figure 7.9: Geometry and boundary conditions of the THM problem.

The results of the numerical simulation were very close to the experimental results obtained for the fluid cavity pressure and temperatures in the Stanstead Granite sample. Also, no hysteresis behaviour was observed during the THM experiments and the results were repeatable.

Figure 7.10 shows the change of cavity pressure versus temperature, plotted on the state diagram of water. It can be seen that the temperature and pressure change in the experiment does not change the pore fluid to a vapor, since the entire cycle of the THM experiment is in the liquid region of the phase diagram of water. Also, the sample is kept continuously immersed in the water with no chance for air to enter the porous medium. Hence, although the sample experiences negative pore pressure, based on the two reasons mentioned, it can be inferred that the sample remains saturated during the THM test cycles and therefore the thermohydro-mechanical formulation presented earlier can be used to model the experiment.

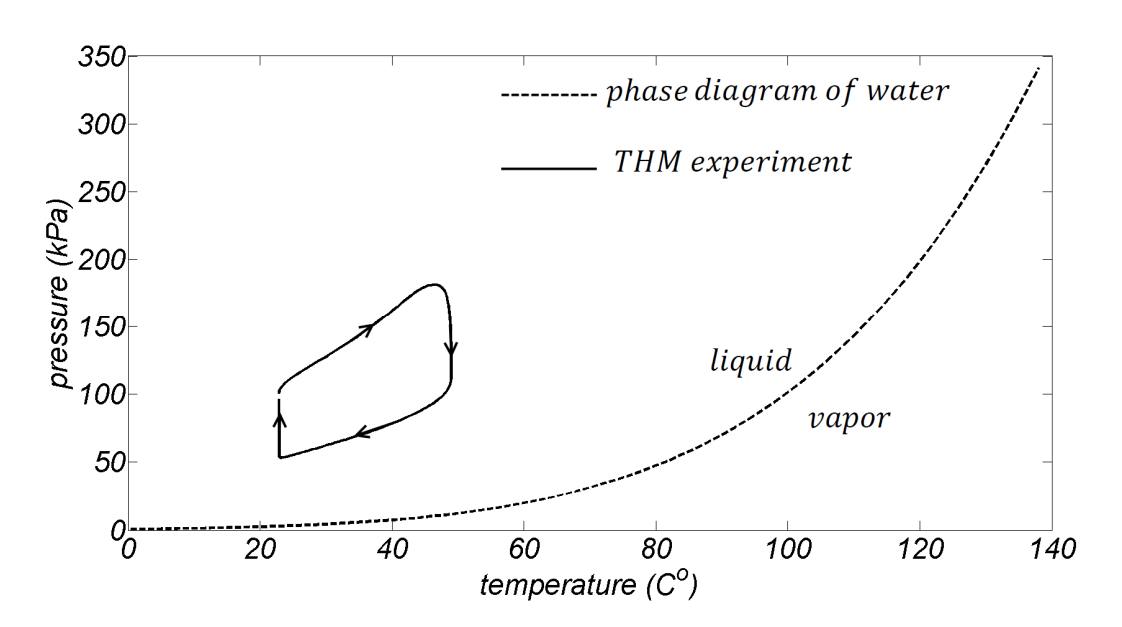


Figure 7.10: Change of cavity pressure with respect to cavity temperature change, plotted on the phase diagram of water (The pressure in this diagram is absolute pressure).

# 7.5. Thermo-hydro-mechanical experiment under controlled temperature changes

In this section, the thermo-hydro-mechanical processes in a fluid-filled cavity located in a saturated Stanstead Granite cylinder measuring 15.24 cm in diameter and 30.48 cm in height was investigated. The sample contains a sealed central cavity 2.54 cm in diameter and 15.24 cm in height, which is filled with water. The outer boundary of the sample was subjected to a controlled temperature change and the temperature and pressure changes within the central cavity were measured.

## 7.5.1. The testing apparatus

A schematic view of the test facility is shown in Figure 7.11. The sample was initially vacuum saturated for 7 days and was then placed inside the water container with the central cavity facing down. An annular neoprene rubber gasket with the hardness of 60A (external diameter: 15.24 cm; internal diameter: 2.54 cm; thickness: 0.16 cm) was used to develop a seal between the bottom surface of the sample and the stainless steel plate of the container. This contact area was sealed against leakage by applying a 1MPa sealing stress to the top of the sample using a hydraulic jack. A 0.635 cm diameter hole at the center of the stainless steel plate allowed access to the central cavity. The stainless steel fitting attached to the hole was connected to a temperature compensated pressure transducer (Model: MMG150V5K4C1T4A6S; supplier: OMEGADYNE; maximum pressure: 1MPa; accuracy: 0.2%) to measure the pressure change in the cavity during the experiment. A Swagelok valve was incorporated at the stainless steel fitting to allow water inflow. Two thermocouples (type K) were placed in the top and bottom of the cavity to record the temperatures within the cavity. Following the procedure developed in previous research (Selvadurai, 1996b, 2002) the wires were passed through the fittings and marine epoxy was used to ensure that the connections were sealed. It should be noted that the fittings were thermally insulated using a foil-backed self adhesive foam to minimize heat loss to the ambient environment which was maintained at approximately 25 °C.

(7) pressure transducer (13) solenoid valve (1) Stanstead Granite (2) fluid-filled cavity inlet/outlet valve (14) submersible heater 3 circulation pump Quizix precision pump (15) load cell 4 accumulator (10) water supply (16) loading plate 5 hydraulic jack (11) data acquisition system 6 hydraulic hand pump (12) cold water tank

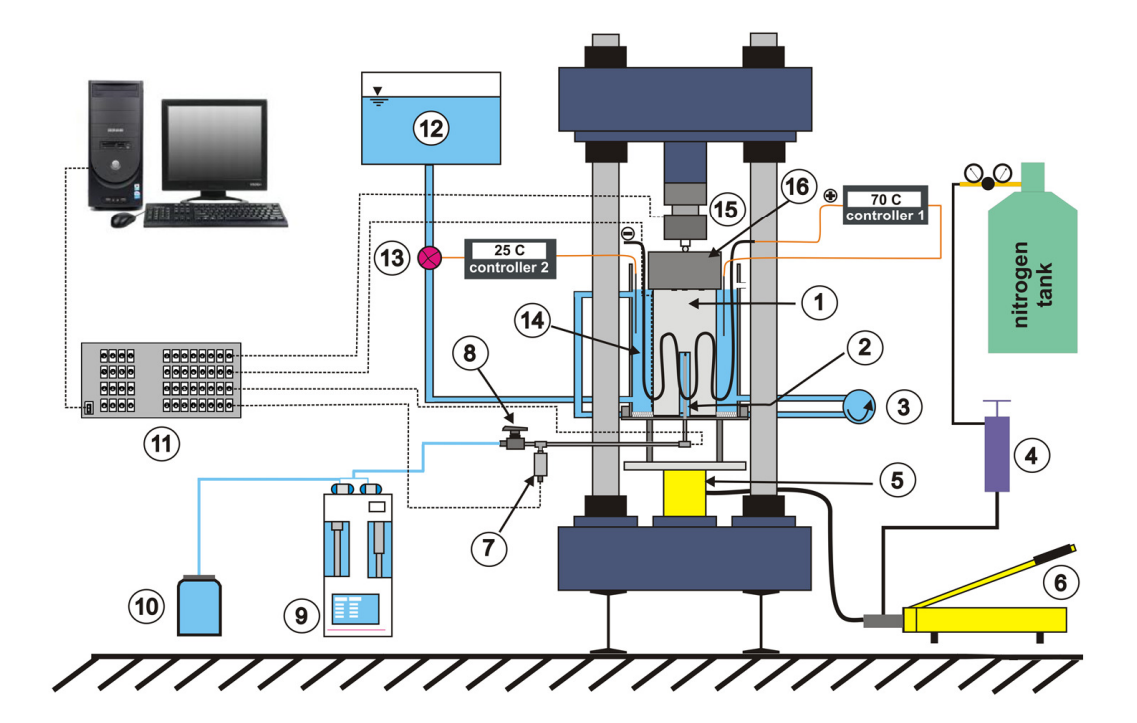


Figure 7.11: Schematic view of the THM setup

The placement of the sample inside the container was carried out under water in a large container in order to make sure that the central cavity was completely filled with water and with minimal air bubbles trapped within the cavity. Trapping of air can be caused by air bubbles that stick to the inner surfaces of the fittings.

The temperature of the water surrounding the sample was controlled using two submersible heaters connected to a temperature controller unit and a thermocouple was used to measure the temperature of the water inside the container. The heaters were in a configuration that allowed heating of the water around the sample without touching the surface of the sample. For cooling purposes, a solenoid valve was connected to a cold water reservoir and controlled

by a separate temperature controller unit and a thermocouple that measured the temperature of the water within the container. In order to keep the temperature of the water within the container uniform, the water was circulated using a fluid pump. The pump constantly extracted water from the upper region of the container and pumped it back into system at a lower section of the container.

Also, since any temperature change during the experiment can cause the sample to shrink or expand, the sealing load that was applied by the hydraulic jack could change. Therefore, an accumulator with an adjustable pressure release valve was connected to the hydraulic jack in order to maintain the sealing pressure in the correct range (1 MPa  $\pm$  0.05) during the experiment. The accumulator has a piston connected to a Nitrogen tank with an adjustable gas pressure regulator; this maintained the load during the cooling process and a pressure release valve guaranteed that the expansion of the sample did not result in an increase in the sealing load during the heating process. It should be noted that the sealing load was measured using a load cell that was in contact with the upper platen of the loading arrangement.

The temperature change at both the cylindrical and top surface of the sample was measured using six thermocouples: three thermocouples measured the temperatures at the upper, mid-height and lower levels on the boundary of the sample and three thermocouples measured the temperature on the upper surface of the sample (one in the center, one 2.54 cm away from the center and the third 5.08 cm away from the center). These measurements were used as temperature boundary conditions in the numerical modelling. The outer surface of the water container was dealt with thermal insulation (moisture-resistant Polystyrene foam insulation, heat flow rate of 0.26 at 24 °C) in order to minimize heat loss through the Plexiglas and hence expedite the temperature increase inside the container.

#### 7.5.2. Permeability measurement

Prior to performing the THM experiment, the permeability of the sample was measured using a steady state isothermal test. Three steady state tests were performed on the sample in an isothermal condition at 25 °C. The experiments were performed by pumping water at a constant flow rate of 0.02 ml/min using a Quizix precision pump (Model: QX-6000; minimum flow rate, 0.00034 ml/min; accuracy of the flow rate +/- 0.1% of set flow rate; maximum pressure: 41000 MPa). The fluid flow was continued until the fluid pressure in the cavity reached a steady state. The results of three repeatable steady state tests were used to estimate the permeability of the Stanstead Granite sample. The COMSOL Multiphysics The finite element code was used to model the experiments. The permeability of the Stanstead Granite estimated from a computational analysis of the experiments was  $5.25\times10^{-18}$  m². In order to evaluate the efficiency of the sealing technique under high temperatures, the same steady state test was repeated using the same flow rate while the sample was kept at 70 °C. The average permeability was  $5.25\times10^{-18}$  m² ± 2.5%, which validated the efficiency of the sealing technique at a temperature of 70 °C.

In order to calibrate the air-water mixture compressibility equation (i.e. Eq. (7.16)), the sample was first brought to a steady-state condition in the permeability measurement tests. The inlet valve was then closed and the decay of the cavity fluid pressure was recorded. The transient part of the experiments was used to estimate the  $\varphi$  parameter in the compressibility equation (i.e. Eq. (7.16)). The results of the experiments are shown in Figure 7.12. It should be noted that, at the initial stage of the experiment as the cavity pressure increases from 0 to the steady state pressure value, the volume of the cavity was 116.5 ml, which included the cavity inside the sample, the fittings and connections and also the volume of the cylinder of the Quizix pump. In transient tests, the volume of the compressible fluid in the cavity was 98.2 ml.

The parameters used in the COMSOL Multiphysics<sup>TM</sup> computational modelling are as follows: Young's modulus (E) = 61 GPa, Poisson's ratio (v) = 0.17; porosity (n) = (0.5 to 1.4) %; Biot coefficient  $(\alpha) = 0.44$ . The bounding range of  $\varphi^0 = (0.003 \text{ to} 0.005)$  provided the best estimate for the permeability experiment,

followed by a transient cavity pressure decay, as shown in Figure 7.12. The air fraction values were adjusted in the model for the decrease of cavity volume during the cavity pressure decay stage. Since the initial air fraction is within the range of  $\varphi^0 = (0.003 \text{ to } 0.005)$ , the estimated air volume in the cavity would be (0.29 to 0.49) ml.

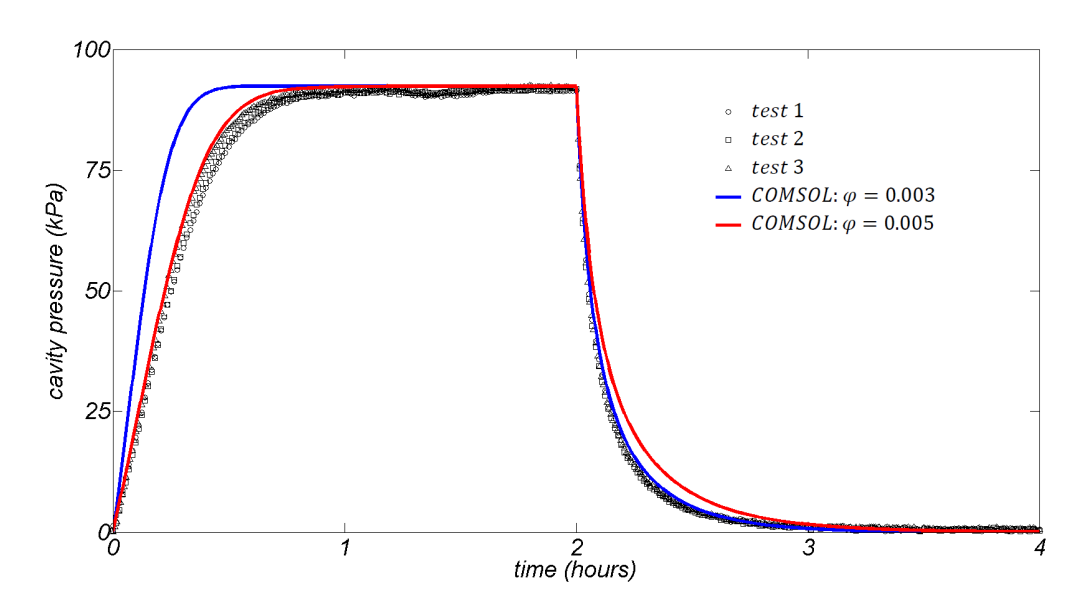


Figure 7.12: Steady state tests with a flow rate of 0.02 ml/min (for 7200 seconds), followed by transient decay tests.

In order to verify the sealing efficiency of the gasket technique that was used in the above mentioned permeability test, a set of steady state tests was performed on a stainless steel sample. The cylinder had the diameter of 10.16 cm and height of 30.48 cm, containing a cylindrical cavity with the diameter of 2.54 cm and height of 15.24 cm. In order to minimize the trapping of air bubbles in the central cavity of the stainless steel cylinder, the sample was placed in the testing device under water in a large container, similar to the emplacement of the granite sample. A sealing pressure of 1 MPa was applied to the gasket and a series of constant pressure steady state tests was performed on the sample. For each test, the cavity pressure was set to a constant value using the Quizix pump, which employs a PID controlling technique and is capable of keeping the pressure constant with a high accuracy (± 1 kPa). The decrease in the inlet flow rate to the stainless steel

sample was monitored until it reached steady state condition. Table 7.2 shows the results of these experiments. It was observed that the leakage through the system was dependent on the cavity pressure; as expected, a higher cavity pressure corresponded to a larger amount of leakage. The maximum leakage that was measured for the 200 kPa constant pressure test was 0.000769 ml/min.

Table 7.2: The results of sealing tests performed on a stainless steel cylinder.

P (kPa)	Q (ml/min)	$T(C^{\circ})$
200	0.000769	21.49
100	0.000240	21.16
50	$8.00 \times 10^{-5}$	21.50
25	$2.00\times10^{-5}$	21.50

Since the 0.02 ml/min steady state flow rate on the granite sample corresponded to 91 kPa cavity pressure, a leakage of 0.000769 ml/min corresponds to a cavity pressure change of 3.5 kPa. The value for the cavity pressure of 100 kPa is 1.1 kPa, which is the maximum cavity pressure achieved in the current THM test on the granite sample. Since the diameter of the stainless steel cylinder is 33% shorter than the Stanstead sample the estimated leakage is an upper bound for the leakage in granite sample tested, and thus the leakage through the system definitely can be neglected.

#### 7.5.3. Thermo-hydro-mechanical experiment

Three heating-cooling cycles were performed on the sample by changing the temperature of the water within the container. A general view of the THM test configuration is shown in Figure 7.13. The temperature was initially increased from 25°C (laboratory temperature) to 70°C and kept constant. The heating process, including the initial temperature increase step and maintaining a constant temperature, took 4 hours. The temperature at the surface of the cylinder was then

reduced from 70 °C to 25 °C and kept constant by circulating water at 20 °C into the container. The cooling process took 8 hours.



Figure 7.13: The apparatus prepared for performing the THM experiment.

This heating-cooling cycle was repeated three times and the temperature and pressure within the cavity were recorded. Each new cycle commenced after sufficient time was allowed for complete dissipation of both temperature and pressure. Preliminary computational estimates suggest that both the pressure and temperature within the granite reduced to steady values at approximately 12 hours. The change in temperature at the circumference and at the upper surface of the sample obtained for the three cycles are shown in Figures 7.14 and 7.15. These results were used as the temperature boundary conditions in the computational modelling.

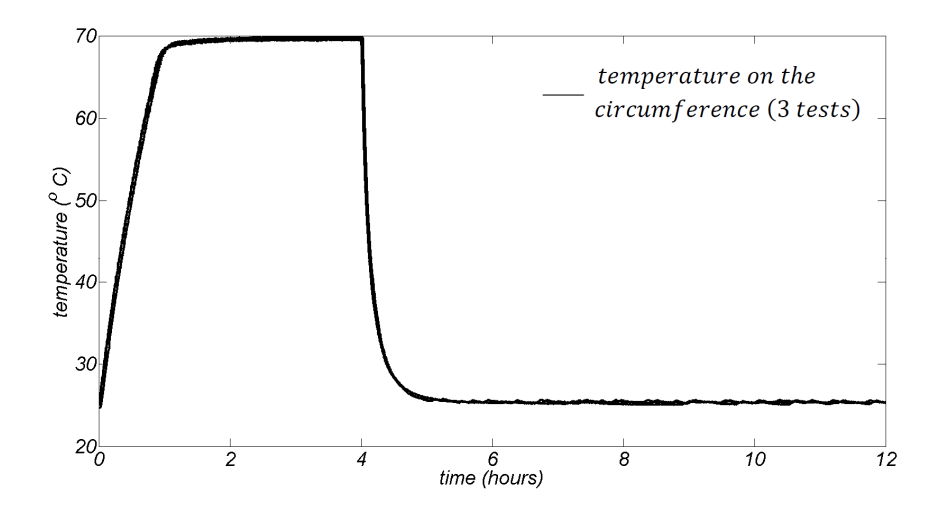


Figure 7.14: The measured temperature on the circumference of the sample during three experiments.

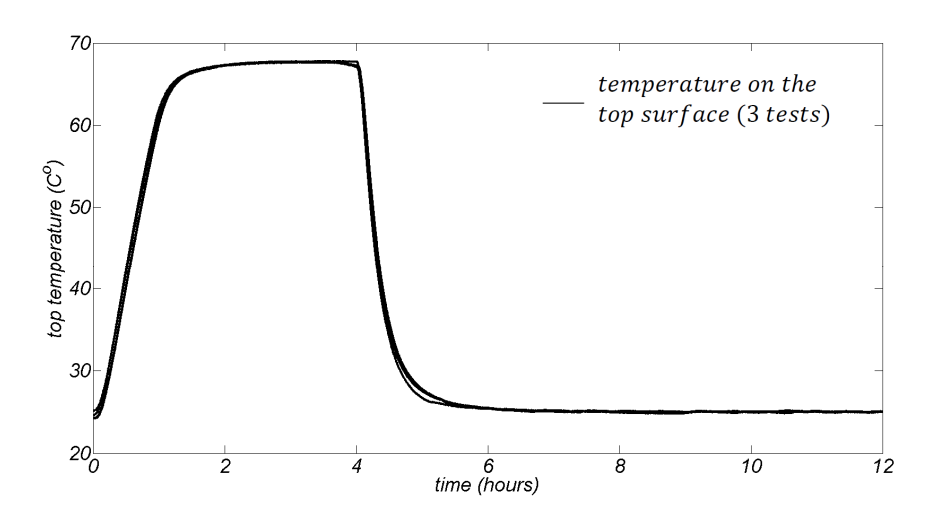


Figure 7.15: The measured change of temperature on the top surface of the sample during three experiments.

## 7.5.4. Experimental results and computational modelling

The cavity temperature and cavity pressure measured from the three heating-cooling cycles performed on the Stanstead Granite sample are shown, respectively, in Figures 7.16 and 7.17. The trend in the change in cavity temperature is very similar to the boundary temperature change. However, there is an average time lag of 130 seconds between the start of the temperature change on

the surface of the sample and that in the central cavity, resulting from the heat conduction process.

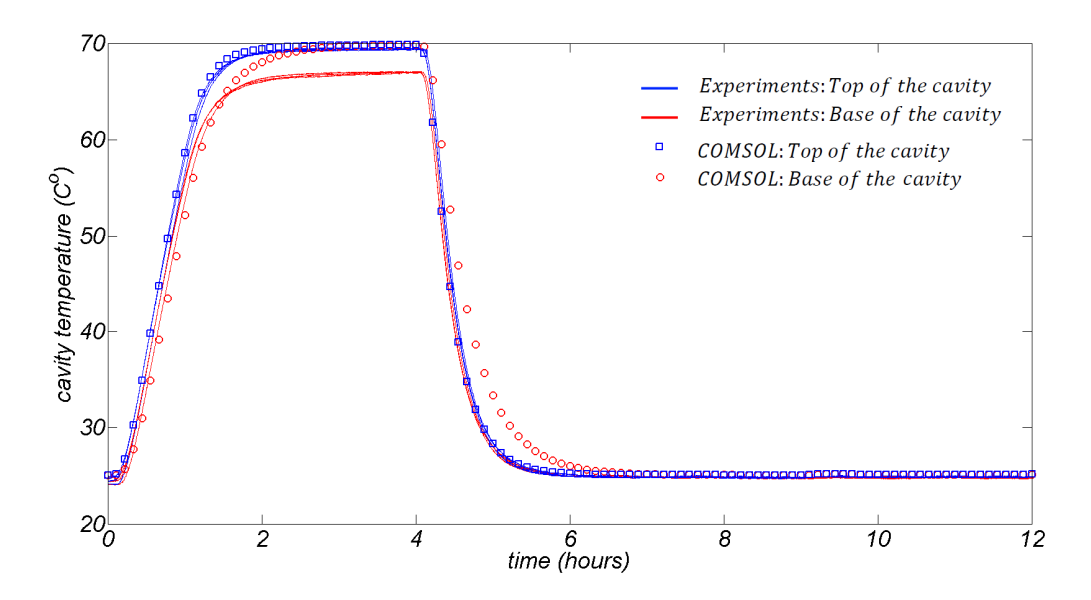


Figure 7.16: The change in the cavity temperature during the three cycles of heating and cooling.

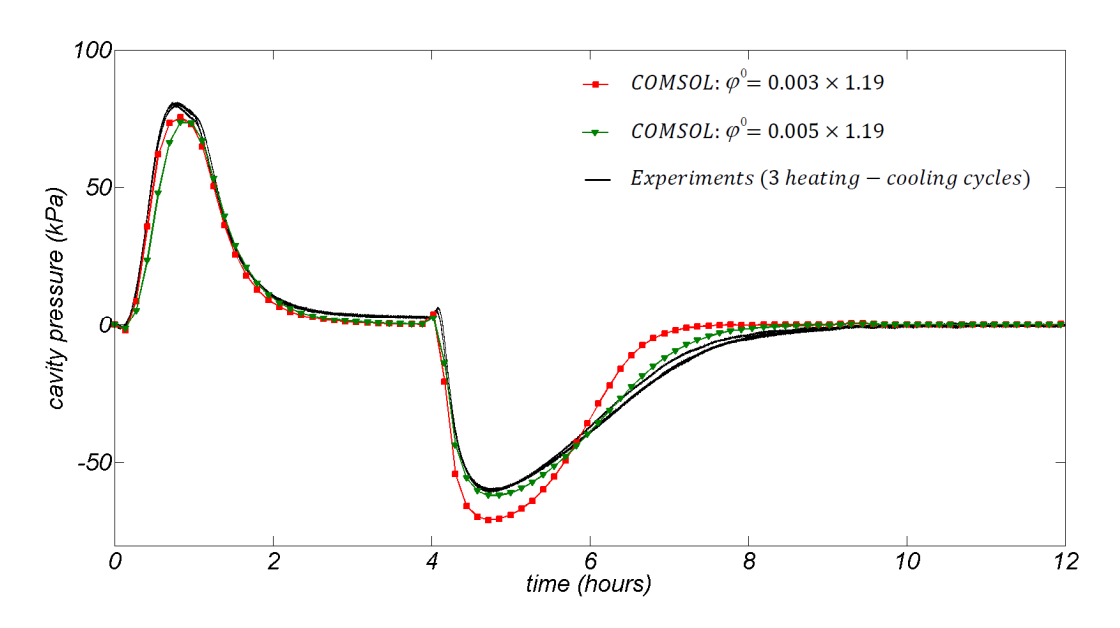


Figure 7.17: Comparison of the results of THM experiments with computational results using pressure dependent compressibility values for the cavity fluid.

The cavity pressure initially increased due to thermal expansion of the fluid inside the cavity and due to the temperature-induced fluid flow from the porous medium towards the cavity. Note that the thermal expansion of the cavity fluid is more than the thermal expansion of the cavity itself. The pressure in the cavity reached a maximum value of 81 kPa and then started to decay due to the dissipation of excess pore pressure through the porous medium.

It can be seen that after 4 hours (14400 seconds) the cavity pressure reduced to zero. At this point the cooling cycle was started and the cavity pressure became negative. The minimum cavity pressure was recorded at -61 kPa. The negative pressure then started to decay over the next 8 hours (28800 seconds).

With respect to the rate of heating and cooling, the cooling rate in the linear range was 1.8 times faster than the heating rate. However, the maximum cavity pressure during heating was higher than the maximum cavity pressure during cooling. This is due to the fact that, although the cavities and fittings were filled with water, there were still air bubbles trapped in the fluid inclusion which caused the compressibility of air to be pressure dependent. Based on Eq. (7.16), the compressibility of the air-water mixture is higher under negative pressure than positive pressure. Thus, the cavity pressure increase is greater during heating than in the cooling phase of the test.

The geometry and boundary conditions of the problem used in the computational modelling are shown in Figure 7.18. The upper surface and the circumference of the sample had a zero fluid pressure boundary conditions. The bottom surface, which was sealed by a rubber gasket, was modelled as a no-flow boundary condition. The temperature boundary condition for the circumference and top surface of the sample was the temperature measured for these two surfaces;  $T_1(t)$  and  $T_2(t)$  are, respectively, the average temperature values measured for the three points at the top, mid-height and bottom of the circumference and at the center, mid-radius and the edge of the top surface of the sample.

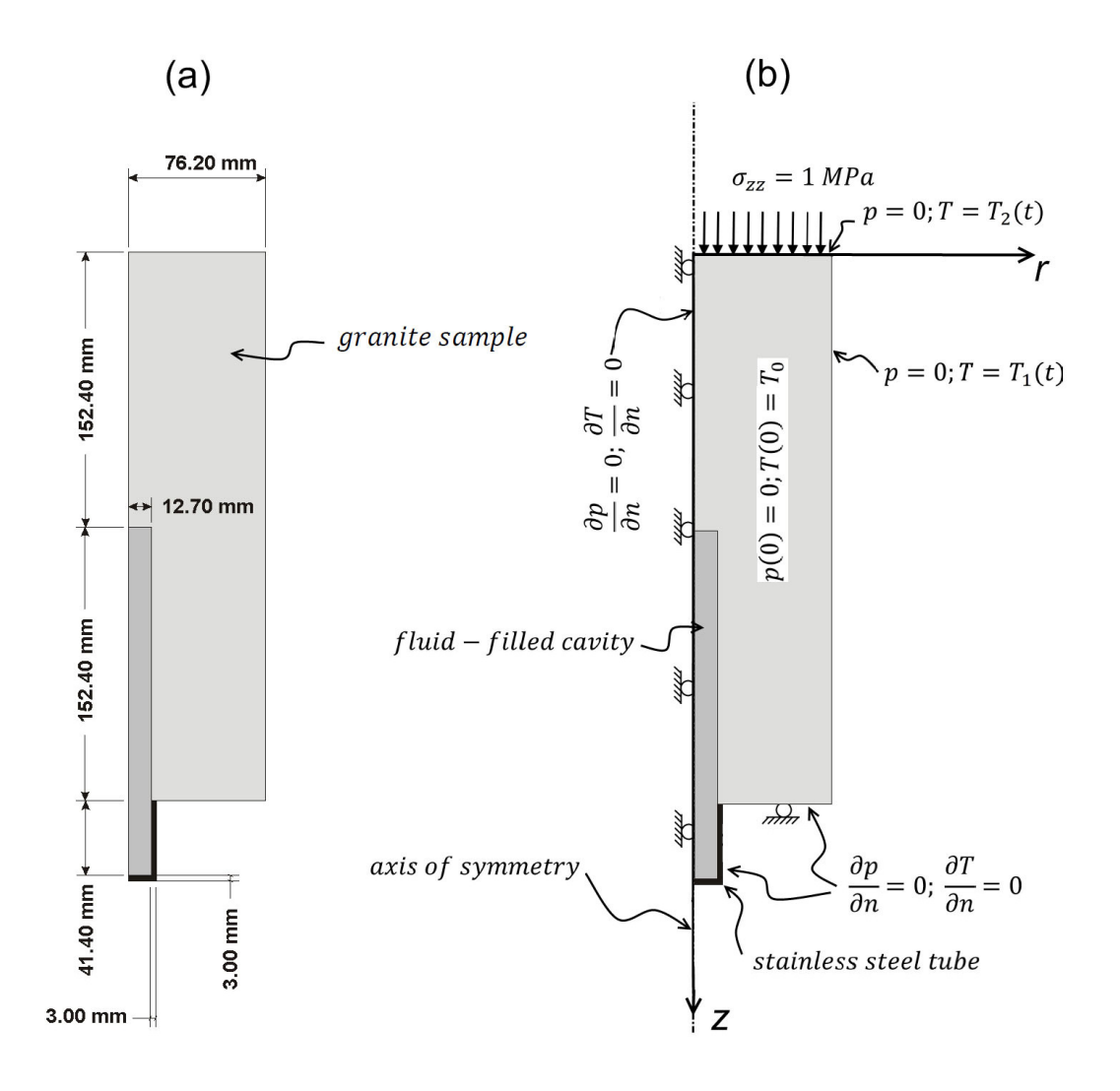


Figure 7.18: Geometry and boundary conditions of the THM problem.

The bottom surface of the sample, which was in contact with the sealing gasket, was assumed to be thermally insulated. Also, the fittings and the connection tube were modelled as a stainless steel tube with an even thickness of 3 mm (which was the average thickness of the connections used). The outer surface of the connection tubes were thermally insulated in the experiment and thus a null Neumann temperature boundary condition was assumed for that surface. A constant sealing pressure of 1MPa was applied to the top surface of the sample. Since the sealing pressure was kept constant during the experiments, the thermomechanical deformation of the sample was allowed in the THM process. The parameters used in the numerical simulations are shown in Table 7.3. The

dynamic viscosity ( $\mu(T)$ ), volumetric thermal expansion coefficient ( $\beta_f(T)$ ) and specific unit weight ( $\rho_f(T)$ ) of water were assumed to be temperature dependent (Holzbecher, 1998).

The estimated temperature changes on the top and the bottom of the cavity are shown in Figure 7.16. The experimental and computational results are in agreement with each other for the temperature in the top of the cavity. However, there is a slight discrepancy in the estimated temperature value at the bottom of the cavity compared to the measured value. The temperature difference at the end of the heating process is 2.45 °C. The reason for the discrepancy could be the fact that the bottom surface of the sample, which is in contact with the rubber gasket, was assumed to be thermally insulated in the computations. However, based on the experimental results obtained, there is a slight heat loss through this surface.

Table 7.3: Values of the parameters in the computational modelling of the THM experiment.

Donous ston	Crarita	Water	Stainless
Parameter	Granite	Water	Steel
Young's modulus (GPa)	61	-	200 b
Poisson's ratio	0.17	0.49	0.3 <sup>b</sup>
Porosity (%)	0.6	100	-
Biot Coefficient	0.44	-	-
permeability (m <sup>2</sup> )	$5.25 \times 10^{-18}$	$(5.25\times10^{-18})\times10^6$	-
volumetric thermal expansion	3.0×10 <sup>-5 c</sup>	$oldsymbol{eta}_f(T)$ a	4.9×10 <sup>-5 b</sup>
coefficient (°C <sup>-1</sup> )	3.0X10	$\rho_f(I)$	
thermal conductivity (W.m <sup>-1</sup> .°C <sup>-1</sup> )	3.0 °	0.58 <sup>a</sup>	16.5 <sup>b</sup>
specific heat capacity (J.kg <sup>-1</sup> .°C <sup>-1</sup> )	790 <sup>c</sup>	4187 <sup>a</sup>	480 <sup>b</sup>

<sup>&</sup>lt;sup>a</sup>. Holzbecher (1998)

<sup>&</sup>lt;sup>b</sup>. McGuire (2008)

<sup>&</sup>lt;sup>c</sup>. Nguyen et al. (2009)

The results of the computational modelling of cavity pressure are shown in Figure 7.17. The problem was solved using the two bounding air fraction values (i.e. 0.003 and 0.005) for the fluid cavity compressibility equation which were obtained from the isothermal transient test presented in section 7.5.2. The results satisfactorily agree with the experimental measurements. The cavity compressibility equation with  $\varphi^0$ =0.003 provided the best estimate for the positive range and the function with  $\varphi^0 = 0.005$  provided the best estimate for the negative range of pressure change. A possible reason for the slight discrepancy is that the dissolution of air in water was not taken into account in the current study. Dissolution of air in water decreases the pressure in the cavity. Since in the current THM experiment the pressure changes in the negative range (i.e. cooling stage) is much slower than in the positive range (i.e. heating stage), there is more time for the trapped air to partially dissolve in the water and release the pressure in the cooling stage than the heating stage. Hence, the upper bound of the estimated air fraction better simulates the negative range. For the similar reason, the pressure build-up stage in the isothermal permeability experiment which was slower than the pressure decay stage was better fitted with  $\varphi^0 = 0.005$ . The airwater compressibility range used in the modelling is shown in Figure 7.19.

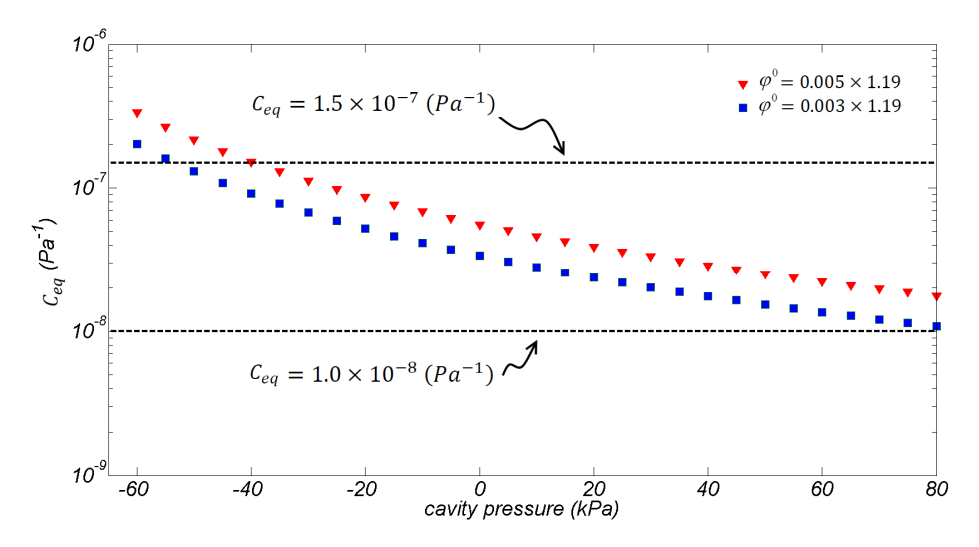


Figure 7.19: Comparison of compressibility changes with pressure for cavity fluids containing different amounts of dissolved air contributing to the compression.

For the purpose of comparison, the experimental results were also fitted with constant cavity fluid compressibility values. The compressibility value of  $C_{eq} = 1.0 \times 10^{-8} \text{ Pa}^{-1}$  provides the best estimation for the positive pressure range and the compressibility value of  $C_{eq} = 1.5 \times 10^{-7} \text{ Pa}^{-1}$  provides the best estimation for the negative pressure range. The results are shown in Figure 7.20.

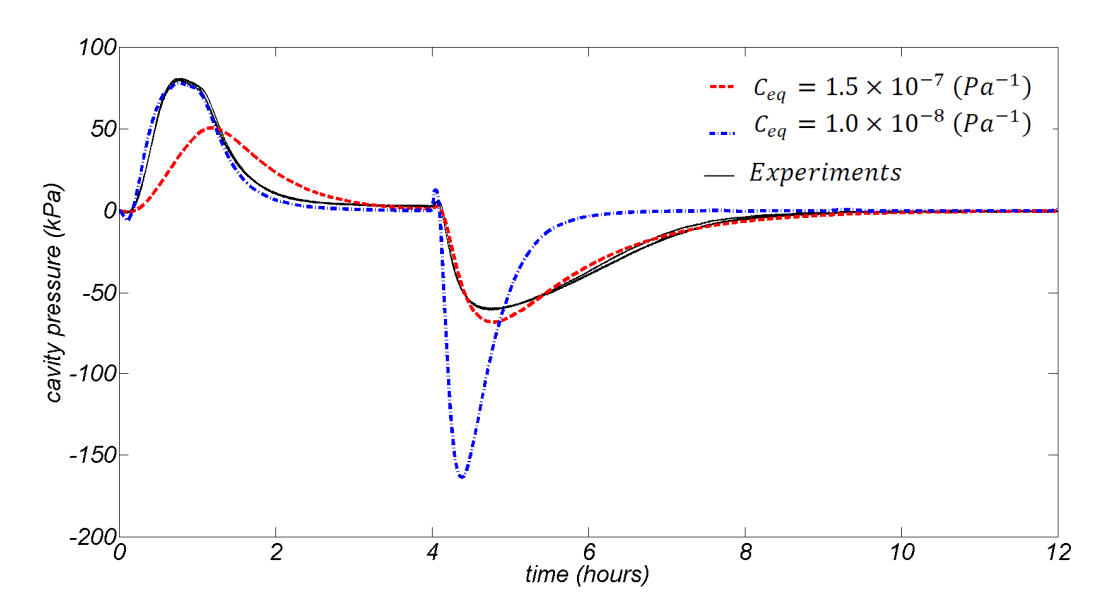


Figure 7.20: Comparison of the results of THM experiments with computational results using constant compressibility values for the cavity fluid.

Another observation is that the cavity pressure changes at the early stages of heating and cooling, when the temperature change has not yet affected the cavity fluid. These effects are shown in Figures 7.21 and 7.22. Immediately after the start of the heating stage, the cavity pressure begins to decrease, reaching – 1 kPa and then reducing to zero pressure after 500 seconds. Similarly, at the very early stage of cooling, the cavity pressure increases from 2.7 kPa and reaches a maximum pressure of 6.5 kPa; it then decreases and returns to 2.7 kPa after almost 500 seconds. This phenomenon is due to the fact that the very early temperature change on the surface of the sample causes the surface region of the sample to expand or shrink in heating and cooling, respectively. This is the

Mandel-Cryer effect associated with temperature change (Kodashima and Kurashige, 1996; Selvadurai and Suvorov, 2012).

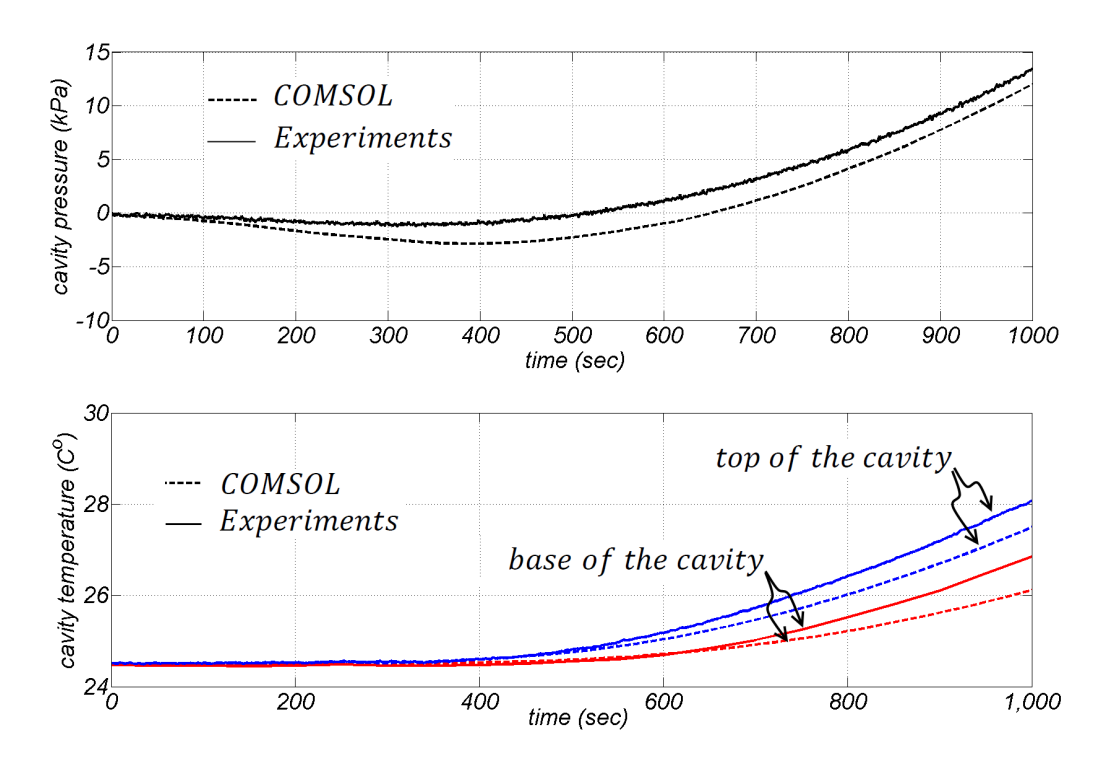


Figure 7.21: Volumetric expansion of the cavity due to a temperature increase on the sample surface at the start of the heating stage ( $\varphi^0 = 0.005$ ).

In order to study the possibility of de-saturation during the heating-cooling cycles, the change in the maximum absolute pressure versus temperature for the cavity was plotted on the state diagram of water (see Figure 7.23). Since the whole cycle of pressure-temperature change in the experiment is in the liquid state, it can be inferred that there is no possibility of de-saturation of the sample during the experiment and therefore the saturated THM formulation is applicable for modelling purposes.

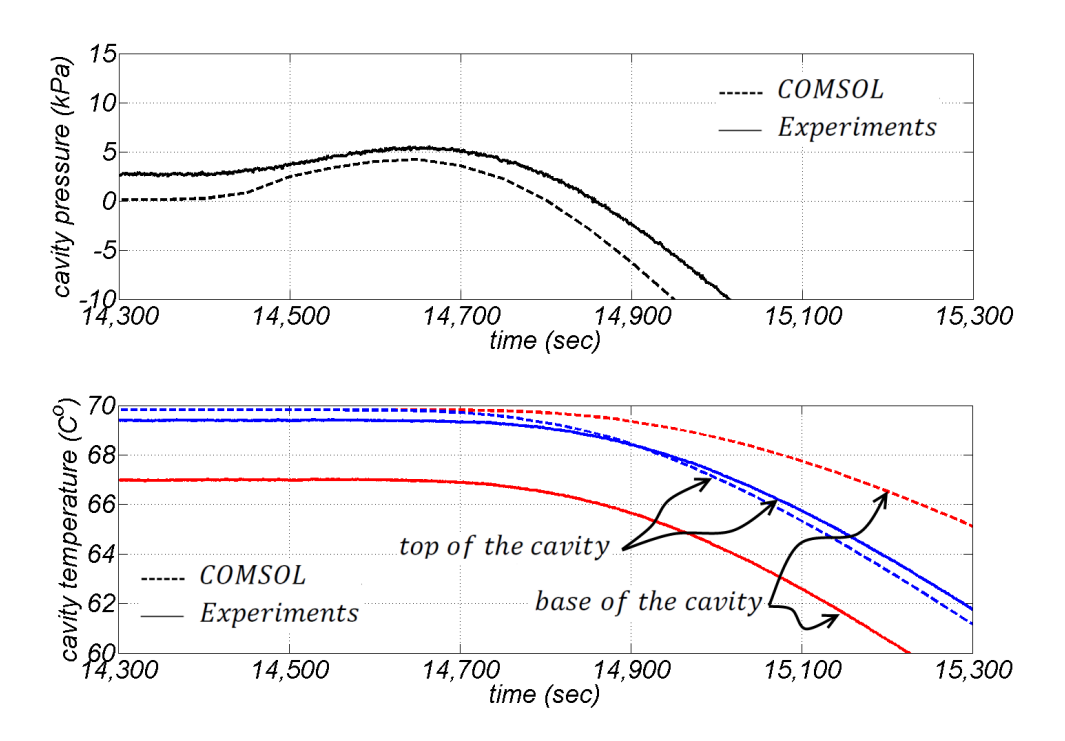


Figure 7.22: Volumetric contraction of the cavity due to a temperature decrease on the sample surface at the start of the cooling stage ( $\varphi^0 = 0.005$ ).

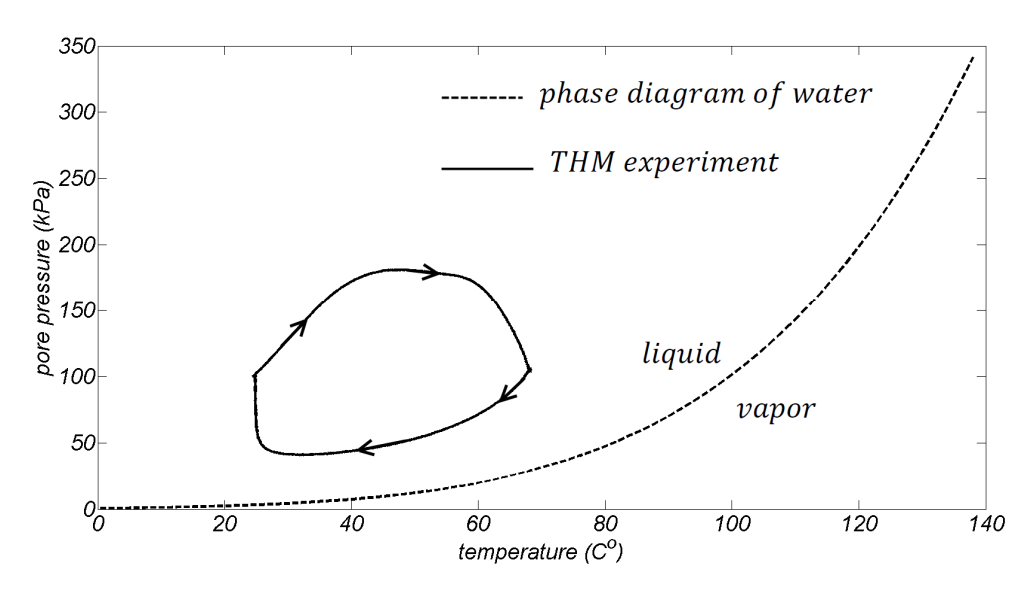


Figure 7.23: Change of cavity pressure (Absolute pressure) with respect to the cavity temperature change, plotted on phase diagram of water.

## 7.6. Summary

In this chapter, the Thermo-Hydro-Mechanical (THM) behavior of Stanstead Granite was studied both theoretically and experimentally. The formulation for

non-isothermal poroelasticity in saturated geomaterials was summarized and two experimental investigations were performed to verify the accuracy of the THM formula. The experiments were conducted to examine the THM processes that can be generated in a granite cylinder with permeability in the range (3 to 6)  $\times 10^{-18}$ m<sup>2</sup>. A fluid-filled cavity within a Stanstead Granite cylinder is used to examine the process of pressure generation during heating of the outer surface. The first experiment was performed on a Stanstead Granite cylinder measuring roughly 5 cm in diameter and 10 cm in height. The sample was subjected to cycles of heating and cooling at the boundary by immersion in hot and cold reservoirs and the experiments were repeated 6 times. The second experiment was performed on a larger Stanstead Granite cylinder measuring 15 in diameter and 30 cm in height. The temperature was increased and decreased as a ramp function, using PID temperature controllers. The heating-cooling cycles were repeated 3 times. The experimental results for each experiment were evaluated within the content of a THM model that takes into account heat conduction in the saturated granite and Darcy flow-based classical poroelasticity. Nominal calculations were also performed to account for (i) temperature dependency of the density and fluid viscosity and (ii) alteration in the compressibility of the pore fluid in the system due to the presence of any air. The result of the experiments indicates that pressure changes can be modelled accurately using the finite element software COMSOL<sup>TM</sup> that can examine THM processes. The factor that contributes to the slight discrepancy between experimental and computational results is identified as possible air entrainment (through parametric computational evaluation), which also accounts for the pressure-dependent compressibility. The experimentation can be further improved by adapting the procedures to eliminate the influences of air content, both free and dissolved, on the THM processes. Such refinements are considered to be much too artificial since in practice, where the theories are used to estimate the THM behavior of rocks in situ, there are no assurances of complete saturation. The research work indicates that conventional THM models can be used to model the heating behavior of granite relatively accurately. The development of pressure within a fluid-filled cavity is the candidate problem examined to validate the modelling.

#### **CHAPTER 8**

#### CONCLUSIONS AND SCOPE FOR FUTURE RESEARCH

# 8.1. Summary and concluding remarks

Biot's theory of linear poroelasticity can be extended to include thermal effects. The study of the thermo-hydro-mechanical (THM) behaviour of porous media is of interest in several disciplines of engineering; the major areas of application in geotechnical engineering are deep disposal of nuclear wastes in geological repositories, oil and gas recovery, geothermal energy, and CO<sub>2</sub> sequestration. The focus of this thesis has been on the non-isothermal transport of fluid in Stanstead Granite, which is a low permeability geomaterial similar to those being considered as candidate rocks for the deep geological disposal of nuclear wastes. The THM behaviour of the rock was studied both theoretically and experimentally. The following is a summary of the research performed on the interpretation of non-isothermal transport in Stanstead Granite:

• The physical and mechanical characterization of Stanstead Granite was performed through a series of laboratory experiments. The chemical composition of the rock was studied through X-ray fluorescence spectrometry

tests performed on the material in the Earth and Planetary Science Department of McGill University. The two major elements identified were silicon (70%) and aluminum (15%), which is similar to other granitic rocks. The porosity of the rock was measured using both a saturation technique and mercury intrusion porosimetry (MIP). The porosity was measured to be (0.4% to 0.7%) from the saturation technique and (0.7% to 1.4%) using MIP. Since the MIP technique measures the total area of the pores on the surface, including the non-connected pores, the result is an upper bound for the porosity. The bulk dry density and the grain density of the rock were measured as (2630 kg/m<sup>3</sup> to 2660 kg/m<sup>3</sup>) and (2650 kg/m<sup>3</sup> to 2670 kg/m<sup>3</sup>) respectively. Also, 4 unconfined compressive strength (UCS) tests were performed on cylindrical samples of Stanstead Granite that measured 5 cm in diameter and 10 cm in height; the rocks showed linear elastic behaviour and failed at an average uniaxial compressive stress of 132 MPa. The average Young's modulus was measured at 61 GPa and the Poisson's ratio was 0.17. The physical and mechanical parameters measured compare favourably with similar results for intact granitic rocks reported in the literature.

The isothermal transport of fluid through porous media was theoretically studied (Chapter 3). Terzaghi's theory of one-dimensional consolidation was presented along with its three-dimensional extension. The theory weakly takes into account the effect of skeletal deformation on the transient flow of fluid induced by the application of traction on the surface of a one-dimensional column of soil. Biot's theory of linear poroelasticity was also presented. This formulation takes into account the coupling effects between the pore pressure and skeletal deformation. It also assumes that the solid skeleton, the permeating fluid, and the solid grains are compressible; the latter two are assumed to be incompressible in Terzaghi's consolidation theory. In the limiting case where the pore pressure uncouples from the stress field, the fluid phase equation in Biot's formulation reduces to the piezo-conduction equation, which has only the pore pressure as a variable.

- For low permeability geomaterials, the preferred method for measuring permeability is through hydraulic pulse testing. An analysis of the experimental results can be performed by the application of either Biot's theory of linear poroelasticity or the piezo-conduction equation. The accuracy of using the piezo-conduction equation to estimate the permeability was studied using published data on the material properties of two different rocks types: Westerly Granite, and Indiana Limestone. It was seen that the application of the commonly used piezo-conduction equation, which neglects the compressibility of solid grains, results in a noticeable overestimation of permeability. However, the use of the piezo-conduction equation with a specific storage term that takes into account the effect of compressibility of solid grains, gives a negligible error. Also it was seen that the above mentioned modelling error is highest for the one-dimensional test, and is lower for the radial flow and patch pulse tests, respectively.
- A series of steady state tests was performed on 7 different samples of Stanstead Granite. The tests were performed on partially drilled and undrilled cylindrical samples with dimensions varying from the smallest with a diameter of D=5 cm and a length of L=10 cm to the largest with D=15 cm and L=30 cm. The tests on the samples with the partially drilled cavity provided both radial and axial flow patterns; however, for the geometries of the tested samples, the shortest path from the central cavity to the outer surface of the samples was radial (i.e. the dominant flow pattern was radial). The permeability was in the range of  $(3 \text{ to } 6) \times 10^{-18} \text{ m}^2$  for unstressed samples. The one-dimensional flow tests were performed under isotropic stress in a triaxial cell. For the samples tested under an isotropic stress of 5 MPa, the permeability was within the range of  $(1 \text{ to } 2) \times 10^{-18} \text{ m}^2$ .
- A series of hydraulic pulse tests were also performed on 4 different samples of Stanstead Granite. The tests included radially-symmetric flow, patch pulse tests and tests on partially drilled samples. It was seen that, no matter how precise the attempts to fill the cavity with de-aired water were, air bubbles

still remain in the system. This can significantly affect the compressibility of water and the permeability estimates from the hydraulic pulse tests can be orders of magnitude lower than in reality; therefore, the compressibility has to be corrected for unwanted air entrained as air bubbles in the cavity. The air-water mixture compressibility was discussed and a relationship was presented. Following the proposed algorithm for estimating the amount of trapped air bubbles in the fluid cavity, the permeability of the tested Stanstead Granite samples was estimated to be  $(3 \text{ to } 6) \times 10^{-18} \text{ m}^2$ .

The alteration in the permeability of Stanstead Granite under isotropic loading and unloading was experimentally studied, using a steady state permeability measurement technique. Rock specimens in the lab are under zero stresses whereas an in-situ rock mass is subject to geostatic stresses. Any change in the confining stress can alter the permeability of geomaterials. A series of constant flow rate steady state tests was performed on 3 cylindrical samples of Stanstead Granite, under various confining pressures. The tests were performed in a GDS triaxial cell. It was seen that when the confining pressure is increased to 30 MPa the permeability decreased by almost one order of magnitude and, after unloading, it returned to its preloaded value. Loading the samples up to 60 MPa decreased the permeability between (2 to 3) orders of magnitude. When the samples were unloaded, although the permeability increased, it did not return to its original value. This temporary decrease in permeability under isotropic loading can be associated with the elastic closure of pores and micro-cracks, whereas the permanent decrease can be due to pore collapse. In order to study the hydraulic anisotropy in the rock, one sample was cored, with its central axis perpendicular to that in the other two samples. The Stanstead Granite samples tested showed isotropy in permeability up to the confining pressure of 40 MPa. However, a further increase of confining pressure to 60 MPa showed that anisotropy developed with the ratio of 1:3. This ratio was retained during unloading.

The thermo-hydro-mechanical behaviour of Stanstead Granite was also studied. The non-isothermal extension of Biot's theory of linear poroelasticity was presented. Since the measurement of fluid pressure and temperature in the sealed cavity is experimentally feasible, this was implemented in the research. Nominal calculations were also performed to account for temperature dependency in the density and viscosity of the fluid; alteration in the compressibility of the pore fluid in the system due to any presence of air was also accounted for. A thermal damage test was performed on a cylindrical sample measuring 15 cm in diameter and 30 cm in height. It was observed that after an abrupt temperature increase of 80 C° the permeability increased between 25% to 40%. Two different THM experiments were performed and the results were used to investigate the accuracy of the presented THM formulation. In the first experiment, a sample was heated by immersion in a hot water bath and cooled by immersion in a cold water bath. For the second THM experiment, a unique apparatus was designed and fabricated; this test facility is capable of changing the temperature in a controlled fashion. The sealing of the system was verified by performing tests on a stainless steel cylinder, with the result that a sealing load could be kept constant during the temperature variations. In both of the experiments, the change of temperature and pressure in the sealed fluid cavity was monitored. The problems were computationally modelled using the presented formulation. The COMSOL Multiphysics TM finite element code was used to solve the governing partial differential equations. The results obtained in the simulations compared favourably with the measured temperature and pore pressure values. The slight discrepancy was associated with the existence of air bubbles in the fluid-filled cavity.

#### 8.2. Scope for future research

In the current research, the isothermal and non-isothermal fluid transport in Stanstead Granite was studied, both theoretically and experimentally. The following investigations can be suggested as future work:

- In this research, fluid flow was studied only in saturated geomaterials, whereas in many practical situations the medium is unsaturated. Any future research can extend the theoretical and experimental work to the study of the unsaturated thermo-hydro-mechanical behaviour of low permeability geomaterials.
- The alteration in the permeability of Stanstead Granite due to isotropic loading and unloading was studied; it was observed that, after a certain level of confining pressure, the pore closure and subsequent permeability decrease becomes partially irreversible. Further investigations can be performed by comparing CT-scanned images of a rock sample before and after an isotropic load. A further approach would be to perform the same comparison between the results of mercury intrusion porosimetry tests before and after an isotropic load.
- The compressibility of the air-water mixture was studied and an algorithm was proposed to correct for the effect of air entrainment in the sealed cavity used in hydraulic pulse testing. It was mentioned that the air bubbles can go into solution, according to Henry's Law and the rate of dissolution follows Fick's Law. However, the transient process of dissolution of air into water was neglected. Further investigations could be conducted to take this effect into account.
- Any thermal, hydrological, or mechanical process can induce damage to the fabric of a porous medium. In the current research, the range of the thermohydro-mechanical loads was restricted to values that do not alter the characteristics of the rock and therefore no damage was observed in the experiments. An extension of this research could be the study of the THM behaviour of damage-susceptible geomaterials.
- The samples used in the THM tests were cylinders with partially drilled central cavities, heated on the outer boundaries. Performing tests on samples with different geometries and boundary conditions, along with strain gauge

instrumentation of the samples, could provide more information on the coupling behaviour of low permeability rocks under thermal loads.

## REFERENCES

- Aboustit, B.L., Advani, S.H. & Lee, J.K. (1985), Variational principles and finite element simulations for thermo-elastic consolidation. *International Journal for Numerical and Analytical Methods in Geomechanics*, Vol. **9**, 49-69.
- Adachi, J. & Detournay, E. (1997), A Poroelastic solution of the oscillating pore pressure method to measure permeabilities of "tight" rocks. *International Journal of Rock Mechanics and Mining Sciences and Geomechanics Abstracts*, 1997; 430.
- Aligizaki, K.K. (2006), Pore Structure of Cement-based Materials: Testing, Interpretation and Requirements, Taylor & Francis, New York.
- Alonso, E.E., Alcoverro, J., Coste, F., Malinsky, L., Merrien-Soukatchoff, V., Kadiri, I., Nowak, T., Shao, H., Nguyen, T.S., Selvadurai, A.P.S., Armand, G., Sobolik, S.R., Itamura, M., Stone, C.M., Webb, S.W., Rajeb, A., Tijani, M., Maouche, Z., Kobayashi, A., Huikami, H., Ito, A., Sugita, Y., Chijimatsu, M., Borgesson, L., Hernelind, J., Rutqvist, J., Tsang, C.F. & Jussia, P. (2005), The FEBEX benchmark test: case definition and comparison of modelling approaches. *International Journal of Rock Mechanics and Mining Sciences*, Vol. 42, 611-638.
- ASTM D2936-08 (2004), Standard test method for direct tensile strength of intact rock core specimens.
- ASTM D3967-08 (2004), Standard test method for splitting tensile strength of intact rock core specimens.
- ASTM D4404-84 (2004), Standard test method for determination of pore volume and pore volume distribution of soil and rock by mercury intrusion porosimetry.

- ASTM D7012-04 (2004), Standard test method for compressive strength and elastic moduli of intact rock core specimens under varying states of stress and temperature.
- Bachu, S. (2008), CO<sub>2</sub> storage in geological media: role, means, status and barriers to deployment. *Progress in Energy and Combustion Sciences*, Vol. **34**, 254-273.
- Bai, M & Roegiers, J.C. (1994), Fluid flow and heat flow in deformable fractured porous media. *International Journal of Engineering Science*, Vol. **32**, 1615-1633.
- Barenblatt, G.I., Entov, V.M. & Ryzhik, V.M. (1989), *Theory of Fluid Flows through Natural Rocks*. Kluwer Academic Publishers, Boston.
- Barron, R.A. (1948), The influence of drain wells on the consolidation of fine-grained soils. *Transact ASCE*, Vol. **113**, 718-742.
- Bear, J. (1972), *Dynamics of Fluids in Porous Media*. Dover Publications, New York.
- Belotserkovets, A. & Prevost, J.H. (2011), Thermoporoelastic response of a fluid-saturated porous sphere: An analytical solution. *International Journal of Engineering Science*, Vol. **49**, 1415-1423.
- Berge, P.A., Wang, H.F. & Bonner, B.P. (1993), Pore pressure buildup coefficient in synthetic and natural sandstones. *International Journal of Rock Mechanics and Mining Sciences and Geomechanics Abstracts*, Vol. **30**, 1135-1141.
- Bernabe, Y. (1986), The effective pressure law for permeability in Chelmsford Granite and Barre Granite. *International Journal of Rock Mechanics and Mining Science*, Vol. **23**, 267-275.
- Biot, M.A. (1941a), General theory of three-dimensional consolidation. *Journal of Applied Physics*, Vol. **12**, 155-164.
- Biot, M.A. (1941b), Consolidation settlement under a rectangular load distribution. *Journal of Applied Physics*, Vol. **12**, 426-430.

- Biot, M.A. (1955), Theory of elasticity and consolidation for a porous anisotropic solid. *Journal of Applied Physics*, Vol. **26**, 182-185.
- Biot, M.A. (1956), General solutions of the equations of elasticity and consolidation for a porous material. *Journal of applied Mechanics*, Vol. **23**, 91-96.
- Biot, M.A. & Clingan, F.M. (1941), Consolidation settlement of a soil with an impervious top surface. *Journal of Applied Physics*, Vol. **12**, 578-581.
- Biot, M.A. & Clingan, F.M. (1942), Bending settlement of a slab resting on a consolidating foundation. *Journal of Applied Physics*, Vol. **13**, 35-40.
- Biot, M.A. & Willis, D.G. (1957) The elastic coefficients of the theory of consolidation. *Journal of Applied Mechanics*, Vol. **24**, 594-601.
- Blatt, H., Tracy, R. & Owens, B. (2005), *Petrology: Igneous, Sedimentary, and Metamorphic*, WH Freeman, New York.
- Booker, J.R. & Savvidou, C. (1984), Consolidation around a spherical heat source. *International Journal of Solids and Structures*, Vol. **20**, 1079-1090.
- Booker, J.R. & Savvidou, C. (1985), Consolidation around a point heat source. *International Journal for Numerical and Analytical Methods in Geomechanics*, Vol. **9**, 173-184.
- Boone, T.J. & Detournay, E. (1990), Response of a vertical hydraulic fracture intersecting a poroelastic formation bounded by semi-infinite impermeable elastic layer. *International Journal of Rock Mechanics and Mining Sciences and Geomechanics Abstracts*, Vol. 27, 189-197.
- Bowen, R.M. (1980), Incompressible porous media models by use of the theory of mixtures. *International Journal of Engineering Science*, Vol. **18**, 1129-1148.
- Brace, W.F., Walsh, J.B. & Frangos, W.T. (1968), Permeability of granite under high pressure. *Journal of Geophysical Research*, Vol. **73**, 2225-2236.

- Bredehoeft, J.D. & Papadopulos, S.S. (1980), A method for determining the hydraulic properties of tight formations. *Water Resources Research*, Vol. **16**, 233-238.
- Brownell, Jr D.H., Garg, S.K. & Pritchett, J.W. (1977), Governing equations for geothermal reservoirs. *Water Resources Research*, Vol. **13**, 929-934.
- Bodvarsson, G.S. & Stefansson, V. (1989), Some theoretical and field aspects of reinjection in geothermal reservoirs. *Water Resources Research*, Vol. **25**, 1235-1248.
- Burbey, T. (2008), The influence of geologic structure on deformation due to ground water withdrawal. *Ground Water*, Vol. **46**, 202-211.
- Carmichael, R.S. (1982), *Handbook of Physical Properties of Rocks*, CRC Press, Florida.
- Carnaffan, P. (1994), An experimental technique for determining the permeability of rock, concrete and cement grout, M.Eng. thesis, Department of Civil Engineering and Environmental Engineering, Carlton University, Ottawa.
- Carsla,w H.S. & Jaeger, J.C. (1959), *Conduction of heat in solids*, Oxford University Press, London.
- Chen, Y., Zhou, C. & Jing, L. (2009), Modeling coupled THM processes of geological porous media with multiphase flow: theory and validation against laboratory and field scale experiments. *Computers and Geotechnics*, Vol. **36**, 1308-1329.
- Chijimatsu, M., Nguyen, T.S., Jing, L., De Jonge, J., Kohlmeire, M., Millard, A., Rajeb, A., Rutqvist, J., Souley, M. & Sugita, Y.(2005), Numerical study of the THM effects on the near-field safety of a hypothetical nuclear waste repository—BMT1 of the DECOVALEX III project. Part 1: conceptualization and characterization of the problems and summary of results. *International Journal of Rock Mechanics and Mining Sciences*, Vol. **42**, 720-730.

- Cooper, Jr H.H., Bredehoeft, J.D. & Papadopulos, I.S. (1967), Response of a finite-diameter well to an instantaneous charge of water. *Water Resources Research*, Vol. **3**, 263-269.
- Coussy, O. (1989), A general theory of thermoporoelastoplasticity for saturated porous materials. *Transport in Porous Media*, Vol. **4**, 281-293.
- Coussy, O. (1995), *Mechanics of Porous Continua*, John Wiley & Sons, Chichester.
- Cryer, C.W. (1963), A comparison of the three-dimensional consolidation theories of Biot and Terzaghi. *The Quarterly Journal of Mechanics and Applied Mathematics*, Vol. **16**, 401-412.
- Darcy, H. (1856), Les Fontaines Publiques de la Ville de Dijon, Dalmont, Paris.
- de Boer, R. (1999), *Porous Media: Theory and Experiments*, Kluwer Academic, New York.
- de Boer, R. (2005), *The Engineer and the Scandal: a Piece of Science History*, Springer, Berlin.
- de Jong, G.J. & Verruijt, A. (1965), Primary and secondary consolidation of a spherical clay sample. In *Proceedings of the Sixth International Conference on Soil Mechanics and Foundation Engineering. Montreal, Canada*, Vol. 1, pp. 254-258. Toronto: University of Toronto Press.
- de Wet, J. (1962), Highway Research Board, US Nat. Acad. Sc. Bulletin.
- Dewiere, L., Plas, F. & Tsang, C.F. (1996), Lessons learned from DECOVALEX. Developments in Geotechnical Engineering, Vol. 79, 495-504.
- Detournay, E. & Cheng, A.H-D. (1990), Plane strain analysis of a stationary hydraulic fracture in a poroelastic medium. *International Journal of Solids and Structures*, Vol. **27**, 1645-1662.
- Detournay, E & Cheng, A.H-D. (1993), Fundamentals of poroelasticity. In *Comprehensive Rock Engineering* (ed. J.A. Hudson), pp. 113-171. New York: Pergamon Press.

- Dewiere, L., Plas, F. & Tsang, C.F. (1996), Lessons learned from DECOVALEX. *Developments in Geotechnical Engineering*, Vol. **79**, 495-504.
- Fillunger, P. (1936), Erdbaumechanik?, Selbstverl, Vienna.
- Fredlund, D.G. (1976), Density and compressibility characteristics of air-water mixtures. *Canadian Geotechnical Journal*, Vol. **13**, 386-396.
- Geertsma, J. (1973), Land subsidence above compacting oil and gas reservoirs. *Journal of Petroleum Technology*, Vol. **25**, 734-744.
- Gens, A., Garcia-Molina, A.J., Olivella, S., Alonso, E.E. & Huertas, F. (1998), Analysis of a full scale in situ test simulating repository conditions. *International Journal for Numerical and Analytical Methods in Geomechanics*, Vol. 22, 515-548.
- Gibson, R.E., Gobert, A. & Schiffman, R.L. (1989), On Cryer's problem with large displacements. *International Journal for Numerical and Analytical Methods in Geomechanics*, Vol. **13**, 251-262.
- Gibson, R., Knight, K. & Taylor, P. (1963), A critical experiment to examine theories of three-dimensional consolidation. In *Proceedings of European Conference on Soil Mechanics and Foundation Engineering*, Vol. 1, pp. 69-76, Wiesbaden: Deutsche Gesellschaft für Erd-und Grundbau.
- Gorban, B.D., Brigham, W.E. & Ramey Jr, H.J. (1987), Absolute permeability as a function of confining pressure, pore pressure, and temperature. *Society of Petroleum Engineering-Formation Evaluation*, Vol. **2**, 77-84.
- Gurtin, M.E. (1966), Variational principles for linear initial value problems. *Quarterly of Applied Mathematics*, Vol. **12**, 252-256.
- Gutierrez, M. & Makurat, A. (1997), Coupled THM modelling of cold water injection in fractured hydrocarbon reservoirs. *International Journal of Rock Mechanics and Mining Science*, Vol. **34**, 113.e1-113.e15.
- Hansbo, S. (1979), Consolidation of clay by band-shaped prefabricated drains. *Ground Engineering*, Vol. **12**, 16-25.

- Hansbo, S. (1981), Consolidation of fine-grained soils by prefabricated drains. In *Proceedings of the 10<sup>th</sup> International Conference on Soil Mechanics and Foundation Engineering, Stockhom*, (ed. Publications Committee of X. ICSMFE), pp. 677-682. Rotterdam: Balkema
- Hart, D.J. & Wang, H.F. (1995), Laboratory measurements of a complete set of poroelastic moduli for Berea sandstone and Indiana limestone. *Journal of Geophysical Research*, Vol. **100**, 17741-17751.
- Hart, D.J. & Wang, H.F. (1998), Poroelastic effects during a laboratory transient pore pressure test. In *Poromechanics* (ed. J.F. Thimus, Y. Abousleiman, A.H.-D. Cheng, O. Coussy & E. Detournay), pp. 579-582. Rotterdam: Balkema.
- Heiland, J. (2003), Laboratory testing of coupled hydro-mechanical processes during rock deformation. *Hydrogeology Journal*, Vol. **11**, 122-141.
- Heinrich, V.G. & Desoyer, K. (1961), Theorie dreidimensionaler Setzungsvorgänge in Tonschichten. *Archive of Applied Mechanics*, Vol. **30**, 225-253.
- Heystee, R. & Roegiers, J.-C. (1981), The effect of stress on the primary permeability of rock cores-a facet of hydraulic fracturing. *Canadian Geotechnical Journal*, Vol. **18**, 195-204.
- Holzbecher, E.O. (1998), Modeling Density-Driven Flow in Porous Media: Principles, Numerics, Software, Springer, New York.
- Hsieh, P.A. (1996), Deformation-induced changes in hydraulic head during ground-water withdrawal. *Ground Water*, Vo. **34**, 1082-1089.
- Hsieh, P.A., Tracy, J.V., Neuzil, C.E., Bredehoeft, J.D. & Silliman, S.E. (1981), A transient laboratory method for determining the hydraulic properties of 'tight'rocks—I. theory. *International Journal of Rock Mechanics and Mining Sciences and Geomechanics Abstracts*, Vol. 18, 245-252.
- Ilyasov, M., Ostermann, I. & Punzi, A. (2010), Modelling deep geothermal reservoirs: recent advances and future problems. In *Handbook of*

- *Geomathematics* (ed. W., Freeden, M.Z. Nashed & T., Sonar), pp. 679-711. Berlin: Springer.
- Iqbal M.J. & Mohanty, B. (2007), Experimental calibration of ISRM suggested fracture toughness measurement techniques in selected brittle rocks. *Rock Mechanics and Rock Engineering*, Vol. **40**, 453-475.
- Jing, L., Tsang, C.F. & Stephansson, O. (1995), DECOVALEX-an international co-operative research project on mathematical models of coupled THM processes for safety analysis of radioactive waste repositories. *International Journal of Rock Mechanics and Mining Sciences and Geomechanics Abstracts*, Vol. 5, 389-398.
- Kiyama, T., Kita, H., Ishijima, Y., Yanagidani, T., Aoki, K. & Sato T. (1996), Permeability in anisotropic granite under hydrostatic compression and triaxial compression including post-failure region. In *Proceedings of 2<sup>nd</sup> North American Rock Mechanics Symposium* (ed. M. Aubertin, F. Hassani & H. Mitri), pp. 1643-1650. Rotterdam: Taylor & Francis.
- Kodashima, T. & Kurashige, M. (1996), Thermal stresses in a fluid-saturated poroelastic hollow sphere. *Journal of Thermal Stresses*, Vol. **19**, 139-151.
- Kranz, R.L., Frankel, A.D., Engelder, T. & Scholz, C.H. (1979), The permeability of whole and jointed Barre granite. *International Journal of Rock Mechanics and Mining Sciences and Geomechanics Abstracts*, Vol. **16**, 225-234.
- Kranz, R.L., Saltzman, J.S. & Blacic, J.D. (1990), Hydraulic diffusivity measurements on laboratory rock samples using an oscillating pore pressure method. *International Journal of Rock Mechanics and Mining Sciences and Geomechanics Abstracts*, Vol. 27, 345-352.
- Lecampion, B., Constantinescu, A. & Malinsky, L. (2006), Identification of poroelastic constants of "tight" rocks from laboratory tests. *International Journal of Geomechanics*, Vol. 6, 201-208.

- Lemieux, J.-M. (2011), Review: the potential impact of underground geological storage of carbon dioxide in deep saline aquifers on shallow groundwater resources. *Hydrogeology Journal*, Vol. **19**, 757-778.
- Lewis, R.W. & Schrefler, B.A. (1998), The Finite Element Method in the Static and Dynamic Deformation and Consolidation of Porous Media, John Wiley, Chichester.
- Lin, W. (1977), Compressible fluid flow through rocks of variable permeability. *Lawrence Livermore Laboratory*, Livermore, California, Rept. UCRL-52304.
- Mandel, J. (1953), Consolidation des sols (Étude Mathématique). *Geotechnique*, Vol. **3**, 287-299.
- Mason, D.P., Solomon, A. & Nicolaysen, L.O. (1991), Evolution of stress and strain during the consolidation of a fluid-saturated porous elastic sphere. Journal of Applied Physics, Vol. **70**, 4724-4740.
- McGuire, M.F. (2008), *Stainless Steels for Design Engineers*, ASM International, Ohio.
- McNamee, J. & Gibson, R.E. (1960a), Displacement functions and linear transforms applied to diffusion through porous elastic media. *The Quarterly Journal of Mechanics and Applied Mathematics*, Vol. **13**, 98-111.
- McNamee, J. & Gibson, R.E. (1960b), Plane strain and axially symmetric problems of the consolidation of a semi-infinite clay stratum. *The Quarterly Journal of Mechanics and Applied Mathematics*, Vol. **13**, 210-227.
- McTigue, D.F. (1986), Thermoelastic response of fluid-saturated porous rock. *Journal of Geophysical Research: Solid Earth*, Vol. **91**, 9533-9542.
- Millard. A., Rajeb, A., Chijimatsu, M., Jing, L., De Jonge, J., Kohlmeier, M., Nguyen, T.S., Rutqvist, J., Souley M. & Sugita, Y. (2005), Numerical study of the THM effects on the near-field safety of a hypothetical nuclear waste repository—BMT1 of the DECOVALEX III project. Part 2: effects of THM

- coupling in continuous and homogeneous rocks. *International Journal of Rock Mechanics and Mining Sciences*, Vol. **42**, 731-744.
- Morin, R.H & Olsen, H.W. (1987), Theoretical analysis of the transient pressure response from a constant flow rate hydraulic conductivity test. *Water Resources Research*, Vol. **23**, 1461-1470.
- Morland, L.W. (1978), A theory of slow fluid flow through a porous thermoelastic matrix. *Geophysical Journal of the Royal Astronomical Society*, Vol. **55**, 393-410.
- Murayama, S. & Akai, K. (1954), Failure of the embankment foundation (Studies on the failure and the settlement of foundations). *Bulletins-Disaster Prevention Research Institute, Kyoto University*, Vol. **8**, 1-15.
- Nasseri, M.H.B, Grasselli, G & Mohanty, B. (2010), Fracture toughness and fracture roughness in anisotropic granitic rocks. *Rock Mechanics and Rock Engineering*, Vol. **43**, 403-415.
- Nakao, S, & Ishido, T. (1998), Pressure-transient behaviour during cold water injection into geothermal wells. *Geothermics*, Vol. **27**, 401-413.
- Naylor, A.H. (1948), Precise determination of primary consolidation. In *Proceedings of the 2<sup>nd</sup> International Conference on Soil Mechanics and Foundation Engineering, Rotterdam, the Netherlands* (ed. Publications Committee of II. ICSMFE), pp. 34-40. Rotterdam: Balkema
- Neuzil, C.E., Cooley, C., Silliman, S.E., Bredehoeft, J.D. & Hsieh, P.A. (1981), A transient laboratory method for determining the hydraulic properties of 'tight'rocks—II. Application. *International Journal of Rock Mechanics and Mining Sciences and Geomechanics Abstracts*, Vol. **18**, 253-258.
- Nguyen, T.S. & Selvadurai, A.P.S. (1995), Coupled thermal-mechanical-hydrological behaviour of sparsely fractured rock: Implications for nuclear fuel waste disposal. *International Journal of Rock Mechanics and Mining Sciences*, Vol. **32**, 465-479.

- Nguyen, T.S., Selvadurai, A.P.S. & Armand, G. (2005), Modelling the FEBEX THM experiment using a state surface approach. *International Journal of Rock Mechanics and Mining Sciences*, Vol. **42**, 639-651.
- Nguyen, T.S., Borgesson, L., Chijimatsu, M., Hernelind, J., Jing, L., Kobayashi, A. & Rutqvist, J. (2009), A case study on the influence of THM coupling on the near field safety of a spent fuel repository in sparsely fractured granite. *Environmental Geology*, Vol. 57, 1239-1254.
- Noorishad, J., Tsang, C.F. & Witherspoon, P.A. (1984), Coupled thermal-hydraulic-mechanical phenomena in saturated fractured porous rocks: Numerical approach. *Journal of Geophysical Research: Solid Earth*, Vol. **89**, 10365-10373.
- Pao, W.K.S., Lewis, R.W. & Masters, I. (2001), A fully coupled hydro-thermo-poro-mechanical model for black oil reservoir simulation. *International Journal for Numerical and Analytical Methods in Geomechanics*, Vol. **25**, 1229-1256.
- Papadopulos, S.S., Bredehoeft, J.D. & Cooper, H.H. (1973), On the analysis of 'slug test'data. *Water Resources Research*, Vol. **9**, 1087-1089.
- Paria, G. (1957), Axisymmetric consolidation for a porous elastic material containing a fluid under an impulsive force. *J Sc Enggr Res, Kharagpur*, Vol. **1**, 185-194.
- Paria, G. (1963), Flow of fluids through porous deformable solids. *Applied Mechanics Reviews*, Vol. **6**, 901–907.
- Pietruszczak, S. & Pande, G.N. (1996), Constitutive relations for partially saturated soils containing gas inclusions. *Journal of Geotechnical Engineering-ASCE*, Vol. **122**, 50-59.
- Rehbinder, G. (1995), Analytical solutions of stationary coupled thermo-hydromechanical problems. *International Journal of Rock Mechanics and Mining Sciences and Geomechanics Abstracts*, Vol. **32**, 453-463.

- Rendulic, L. (1936), Porenziffer und poren wasserdruck in Tonen. *Bauingenieur*, Vol. **17**:559-564.
- Rice, J.R. & Cleary, M.P. (1976), Some basic stress diffusion solutions for fluid-saturated elastic porous media with compressible constituents. *Reviews of Geophysics*, Vol. **14**: 227-241.
- Richart, F.E. (1957), A Review of the Theories for Sand Drains, University of Florida, Florida.
- Ritter, H.L. & Drake, L.C. (1945), Pore size distribution in porous materialspressure porosimeter and determination of completer macropore-size distributions. *Industrial and Engineering Chemistry Analytical Edition*, Vol. 17, 782-786.
- Rootare, H.M., Prenzlow, C.F. (1967), Surface areas from mercury porosimeter measurements. *The Journal of Physical Chemistry*, Vol. **71**, 2733-2736.
- Rowe, P.W. (1966), A new consolidation cell. Geotechnique, Vol. 16, 162-170.
- Rowe, P.W. (1968), The influence of geological features of clay deposits on the design and performance of sand drains. *ICE Proceedings*, Vol. **39**, 465-466.
- Rutqvist, J., Borgesson, L., Chijimatsu, M., Kobayashi, A., Jing, L., Nguyen, T.S., Noorishad, J. & Tsang, C.F. (2001), Thermohydromechanics of partially saturated geological media: governing equations and formulation of four finite element models. *International Journal of Rock Mechanics and Mining Sciences*, Vol. 38, 105-127.
- Rutqvist, J., Chijimatsu, M., Jing, L., Millard, A., Nguyen, T.S., Rajeb, A. Sugita, Y. & Tsang, C.F. (2005), A numerical study of THM effects on the near-field safety of a hypothetical nuclear waste repository—BMT1 of the DECOVALEX III project. Part 3: Effects of THM coupling in sparsely fractured rocks. *International Journal of Rock Mechanics and Mining Sciences*, Vol. 42, 745-755.
- Savvidou, C. & Booker, J.R. (1988), Consolidation around a spherical heat source with a decaying power output. *Computers and Geotechnics*, Vol. **5**, 227-244.

- Schanz, M. (2009), Poroelastodynamics: linear models, analytical solutions, and numerical methods. *Applied Mechanics Reviews*, Vol. **62**: 1-15.
- Scheidegger, A.E. (1960), Flow through porous media. *Applied Mechanics Reviews*, Vol. **13**, 313–318.
- Schiffman, R.L., Chen, A.T. & Jordan, J.C. (1969), An analysis of consolidation theories. *Journal of Soil Mechanics and Foundations Div.*, *ASCE*, Vol. **95**, 285-312.
- Schmertmann, J.H. (1953), Estimating the true consolidation behaviour of clay from laboratory test results. *Proceedings ASCE*, Vol. **79**, 1-26.
- Schuurman, I.E. (1966), The compressibility of an air-water mixture and a theoretical relation between the air and water pressures. *Geotechnique*, Vol. **16**, 269-281.
- Scott, R.F. (1961), New method of consolidation coefficient evaluation. *Journal of Soil Mechanics and Foundation Division, ASCE*, Vol. **87**, 29-39.
- Selvadurai, A.P.S. (1996a), *Mechanics of Poroelastic Media*, Kluwer Academic Publishers, Boston.
- Selvadurai, A.P.S. (1996b), Heat-induced moisture movement in a clay barrier I. Experimental modelling of borehole emplacement. *Engineering Geology*, Vol. **41**, 239-256.
- Selvadurai, A.P.S. (2000a), Partial Differential Equations in Mechanics 1: Fundamentals, Laplace's Equation, Diffusion Equation, Wave Equation, Springer, New York.
- Selvadurai, A.P.S. (2000b), Partial Differential Equations in Mechanics 2: The Biharmonic Equation, Poisson's Equation. Springer, New York.
- Selvadurai, A.P.S. (2002), Influence of pressurized water influx on the hygrothermal behaviour of an engineered clay barrier in a waste emplacement borehole. *Engineering Geology*, Vol. **64**, 157-178.

- Selvadurai, A.P.S. (2007), The analytical method in geomechanics. *Applied Mechanics Reviews*, Vol. **60**, 87-106.
- Selvadurai, A.P.S. (2009), Influence of residual hydraulic gradients on decay curves for one-dimensional hydraulic pulse tests. *Geophysical Journal International*, Vol. **177**, 1357-1365.
- Selvadurai, A.P.S. (2013), Caprock breach: a potential threat to secure geologic sequestration of CO<sub>2</sub>. In *Geomechanics in CO2 Storage facilities* (ed. G. Pijaudier-Cabot, J.-M., Pereira), pp. 75-94. New York: John Wiley & Sons.
- Selvadurai, A.P.S. (2013), Mechanics of Groundwater Flow, Lecture notes. McGill University.
- Selvadurai, A.P.S & Carnaffan, P. (1997), A transient pressure pulse method for the measurement of permeability of a cement grout. *Canadian Journal of Civil Engineering*, Vol. **24**, 489-502.
- Selvadurai, A.P.S & Głowacki, A. (2008), Permeability hysterisis of limestone during isotropic compression. *Groundwater*, Vol. **46**, 113-119.
- Selvadurai, A.P.S. & Ichikawa, Y. (2013), Some aspects of air-entrainment on decay rates in hydraulic pulse tests. *Engineering Geology*, http://dx.doi.org/10.1016/j.enggeo.2013.05.023
- Selvadurai, A.P.S. & Jenner, L. (2013), Radial flow permeability testing of an argillaceous limestone. *Groundwater*, Vol. **51**, 100-107.
- Selvadurai, A.P.S. & Nguyen, T.S. (1995), Computational modelling of isothermal consolidation of fractured porous media. *Computers and Geotechnics*, Vol. **17**, 39-73.
- Selvadurai, A.P.S & Nguyen, T.S. (1997), Scoping analyses of the coupled thermal-hydrological-mechanical behaviour of the rock mass around a nuclear fuel waste repository. *Engineering Geology*, Vol. **47**, 379-400.
- Selvadurai, A.P.S. & Selvadurai, P.A. (2007), On cavity flow permeability testing of a sandstone. *Ground Water*, Vol. **45**, 93-97.

- Selvadurai, A.P.S. & Selvadurai, P.A. (2010), Surface permeability tests: experiments and modelling for estimating effective permeability. *Proceedings of the Royal Society A: Mathematical, Physical and Engineering Science*, Vol. **466**, 2819-2846.
- Selvadurai, A.P.S & Shirazi A. (2004), Mandel–Cryer effects in fluid inclusions in damage-susceptible poroelastic geologic media. *Computers and Geotechnics*, Vol. **31**, 285-300.
- Selvadurai, A.P.S & Suvorov, A. (2010), Application of the COMSOL Multiphysics code for coupled thermo-hydro-mechanical modeling relevant to deep geologic repositories. *Nuclear Waste Management Office Report NWMO* TGS-509, ON, Canada.
- Selvadurai, A.P.S. & Suvorov, A. (2012), Boundary heating of poro-elastic and poro-elasto-plastic spheres. *Proceedings of the Royal Society A: Mathematical, Physical and Engineering Science*, **doi**: 10.1098/rspa.2012.0035.
- Selvadurai, A.P.S, Boulon, M.J. & Nguyen, T.S. (2005), The permeability of an intact granite. *Pure and Applied Geophysics*, Vol. **162**, 373-407.
- Selvadurai, A.P.S., Letendre, A. & Hekimi, B. (2011a), Axial flow hydraulic pulse testing of an argillaceous limestone. *Environmental Earth Sciences*, Vol. **64**, 2047-2058.
- Selvadurai, A.P.S., Suvorov, A. & Selvadurai, P.A. (2011b), Application of the COMSOL Multiphysics code for coupled thermo-hydro-mechanical modeling of fractured rock mass subjected to glaciation Loads. *Nuclear Waste Management Office Report NWMO* TGS-510, ON, Canada.
- Selvadurai, P. (2010), *Permeability of Indiana Limestone: experiments and theoretical concepts for interpretation of result*, M.Eng. thesis, Department of Civil Engineering and Applied Mechanics, McGill University, Montreal.
- Shackley, M.S. (2011), X-ray Fluorescence Spectrometry (XRF) in Geoarchaeology, Springer, New York.

- Scheidegger, A.E. (1960), Flow through porous media. *Applied Mechanics Reviews*, Vol. **13**, 313–318.
- Shiping, L., Yushou, L. Yi, L., Zhenye, W. & Gang, Z. (1994), Permeability-strain equations corresponding to the complete stress-strain path of Yinzhuang Sandstone. *International Journal of Rock Mechanics and Mining Sciences and Geomechanics Abstracts*. Vol. **31**, 383-391.
- Shukla, R., Ranjith, P.G. & Choi, S.K. (2012), A novel testing apparatus for hydromechanical investigation of rocks: geo-sequestration of carbon dioxide. *Rock Mechanics and Rock Engineering*. Vol. **45**, 1073-1085.
- Sills, G.C. (1975), Some conditions under which Biot's equations of consolidation reduce to Terzaghi's equation. *Geotechnique*. Vol. **25**, 129-132.
- Song, I. & Renner, J. (2006), Linear pressurization method for determining hydraulic permeability and specific storage of a rock sample. *Geophysical Journal International*, Vol. **164**, 685-696.
- Stephansson, O., Hudson, J.A. & Jing, L. (2004), Coupled Thermo-hydro-mechanical-chemical Processes in Geo-systems: Fundamentals, Modelling, Experiments and Applications. Elsevier, Boston.
- Suvorov, A. & Selvadurai, A.P.S. (2010), Macroscopic constitutive equations of thermo-poroviscoelasticity derived using eigenstrains. *Journal of the Mechanics and Physics of Solids*, Vol. **58**, 1461-1473.
- Terzaghi K. (1923), Die berechnung der durchlassigkeitsziffer des tones aus dem verlauf der hydrodynamischen spannungserscheinungen. *Akad Wissensch Wien Sitzungsber Mathnaturwissensch Klasse IIa*, Vol. **142**, 125-138.
- Terzaghi, K. (1943), Theoretical Soil Mechanics, John Wiley & Sons, New York.
- Teunissen, J.A.M. (1982), Mechanics of a fluid-gas mixture in a porous medium. *Mechanics of Materials*, Vol. 1: 229-237.
- Tidwell, V.C. & Wilson, J.L. (1997), Laboratory method for investigating permeability upscaling. *Water Resources Research*, Vol. **33**, 1607-1616.

- Trimmer D. (1982), Laboratory measurements of ultralow permeability of geologic materials. *Review of Scientific Instruments*, Vol. **53**, 1246-1254.
- Tsang, C.F., Jing, L., Stephansson, O. & Kautsky, F. (2005), The DECOVALEX III project: a summary of activities and lessons learned. *International Journal of Rock Mechanics and Mining Sciences*, Vol. **42**, 593-610.
- Tsang, C.F., Barnichon, J.D., Birkholzer, J., Li, X.L., Liu, H.H. & Sillen, X. (2012), Coupled thermo-hydro-mechanical processes in the near field of a high-level radioactive waste repository in clay formations. *International Journal of Rock Mechanics and Mining Sciences*, Vol. **49**, 31-44.
- Tsang, C.F., Stephansson, O. & Hudson, J. (2000), A discussion of thermohydro–mechanical (THM) processes associated with nuclear waste repositories. *International Journal of Rock Mechanics and Mining Sciences*, **37**, 397-402.
- Vaziri, H.H (1988), Coupled fluid flow and stress analysis of oil sands subject to heating. *Journal of Canadian Petroleum Technology*, **27**, 84-91.
- Verruijt, A. (1965), Discussions. In *Proceedings of the Sixth International Conference on Soil Mechanics and Foundation Engineering. Montreal, Canada*, Vol. **3**, 401-402. Toronto: University of Toronto Press.
- Walder, J. & Nur, A. (1986), Permeability measurement by the pulse-decay method: Effects of poroelastic phenomena and non-linear pore pressure diffusion. *International Journal of Rock Mechanics and Mining Sciences and Geomechanics Abstracts*, Vol. 23, 225-232.
- Wang, H.F. (1993), Quasi-static poroelastic parameters in rock and their geophysical applications. *Pure and Applied Geophysics*, Vol. **141**, 269-286.
- Wang, H.F. (2000), Theory of Linear Poroelasticity with Applications to Geomechanics and Hydrogeology, Princeton University Press, Princeton.
- Wang, H.F. & Hart, D.J. (1993), Experimental error for permeability and specific storage from pulse decay measurements. *International Journal of Rock*

- Mechanics and Mining Sciences and Geomechanics Abstracts, Vol. 30, 1173-1176.
- Wang, W., Rutqvist, J., Görke, U-J., Birkholzer, J.T. & Kolditz, O. (2011), Non-isothermal flow in low permeable porous media: a comparison of Richards' and two-phase flow approaches. *Environmental Earth Sciences*, Vol. 62, 1197-1207.
- Washburn, E.W. (1921), Note on a method of determining the distribution of pore sizes in a porous material. In *Proceedings of the National Academy of Sciences*, Vol. 7, 115-116. USA: The academy.
- White, F.M. (1986), Fluid Mechanics, McGraw-Hill, Boston, USA.
- Yue, Z.Q. (1992), *Mechanics of rigid disc inclusions in fluids saturated poroelastic media*. Ph.D. thesis, Department of Civil Engineering and Environmental Engineering, Carlton University, Ottawa.
- Zhou, Y., Rajapakse, R.K.N.D. & Graham, J. (1998), Coupled consolidation of a porous medium with a cylindrical or a spherical cavity. *International Journal for Numerical and Analytical Methods in Geomechanics*, Vol. **22**, 449-475.
- Zhu, W. & Wong, T.-f. (1997), The transition from brittle faulting to cataclastic flow: permeability evolution. *Journal of Geophysical Research-Solid Earth*, Vol. **102**, 3027-3041.
- Zimmerman, R.W. (2000), Coupling in poroelasticity and thermoelasticity. *International Journal of Rock Mechanics and Mining Sciences*, Vol. **37**, 79-87.
- Zoback, M.D. & Byerlee, J.D. (1975), The effect of microcrack dilatancy on the permeability of Westerly Granite. *Journal of Geophysical Research*, Vol. **80**, 752-755.

### APPENDIX A

# PETROLOGICAL DESCRIPTION OF STANSTEAD GRANITE (UNPUBLISHED REPORT)

- Stanstead Gray Beebe PQ

Sample 37 Granodiorite

#### Hand Specimen

This is a medium gray, medium to coarse-grained stone with a very fresh appearance. Minerals are clear, sharply defined quartz (2.5 to 5 mm); feldspar laths (2 to 3 mm) which are semi-transparent to milky white; muscovite flakes (0.5 mm) in small amounts; sharply contrasting biotite in flakes and clusters (3 mm); and some chlorite flakes (to 1 mm). No opaque minerals are seen. A polished face at 15 feet is medium dark gray (N 4) and a honed face is medium gray (N 5).

#### Thin Section

The grains are subhedral and give an interlocking granular fabric. There is some interstitial mica and epidote and a trace amount of minute, interstitial feldspar grains.

Slightly to moderately crushed quartz (36.7%) occurs as anhedra (3 to 4 mm) with occasional larger grains (to 6 mm). Plagioclase (An<sub>15-25</sub>; 37.8%; 2 to 4 mm) is commonly twinned and zoned and is somewhat altered. Potassium feldspars (12.5%) are microcline (2 to 3 mm) and orthoclase(?). Muscovite flakes (3.7%; to 1.5 mm) are subhedral to euhedral and are rarely vermicular. Biotite (7.8%) occurs in euhedral flakes (1 to 1.5 mm) and aggregates (3 to 4 mm); biotite forms small anhedral inclusions in quartz and feldspar. Epidote (1.3%; 0.5 to 1.5 mm) forms irregular grains. Opaque minerals are only found along cleavage planes of plagioclase(?) and fractures of quartz. Minerals in trace amounts are zircon and apatite.

#### Alteration

As much as 10% of a typical plagioclase grain is made of well-formed muscovite flakes (to 1 mm) that are subhedral to euhedral inclusions. Sericitization and other cloudy alteration of plagioclase is moderate and occurs along cleavage planes and zone boundaries. Zoned plagioclase grains contain some euhedral epidote inclusions. The potassium feldspar grains (microcline, orthoclase?) show little or no alteration. There are a few chlorite flakes but no partly chloritized biotite flakes.

Paul Cousins Brewster Baldwin Jan, 1975